

Sheffield Hallam University

The effect of notches and pits on corrosion fatigue strength.

TATNER, Ian.

Available from the Sheffield Hallam University Research Archive (SHURA) at:

<http://shura.shu.ac.uk/20424/>

A Sheffield Hallam University thesis

This thesis is protected by copyright which belongs to the author.

The content must not be changed in any way or sold commercially in any format or medium without the formal permission of the author.

When referring to this work, full bibliographic details including the author, title, awarding institution and date of the thesis must be given.

Please visit <http://shura.shu.ac.uk/20424/> and <http://shura.shu.ac.uk/information.html> for further details about copyright and re-use permissions.

SHEFFIELD HALLAM UNIVERSITY
LEARNING CENTRE
CITY CAMPUS, POND STREET,
SHEFFIELD S1 1WB.



L2000

Fines are charged at 50p per hour

13/7/07
SPM

16/11/07
SPM

18 SEP 2007

SPM

18 SEP 2007 5.00p

28/9/07
18.00



REFERENCE

ProQuest Number: 10701070

All rights reserved

INFORMATION TO ALL USERS

The quality of this reproduction is dependent upon the quality of the copy submitted.

In the unlikely event that the author did not send a complete manuscript and there are missing pages, these will be noted. Also, if material had to be removed, a note will indicate the deletion.



ProQuest 10701070

Published by ProQuest LLC (2017). Copyright of the Dissertation is held by the Author.

All rights reserved.

This work is protected against unauthorized copying under Title 17, United States Code
Microform Edition © ProQuest LLC.

ProQuest LLC.
789 East Eisenhower Parkway
P.O. Box 1346
Ann Arbor, MI 48106 – 1346

The Effect of Notches and Pits on Corrosion Fatigue Strength

Ian Tatner

A thesis submitted in partial fulfilment of the requirements of
Sheffield Hallam University for the degree of Doctor of
Philosophy



January 2004

Abstract

An investigation has been undertaken to examine the fatigue behaviour of two martensitic steels in air and aggressive environments. The steels studied are, 18% Ni maraging steel and FV520B, the later being a stainless steel turbine blade material and the former being a maraging steel that suffers general corrosion in mild environments. Both steels were heat treated to give similar tensile strength.

The design and manufacture of an autoclave allowed push-pull fatigue tests to be conducted in aggressive environments at elevated temperatures.

Corrosion potential was monitored using a three electrode cell and was controlled during testing. Base-line fatigue tests were conducted with a range of constant corrosion potentials, using both notched and plain FV520B specimens. In addition fatigue tests with pulsed corrosion potential were performed to asses the effect of transient corrosion conditions on the corrosion fatigue strength. The pulsed tests were designed to simulate service transients in the oxygen content and general chemical hostility in the condensing steam environment during start-up and shut down of the steam turbine.

Post test examination of fractured samples was performed using Scanning Electron Microscopy (SEM) and optical microscope techniques. The fractography results were used to quantify microstructural and fracture features of the steels.

A model based on the size and geometry of the initial corrosion pitting has been proposed to asses the fatigue life of FV520B in an aggressive environment.

The effect of pitting on the corrosion fatigue strength of FV520B has been modelled using linear elastic fracture mechanics (LEFM) type approach. The model has shown a good correlation between predicted fatigue lives with experimental results.

The results suggest that the fatigue life is governed by the mechanical stress concentrating effect of the pits rather than the electrochemical damage caused by the environment.

Finite Element Analysis (FEA) of the notch allowed calculation of the elastic stress intensity factor (K_t) for the specimen geometry used. The experimental results together with numerical results of FEA were used to calculate of the notch strength reduction factor (K_f) for the material. This has been used to derive the notch sensitivity factors (q) for both materials.

The results of fatigue tests in air showed that although both materials have similar tensile strength their plain fatigue strengths are different. The sensitivity of the fatigue strength to notches was also found to be significantly different. The maraging steel showed a higher sensitivity to a notch than the FV520B.

An empirical model has been proposed to quantify the notch sensitivity and the effects of various microstructural features on the fatigue strength. A model has been developed to predict the serviceable life of a peak hardened FV520B turbine blade subjected to aggressive low load conditions during start-up and non-aggressive high load conditions during continual running. The model is based on the conclusions suggested in the work of a threshold stress intensity factor being reached where a fatigue crack will grow from a corrosion pit at the root of a notch. The model is then used to highlight the life reduction caused to steam turbine blades due to increased numbers of start-up cycles.

Keywords

FV520B, Maraging, Corrosion Pitting, Corrosion Potential, High Temperature, Fatigue, Pulsed Damage, TRIP Steels

Statement of Postgraduate Study

During the period of research several lectures and seminars have been attended, details are given below.

- Delivery of research seminars at Sheffield Hallam University
- Attendance at Fatigue 2000 "Fatigue & Durability Assessment of Materials, Components and Structures" The fourth international conference of the Engineering Integrity Society, April 2000, Cambridge.
- Presentation of poster entitled "The Effect of Potential on the Corrosion Fatigue Strength of Turbine Blade Steels" at the Materials Congress 2002, 9-11 April 2002, London, UK.
- Full training on Philips XL40 Scanning Electron Microscope (S.E.M) held over six weeks at the Materials Research Institute Sheffield Hallam University.
- Attendance at series of lectures and tutorials at Sheffield Hallam University leading to MSc. units in Research Methods and Research Studies.
- Attendance and completion at a Research Councils' Graduate School. A five day residential course at the University of Stirling that covered: Awareness of personal transferable skills and attributes, skills and processes required for team building and techniques needed for personal career management.

Acknowledgments

I would like to thank Prof. Atkinson for his support and advice throughout this project. I would also like to thank Dr R. Akid and Dr U. Fernando for their help and advice at various stages of the work.

The continued encouragement of friends and family even though they're not sure what it was I was doing made completion possible. I would like to acknowledge the following people amongst others for making me happy and inspiring me, Nick, Alice, Tanya, Lee, Stella, and James Lorbiecki.

I want to thank the technical staff in the School of Engineering at Hallam University for their help and work, in particular John Bradshaw for invaluable assistance, Brian Palmer for his help with instrumentation, Roger, John and Brian for workshop assistance, and Keith and Tim for helping with experimental work.

"This is just a ride" Bill Hicks

Contents

Abstract	I
Statement of Postgraduate Study.....	III
Acknowledgments.....	IV
Contents.....	V
. Nomenclature.....	X
List of Figures	XII
List of Tables.....	XXVI
1 Introduction	1
2 Literature Review.....	4
2.1 Introduction	4
2.2 Turbine Blades	4
2.2.1 Steam Turbines.....	4
2.2.2 Stresses Acting on LP Turbine Blades.....	5
2.2.3 Environmental Conditions Near an LP Steam Turbine Blade	6
2.2.4 Steam Turbine Blade Materials.....	7
2.2.5 Failures in LP Turbine Blades.....	12
2.2.6 Corrosion Fatigue Strength of Turbine Blade Materials	13
2.3 Maraging Steels	14
2.3.1 18%Ni Maraging Steels.....	14
2.3.2 Heat Treatment of Maraging Steels.....	18
2.3.3 TRIP Steels.....	18
2.3.4 Corrosion Properties Maraging Steels.....	20

2.3.5	Stress Corrosion Cracking of 18% Ni Maraging Steels	21
2.3.6	Air Fatigue And Corrosion Fatigue of 18% Ni Maraging Steel	21
2.4	Air Fatigue	24
2.4.1	A Brief Historical Review	24
2.4.2	Crack Initiation	26
2.4.3	Fatigue Crack Propagation	29
2.4.4	Linear Elastic Fracture Mechanics	30
2.5	Effect of Grain Size on Fatigue Strength of Metals	35
2.6	Fatigue at Notches	39
2.6.1	Fatigue Crack Growth at Notches	40
2.6.2	The Initiation of Fatigue Cracks From Notches	42
2.6.3	Models of fatigue Crack Propagation From a Notch	51
2.7	Non-Metallic Inclusions	54
2.7.1	Effect of Inclusions on in Air Fatigue Strength	54
2.7.2	Models Used To Account For Non-Metallic Inclusions And Their Effect On Fatigue Strength	56
2.8	Corrosion	61
2.8.1	Introduction	61
2.8.2	Pitting Corrosion	61
2.8.3	Models of Pit Growth	63
2.8.4	Effect of Notches on Electrochemical Corrosion Processes	67
2.8.5	Corrosion At Inclusion Sites	68
2.9	Corrosion Monitoring and Control	72
2.9.1	Introduction	72
2.9.2	Theory of Potential control	72

2.9.3	The Three Electrode Cell	73
2.10	Corrosion fatigue.....	76
2.10.1	Introduction	76
2.10.2	Corrosion Fatigue Crack Initiation.....	78
2.10.3	Corrosion Fatigue Crack Propagation	87
2.10.4	Electrochemical Effects in Corrosion fatigue	89
2.11	Models of Corrosion Fatigue.....	96
2.11.1	Introduction	96
2.11.2	Superposition Model of Corrosion Fatigue Crack Growth	96
2.11.3	Process Competition Model	97
2.11.4	Stress Corrosion Cracking (SCC)	109
2.12	Potential Control and Monitoring of Corrosion Fatigue Tests.....	111
2.12.1	Introduction	111
2.12.2	Effect of Potential on Corrosion Fatigue.....	111
2.12.3	Effect of Applied Stress on Corrosion Potential	112
2.12.4	Effect of Dissolved Oxygen on The Fatigue Strength of Steels.....	114
2.12.5	Effect of Dissolved Oxygen Concentration on Potential	115
3	Experimental Procedure	116
3.1	Introduction	116
3.2	Experimental Progam	116
3.3	Material Characterisation	117
3.3.1	FV520B	117
3.3.2	18 % Ni Marageing Steel	117
3.3.3	Heat Treatment.....	118
3.4	Determination of Static Material Properties	120

3.4.1	Tensile Testing.....	120
3.4.2	Material Hardness Testing	121
3.4.3	Slow Strain Rate Testing.....	121
3.4.4	Electrochemical Testing.....	122
3.4.5	Non-Metallic Inclusion Counting.....	123
3.4.6	Scanning Electron Microscopy	123
3.4.7	Finite Element Analysis	124
3.5	Fatigue Testing Program.....	125
3.5.1	Fatigue Specimen Design.....	125
3.5.2	Air Fatigue Tests	126
3.5.3	Corrosion Fatigue.....	126
4	Results of Experimental Program.....	136
4.1	Introduction.....	136
4.2	Static Material Testing	136
4.2.2	Potentiodynamic Test Results	139
4.2.3	Non-Metallic Inclusion Count Results.....	141
4.2.4	F.E.A Test Results.....	142
4.3	Air Fatigue Test Results	143
4.3.1	Corrosion Fatigue Test Results	146
4.3.2	Pulse Damage Corrosion Fatigue Test Results	154
5	Discussion	155
5.1	Introduction.....	155
5.2	Interpretation of Slow Strain Test Results	155
5.3	Interpretation of Potentiodynamic Electrochemical Test Results.....	158

5.4	Effect of Microstructure on Air Fatigue Behaviour	159
5.4.1	The Effects of Non-Metallic Inclusion on Air Fatigue Strength.....	162
5.4.2	Air Fatigue Notch Response	165
5.5	Corrosion Fatigue.....	177
5.5.1	Role of Environment.....	177
5.5.2	Effect of Temperature	178
5.5.3	Imposed Potential Corrosion Fatigue Behaviour	183
5.5.4	Corrosion Fatigue in Plain Specimens	193
5.5.5	Pulsed Imposed Potential Corrosion Fatigue Test Remarks	205
5.5.6	Fracture Surfaces of Pulsed Potential Corrosion Fatigue Tests	210
5.5.7	Modelling of Pulsed Corrosion Testing Threshold.....	220
5.6	Modelling of Experimental Fatigue Life.....	225
5.6.1	Introduction.....	225
5.6.2	Fatigue Crack Initiation from a Corrosion Pit.....	225
5.6.3	Fatigue Crack Propagation.....	228
5.6.4	Calculation of Total Life.....	232
5.7	The Effect of The Number of Start-Up Cycles on The Life of a Steam Turbine Blade.....	234
5.7.1	Introduction.....	234
5.7.2	Assumptions.....	234
6	Conclusions.....	239
7	Future Work.....	241
8	References.....	242

Nomenclature

ΔK	Stress Intensity Factor Range	$MPa\sqrt{m}$
α	Geometry Factor	
σ	Stress	MPa
a	Crack length	μm
C,m	Paris Constants	
$\frac{da}{dN}$	Crack Growth Rate with Respect to Load Cycles	$\mu m/cycle$
σ_y	Yield Stress	MPa
d	Average Grain Diameter	μm
k_y	Constant Associated with the Generation of Dislocations	
σ_i	Constant Associated with the Resistance of a Metal to the Movement of dislocations	
ΔK_{th}	Threshold Stress Intensity Factor Range	$MPa\sqrt{m}$
K_c	Fracture Toughness	$MPa\sqrt{m}$
ρ	Notch Root Radius	mm
N_i	Number of Load Cycles Required to Initiate a Fatigue Crack	
σ_w	Fatigue Limit	MPa
τ	Shear Stress Amplitude	MPa
R	Stress Ratio	
Q	Depth of Metal Removed due to applied Current	μm
z	Number of Eletrons Released During Anodic Metal Dissolution	
M	Molecular Weight	g/mol

F	Faraday's Constant	96500C/mol
ω	Frequency of Applied Load	Hz
ΔH	Activation Enthalpy	J/mol
R	Universal Gas Constant	8.3143J/mol-K
$\frac{da}{dt}$	Crack Growth Rate with Respect to Time	$\mu m/hour$
M_s	Martensite Start Temperature,	$^{\circ}C$
M_d	Temperature above Which Strain Induced Transformation of Austenite to Martensite no Longer Occurs	$^{\circ}C$
N_f	Number of Cycles to Cause Failure	
K_t	Elastic Stress Concentration Factor	
K_f	Fatigue Notch Factor	
q	Notch Sensitivity Factor	
l_t	Transition Length of a Fatigue Crack,	μm
K_{ISCC}	Stress Corrosion Cracking Threshold Stress Intensity Factor,	$MPa\sqrt{m}$
a_f	Crack Length at Fracture,	μm
N_p	Number of Cycles to Propagate an Initiated Crack to Failure	
d	Max Pit Depth,	μm
A	Constant dependant upon the material environment combination	
t	Time,	Seconds
n	Exponent of pit growth law	

List of Figures

Figure 1 - Schematic Arrangement of a Typical Three Cylinder Steam Turbine	5
Figure 2 - Schematic Illustration Of Stresses Acting on a Typical Turbine Blade.	6
Figure 3 - Effect of Carbon, Manganese, Silicon and Sulphur on The Transverse Properties of 18% Ni Maraging Steel.....	18
Figure 4 - S-N Curves For Double Vacuum Melted 18 % Ni Maraging Steel, Test Conducted At 14 Hz in Laboratory Air or Aerated 3.5 % NaCl.	22
Figure 5 - Percentage of Inclusions Associated With Cracks At 5% of Expected Life Versus Stress Amplitude.	23
Figure 6 - Schematic Illustration Of The Three Stages Of Fatigue Crack Growth Under Reversed Tensile Loading.	29
Figure 7 - The Three basic modes of Fracture. (a) Tensile Opening (mode I). (b) In- Plane Sliding (mode II). (c) Anti-Plane Shear (mode III).	31
Figure 8 - Schematic Illustration of the Different Regimes of Stable Fatigue Propagation.	33
Figure 9 - The Effect of Grain Size on The Threshold Stress Intensity Factor.	36
Figure 10 - Influence of Plastic Grain Size, Relative to Mean Packet Size, Upon The Development of Bilinear Form of Fatigue Crack Growth Behaviour.	38
Figure 11 - Effects of Notches on an the Fatigue Strength of an Aluminium Alloy.	39
Figure 12 - Elastic and Plastic Stress Strain Fields at the Notch Root.....	41
Figure 13 - Two Processes Of Fatigue Crack Growth From A Notch.	42
Figure 14 - The Influence of Notch Root Radius (ρ) on the Number of Cycles to Initiate a Crack (N_i) From a 2.54 (mm) Deep Notch. For a Mild Steel. Stress Range = 0 - 200 (MPa).....	43

Figure 15 - Effect of Notch Root Radius on Number of Cycles to Initiation for 2.5%NiCrMoV Under Constant Stress Range.	44
Figure 16 - The Influence of Effective Stress Intensity Factor ($\Delta K/\rho^{1/2}$) (Ksi) on the Number of Cycles to Failure.	45
Figure 17 - $\frac{\Delta K}{\rho^{1/2}}$ Versus The Number of Cycles To Initiate a Fatigue Crack For Three Heat Treatments on 4140 Steel.	46
Figure 18 - $\frac{\Delta K}{\rho^{1/2}}$ Versus Number of Cycles To Initiate a Fatigue Crack For Various Notch Root Radii. All Tests Conducted in Laboratory Air at Room Temperature.	48
Figure 19 - $\frac{\Delta K}{\rho^{1/2}}$ Versus Number of Cycles To Initiate a Fatigue Crack For Various Notch Root Radii in Type 403 Stainless Steel.	50
Figure 20 - Fatigue Behaviour of Notched Components.	52
Figure 21 - Effect of Crack Length on Stress Intensity Factor Range.....	53
Figure 22 - Model Of Non-Metallic Inclusion Debonding.	55
Figure 23 - Time Dependence on Maximum Pit Depth of 3%NiCrMnV Steel in 0.02M Na ₂ B ₄ O ₇ +0.001M NaCl Solution.	64
Figure 24 - Effect of Surface Geometry on Current Density With Respect To Applied Load Level.....	68
Figure 25 - Pitting at a Manganese Sulphide Inclusion in FV520B During Constant Potential Testing in the range +50 - +200(mV) _{SCE} in 0.1M Sodium Chloride Solution at Room Temperature.	69
Figure 26 - Schematic of Pit Nucleation Processes at Inclusion Sites.	70

Figure 27 - Typical Three-Electrode Cell.	74
Figure 28 - Endurance Data for Air and Chloride Environments.	77
Figure 29 - Variation Of pH and Potential AT The Tip Of a Propagating Crack Under Cyclic Loading of 40Kh13 Steel Beam Specimen Exposed To An Aqueous Solution With A pH of 8.	80
Figure 30 - Dependency of Pit Density on Applied Cyclic Stress Level Under Fully- Reversed Loading in 0.6M, Aerated Sodium Chloride Solution.	82
Figure 31 - Effects of Non-Active Pits on the Fatigue Strength of LP Turbine Shaft Steel.....	84
Figure 32 - Effect of Active Pits, Tests conducted in non-deaerated, deionised water at 80°C. Loading frequency = 100(Hz). Pre-Pitted in Condensing Steam.....	84
Figure 33 - Effect of Non-Active and Active Pits on the Threshold Stress Intensity Range for Fatigue Crack Initiation in LP Shaft Steel.....	85
Figure 34 - SEM Micrograph of Fatigue Crack Initiation At a Corrosion Pit In 3.5%NiCrMoV Steel tested In Water At 80°C.	86
Figure 35 - Variation of Transient Peak Current at Open Circuit Potential With Respect to Number of Strain Cycles.	91
Figure 36 - Waveforms of Current Transients and Phase Relationship with Cyclic Stress for Passive and Transpassive Ranges.	93
Figure 37 - Schematic Illustration of Basic Types of Corrosion Fatigue Crack Growth Behaviour.	99
Figure 38 - Fatigue Crack Initiation Process.....	100
Figure 39 - Model of transition From Corrosion Pit to Fatigue Crack.	101
Figure 40 - Schematic of Brown-Hobson Crack Growth Model.	102
Figure 41 - Schematic of Navarro - de los Rios Crack Growth Model in Air.	103

Figure 42 - Schematic of Brown-Hobson Crack Growth Model with Akid and Miller Metal Dissolution Term Included.	105
Figure 43 - Schematic of Navarro and de los Rios Crack Growth Model with Akid and Miller Metal Dissolution Term Included.....	105
Figure 44 - Effect of Pit Depth On Endurance Limit 12 Cr stainless steel R=0.8 ...	108
Figure 45 - Schematic Representation of Growth Characteristics For CF and SCC.	110
Figure 46 - S-N Curves for a 21%Cr 7%Ni Stainless Steel Under Rotating-Bending Fatigue Tests in Various Environments.	112
Figure 47 - Results of Potentio-Dynamic Testing on a 21%Cr 7Ni Stainless Steel in 3% NaCl on a Rotating Bending Fatigue Machine with Zero Load Applied. .	113
Figure 48 - S-N Curve for a 13%Cr Martensitic Stainless Steel in 3% NaCl Aqueous Solution at 80°C.....	114
Figure 49 - Electrochemical Potential Data for SA 333-6 Carbon Steel in Water as a Function of Oxygen Concentration and Temperature.	115
Figure 50 - Tensile Specimen Design All Dimensions in mm.....	120
Figure 51 - Slow Strain Rate Testing Specimen Design All Dimensions in mm	121
Figure 52 - F.E.A Mesh Of Notched Fatigue Specimen Experimental Results.....	124
Figure 53 - Plain Fatigue Specimen Design For Air and Corrosion Fatigue. Dimensions in mm	125
Figure 54 - Notched Fatigue Specimen Used For Air and Corrosion Fatigue All Dimensions in mm.	126
Figure 55 - Schematic Arrangement of Autoclave and Water Loop System	127
Figure 56 - Sectioned View of Autoclave.....	128
Figure 57 - Corrosion Fatigue Test Rig in Operation.	129

Figure 58 - Insulating Grip System Used for Corrosion Fatigue Testing	131
Figure 59 - An External Ag/AgCl Electrode for High Temperature, High Pressure Use.	133
Figure 60 - Schematic of an External Reference Electrode	134
Figure 61 - Effect of Temperature on the Slow Strain Rate Response of Softened Overaged FV520B-B.....	138
Figure 62 - Graph To Show Effect of Temperature on the Slow Stain Rate Response of Peak Hardened FV520B-A.	138
Figure 63 - The Effect of Temperature on Reduction in Area and Elongation for Slow Strain Rate Tests on Various Blading Materials.	139
Figure 64 - The Effect of Temperature on Tensile Strength for Slow Strain Rate Tests on Various Blading Materials.	139
Figure 65 - Polarisation Curves For 18%Ni Marageing Steel and Peak Hardened FV520B. Tests Conducted Open To Air in 0.3% NaCl At Room Temperature, S.C.E Reference Electrode, Scan Rate = 10(mV/s)	140
Figure 66 - A Graph of Show The Number and Size of Inclusions In FV520B and 18%Ni Marageing Steel.	141
Figure 67 - The Ratio of Area of Inclusions For FV520B and 18% Ni Marageing Steels to the Total Area Checked.	142
Figure 68 - Deformed F.E.A. Mesh Showing Von Mises Equivalent Stresses at the Notch Root. Stress in Pa.	143
Figure 69 - Cycles To Failure Against Applied Stress Amplitude For Both Notched and Plain Specimen 18% Ni Marageing Steel, R=-1, K_t of Notch = 2.29 All Tests Conducted in Laboratory Air.	145

Figure 70 - Cycles To Failure Against Applied Stress Amplitude For Notched Specimen FV520B Peak Hardened FV520B, R=-1, K_t of Notch = 2.29 All Tests Conducted in Laboratory Air.	145
Figure 71 - Schematic showing Notation for Pulsed Potential Testing	150
Figure 72 - Cycles To Failure Against Applied Stress Amplitude For Notched Specimen Peak Hardened FV520B-A, R=-1, K_t of Notch = 2.29 All Tests Conducted Within The Autoclave in Distilled Water at 2Hz.	150
Figure 73 - Cycles To Failure Against Applied Stress Amplitude For Notched and Plain Specimen Peak Hardened FV520B-A and 18% Ni Maraging Steel, R=-1, K_t of Notch = 2.29. All Tests Conducted Within The Autoclave in 0.3% Sodium Chloride at 100°C at 2Hz.	151
Figure 74 - Cycles To Failure Against Applied Stress Amplitude For Notched and Plain Specimen Peak Hardened FV520B-B and 18% Ni Maraging, R=-1, K_t of Notch = 2.29. All Tests Conducted Within The Autoclave in 0.3% Sodium Chloride at 100°C at +200(mV) _{Ag/AgCl} . All Tests at 2 (Hz) Unless Otherwise Stated.	152
Figure 75 - Cycles To Failure Against Applied Stress Amplitude For Notched Specimen Peak Hardened FV520B-B, R=-1, K_t of Notch = 2.29. All Tests Conducted Within The Autoclave in 0.3% Sodium Chloride at 100°C at - 200(mV) _{Ag/AgCl} at 2(Hz).	152
Figure 76 - Cycles To Failure Against Applied Stress Amplitude For Notched Specimen Peak Hardened FV520B-B, R=-1, K_t of Notch = 2.29. All Tests Conducted Within The Autoclave in 0.3% Sodium Chloride at 100°C at - 0(mV) _{Ag/AgCl} at 2(Hz)	153

Figure 77 - Cycles To Failure Against Period at $+200(\text{mV})_{\text{Ag}/\text{AgCl}}$ in cycles. For Notched Specimen Peak Hardened FV520B-B, $R=-1$, K_t of Notch = 2.29. All Tests Conducted Within The Autoclave in 0.3% Sodium Chloride at 100°C at 2(Hz).	154
Figure 78 - Vickers Hardness Results For Slow Strain Rate Specimen Stubs.....	157
Figure 79 - Microstructure of Maraging Steel (Etched With 2% Picral)	159
Figure 80 - Microstructure of FV520B Peak Hardened (Etched With 2% Picral)...	160
Figure 81 - Fatigue Limit Verses Inverse Root of Grain Size. Taira et al Data for a low Carbon Steel.....	161
Figure 82 - Calculated and Experimental Values of Fatigue Limit Versus Inclusion Size.....	163
Figure 83 - Peterson Constant (a) Versus Vickers Hardness Number	166
Figure 84 - Graph To Show Plain Fatigue Data for FV520B Plotted With Calculated Notched Data.....	167
Figure 85 - Graph To Show Plain Fatigue Data for 18Ni Maraging Steel Plotted With Calculated Notched Data.....	168
Figure 86 - Cycles To Failure Versus Stress Amplitude For Peak Hardened FV520B.	169
Figure 87 - Cycles To Failure Versus Stress Amplitude For 18% Ni Maraging Steel	170
Figure 88 - Fatigue Notch Factor Versus Cycles To Failure For FV520B and 18% Ni Maraging Steel.....	170
Figure 89 - Notch Sensitivity Factor Versus Cycles To Failure For FV520B and 18% Ni Maraging Steel.....	171

Figure 90 - Fracture Surface of 18% Ni Marageing Steel Tested in Air at ± 300 (MPa), 7(Hz), $N_f = 127080$	173
Figure 91 - Fracture Surface of 18% Ni Marageing Steel Tested in Air at ± 300 (MPa), 7(Hz), $N_f = 127080$. Showing Striations.....	174
Figure 92 - Fracture Surface of 18% Ni Marageing Steel Tested in Air at ± 300 (MPa), 7(Hz), $N_f = 127080$. Showing Striations.....	175
Figure 93 - Typical Fracture Surface from Failed Peak Hardened FV520B Fatigue Specimen Tested in Laboratory Air (20°C) ± 390 (MPa) $N_f = 158090$	176
Figure 94 - Stress Amplitude Versus Cycles To Failure For Plain and Notched Marageing Steel.....	177
Figure 95 - Stress Amplitude Versus Cycles To Failure Data for Plain 18 Ni Marageing Steel, Cottis Data @ 14(Hz) Laboratory Temperature, Tatner Data @ 2(Hz) 100°C	179
Figure 96 - View of A Fractured Plain Marageing Steel Specimen Showing General Corrosion. Tested At ± 300 (MPa), $R = -1, 2$ (Hz), in 0.3% NaCl at FCP at 100°C, $N_f = 33608$	180
Figure 97 - Cycles To Failure Versus Stress Amplitude For Notched and Plain FV520B In Air , Water And 0.3%NaCl.	180
Figure 98 - View of A Fractured Notched FV520B Steel Specimen Showing No General Corrosion. Tested At ± 300 (MPa), $R = -1, 2$ (Hz), in 0.3% NaCl at FCP at 100°C, Tested for 10^6 Cycles No Failure.	181
Figure 99 - Fracture Surface of a Plain Marageing Specimen Subjected to ± 300 (MPa) in 100°C 0.3% NaCl at FCP.....	182
Figure 100 - Cycles To Failure Versus Stress Amplitude For Notched And Plain Specimen Precipitation Hardening Peak Hardened FV520B Tested In 0.3%	

NaCl Solution At Various Values of Applied Potential ($E_{Ag/AgCl}$), All Tests conducted At 2 (Hz) unless stated, 100°C.	183
Figure 101 - Fracture Away From Notch. Notched FV520B Specimen Subjected to ± 75 MPa at 2Hz, 100°C 0.3% NaCl, 0(mV) $_{Ag/AgCl}$ $N_f = 323310$	184
Figure 102 - Failed Specimen Showing Iron Oxide (Magnetite) Deposited During Testing of Plain Specimen FV520B at 100°C in 0.3% NaCl +200 (mV) $_{Ag/AgCl}$ ± 75 (MPa) 2(Hz), $N_f = 127080$	185
Figure 103 - Fracture Surface of Peak Hardened FV520B, ± 300 (MPa) 2(Hz), R = -1, 0.3% NaCl, 100°C, +200 (mV) $_{Ag/AgCl}$, $N_f = 32610$	186
Figure 104 - Fracture Surface of Peak Hardened FV520B, ± 150 (MPa) 2(Hz), R = -1, 0.3% NaCl, 100°C, +200 (mV) $_{Ag/AgCl}$, $N_f = 52580$	186
Figure 105 - Fracture Surface of Peak Hardened FV520B, ± 75 (MPa) 2(Hz), R = -1, 0.3% NaCl, 100°C, +200(mV) $_{Ag/AgCl}$, $N_f = 211280$	187
Figure 106 - Fracture Surface of Peak Hardened FV520B, ± 300 (MPa) 0.5(Hz), R = - 1, 0.3% NaCl, 100°C, +200(mV) $_{Ag/AgCl}$, $N_f = 7810$	188
Figure 107 - Fracture Surface of Peak Hardened FV520B, ± 75 (MPa) 0.5(Hz), R = - 1, 0.3% NaCl, 100°C, +200 (mV) $_{Ag/AgCl}$, $N_f = 29660$	188
Figure 108 - Fracture Surface of Peak Hardened FV520B, ± 300 (MPa) 2(Hz), R = -1, 0.3% NaCl, 100°C, 0(mV) $_{Ag/AgCl}$, $N_f = 39390$	189
Figure 109 - Fracture Surface of Peak Hardened FV520B, ± 150 (MPa) 2(Hz), R = -1, 0.3% NaCl, 100°C, 0(mV) $_{Ag/AgCl}$, $N_f = 148120$	189
Figure 110 - Fracture Surface of Peak Hardened FV520B, ± 75 (MPa) 2(Hz), R = -1, 0.3% NaCl, 100°C, 0(mV) $_{Ag/AgCl}$, $N_f = 323310$	190
Figure 111 - Definition of Corrosion-Fatigue Transition Point	191

Figure 112 - Corrosion-Fatigue Transition Point Versus Applied Stress Amplitude For FV520B Notched Specimen.	191
Figure 113 - Fracture Surface of Peak Hardened FV520B, ± 150 (MPa) 2(Hz), R = -1, 0.3% NaCl, 100°C, +200(mV) _{Ag/AgCl} , N _f = 52580	192
Figure 114 - Fractured Stub of FV520B-B Plain Specimen Tested at +200(mV) _{Ag/AgCl} in 100°C NaCl, ± 300 (MPa), 2(Hz), R=-1, N _f =10221	194
Figure 115 - Fractured Stub of FV520B-B Plain Specimen Tested at +200(mV) _{Ag/AgCl} in 100°C NaCl, ± 150 (MPa), 2(Hz), R=-1, N _f = 59836.....	194
Figure 116 - Fractured Stub of FV520B-B Plain Specimen Tested at +200(mV) _{Ag/AgCl} in 100°C NaCl, ± 75 (MPa), 2(Hz), R=-1, N _f = 184024.....	195
Figure 117 - Transition Point from Fractured Stub of FV520B-B Plain Specimen Tested at +200(mV) _{Ag/AgCl} in 100°C NaCl, ± 75 (MPa), 2(Hz), R=-1, N _f = 184024.....	195
Figure 118 - Effect of Applied Stress Range on Crack Transition Depth for Plain FV520B-B Corrosion Fatigue Specimen Tested at +200(mV) _{Ag/AgCl} , R=-1, 2(Hz), 100°C in 0.3% NaCl.	196
Figure 119 - Crack Growth at Notch.....	198
Figure 120 - Band of Material Damaged Due to Hydrogen Charging Process	203
Figure 121 - Q Versus N, With an Exposed Area of 2.29×10^{-5} (m ²) 75(MPa) 2(Hz), +200(mV) _{Ag/AgCl} in 0.3% NaCl at 100°C	204
Figure 122 - Notch Area of FV520B-B Corrosion fatigue Specimen Subjected to 90 cycles at +200(mV) _{Ag/AgCl} at The Start of Testing in 0.3% NaCl at 100°C, ± 300 (MPa) 2(Hz)..	206

Figure 123 - Notch Area of FV520B-B Corrosion fatigue Specimen Subjected to 600 cycles at $+200(\text{mV})_{\text{Ag}/\text{AgCl}}$ at The Start of Testing in 0.3% NaCl at 100°C , $\pm 300(\text{MPa})$ 2(Hz).....	207
Figure 124 - Notch Area of FV520B-B Corrosion fatigue Specimen Subjected to 600 cycles at $+200(\text{mV})_{\text{Ag}/\text{AgCl}}$ at The Start of Testing in 0.3% NaCl at 100°C , $\pm 300(\text{MPa})$ 2(Hz).....	207
Figure 125 - Notch Area of FV520B-B Corrosion fatigue Specimen Subjected to 1800 cycles at $+200(\text{mV})_{\text{Ag}/\text{AgCl}}$ at The Start of Testing in 0.3% NaCl at 100°C , $\pm 300(\text{MPa})$ 2(Hz).....	208
Figure 126 - Notch Area of FV520B-B Corrosion fatigue Specimen Subjected to 1800 cycles at $+200(\text{mV})_{\text{Ag}/\text{AgCl}}$ at The Start of Testing in 0.3% NaCl at 100°C , $\pm 300(\text{MPa})$ 2(Hz).....	208
Figure 127 - Notch Area of FV520B-B Corrosion fatigue Specimen Subjected to 1800 cycles at $+200(\text{mV})_{\text{Ag}/\text{AgCl}}$ at The Start of Testing in 0.3% NaCl at 100°C , $\pm 300(\text{MPa})$ 2(Hz).....	209
Figure 128 - Notch Area of FV520B-B Corrosion fatigue Specimen Subjected to 1800 cycles at $+200(\text{mV})_{\text{Ag}/\text{AgCl}}$ at The Start of Testing in 0.3% NaCl at 100°C , $\pm 300(\text{MPa})$ 2(Hz). Showing a Crack Growing From a Corrosion Pit.	209
Figure 129 - Fatigue Crack Initiating From Corrosion Pitting on Fracture Surface of Notched Specimen Subjected to 1800 cycles at $+200(\text{mV})_{\text{Ag}/\text{AgCl}}$ at The Start of Testing in 0.3% NaCl at 100°C , $\pm 533(\text{MPa})$ 2(Hz) R=-1. $N_f = 65828$	212
Figure 130 - Fracture Surface of Notched Specimen Subjected to 14400 cycles at $+200(\text{mV})_{\text{Ag}/\text{AgCl}}$ at The Start of Testing in 0.3% NaCl at 100°C , $\pm 150(\text{MPa})$ 2(Hz) R=-1. $N_f = 153347$	215

- Figure 131 - Fracture Surface of Notched Specimen Subjected to 2400 cycles at
 $+200(\text{mV})_{\text{Ag}/\text{AgCl}}$ at The Start of Testing in 0.3% NaCl at 100°C , $\pm 225(\text{MPa})$
 2(Hz) $R=-1$. $N_f = 139712$ 215
- Figure 132 - Fracture Surface of Notched Specimen Subjected to 7200 cycles at
 $+200(\text{mV})_{\text{Ag}/\text{AgCl}}$ at The Start of Testing in 0.3% NaCl at 100°C , $\pm 225(\text{MPa})$
 2(Hz) $R=-1$. $N_f = 53264$ 216
- Figure 133 - Fracture Surface of Notched Specimen Subjected to 14400 cycles at
 $+200(\text{mV})_{\text{Ag}/\text{AgCl}}$ at The Start of Testing in 0.3% NaCl at 100°C , $\pm 225(\text{MPa})$
 2(Hz) $R=-1$. $N_f = 45810$ 216
- Figure 134 - Fracture Surface of Notched Specimen Subjected to 2400 cycles at
 $+200(\text{mV})_{\text{Ag}/\text{AgCl}}$ at The Start of Testing in 0.3% NaCl at 100°C , $\pm 300(\text{MPa})$
 2(Hz) $R=-1$. $N_f = 5280$ 217
- Figure 135 - Fracture Surface of Notched Specimen Subjected to 2400 cycles at
 $+200(\text{mV})_{\text{Ag}/\text{AgCl}}$ After 500,000 cycles at $\pm 75(\text{MPa})$ in 0.3% NaCl at 100°C ,
 $\pm 300(\text{MPa})$ 2(Hz) $R=-1$. $N_f = 25993$ 217
- Figure 136 - Fracture Surface of Notched Specimen Subjected to 90 cycles at
 $+200(\text{mV})_{\text{Ag}/\text{AgCl}}$ at The Start of Testing in 0.3% NaCl at 100°C , $\pm 400(\text{MPa})$
 2(Hz) $R=-1$. $N_f = 14050$ 218
- Figure 137 - Fracture Surface of Notched Specimen Subjected to 1800 cycles at
 $+200(\text{mV})_{\text{Ag}/\text{AgCl}}$ at The Start of Testing in 0.3% NaCl at 100°C , $\pm 533(\text{MPa})$
 2(Hz) $R=-1$. $N_f = 65828$ 218
- Figure 138 - The Effect of Pulsed Corrosion Damage Fatigue Testing. *=Simnad and
 Evans Mild Steel Corrosion Fatigue in 0.1M Potassium Chloride Solution at
 100 (Hz). Rollins et al High Carbon Steel Tested at 25 (Hz). Tatner FV520B
 Corrosion Fatigue in 0.3% NaCl at $+200(\text{mV})_{\text{Ag}/\text{AgCl}} \pm 75 (\text{MPa})$, 2(Hz), then

Fatigue in Solution, FCP at Stress Level Indicated Until Failure. Arrow Indicates No Failure.	220
Figure 139 - Fracture Surface of a Specimen Subjected to 1800 Cycles at +200(mV) _{Ag/AgCl} ±75(MPa) Prior to Testing at FCP at ±300(MPa) at 100°C in 0.3% NaCl. Specimen did not Fail During Test and was Subsequently Pulled to Cause Failure.....	222
Figure 140 - Fracture Surface of a Specimen Subjected to 2400 Cycles at +200(mV) _{Ag/AgCl} ±75(MPa) Prior to Testing at FCP at ±150(MPa) at 100°C in 0.3% NaCl. Specimen did not Fail During Test and was Subsequently Pulled to Cause Failure.....	222
Figure 141 - High magnification of Fracture Surface of a Specimen Subjected to 1800 Cycles at +200(mV) _{Ag/AgCl} ±75(MPa) Prior to Testing at FCP at ±300(MPa) at 100°C in 0.3% NaCl. Specimen did not Fail During Test and was Subsequently Pulled to Cause Failure.....	223
Figure 142 - High magnification of Fracture Surface of a Specimen Subjected to 2400 Cycles at +200(mV) _{Ag/AgCl} ±75(MPa) Prior to Testing at FCP at ±150(MPa) at 100°C in 0.3% NaCl. Specimen did not Fail During Test and was Subsequently Pulled to Cause Failure.....	223
Figure 143 - Number of Cycles To Initiate a Fatigue Crack Versus $\frac{\Delta K}{\rho^{1/2}}$	226
Figure 144 - $\frac{\Delta K}{\rho^{1/2}}$ Versus The Number of Cycles To Initiate a Fatigue Crack During Pulsed Applied Potential.....	227

Figure 145 - $\frac{\Delta K}{\rho^{1/2}}$ Versus The Number of Cycles To Initiate a Fatigue Crack For Various Notch Root Radii. From Atkinson and Lindley 2.5%NiCrMoV , *Kim et al 4140 Steel and Clark 403 Type SS . With Clark Type 403 SS in Steam at 100°C and Tatner in 0.3% NaCl at 100°C.	228
Figure 146 - Calculated Crack Propagation Life Versus Experimental Crack Propagation Life.....	231
Figure 147 - Experimental Values of Total Life Versus Calculated Values.....	232
Figure 148 - Effect of Crack Length on Fatigue Thresholds.....	235
Figure 149 - Pit Size Versus The Number Of Start Cycles For A Steam Turbine Blade.	236
Figure 150 - A Graph To Stress Intensity Factor Range (MPa m ^{1/2}) Versus The Number Of Start Cycles For A Steam Turbine Blade.....	237
Figure 151 - The Number of Start Cycles Versus Life Prior To Crack Initiation In A Turbine Blade.....	238

List of Tables

Table 1 - Nominal % Mass Composition of Standard Martensitic Stainless Steels.

Table 2 - Composition of 18% Ni Maraging Steels.

Table 3 - Comparison of Measured and Calculated $\frac{\Delta K}{\sqrt{\rho_{th}}}$.

Table 4 - Proof Stress Values For Materials Used in Fatigue Crack Initiation Experiments.

Table 5 - Composition of Materials Tested.

Table 6 - Three Stage Heat Treatment Schedule.

Table 7 – Air Fatigue Tests Conducted.

Table 8 - Tensile Test Results For Peak Hardened FV520B.

Table 9 - Vickers Hardness Results.

Table 10 Air Fatigue Test Results.

Table 11 - Corrosion Fatigue Test Results.

Table 12 - Corrosion Fatigue Potential Pulse Test Results.

Table 13 - Calculated and Experimental Fatigue Limits Based on Inclusion Area.

Table 14 - Crack Data for a Constant Imposed Potential.

Table 15 - Stress Intensity Ranges for Constant Potential Tests Conducted on Notched Specimen.

Table 16 - Results of Thiourea Test.

Table 17 - Results of Pulsed Imposed Potential Corrosion Fatigue Tests.

Table 18 - Results of Pulsed Imposed Potential Corrosion Fatigue Tests.

Table 19 - Comparison of Number of Cycles To Failure for Specimens Tested in Air and Under Pulsed Potential Conditions.

Table 20 - Pit-Crack Transition Stress Intensity Factor Ranges From Previous Works.

Table 21 - Stress Intensity For Corrosion Pits Formed Due To Applied Corrosion Potential.

Table 22 - Threshold Conditions From Pulsed Corrosion Potential Corrosion Fatigue Testing.

Table 23 - Calculated Pit Depths and Stress Intensity Factor Ranges for Threshold Conditions.

1 Introduction

Since the privatisation of the UK electricity industry in the early 1990s there has been much more two shifting at generating plants where turbines are either turned off at times of low demand or follow electricity demand. In either situation turbines designed for high temperature continuous operating conditions are subjected to the fluctuating conditions caused by the continual stop-start of the power station [1]. In the past power generation units would be run for many years on constant demand delivering the base demand for electricity with older units being brought back online at times of high demand. The delivery of base load electricity is now often achieved with the use of more thermally efficient gas fired stations, with older coal fired stations covering peak load, this means older coal fired stations are being turned on and off more often than intended [2]. As the use of 'Green' power is increased this problem will only get worse, 'green energy' is very difficult to schedule and so when high electricity demand is matched with low output from Green sources, fossil sources will be required to make up any short fall until demand drops or output from 'Green' plants is increased. Two-shifting or demand following would cause water chemistry transients, Starr [1] comments "weekend shut downs can upset boiler water treatment. Demineralisation units do not work to specification. Air can be drawn into the system. The upshot is corrosion fatigue.". Reduced feed water quality can also have extremely damaging consequences on corrosion fatigue, Lindley [3] states "From a practical viewpoint, it is of prime importance to limit the time during which a turbine rotor is subject to non-deaerated wet conditions" and more recently "The

major threat to existing plant is reduced feed water quality or contamination"

Atkinson [4].

The present work assesses the effect of water purity transients on the corrosion fatigue strength of a low pressure turbine blade material. The work carried out focuses on FV520B steel, building on the earlier work by Clark [5]. Corrosion fatigue tests were conducted on both FV520B and a 18 % Ni maraging steel. The maraging steel was selected as it possesses similar mechanical characteristics as FV520B but due to its low chromium content has low corrosion resistance in relatively mild environments. Though both materials fail due to corrosion fatigue, due to the different corrosion dynamics of the two materials, it was expected that their failure lives would be different. To this end a high temperature re-circulating corrosion fatigue test rig was designed and built. The test rig also incorporated a potentiostat which allowed simulation of actual service conditions and the damage due to impurities and dissolved oxygen. Fatigue and corrosion damage were quantified using SEM and optical methods. The results from this work facilitated the development of a corrosion damage model based on a LEFM approach. It was shown there is a threshold value below which the corrosion pit fails to develop into a growing crack. The threshold value was seen to be a function of the pit depth and the applied stress level, hence an LEFM type approach was used. By using the initial pit depth as a pseudo crack length a propagation life model was proposed based on an integrated Paris law approach. This was further developed by including consideration of the number of cycles required to initiate a growing crack from a corrosion pit. The initiation and propagation models were combined to give a total life prediction that compared well to experimental values.

The empirical models developed were combined with an equation derived from Faraday's law that was used to predict pit depths using electrochemical data combined with loading data. The combination of the Faraday approach to pit depth prediction and the use of a LEFM type approach, seen to work in the current study produced a tool capable of assessing the effect of the number of start-up cycles on the life of a turbine blade.

2 Literature Review

2.1 Introduction

This chapter will review the published work and the pertinent research carried out in the area of corrosion fatigue.

2.2 Turbine Blades

This section describes and where possible quantifies the mechanical and electrochemical conditions faced by LP turbine blades in service. A brief summary is given on the various LP blading materials and details are given of the known issues in the corrosion fatigue resistance of these materials.

2.2.1 Steam Turbines

Steam turbines convert steam energy into rotational kinetic energy that is used to turn an alternator thus producing alternating current. Large steam turbine generator units are used to produce electrical power in the 100-1300 MW range. These include both fossil fuel and nuclear systems. Fossil fuelled turbines operate at around 50-60 Hz with steam inlet conditions in the order of 550°C at 15-25 MPa and normally produce 660 MW power. Nuclear turbines operate at 30 Hz with steam conditions normally about 250°C at 5 MPa. Nuclear turbines are generally larger in physical size due to the larger volumes of steam to be accommodated at the lower operating speed, Rust and Steltz [6].

In the early stages of steam turbine development there was only one cylinder being driven by a steam generator. Since output demand increased and efficiency was enhanced multi-cylinder turbines were developed. The modern power generation steam turbines are usually made up of several separate turbine cylinders connected on a single shaft. Incoming steam from the steam generator first enters the high pressure (HP) cylinder then subsequently proceeds to the intermediate (IP) and low pressure (LP) cylinders which allow more energy to be extracted from it. See Figure 1.

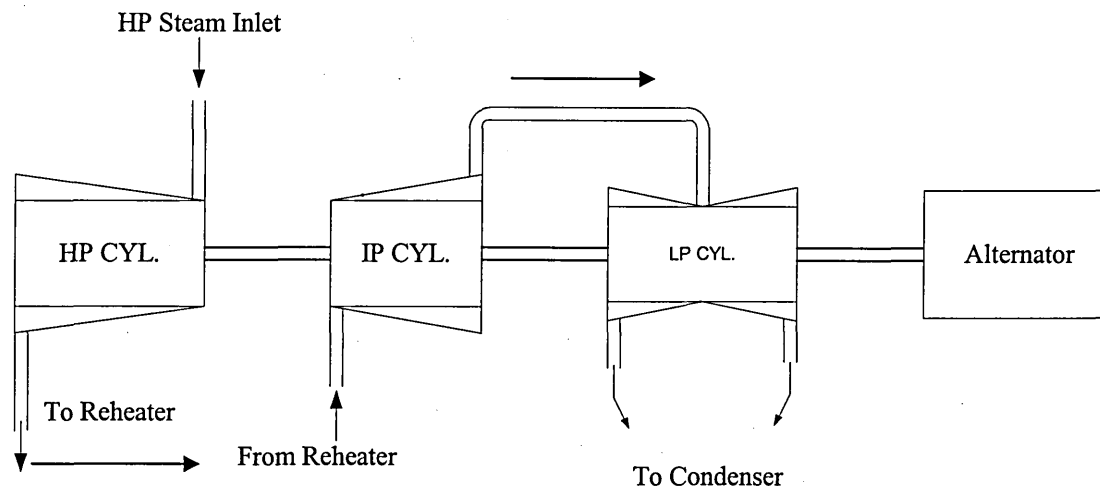


Figure 1 - Schematic Arrangement of a Typical Three Cylinder Steam Turbine

2.2.2 Stresses Acting on LP Turbine Blades

The stresses acting on a LP blade, assuming it is properly tuned are a combination of predominantly steady stresses from centrifugal forces and steam bending.

Superimposed on the steady stresses are alternating stresses caused by cyclic or random variations in the steam flow conditions. See

Figure 2 [7].

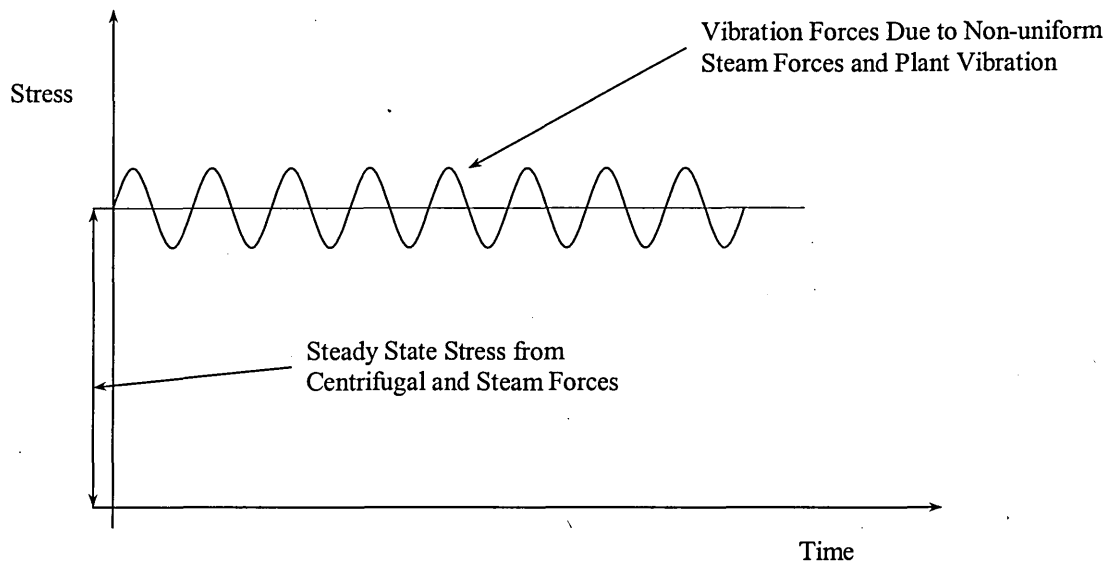


Figure 2 - Schematic Illustration Of Stresses Acting on a Typical Turbine Blade.

The combined effect of alternating stresses and mean stress is a situation that has been seen to initiate fatigue failures in pitted LP blades. The stress concentrating effect of the geometry at the root of blades where they are connected to the rotor should also be considered. There are times when the turbine and hence the blade are subjected to low predominantly static stresses, such as during barring. Barring is a process carried out at times of low power demand where the turbine is rotated at 0.33 Hz otherwise the turbine shaft may bend if rotation is stopped while the turbine is at a higher temperature. However, it is known that the reduction of steam quality during barring leads to localised corrosion attack of the blades.

2.2.3 Environmental Conditions Near an LP Steam Turbine Blade

The steam supplied to turbines is highly controlled to ensure minimal contamination and hence prolong turbine life. However, from time to time steam purity will become transient as a result of problems in steam/water purification plant or due to barring or

two shifting. These occasional breakdowns manifest themselves in pollution of the turbine causing deposits of acids, chlorides and sulphates in the transition region where the incipient moisture condenses.

The superheated steam initially condenses at a point along the turbine known as the Wilson or moisture line. It is the blades in this region that are exposed to the most harmful environmental conditions. Typically the transition from dry to wet steam takes place in the next to last row (L-1) in the LP turbine. Viswanathan et al [8] comments "The initial condensation can have the most marked environmental effect". The most harmful effect of the condensing steam is that of localised or pitting corrosion. The most severe blade corrosion is generally found where the blade is attached to the rotor shaft. Here the corrosion is enhanced by grooves or cracks, it is these grooves that also lead to high local stresses.

2.2.4 Steam Turbine Blade Materials

Steam turbine blade materials are selected on the basis of a number of properties, such as, strength to weight ratio, fatigue strength, corrosion resistance, damping capacity, erosion resistance and cost. Extensive work in material development was carried out in the 1960's and 1970's as turbines became larger (up to 660MW) and blade materials were improved to give higher strength and pitting corrosion resistance.

The standard LP turbine blade material used in steam turbines manufactured world-wide is a martensitic steel containing 12-13%Cr . It is known that the 12%Cr steel is a good blade material that serves well in high purity steam [9].

Due to some failures in LP blades several alternatives to the standard 12%Cr material have been proposed in recent years. The following section details some of the

alternative blading materials, with particular emphasis being paid to the precipitation hardenable stainless steels that are the subject of the current research.

2.2.4.1 Duplex Steels

Duplex steels differ from the 12% Cr martensitic steels as they possess a dual phase microstructure of ferrite and austenite. Due to the high Chromium and Molybdenum contents they have excellent corrosion resistance even in hot concentrated chloride solutions. However, duplex steel strength levels are considerably lower than those achievable with 12% Cr when at elevated temperatures. Reductions of up to 25% of yield strength at 100°C for a 22 Chromium grade Duplex have been reported [10].

2.2.4.2 High Nitrogen 12 Cr

With the invent of high nitrogen steels an attempt was made to apply the concept of substitution of carbon by nitrogen to 12 Cr steels in order to improve corrosion resistance. Leffler [11] comments "Nitrogen increases the resistance to localised corrosion, especially in combination with molybdenum" and goes on to say "in martensitic and martensitic-austenitic steels nitrogen will increase both hardness and strength".

2.2.4.3 Precipitation Hardenable Martensitic Stainless Steels

The martensitic stainless steels with chromium contents of 13-17% were widely used in engineering applications in the early 1900's. Their corrosion resistance was considered good, and their tensile strengths are generally high. Machining in the hard

state was difficult and expensive, and high temperature softening treatments would cause serious surface oxidation and possible distortions.

Fabrication is limited when the material is used in the hardened condition this is due to poor ductility. The high carbon contents caused a reduction in weldability.

Welding causing deep hardening of weldment and the heat affected zone, introducing the risk of cracking. These factors made the use of martensitic steels in critical applications such as nuclear plants, unlikely. A gap existed in the stainless steel range for a material that could be heat treated, was corrosion resistant and above all, was tough and weldable.

In the 1940's Precipitation Hardenable (PH) martensitic steels were developed. The object of precipitation hardening is to create in a heat treated alloy a dense and fine dispersion of precipitate particles in a matrix of deformable metal. The precipitate particles act as obstacles to dislocation movement and thereby increase fatigue strength in the heat treated alloy. The precipitation hardening of a homogeneous material involves three basic steps;

Step 1

Solution treatment- the material is soaked at temperature until a uniform solid solution is obtained.

Step 2

Quenching- the aim of quenching is to lock in the precipitates thus giving a super saturated solid solution. This quenching may occur by simply air cooling depending on the number of barriers within the alloy preventing dissolution of the precipitate.

Step 3

Precipitation hardening (ageing) - this phase of the precipitation treatment controls the size of the precipitate and hence the final strength level.

The time period and temperature of the final heat treatment are controlled to give one of three strength conditions, namely, peak hardened, standard overaged, softened overaged. These conditions can be thought of as controlling the size of the precipitate particle relative to the metal matrix. As the precipitate gets bigger it presents a more comprehensive block to the movement of dislocations thus giving a higher strength material. When the precipitate particle becomes so large it is no longer a coherent part of the metal matrix dislocations can move around the precipitate. The three ageing conditions above relate to the size and spacing of the precipitates relative to the metal matrix. The peak hardened condition corresponds to the largest possible coherent precipitate. The standard overaged is a condition where the precipitate is no longer coherent but does increase strength by blocking the movement of dislocations. The softened overaged material is the same strength level as before ageing treatment but with large incoherent precipitates.

Early grades of PH steels such as 17/4 PH were developed leading to a range of PH grades. Nominal compositions of some standard PH martensitic stainless steels are given in Table 1.

Grade	Chemical Composition %									
	C	Si	Mn	Cr	Ni	Mo	AL	Cu	Ti	Nb
17/4 PH	0.04	0.6	0.3	16	4.2	-	-	3.4	-	-
15/5 PH	0.04	0.04	0.3	15	4.5	-	-	3.4	-	-
Custom 450	0.03	0.25	0.25	15	6	0.8	-	1.5	-	0.3
13/8 PH	0.04	0.03	0.03	13	8.2	2.2	1.1	-	-	-
Custom 455	0.03	0.25	0.25	12	8.5	-	-	2.5	1.2	0.3
FV520B	0.05	0.4	0.8	14	5.5	1.7	-	1.8	-	0.35

Table 1 - Nominal % Mass Composition of Standard Martensitic Stainless Steels [12]

PH steels have found widespread application as turbine blade materials due to their high fatigue strength in air and excellent corrosion resistance along with a high level of toughness.

2.2.4.4 Titanium Alloys

Titanium alloys are considered as one of the most common blading materials in large power generating steam turbines in the USA. The high strength to weight ratio of titanium and its high corrosion resistance make it an ideal turbine blade material. The advantages of using titanium over conventional blading materials apply best in the LP turbine where steam temperatures are low, steam volume are high and blades are longest. The reason for using titanium in the LP turbine is due to increased power capacity. Increasing the power capacity of a turbine demands more steam flow. This can be fulfilled either by increasing blade lengths or increasing the diameter on which the blade rotates. In either case the centrifugal forces imposed on the blade will be significantly increased.

Titanium is lower in density than steel so by using Titanium the length of the blade can be increased without increasing stresses in the blade itself or the shaft that carries the blade. Since the Titanium and 12% Cr blades share similar dynamic vibration characteristics little alteration would be required for a set of 12% Cr blades to be replaced with Titanium [6].

There is however little interest in the UK for using Titanium as a turbine blade material. This is probably due to the fact that titanium blades are considerably more expensive than 12% Cr blades. Recently Titanium has been suggested as a solution for turbine blade corrosion problems [6]. However, change of material to Titanium is not the only solution to these problems, better steam purity, design and possible coating of the blade are options that could reduce corrosion effects. At present, the market conditions do not demand Titanium blades, current economic factors in the power industry do not justify the development and acquisition of new plants.

2.2.5 Failures in LP Turbine Blades

As a result of the environmental and stress systems detailed blade failures in the area of the Wilson line are by far the main source of failures in the entire turbine [13], and as such have received international research attention.

Viswanathan et al [8] comments, "Corrosion-fatigue is probably the major source of steam turbine blade fatigue failures." It has been shown by many investigators that the alternating and static stresses on blades alone were in many situations insufficient to cause failure. Laboratory controlled corrosion-fatigue tests have shown considerable reduction in a materials fatigue strength, by up to seventy percent or a complete loss of the fatigue limit.

Broadly speaking the blade failure problem has seen a two pronged attack, one approach developed mainly by Chemists is to improve steam quality and reduce water chemistry transients. The second approach used was to accept that steam quality will vary and to either reduce the blade stresses to such a level that blades can operate in a pitted condition without failure or change the blade material to a more resistant one. It has been suggested by some workers [14] that by allowing load variations to be arranged in such a way that the transition row (Wilson line) operate wet occasionally then washing effects will allow the conditions that promote the pitting in blades to be avoided.

Several alloys have been used as replacement for conventional 12%Cr steel. Coatings that prevent exposure of the 12%Cr surface to the environment within the steam turbine have been considered however problems with concentrated exposure at small defects in the coating have prevented widespread consideration.

2.2.6 Corrosion Fatigue Strength of Turbine Blade Materials

Corrosion fatigue is the dominant failure process of LP steam turbine blades. Hence a high corrosion fatigue resistance is one of the central demands in selecting a blading material. Pitting has been identified as important in the corrosion fatigue failure process [3]. Pits act as notches in two respects, firstly they are sites of mechanical stress concentration and secondly the electrolyte local to the pit can change becoming more aggressive relative to the bulk solution. The process of corrosion fatigue in notched components such as turbine blades one must also view geometrical notches both in terms of their stress and chemical concentrating capabilities. It has been shown [15] that the pH of the solution within the pit will drop and the chloride concentration will increase. It has also been shown that the electrochemical

conditions within the pit become more cathodic with respect to the bulk [16]. This has led to suggestions that the reduction in service life may be a result of hydrogen embrittlement. A greater effect due to hydrogen is observed in higher strength steels. It is difficult to find a valid ranking of steam turbine materials with respect to their corrosion fatigue resistance. No one material stands out as superior in all conditions. Even materials that are generally regarded as having superior corrosion resistance show weak points under the 'right' conditions [17]. It is difficult to sum up the aggressivity of an environment as complex as that in a working steam turbine. The chloride concentration has been shown to give a good indication of the effectiveness of an aqueous environment in reducing the fatigue strength of turbine blade materials [17].

2.3 Maraging Steels

The term Maraging comes from the ageing of a steel in the martensitic condition. Maraging steels have high strength levels while maintaining high toughness. Maraging steels have found varied uses in the aerospace and aircraft industries. These uses have included rocket motor cases, landing gear components, aircraft forgings and fasteners. Other areas include machine tool and die applications, and extrusion hardware. Uses include hydrofoil systems and aircraft arrester hooks [18].

2.3.1 18%Ni Maraging Steels

Maraging steels were originally developed in the 1950s with nickel contents around 25% by The International Nickel Company [19]. Further developments of these early maraging steels lead to the three 18% Ni steel grades, the so called 18Ni (200), 18Ni

(250) and 18Ni (300) grades. Table 2 shows the typical composition of these widely used 18% Ni maraging steels.

Alloy addition	18% Ni Series		
	200	250	300
Ni	17/19	17/19	18/19
Ti	0.15/0.25	0.3/0.5	0.5/0.8
Al	0.05/0.15	0.05/0.15	0.05/0.15
Co	8/9	7/8.5	8.5/9.5
Mo	3/3.5	4.6/5.1	4.6/5.2
Nb	-	-	-

Table 2 - Composition of 18% Ni Maraging Steels, [20]

Other elements include C 0.3 (max.); Mn 0.12 (max.); Si 0.12 (max.); S 0.01 (max.); P 0.01 (max.); B 0.003 (added); Zr 0.02 (added); Ca 0.05 (added); Si + Mn combined less than 0.20 max.

The addition of around 20% nickel to iron produces a Fe-Ni matrix that has a hysteresis of martensite formation on cooling and reversion to austenite upon heating to around 600° (the A_s temperature). The A_s temperature of the Fe-Ni martensitic matrix is high enough that maraging steels can be aged at around 485°C without reversion of the martensite matrix to austenite. The low levels of carbon in 18% Ni maraging steels help to keep the martensite Fe-Ni matrix ductile [23]. The precipitation hardening reaction gives the high strength/toughness associated with maraging steels. Maraging steels are less notch sensitive than other high strength steels such as 4340 [20]. There is also no evidence of a sharp ductile to brittle transition at lower temperatures [20] this is due to the nickel content [21].

All conventional grades of 18 %Ni maraging steel are either single or double vacuum re-melted to ensure good cleanliness [23]. The specific strength level that may be achieved from a heat of 18%Ni maraging steel mainly depends on the levels

of titanium, molybdenum and cobalt [23]. It is believed [20] that around 50% of the final yield strength of the fully heat treated 18% Ni maraging steel comes from the martensitic matrix. The strengthening contributions to 18% Ni maraging steels have been shown to be as follows [20];

- cobalt gives an incremental effect on the yield stress of 7-14 MPa per 0.1% added
- Molybdenum gives an incremental effect on the yield stress of 14-21 MPa per 0.1% added.
- Titanium gives an incremental effect on the yield stress of 0.3-0.5 MPa per 0.1% added

The basic strengthening mechanism comes from titanium and molybdenum with cobalt simply providing a denser martensitic matrix with a uniform distribution of dislocations. In the annealed alloy this provides many easy nucleation sites for the rapid precipitation of fine and uniformly spaced particles when the material is subsequently aged. It has also been suggested that the presence of cobalt might lower the solubility of molybdenum in the matrix therefore increasing the amount of molybdenum precipitate [19] and [22].

The strengthening portion due to ageing is as a result of the precipitation of intermetallic compounds; Ni_3Mo , Ni_3Ti . The reason that the 18% Ni maraging steels provide good toughness along with high strength levels [23] is the way the precipitates affect dislocation movement. In most common high strength steels the movement of dislocations is restricted, this can cause the locking and piling up of dislocations leading to the generation of fracture nuclei, the precipitates in maraging steels on the otherhand simply slow down the movement of dislocations [20].

The 18% Ni maraging steel is a complex alloy with all the elements synergistically combining to form a material with a greater strength than the sum of its constituent parts. The quantities of each of the elements added to the steel must be carefully controlled to ensure optimum affect. The alloying elements commonly used in maraging steels have the affect of reducing the martensite start temperature (M_S) temperature with the exception of cobalt, Floreen [19] comments " In practical terms, this affect of cobalt has been very helpful in allowing higher alloy contents to be added to the steels.". Other workers have also observed the M_S elevating effect of cobalt in maraging steels [23]. The M_S temperature of maraging steels must be strictly controlled in order to ensure complete transformation of austenite to martensite on air cooling to room temperature, this transformation to martensite is critical as the precipitates will only age harden martensite [24].

Levels of titanium above 0.54% lead to a reduction of the M_S temperature, this means that excessive titanium or insufficient homogenisation may result in retained austenite. Titanium is also used to scavenge residual carbon thus preventing the formation of molybdenum carbides that would tie up molybdenum and prevent the formation of Ni_3Mo and hence reduce ageing.

Carbon contents above 0.03% can have deleterious effects on toughness due to the formation of molybdenum and titanium carbides thus reducing the amounts of molybdenum and titanium for ageing.

Both silicon and manganese increase strength but in excessive quantities can have an adverse effect on ductility and notch sensitivity, see Figure 3 [20] and so are kept to 0.2 % combined.

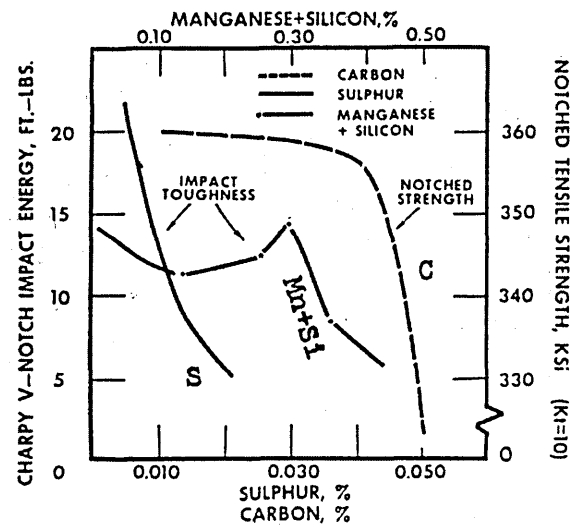


Figure 3 - Effect of Carbon, Manganese, Silicon and Sulphur on The Transverse Properties of 18% Ni Maraging Steel.

Strict control is required to prevent the reduction of the M_S temperature of maraging steels to such a point that reversion to austenite can occur during ageing or such that austenite may be retained after annealing.

2.3.2 Heat Treatment of Maraging Steels

18% Ni steels lend themselves well to production, upon air cooling after annealing they fully transform into a soft martensite that is easily machineable and can be aged by a simple heat treatment at 485°C followed by air cooling. The lack of rapid cooling removes problems of distortion associated with quenching. The low carbon content of the steel means that decarburisation is not a problem thus giving similar material characteristics at the surface or inside a component. Dimensional changes caused by heat shrinking are minimal [20].

2.3.3 TRIP Steels

As previously discussed maraging steels are martensitic precipitation hardenable steels, the martensite is formed upon cooling to room temperature. If during

subsequent heat treatment the material is heated above the austenite start temperature (A_s) around 600°) then the martensite will revert to austenite within the matrix.

The subsequent transformation of the reverted austenite to martensite will occur below the martensite start temperature (M_s). The M_s is a function of the specific alloy content, there are however some empirically based equations that are used to calculate the temperature at which martensite formation will begin, [25].

The transformation of austenite to martensite may also occur as a result of externally applied deformation, this process is known as Transformation Induced Plasticity (TRIP). The driving force for transition is controlled by the free energy difference between the austenite and martensite states and the externally applied stress, [26]. As the free energy between the states increases, with decreasing temperature, the level of externally applied stress required to cause transformation reduces. Conversely as the free energy between the austenitic and martensitic states decreases, with increasing temperature, the level of externally applied stress required to cause transformation will increase. Above a certain temperature, M_d , no deformation - induced transformation is possible. The M_{d30} temperature is the temperature at which 50% martensite is created for a plastic strain of 30%, there are empirical relationships used to find M_{d30} , see Equation 1 [25].

Equation 1

$$M_{d30} \text{ } ^\circ\text{C} = 497 - 462(C + N) - 8.1(Mn) - 20(Ni) - 13.7(Cr) - 18.5(Mo) - 9.2(Si)$$

Strain induced transformation from austenite to martensite has been linked to increased elongation during tensile testing by several authors, [27,28,29,31]. The increase of elongation due to a phase transformation from austenite to martensite may seem eccentric initially as martensite has low ductility and austenite is highly ductile.

The phenomena was first explained by Bressanelli and Moskowitz in 1966, [30]. The work hardening rate of the austenite is insufficient to prevent necking and hence only minimal uniform elongation is achieved before fracture. In metastable austenite, martensite forms in the region of necking, thus increasing the strength of the necked portion so that it is no longer the weakest section. Deformation then occurs in neighbouring regions. It is through this transformation that martensite reduces necking and encourages uniform strain along the gauge length leading to greater elongation.

Only the martensite formed in the latter stages of tensile testing, i.e. during necking, is considered beneficial [29]. Martensite formed prior to necking is detrimental because of the inherently low ductility of the martensite.

Even large quantities of reverted austenite can not be seen optically, this is because the austenite is located within the laths of the martensite in the form of very fine needles or platelets [28]. The volume fraction of reverted austenite within a martensitic matrix can be determined using either X-ray diffraction techniques [29] or by correlating the magnetic response of the material with the martensite content [30] [31].

2.3.4 Corrosion Properties Maraging Steels

The level of corrosion resistance offered by 18% Ni maraging steels is low. Upon exposure to the atmosphere 18% Ni maraging steels corrode uniformly. 18% Ni maraging steels do not display passivity and usually undergo uniform surface attack in common environments.

2.3.5 Stress Corrosion Cracking of 18% Ni Maraging Steels

It is generally agreed that the susceptibility to stress corrosion cracking (S.C.C.) increases with yield stress for ferrous alloys [32], however, when testing different alloy types at the same strength level 18% Ni maraging steels compare favourably to other high strength steels [18].

2.3.6 Air Fatigue And Corrosion Fatigue of 18% Ni Maraging Steel

The air fatigue strength of 18% Ni steels compares well with other high strength steels heat treated to give similar tensile strengths. Vacuum remelted 18% Ni maraging steel has a definite superiority over air melt grade [20], this would be due to the lower number of inclusions in the vacuum remelt steel when compared to the simple air melt.

Cottis and Husain [33] carried out fatigue tests in both air and 3.5% sodium chloride solution. The S-N curves in Figure 4 [33] show the damaging effect of the corrosive environment on the longer tests.

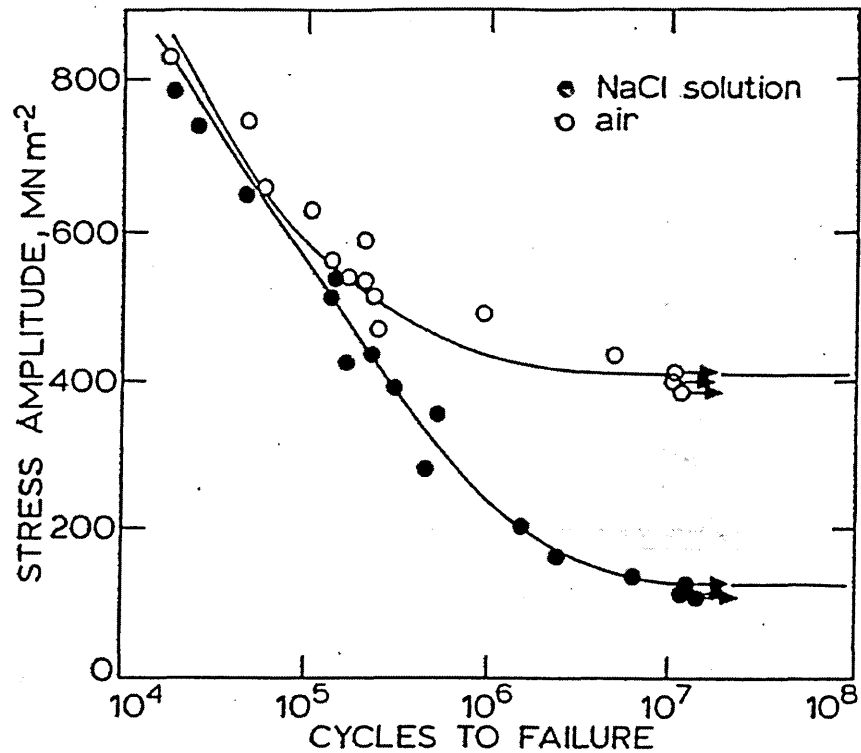


Figure 4 - S-N Curves For Double Vacuum Melted 18 % Ni Maraging Steel, Test Conducted At 14 Hz in Laboratory Air or Aerated 3.5 % NaCl.

Cottis and Husain [33] and later Alp et al [34] found that the initiation of fatigue cracks in both air and 3.5% sodium chloride solution was almost exclusively connected to non-metallic inclusions. The presence of the 3.5% sodium chloride facilitated a greater number of cracks at inclusions. Cottis and Husain [33] also found that the number of cracks initiating at a given inclusion was a function of the applied stress, see Figure 5 [33].

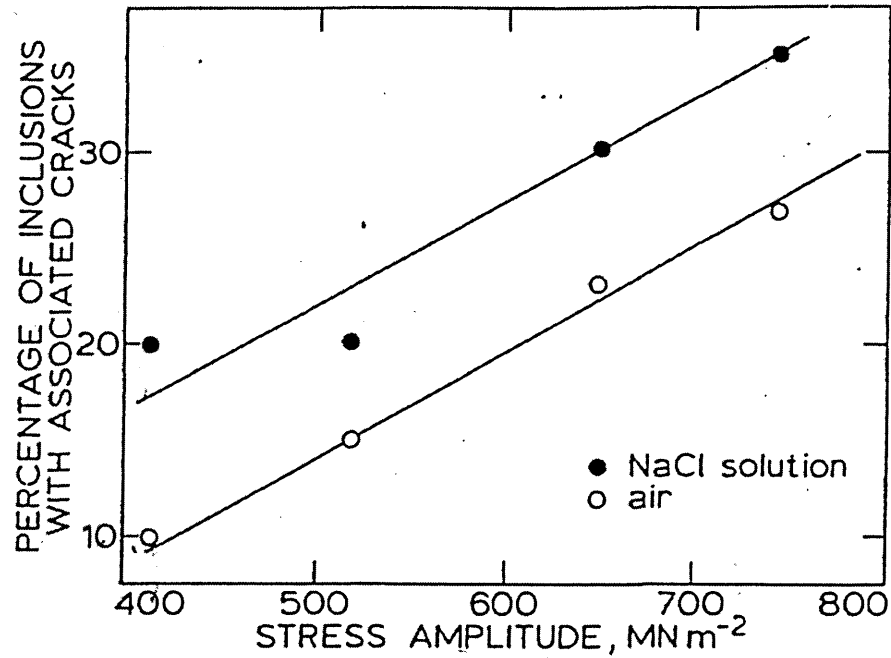


Figure 5 - Percentage of Inclusions Associated With Cracks At 5% of Expected Life Versus Stress Amplitude.

The crack initiation at inclusions is due to the enhanced plastic strain during fatigue loading caused by the stress concentrating effect of the inclusion. The stress concentrating effect of a given inclusion will depend on amongst other parameters its geometry, chemical makeup and the level of debonding between the inclusion and the matrix. The inclusions may corrode in preference to the matrix leaving a hole with its associated stress concentrating effect.

2.4 Air Fatigue

Fatigue is a phenomenon that causes premature failure or progressive damage in a material subjected to cyclic loading. It is a complicated process that is difficult to model on the microscopic level. With the demand increasing for engineering structures and components that last longer and cost less, so too does the level of investment in to fatigue research. Fatigue failure is well recognised as being one the most common modes of failure for metallic components. The fatigue process is generally broken down into two areas, crack initiation and crack propagation. Defining the transition from initiation to propagation is perceived as being difficult and open to interpretation however, this characterisation is still widely used. There have been many reviews of the fundamental work on fatigue, it is not the purpose of this chapter to repeat in detail that work. However, a brief review of the established knowledge was felt appropriate.

2.4.1 A Brief Historical Review

The failure of components due to repeated cyclic loading has been a recognised phenomenon since the first real systematic investigations were carried out by the pioneer of fatigue research August Wöhler. In 1860 Wöhler published the first of his classical papers on fatigue [35]. Wöhler conducted an investigation into the failure of iron chains, the chains had failed after only ten weeks operation. As a results of investigations it was felt that the links had become hardened due to vibration. Wöhler went on to carry out several detailed investigations into the phenomenon of fatigue. For several years the idea of the crystallisation of iron and steel due to vibration received much attention. In 1842 Hood [36] spoke before the Institute of Civil

Engineers about the change from a fibrous to a crystalline state that would result of sufficient force being applied to the material.

In 1886 Bauschinger [37] demonstrated that the elastic limit of a metal in both tension and compression are not fixed but that they could be substantially altered by the application of a cyclic stress.

In 1902 Ewing and Humphrey [37] showed by examining the polished surface of rotating bending specimen at intervals during fatigue life, that above a certain value of cyclic stress some crystals on the surface of the specimen developed bands during each cycle. These are now known as slip bands.

Following the first world war the research into fatigue was split into two main areas with the British adopting a more fundamental approach using metallurgists and physicists. The French, Germans, Japanese and Americans followed a more engineering approach by conducting laboratory tests to investigate the performance of in service components. With the use of heat treatable aluminium alloys in the construction of aeroplanes it soon became apparent that the fatigue limit seen by Wöhler in ferrous materials was not common to all materials.

Much of the work on fatigue published within the last fifty years has been based on these fundamental works, but with advances in science and technology the development of new materials brought new and varied problems. The electron microscope enabled physical confirmation of many earlier observations. The development of fracture mechanics in the sixties and the realisation that the rate of fatigue crack growth could be predicted from the size of the plastically deformed zone of material ahead of the crack tip revolutionised the modelling and analysis of fatigue crack growth.

2.4.2 Crack Initiation

Fatigue crack initiation takes place in areas of, greatest stress, or weakest microstructure. In the absence of any internal defects the initiation of a crack in a ductile material is associated with a free surface Frost et al [38] gave the following reasons for this;

- Surface grains are in intimate contact with the atmosphere; thus, if the environment is a factor in the damage process, surface grains are obviously more susceptible.
- A surface grain is the only part of a polycrystalline material not wholly supported by adjoining grains. Because the slip system in neighbouring grains of a polycrystalline material are not related to each other, a grain having a free surface will be able to deform plastically more easily than a grain in the body of the metal which is surrounded by other grains.
- If the surface of a specimen is hardened, the fatigue strength of a specimen as a whole may be increased. Similarly, any procedure which softens the surface decreases the fatigue strength of the specimen.

The surface of a material is associated with many forms of stress concentrations as result of manufacturing operations such as milling and turning. It is well known that improving the surface finish of a component can lead to large increases in fatigue limit [38]. Altering the surface of a material in such a way as to introduce compressive residual stresses will generally increase fatigue strength. Compressive residual stresses may be imparted to material by several processes;

Processes such as carburising and nitriding are beneficial to fatigue strength on two ways, they produce a higher strength material at the surface and because of volumetric changes that occur during the diffusion processes they also leave compressive residual stresses. Flame and induction hardening also cause volumetric changes that when limited to the surface will cause beneficial surface compressive residual stresses. There are several mechanical processes that can leave a material with compressive residual surface stresses and therefore more resistant to fatigue crack initiation. Both cold rolling and shot peening have been seen to be beneficial for fatigue strength. Recently laser energy has been utilised to induce residual compressive stresses deep into a metal surface [39]. Hot rolling causes surface decarburisation therefore leaving a lower strength material at the surface, the process can also leave residual tensile stresses at the surface. Chromium and Nickel plating steels can cause a reduction in fatigue strength of up to 60% [40]. This is due to the high residual tensile surface stresses generated as a result of the plating process and the presence of cracks within the coated layer.

It is not necessary for the bulk material to deform plastically for failure due to fatigue. Cyclic plastic deformation in one localised region is sufficient for fatigue crack initiation.

Under static loading slip lines form due to the movement of dislocations. As cycling is progressed, certain slip lines in the "softest" grains, i.e., those most favourably orientated for slip, intensify, producing bands of slip [41]. The bands grow wider and denser with large areas between the bands apparently free from slip. Frost et al [38] states "All persistent slip bands more than one grain long were found to open under an applied static tensile load" with fatigue cracks eventually forming at the slip bands.

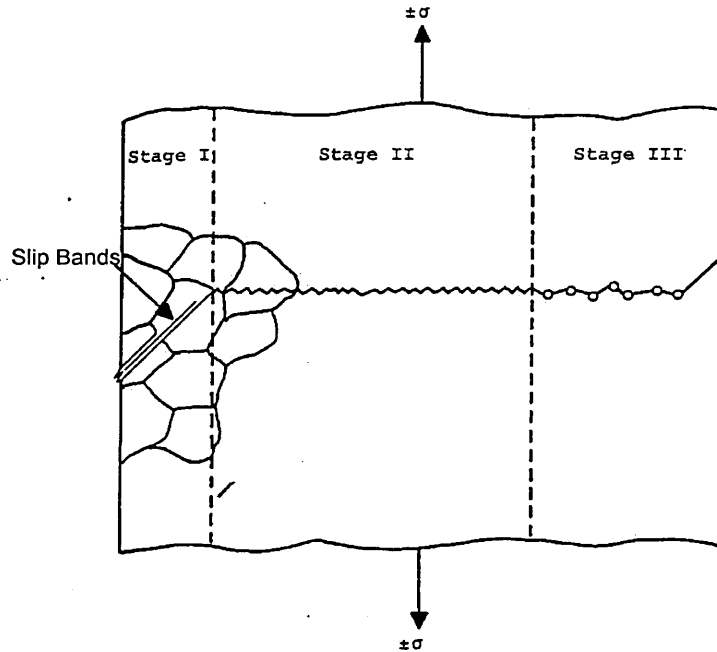
Slip bands lead to the formation of intrusions and extrusions. The process of extrusion was first observed by Forsyth [42] in his tests on 4.5% Cu-aluminium, coarse slip bands were not observed after cyclic loading instead fine slip line markings were observed. Some of these markings became accentuated and cracks appeared to initiate from irregular markings associated with accentuated slip line markings. These markings were found to be ribbon extrusions.

The extrusion process appeared to start suddenly and then stop suddenly after a small number of load cycles. Following this early founding work many workers have observed intrusions and extrusions occurring at slip bands in metals.

Non-metallic inclusions have also been observed to be the site of fatigue crack initiation, more detail will be given on this in the Non-Metallic Inclusions section (see page 54).

2.4.3 Fatigue Crack Propagation

Crack propagation is the period between crack initiation and complete fracture. In general this phase between initiation and fracture is broken into three convenient epochs. Each with its own distinctive growth, Figure 6 [42] illustrates each phase schematically.



- Stage I Shear crack growth on crystallographic slip plane
- Stage II Striation crack growth – crack growth on a plane normal to the applied stress
- Stage III Unstable Rapid crack growth; ductile tearing

Figure 6 - Schematic Illustration Of The Three Stages Of Fatigue Crack Growth Under Reversed Tensile Loading.

2.4.3.1 Stage I Fatigue Crack Growth

Stage I crack growth is dominated by shear with microcracks growing along the plane of greatest shear. This is generally at 45° to the applied nominal stress in uniaxially

loaded polycrystalline material. Under low load high cycle fatigue this period of growth may account for up to 90% of the fatigue crack life. The behaviour of stage I and stage II cracks is extremely different.

The transition from stage I to stage II crack growth is not immediate and generally takes place gradually over a few grains.

2.4.3.2 Stage II fatigue Crack Growth

Stage II crack growth is associated with the magnitude of the tensile strain range in the material just ahead of the crack tip. The cracks grow perpendicular to the applied nominal stress as it is in this plane where the greatest amount of crack displacement is possible leading to the greatest strain range in the material ahead of the crack tip. Stage II cracks are often referred to as macrocracks or long cracks. It is within this relatively stable stage of crack growth that most engineering predictions are made.

2.4.3.3 Stage III Fatigue Crack Growth

Stage III crack growth is at a fast rate and characterised by static modes of fracture such as, cleavage or intergranular separation of the material until complete fracture. In most practical engineering design situations this period of crack growth is ignored due to the speed at which fracture may occur.

2.4.4 Linear Elastic Fracture Mechanics

Crack propagation is almost exclusively described using fracture mechanics. When one considers a growing crack there are three basic modes of crack surface displacement, these are shown schematically in Figure 7 [43]. Under mode I loading the crack surfaces move directly apart, mode II and III are shear modes. For each

mode of displacement there is a characteristic elastic stress field associated with the crack tip.

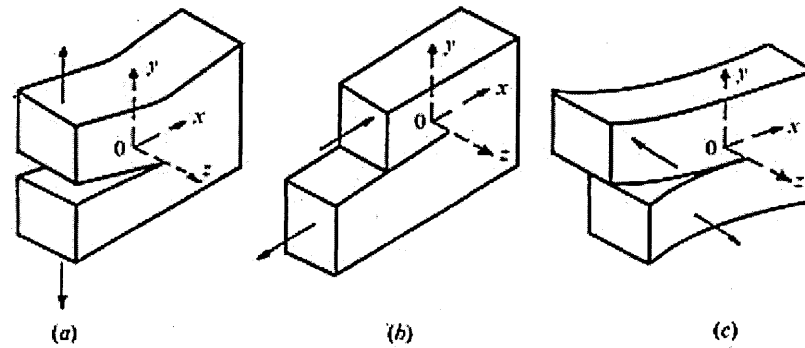


Figure 7 - The Three basic modes of Fracture. (a) Tensile Opening (mode I). (b) In-Plane Sliding (mode II). (c) Anti-Plane Shear (mode III).

The stress fields at the crack tip are quantified using the stress intensity factor (K).

The stress intensity factor solution for mode I loading is given in Equation 2.

Equation 2

$$\Delta K = \alpha \Delta \sigma \sqrt{\pi a}$$

where,

a = Crack length

α = A dimensionless function that depends on the crack geometry and loading configuration.

$\Delta \sigma$ = Remotely applied stress range

Paris and Erdogan [44] suggested that as the stress intensity factor range describes the stress field around the crack tip the (ΔK) should be proportional to the rate of fatigue crack propagation. This relationship is defined with by the Paris law;

Equation 3

$$\frac{da}{dN} = C(\Delta K)^m$$

$$\frac{da}{dN} = \text{Crack growth rate per cycle}$$

C, m = Material constants

Equation 3 assumes that the microstructure of a given material will be homogeneous.

Where the rate of crack growth is appreciably affected by microstructural discontinuities such as grain boundaries the Paris law is no longer applicable. The stress field must also be predominately elastic. Figure 8 [43] shows a plot of crack growth rate with respect to stress intensity factor range regime A,B and C correspond to stage I,II and III in the previous section.

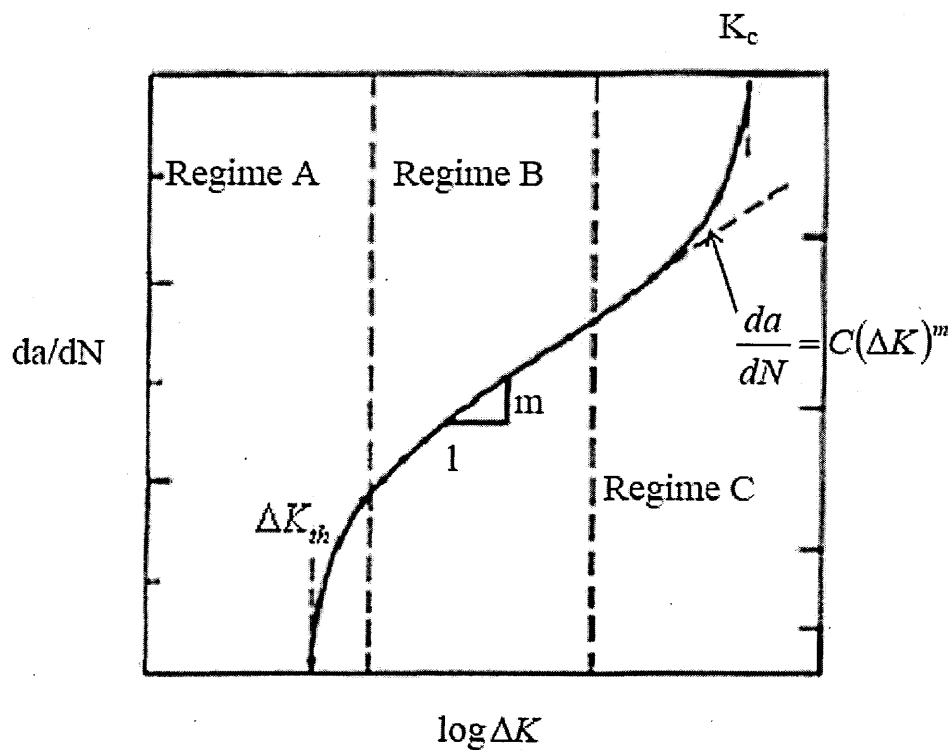


Figure 8 - Schematic Illustration of the Different Regimes of Stable Fatigue Propagation.

It is only in region B where the Paris law is applicable. In region C the effect of microstructural features is large, however, region C is of only limited interest as by the time the crack reaches this stage the majority of component life will have passed. The fatigue threshold stress intensity factor range (ΔK_{th}) is defined as the highest stress intensity range for which no crack growth will occur. (ΔK_{th}) is determined experimentally, a crack growth rate in the order of 1×10^{-6} ($\mu\text{m}/\text{cycle}$) is generally considered as zero crack growth. Within regime A the microstructure of the material can have a large effect on crack growth rate. Cracks in regime A are known as short cracks if they are physically smaller than 0.1mm.

Short Fatigue Crack Growth

The data used to construct (da/dN) - ΔK curves and hence predict crack growth rates rely on laboratory fatigue tests on specimens containing long cracks, typically in the order of tens of millimetres. Suresh [43] states "it has been shown that the growth rates of small flaws can be significantly greater than the corresponding rates of long flaws when characterised in terms of the same nominal driving force." The short crack growth problem is seen as a breakdown of similitude. Similitude is fundamental to the use of fracture mechanics and states that cracked components of different dimensions exhibit the same crack growth rate when subjected to the same value of stress intensity factor. Short cracks have also been observed to grow at

values of stress intensity factor range below the threshold value predicted by laboratory testing of specimens with long cracks.

2.5 Effect of Grain Size on Fatigue Strength of Metals

It has been shown that a correlation exists between the grain size of a metal and its tensile flow characteristics. This relationship is represented with the Hall-Petch equation [45], see Equation 4.

Equation 4

$$\sigma_y = \sigma_i + k_y d^{-1/2}$$

where,

d = Average grain diameter.

σ_i = Constant related to the resistance of a metal to the movement of dislocations.

k_y = Constant associated with the generation of dislocations

If one considers the nucleation of a crack in a virgin surface, the influence of grain size occurs as the grain boundaries obstruct the movement of dislocations. It can be seen that in such a case a reduction in grain size would lead to an increase in the time elapsed in stage I for nucleating a crack of a given length [46]. Earlier work by Masounave and Baflon [46] found there was a relationship between the threshold stress intensity factor and the grain size of a ferritic steel, see Figure 9 [46], $R=0$.

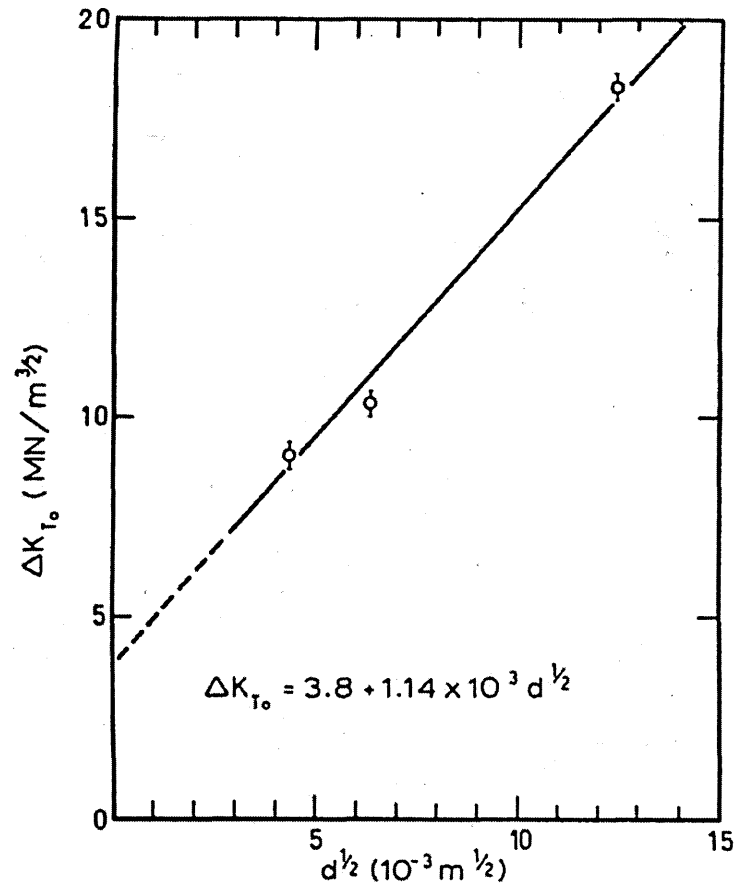


Figure 9 - The Effect of Grain Size on The Threshold Stress Intensity Factor.

Taira et al [47] found that the fatigue limit (σ'_{wo}) of low carbon steel was correlated to the grain size (l) in metres using Equation 5.

Equation 5

$$\sigma'_{wo} = 114 + 3.29 \times 10^{-1} / \sqrt{l}$$

As the nucleated crack grows the influence of grain size diminishes until a point is reached where crack growth is insensitive to microstructure. Yoder et al [48] found a distinct transition occurred as the fatigue crack growth moved from a microstructurally sensitive growth to one of microstructural insensitivity. They termed

this point the transition stress intensity (ΔK_T). A substantial effect of grain size on crack growth rate was also observed both hypo and hypertransition. Yoder et al [48] found that the transition was linked to the cyclic plastic zone size. Prior to the transition the cyclic plastic zone size was smaller than the grain size of the material. After the transition from microstructurally sensitive growth to one of microstructural insensitivity the cyclic plastic zone size was greater than the grain size, see Figure 10 [48].

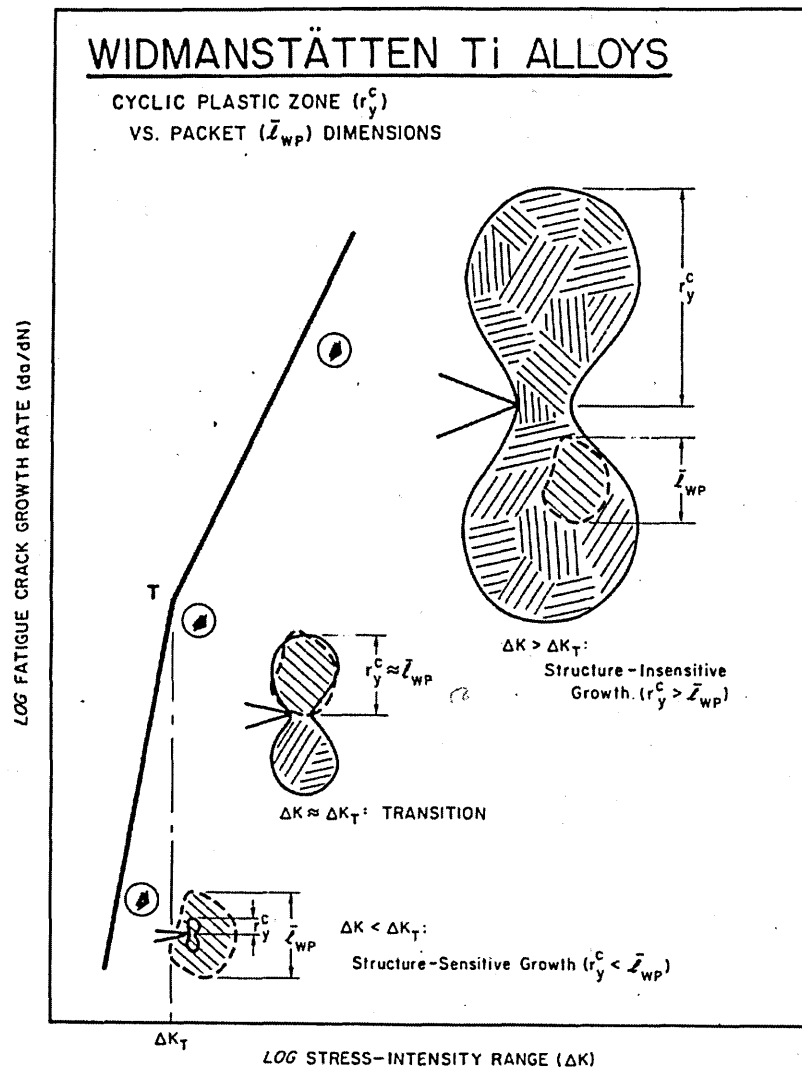


Figure 10 - Influence of Plastic Grain Size, Relative to Mean Packet Size, Upon The Development of Bilinear Form of Fatigue Crack Growth Behaviour.

Yoder et al [48] also found that the transition became more acute the greater the degree of clustering of packet (grain) size about the mean value.

2.6 Fatigue at Notches

In general engineering structures and components are designed such that the bulk stress - strains remain elastic, however, almost all practical engineering components or structures contain some form of geometrical discontinuity known as a notch. These discontinuities or stress raisers often cause local stresses in excess of yield under normal loading conditions. The notch may be a keyway or hole that is essential to the functionality of the component and so cannot be removed. The effect that notches have on the fatigue life of a component can be extremely deleterious and cannot be ignored, Figure 11 [49] clearly shows the effect of notches on fatigue life with S-N curves for plain and notched specimens being plotted.

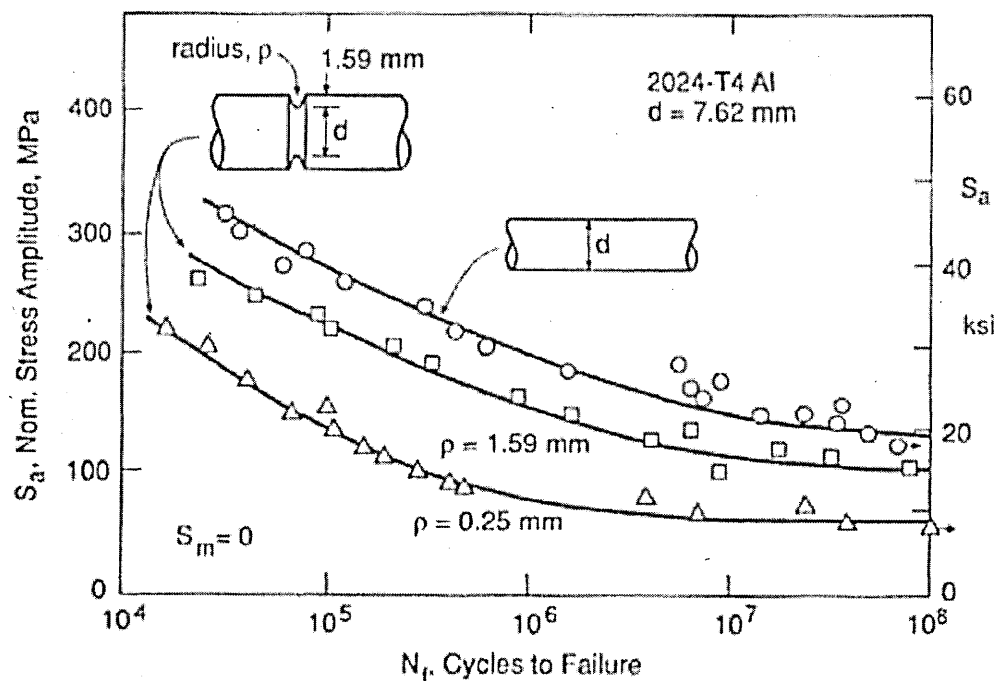


Figure 11 - Effects of Notches on an the Fatigue Strength of an Aluminium Alloy.

Fatigue failure in real components almost invariably begins at the root of a geometrical discontinuity [50].

Analyses of notched components generally try to relate data from plain specimens to produce a strength reduction factor, K_f or K_t . The major failing of such strength reduction factors is that they relate to the bulk stress or strain parameters and not the behaviour of a fatigue crack and its local stress strain field [51].

2.6.1 Fatigue Crack Growth at Notches

The mechanisms that cause fatigue cracks to initiate at notches are essentially the same as those at a plain surface, with slip bands being formed and eventually leading to the nucleation of a crack. Fatigue cracks initiate where there is the greatest stress and the lowest material strength. The stress concentration caused by a notch is sufficiently great that it will overcome many material weaknesses elsewhere in the material and the fatigue crack will initiate at the notch. The stress pattern around a notch is dependent upon the specific geometry; however the greatest stress will be at the notch root decreasing as distance from the notch root increases. Typically there is an area of plasticity around the notch root leading into an elastic region before returning to the level of stress within the bulk of the material. A typical stress distribution around a notch is shown below in Figure 12 [50].

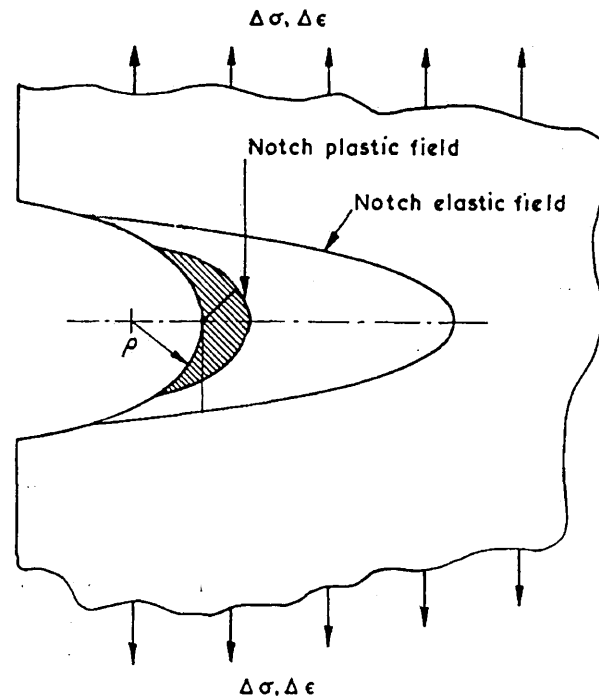


Figure 12 - Elastic and Plastic Stress Strain Fields at the Notch Root.

During experimental fatigue tests on notched specimens a number of observations have repeatedly been observed. In many notched specimens non-propagating cracks have been found. It has also been noted that fatigue cracks growing from notches do so at initially high rates in excess of those based upon long crack growth analysis.

The reason suggested for both non-propagating and short crack phenomena is that of notch root plasticity and stress gradient.

If the applied stress is high enough the stress concentrating effect of the notch will cause localised plasticity, reaching a maximum at the notch root. A fatigue crack may then initiate within this local plastic region. Once initiated the fatigue crack will grow through the plastic region associated with the notch, however the crack will only propagate to failure if it is long enough or the applied stress is high enough for it to generate sufficient crack tip plasticity. If the crack is unable to generate its own crack tip plasticity sufficient to propagate through the elastic bulk of the material and the highly elastic notch field it will not propagate.

The crack growth rates associated with notch induced plasticity are far in excess of the crack growth rates that would be seen due to crack tip generated plasticity. Figure 13 [52] is a schematic of the two processes involved in fatigue crack growth from a notch.

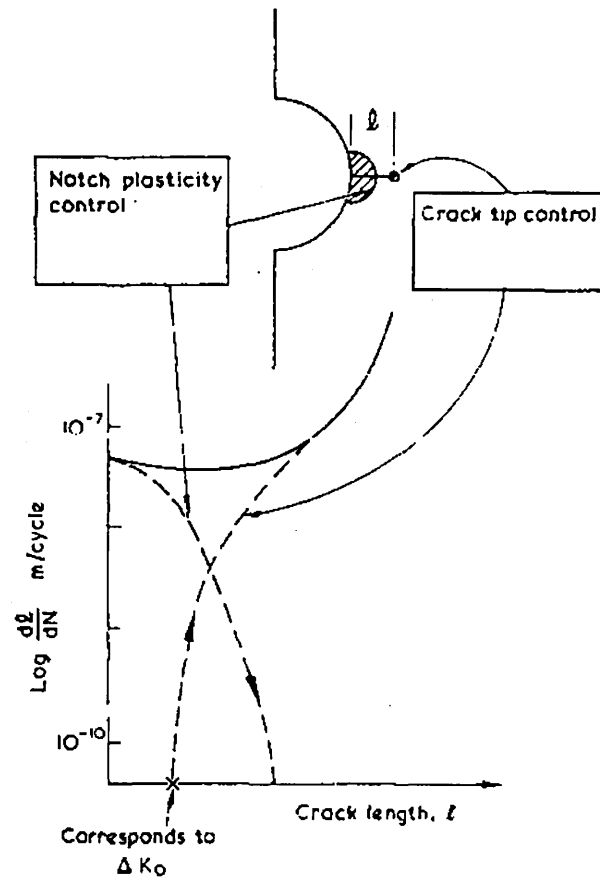


Figure 13 - Two Processes Of Fatigue Crack Growth From A Notch.

2.6.2 The Initiation of Fatigue Cracks From Notches

Several authors [53-60] have found a correlation between the number of cycles to initiate a fatigue crack, N_i , and notch root radius ρ . Figure 14 [53] shows the number of cycles to initiate a crack decrease as the notch becomes sharper.

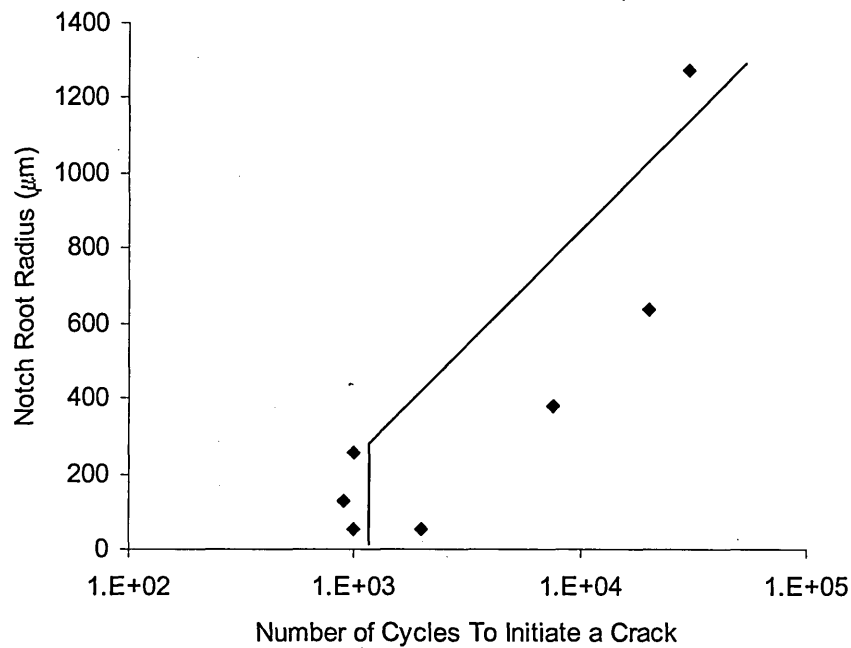


Figure 14 - The Influence of Notch Root Radius (ρ) on the Number of Cycles to Initiate a Crack (Ni) From a 2.54 (mm) Deep Notch. For a Mild Steel. Stress Range = 0 - 200 (MPa).

This correlation seems reasonable, as one could think of a crack as being a notch with a near zero root radius. It can be seen from Figure 14 [53] that below a critical value of notch root radius the relationship no longer exists, various values for this critical value of notch root radius have been proposed Atkinson and Lindley [54] showed a good correlation down to a notch root radius of at least 40 (μm), see Figure 15 [54].

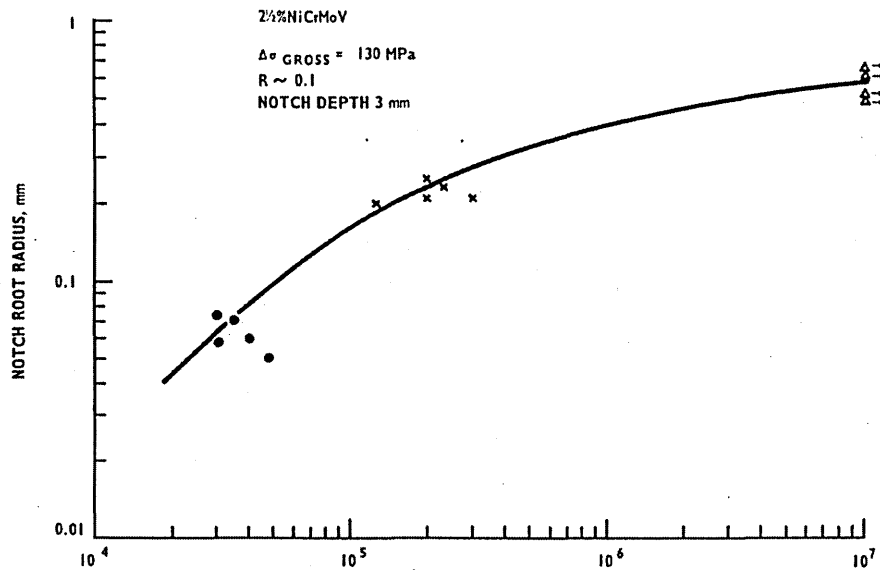


Figure 15 - Effect of Notch Root Radius on Number of Cycles to Initiation for 2.5%NiCrMoV Under Constant Stress Range.

The correlation between notch root radius (ρ) and the number of cycles to initiate a fatigue crack (N_i) is also a function of applied stress.

Jack and Price [53] found above the notch root radius limit (ρ_o) the number of cycles to initiate a fatigue crack could be related to the notch root radius using the following relationship.

Equation 6

$$N_i \propto (\Delta K)^{-4}$$

Figure 16 [53] shows that a good correlation existed between $\frac{\Delta K}{\rho^{1/2}}$ and N_i .

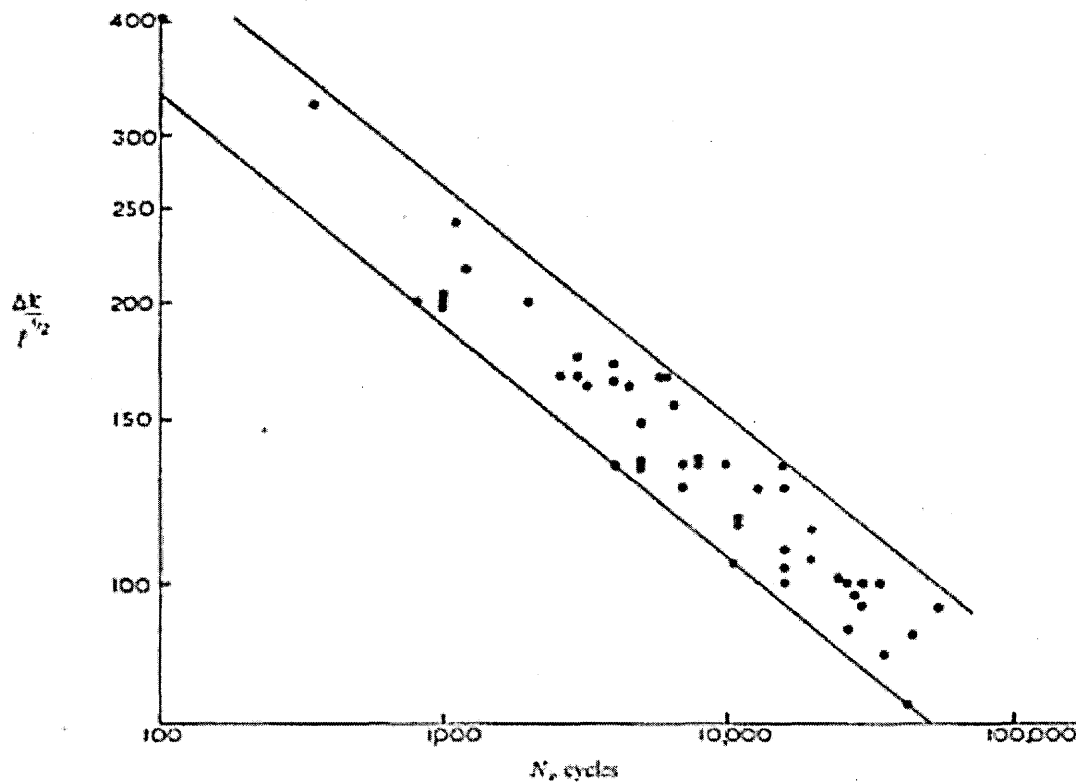


Figure 16 - The Influence of Effective Stress Intensity Factor ($\Delta K/\rho^{1/2}$) (Ksi) on the Number of Cycles to Failure.

In a later work for notch root radii equal or less than 250 (μm) Jack and Price [55] proposed the following relationship

Equation 7

$$N_i = \frac{2.63 \times 10^8}{(\Delta K / 1.0957)^4}$$

Work reported by Barsom [56] and Clark [57] also showed the importance of $\frac{\Delta K}{\rho^{1/2}}$

for characterizing the resistance of a metal to the initiation of a fatigue crack. Later work by Kim et al [58] further developed the idea of a common threshold value of

$\frac{\Delta K}{\rho^{1/2}}$ for long lifetimes previously suggested by Barsom [56] and Clark [57]. Figure

17 [58] shows the results of work conducted by Kim et al [58] on notched specimens of 4140 steel in the as quenched condition and with two different tempering conditions.

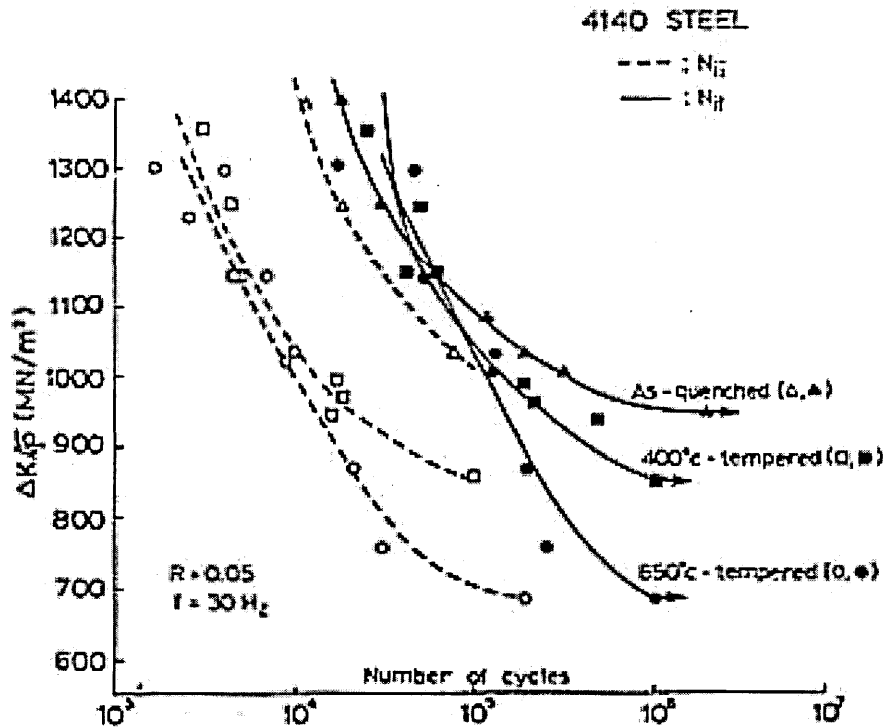


Figure 17 - $\frac{\Delta K}{\rho^{1/2}}$ Versus The Number of Cycles To Initiate a Fatigue Crack For Three Heat Treatments on 4140 Steel.

In Figure 17 [58] two initiation conditions are plotted, N_{ii} corresponds to a 3 (μm) crack depth while N_{if} is the number of cycles to initiate a crack extending across the full lateral dimension of the notch (3.2 mm). It can be seen from the above figure that there is a threshold value of $\frac{\Delta K}{\rho^{1/2}}$ for each heat treatment condition. The threshold condition is a function of material strength. Kim et al [58] used two equations that

relate material strength to the threshold value of $\frac{\Delta K}{\rho^{1/2}}$, $\frac{\Delta K}{\sqrt{\rho_{th}}}$, the first, Equation 8,

proposed by Barsom and Rolfe [59] and the second, Equation 9, by Barsom [60]

Equation 8

$$\Delta K / \sqrt{\rho_{th}} \cong 9.5 \times (\sigma_{y.s.})^{2/3}$$

Equation 9

$$\Delta K / \sqrt{\rho_{th}} \cong 26 \times (\sigma_{y.s.})^{1/2}$$

Kim et al [58] found better agreement with experimental results when using Equation 9, see Table 3.

$\Delta K / \sqrt{\rho_{th}}$ (MPa)	
Experimental	Calculated Equation 9
950	918
890	938
660	749

Table 3 - Comparison of Measured and Calculated $\frac{\Delta K}{\sqrt{\rho_{th}}}$.[58].

Atkinson and Lindley [54] found a common threshold value of $\frac{\Delta K}{\rho^{1/2}}$ that was

independent of notch root radius, for the 2.5%NiCrMoV steel tested a threshold value of approximately 650(MPa) was proposed. Figure 18 [54, 57, 58] shows results

from the initiation tests on notched 2.5%NiCrMoV rotor steel specimens with notches ranging from 75(μm) to 1000 (μm) [54] plotted along with data from Kim et al [58] for 4140 steel in three different heat treatment conditions, and data from the work of Clark [57] looking at fatigue crack initiation in notched specimens of 403 type stainless steel.

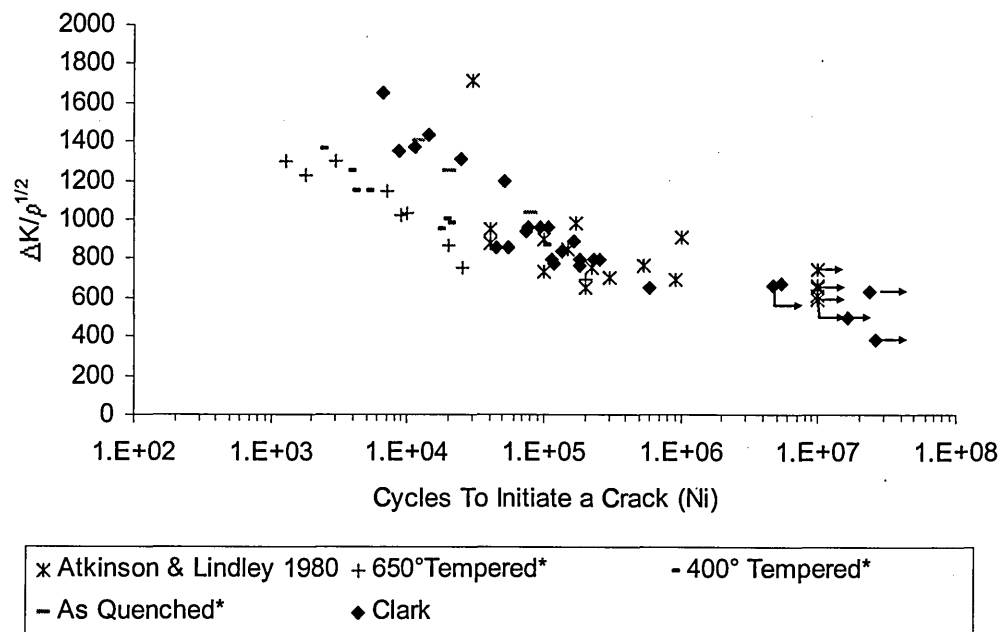


Figure 18 - $\frac{\Delta K}{\rho^{1/2}}$ Versus Number of Cycles To Initiate a Fatigue Crack For Various Notch Root

Radii. All Tests Conducted in Laboratory Air at Room Temperature.

It can be seen from Figure 18 [54, 57, 58] that there is some scatter between the data this is due in part to the different strengths of the materials used, see Table 4.

Material	Proof Stress (0.2) (MPa)
403-SS 57	645
2.5%NiCrMoV 54	633
4140 58	-
As Quenched	1220
400°C Temp	1280
600°C Temp	820

Table 4 - Proof Stress Values For Materials Used in Fatigue Crack Initiation Experiments

2.6.2.1 The Initiation of Fatigue Cracks From Notches In a Corrosive Environment.

Clark [57] conducted fatigue crack initiation experiments on 403 type stainless steel using 25.4 (mm) thick WOL type compact tension specimens in both laboratory air and a high oxygen steam environment. The specimens were subject to oxygenated steam at 100°C, the longest period of exposure during testing was 2 weeks. Clark [57] saw no effect of the environment on fatigue crack initiation, see Figure 19 [57].

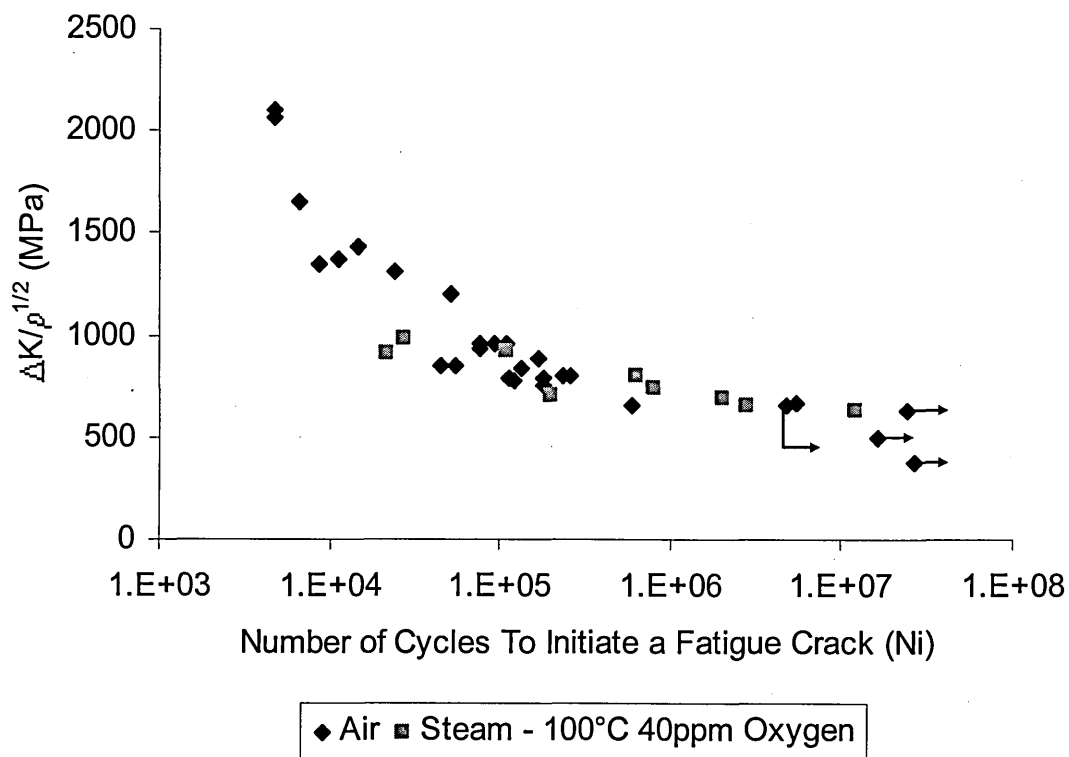


Figure 19 - $\frac{\Delta K}{\rho^{1/2}}$ Versus Number of Cycles To Initiate a Fatigue Crack For Various Notch Root

Radii in Type 403 Stainless Steel.

2.6.3 Models of fatigue Crack Propagation From a Notch

Within the literature there exist several models for fatigue crack growth from a notch.

Many of the more recent approaches have moved away from notch fatigue studies via stress concentration factors, fatigue strength reduction factors, etc., as these

approaches fail to take into account the fatigue crack and the way in which it grows.

At low stress levels fatigue crack initiation can take up to 90% of fatigue life, where

as at high stress levels over 90% of crack growth could be considered as stage II.

Smith & Miller [51] suggested that as the notch causes localised high strain the

initiation period could be neglected and hence all growth takes place in the stage II

region of crack growth allowing the use of a fracture mechanics approach. They then

go on to state that all the microscopic features of crack growth, crack opening

displacement, size or shape of the crack tip plastic zone etc., are reflected in the crack

growth rate. So a fatigue crack of length (L) growing in an un-notched specimen can

be likened to a fatigue crack of length (l) in a notched specimen if they both have the

same instantaneous crack growth rate. Obviously $L > l$ Smith & Miller [51] postulate

that the notch contribution to crack length (e) can be defined using Equation 10.

Equation 10

$$e = L - l$$

They go on to produce a theoretical solution of this equation and show that when the

crack is outside the zone of the notch influence the depth of the pseudo crack is the

fatigue crack length plus the notch depth. The theoretical equation for the notch

contribution to crack length within the influence of the notch is given in Equation 11

Equation 11

$$e = 7.69l \sqrt{\left(\frac{D}{\rho}\right)}$$

Smith & Miller [51] showed that fatigue crack growth from notches is a two stage process with crack initiation and early growth being controlled by notch plastic zone and later growth being controlled by the crack tip plastic zone. They defined the stress required to initiate and grow a crack to failure as,

Equation 12

$$\sigma = 0.5 \frac{\Delta K_{th}}{\sqrt{D}}$$

Below this stress level fatigue cracks may initiate but will arrest before leaving the notch plastic zone. Figure 20 [61] shows the three regions of crack behaviour.

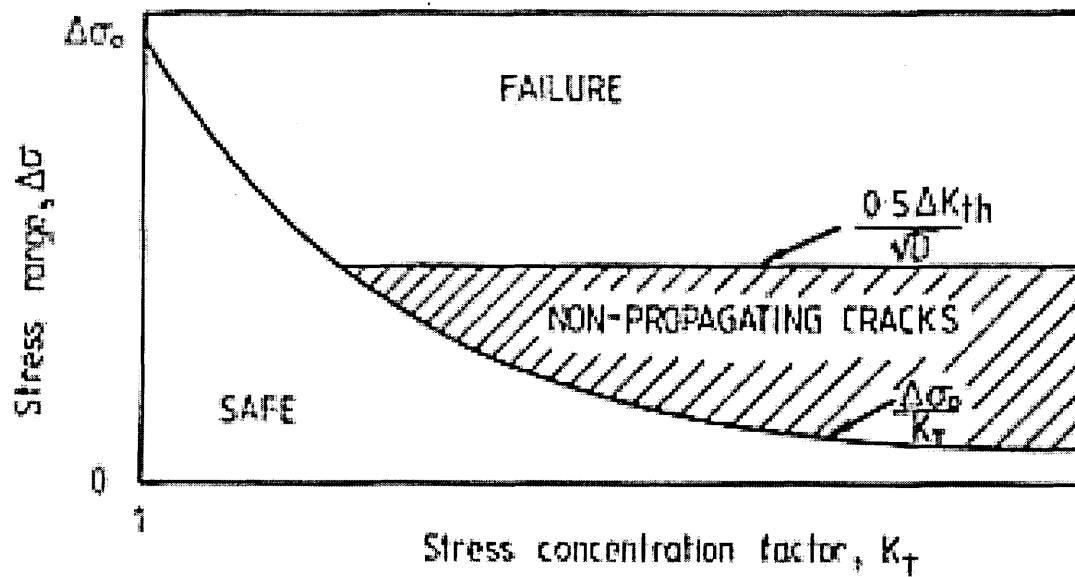


Figure 20 - Fatigue Behaviour of Notched Components.

Yates & Brown [61] built on the earlier work of Smith and Miller [51] [52] in the prediction of the length of non-propagating cracks. Using the Kitagawa & Takahashi [149] diagram they showed the effect of crack length on threshold stress intensity factor range for crack propagation. Using equations taken from Smith & Miller [51] [52] Yates and Brown [61] were able to estimate the stress intensity factor range both remote from the notch and in the vicinity of the notch. By combining the curve produced in accounting for the notch and the curve produced for a plain specimen it is possible to gain one of three situations, namely no crack growth, continuous crack growth to failure and finally the crack will initiate but fail to propagate to failure. See Figure 21 [61].

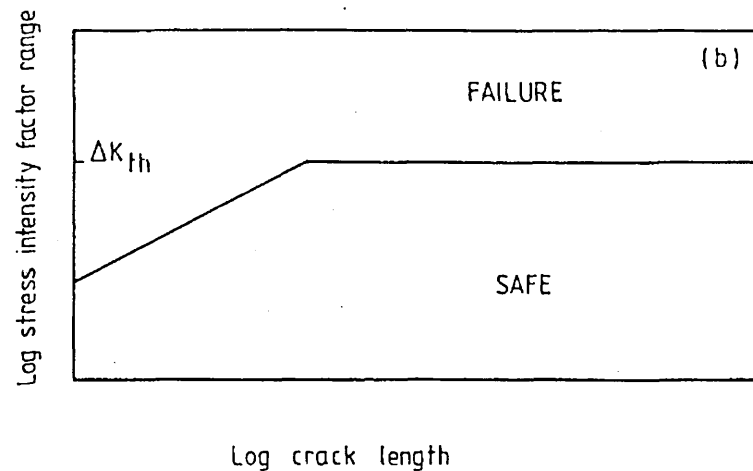


Figure 21 - Effect of Crack Length on Stress Intensity Factor Range.

2.7 Non-Metallic Inclusions

It has been estimated that each tonne of steel may contain between 10^{10} and 10^{15} inclusions [62]. Inclusions or more specifically non-metallic inclusions occur in commercial steels as a result of the steel making process. In commercial steel inclusions are principally either oxides, or sulphides. The main sulphide in commercial steel is manganese sulphide.

It is possible to classify inclusions into one of two groups based on their origins. Endogenous inclusions are caused as a direct result of additions made during the steel making process. The origins of exogenous inclusions are found external to the steel making process i.e. the reaction of the steel to its containing environment or the atmosphere.

Inclusions can have notable effects on both the mechanical properties of the steel and its processing properties beyond the scope of this report. It should be noted that not all inclusions are detrimental to the steel and some are purposefully added in order that the steel maker produces the required characteristics, the most noticeable example of this is the addition of sulphur to ensure that free cutting steel is produced.

2.7.1 Effect of Inclusions on in Air Fatigue Strength

Inclusions can have a very marked effect on the initiation and propagation of fatigue cracks. Atkinson [63] stated the following "It is generally agreed that fatigue resistance is one of the properties most sensitive to the influence of inclusions and that ultra-high-tensile steels are most susceptible". This pernicious effect of inclusions on fatigue strength is normally attributed to the localised stress and strain

concentration where the inclusion meets the steel matrix. The conflict that causes stress/strain concentration is due to the relative difference between the chemical, mechanical and thermal characteristics of the inclusion and the steel matrix. A further explanation of the crack nucleating effects of inclusions is that of the debonding that occurs between the inclusion and steel matrix leading to the creation of stress/strain concentrations. As the steel matrix and inclusion debond from each other the formation of point surface defects or microvoids a few micrometers from the inclusions is observed, as shown in Figure 22 [64].

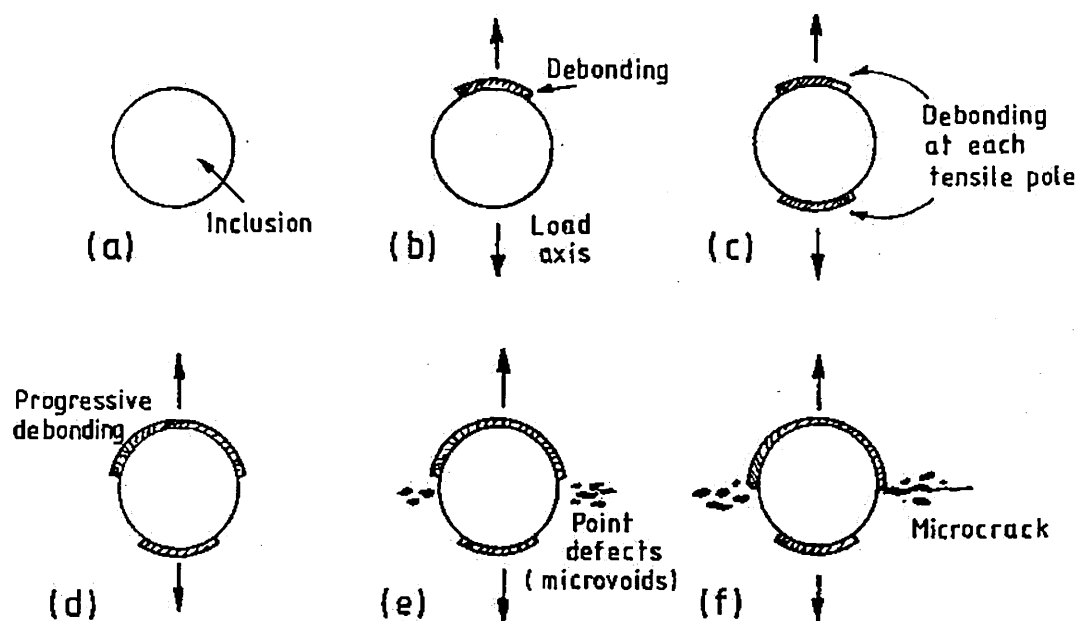


Figure 22 - Model Of Non-Metallic Inclusion Debonding.

Debonding between the inclusion and the matrix may also result from differential thermal contraction [65].

In high strength steels it has been shown that alumina inclusion particles are among the most effective at nucleating fatigue cracks by causing stress/strain concentrations.

Some inclusions have been observed to improve fatigue strength, manganese

sulphide inclusions actually counteract the stress raising potential of alumina particles. It has been reported [66] that surface inclusions are more harmful than subsurface ones and that the critical inclusion size for initiating fatigue cracks increases with the distance from the free surface. It is well understood that the number, size and type of inclusions are important in determining their effects on subsequent fatigue behaviour the properties of the parent metal and the modification of those properties in the vicinity of the inclusions also any residual stress systems set up during manufacture. The crack nucleation behaviour is affected by the arrangement of the inclusions with respect to the axis of loading and hence orientation of the stress field around the inclusion. The deformability of the inclusion with respect to the steel matrix is extremely important in considering crack nucleation. Inclusions with low deformability can cause microcracks to initiate at the inclusion matrix boundary during manufacturing processes prior to service loading, essentially meaning cracks have initiated even before the material is put into service. It is well established that high strength steels have relatively low fracture toughness, meaning that the critical stress intensity factor value at which unstable fracture will occur is relatively low, therefore even a small defect could lead more easily to catastrophic failure in high strength steel. High strength steels are also intolerant to small surface defects when used in high stress applications. For both of the above reasons higher strength steels are more susceptible to the detrimental effects of inclusions.

2.7.2 Models Used To Account For Non-Metallic Inclusions And Their Effect On Fatigue Strength

The effects of inclusions on fatigue strength are so complicated that no integrative approach for quantifying their effect on fatigue life has been arrived at. As previously mentioned the shape size, location, orientation and chemical composition are a few of the parameters that affect the ability of an inclusion to influence fatigue life.

The Fox inclusion count was used for many years to assess the non-metallic content of a steel however it has been reported that there is no relationship between the Fox inclusion count and fatigue properties [63]. Other methods that have been proposed include the Fairley inclusion count with this approach it is assumed that the inclusion behaves in a similar manner to cavities, especially under tensile loading conditions, and that the stress concentration factor caused by an inclusion may be assessed by considering its shape much like a notch. The Fairley count works by assuming the most adversely shaped inclusion likely to be encountered is a sphere, and that inclusions are normally orientated with their major axis parallel to the direction of working. It is also assumed that it is the shape of the inclusion rather than the chemical composition which determines its effect on the fatigue strength of a material. The Fairley count works by counting the number of inclusions in a plane parallel to the direction of applied stress, in order to achieve such count a representative area of the material is polished and magnified by 200 times. It is simply a matter of using a chart to assess the stress concentrating effects of the inclusion. Most works carried out into the effects of inclusions on fatigue life are similar in approach to the Fairley count and may be considered in one of three ways [67].

- Stress concentration introduced by defects or inclusions

- Classification of defects and inclusions
- Size of defects and inclusions

There are several problems associated with these approaches.

When considering the effect of inclusions solely in terms of the stress concentrating effects one must consider the extremely complex geometry of some inclusions.

Inclusion counts like the Fairley one discussed produce a stress concentration based on simple approximations and are unable to give accurate results. It is also well understood that fatigue failure is not bought about simply by the stress with the greatest magnitude but by the range of stresses a material is subjected to [35].

The classification of inclusions has traditionally been achieved by considering their metallurgical and shape characteristics, with silicates and aluminium oxides being the most harmful. It has also been shown that some inclusion have little or no effect on fatigue life. Some researchers have attributed this to the static ultimate tensile strength being below a certain level, however there have been many varied reports on the actual critical tensile strength required.

The size of defects is very important as it has been reported by some authors [67] that different fatigue strengths have been reported for two geometrically similar but unequally sized defects or inclusions in spite of the same stress concentration factor. Several empirically based models have been proposed for the effect of inclusions on fatigue life, one of the first being proposed by [68] see Equation 13.

Equation 13

$$\sigma_w^3 I = k$$

Where σ_w is fatigue strength, I is defect length and k is a material constant.

This equation was based on work carried out on relatively large inclusions however it has been shown to be appropriate for use with inclusions ranging in size from 100(μm) to 20 (mm). Congleton and Wilks [69] working on a 13% Cr turbine blade steel used the above equation and found reasonably close agreement with the observed fatigue limit.

An equation proposed by Kobayashi & Nakazawa [70] gives more accurate results for inclusion sizes from 30(μm) to 1000(μm) see Equation 14.

Equation 14

$$\sigma_w^4 I = k$$

Where σ_w is fatigue strength, I is defect length and k is a material constant.

A different approach is to approximate the inclusion as a small crack and use fracture mechanics, this approach was used by Murikami et al [71]. The bases of this method is that the threshold stress intensity factor range is the same for an inclusion as it is for a small crack. Murikami et al [71] state that the threshold stress intensity factor range for an inclusion is controlled by the projected area of the inclusion and propose Equation 15.

Equation 15

$$\Delta K_{TH} = 3.3 \times 10^{-3} (Hv + 120) \left(\sqrt{\text{area}} \right)$$

Where H_v is the Vickers hardness value and the area is the projected area of the inclusion. Murikami et al [71] then go on to present the following relationships Equation 16 for a surface inclusion and Equation 17 for a sub surface defect

Equation 16

$$\sigma_w = \frac{1.43H_v + 120}{(\sqrt{area})^{\frac{1}{2}}}$$

Equation 17

$$\sigma_w = \frac{1.56H_v + 120}{(\sqrt{area})^{\frac{1}{2}}}$$

2.8 Corrosion

2.8.1 Introduction

Corrosion is the degradation of a metal by an electrochemical reaction with its environment. From this simple definition it should be appreciated that corrosion is a system property and not a material one. In order to understand a corrosion reaction one must know about the material and environment conditions.

Simplistically it may be seen that there are two types of corrosion, generalised and localised corrosion. The type of corrosion is generally dependant upon the metal or alloy being considered. Localised or more specifically pitting corrosion will receive most attention here as it is the most pertinent when considering stainless steels.

Under these conditions certain localised areas of the metal surface corrode at higher rates. These variable rates are attributed to the heterogeneity of the metal, the environment or the geometry of the structure.

2.8.2 Pitting Corrosion

Pitting corrosion is a highly localised form of corrosion that occurs at specific areas on a material surface. Pitting can be particularly damaging due to the concentration of attack at a few sites.

The reason stainless steels are so susceptible to pitting corrosion is that they depend upon the presence of a passive film for their good corrosion resistance. Stainless steels are protected from corrosion by the passive film that is formed as the chromium content reaches approximately 11%. However it is known that FV520B and other 12-14% Cr martensitic stainless steels suffer from pitting corrosion in aqueous environments containing chloride ions [72].

If the passive film breaks down locally and does not re-form pitting may ensue.

Generally pitting corrosion is divided into two stages, pit initiation and pit propagation.

2.8.2.1 Corrosion Pit Initiation

During pit initiation the passive film breaks down and active dissolution of the freshly exposed metal occurs. The locations where pits initiate is influenced by many factors among others, variations in structure or composition of the metal surface, difference in the concentration of dissolved oxygen or the local breakdown of a passive film due to an applied stress being concentrated by some geometry. The pits often tend to be located randomly around the metal surface [73], [74].

In these early stages pits grow in a metastable manner [75]. Metastable pit growth may be terminated at any time, in which case the pit surface repassivates and growth ceases. The greater the corrosion potential difference across the pit the greater the chance of stable growth.

2.8.2.2 Corrosion Pit Propagation

For the electrochemical corrosion of a metal to take place there must be anodic reactions coupled with a cathodic reaction. For the example of steel in an aqueous solution the reaction below would occur;

Equation 18



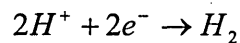
This anodic reaction occurs at the bottom of a growing pit where the level of dissolved oxygen is low, Scully [76] states "Anode sites occur where the access of oxygen is the most difficult". In order for the oxidation process to occur at the anodic

site a simultaneous reduction process, whereby the electrons given up in the oxidation process are gained at a cathodic site. The two most likely reduction reactions are the reduction of dissolved oxygen in neutral water, Equation 19, or in acids the reduction of hydrogen ions leading to the evolution of hydrogen gas at the metal surface (Equation 20).

Equation 19



Equation 20



During the course of these reactions, the level of dissolved oxygen within the pit will fall as a result of the reduction. Very often pits are covered by a membrane of corrosion product that severely restricts the access of oxygen from the bulk solution [15], [77]. In more established pits the depth of the pit will provide its own diffusion barrier to maintain a gradient in dissolved oxygen concentration thus allowing pit growth to continue.

2.8.3 Models of Pit Growth

Several authors have found a relationship between the period of time (t) a material is exposed to an aggressive environment and the maximum corrosion pit depth (d), [78,79,106,123,145]. The relationship is generally of the form shown in Equation 21.

Equation 21

$$d = At^n$$

Where A and n are constants.

Figure 23 [145] shows experimental pit growth data plotted along with calculated pit depths using

Equation 21.

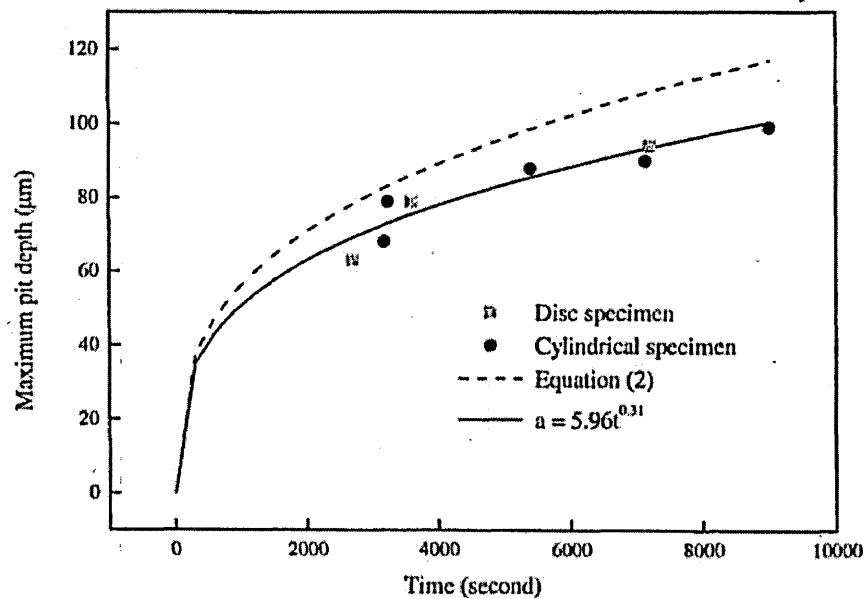


Figure 23 - Time Dependence on Maximum Pit Depth of 3%NiCrMnV Steel in 0.02M $\text{Na}_2\text{B}_4\text{O}_7$ +0.001M NaCl Solution.

Work conducted by Sparkes et al and Mulvihill [79,106] into the pit growth rate of 2.5NiCrMoV and 3.5 NiCrMoV turbine rotor steels in condensing steam used Equation 21 to predict maximum pit depths. Both Sparkes et al and Mulvihill [106, 79] found good agreement between empirical and calculated max pit depths when using a pit growth law exponent (n) of 0.5. Kondo [123] conducted work on similar steels as Sparkes et al and Mulvihill [79,106] but at 90° C in water containing

dissolved oxygen around 100ppb, however, Kondo [123] found the pit growth law exponent to be 0.33. Zhou and Turnbull [145] carried out studies in the pit growth behavior of 3NiCrMoV steel in $\text{Na}_2\text{B}_4\text{O}_7$ and NaCl solutions and also found good agreement between calculated and experimental values when using

Equation 21 with a pit growth law exponent of 0.31, see Figure 23. The ASTM standard on the examination and evaluation of pitting corrosion [80] suggests using Equation 21 with a pit growth law exponent of 0.33 based on the earlier work of Godard [81] looking at the exposure of several aluminium alloys to water.

From the work in literature it is clear that a power law relationship exists between pit depth and exposure time, this relationship has been seen dependent upon constants to remain valid across a spectrum of material and environmental combinations.

2.8.3.1 A Parameter to Account for Corrosion Damage to a Cyclically Deformed Surface

Dmytrakh et al [85] conducted rotating bending corrosion fatigue tests on 0.2%C steel in artificial sea water to assess the electrochemistry of deformed smooth surfaces.

Tests were conducted under potentiostatic conditions. In order to develop a relationship between corrosion fatigue crack growth and anodic dissolution the parameter Q was proposed to quantify the anodic dissolution taking place as a result of the corrosion current produced due to an applied potential under cyclic loading.

Dmytrakh et al [85] give the following equation for Q;

Equation 22

$$Q = \frac{M}{zF\rho} \left(\frac{1}{\omega} \right) \int_{N_0}^N i(N) dN$$

where;

z = the number of electrons released during anodic metal dissolution.

N_0 = number of cycles at which anodic metal dissolution begins.

M = molecular weight

F = Faraday's constant

ρ = density

ω = frequency of applied load

Q has the dimensions of length and in a physical sense is the thickness of material removed for a given area of material as a function of the number of applied load cycles. This approach has also been used by Akid and Dmytrakh [82] and Dmytrakh et al [86]. Dmytrakh et al [86] applied Q to notched specimens of 0.2%C steel in artificial seawater.

More recently González-Sánchez [83] used an equation proposed by Harlow and Wei [84] to predict the pit depth at which the pit-crack transition occurs for 316L stainless steel in artificial seawater. Using this Equation 23 González-Sánchez [83] found the pit-to-crack transition depth to be 200(μm) for an applied stress range of 220 (MPa).

Equation 23

$$a = \left[\left(\frac{3MI_{p0}}{2\pi z F \rho} \right) \exp\left(-\frac{\Delta H}{RT} \right) t + a_0^3 \right]^{1/3}$$

where;

$a = P_d$, pit depth at pit-to-crack transition (cm)

ΔH = activation enthalpy

T = absolute temperature

R = universal gas constant

I_{OP} = pit current

t = time for pit to reach the size (sec)

a_0 = initial pit depth (cm)

No physical confirmation of the values of Q calculated were given in any of the publications.

2.8.4 Effect of Notches on Electrochemical Corrosion Processes

Recently work has been conducted looking at the effect of geometrical features (notches) on electrochemical characteristics. Dmytrakh et al [85] carried out experiments on 0.2%C steel in artificial sea water, they found that under both static and cyclic loading an intensification of the electrochemical activity on the metallic surface was observed with increasing strain. This intensification of electrochemical activity is felt to be due to a damaged metal surface due to the loading. This approach was extended to notched low carbon steel in a 3% sodium chloride solution [86].

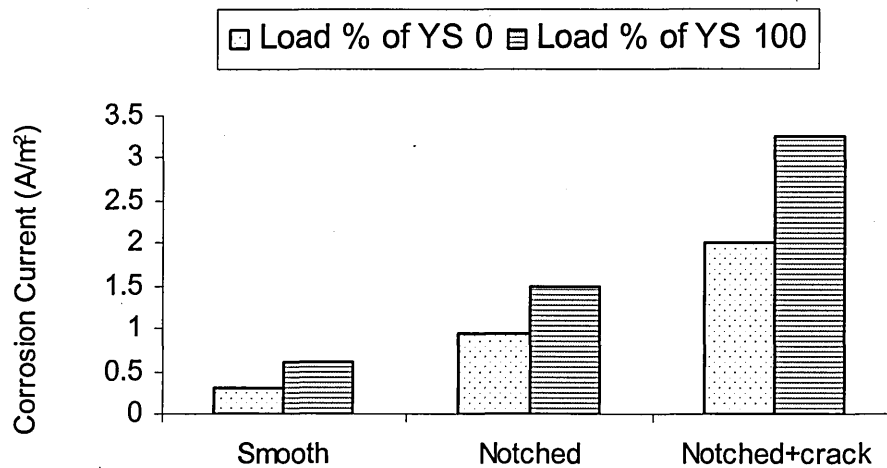


Figure 24 - Effect of Surface Geometry on Current Density With Respect To Applied Load Level.

Notches can be thought of as concentrating both stresses and electrochemical conditions. The electrolyte within the pit can change and become more aggressive with respect to the bulk. The decrease of pH within the notch is due to hydrolysis of corrosion products and the migration of aggressive ions such as chlorides in the notch electrolyte. Dmytrakh et al [86] state " notches can be considered as objects where the typical form of localized corrosion is expected.". The application of a stress to a notched component leads to an additional intensification of the electrochemical action as can be seen in Figure 24 [86]. The increase in electrochemical activity is felt to be due to the formation of electrochemical inhomogeneity of the surface of the notch due to the stress gradient. It is for this reason that the base of the notch is the area of greatest corrosion intensity.

2.8.5 Corrosion At Inclusion Sites

The main corrosion problem associated with non-metallic inclusions is pitting. This can occur in low alloy and stainless steels [62]. Figure 25 shows pitting at a

manganese sulphide inclusion in FV520B. The inclusion in Figure 25 [87] is cathodic relative to the steel, this means that the material around the inclusion will corrode rather than the inclusion itself.

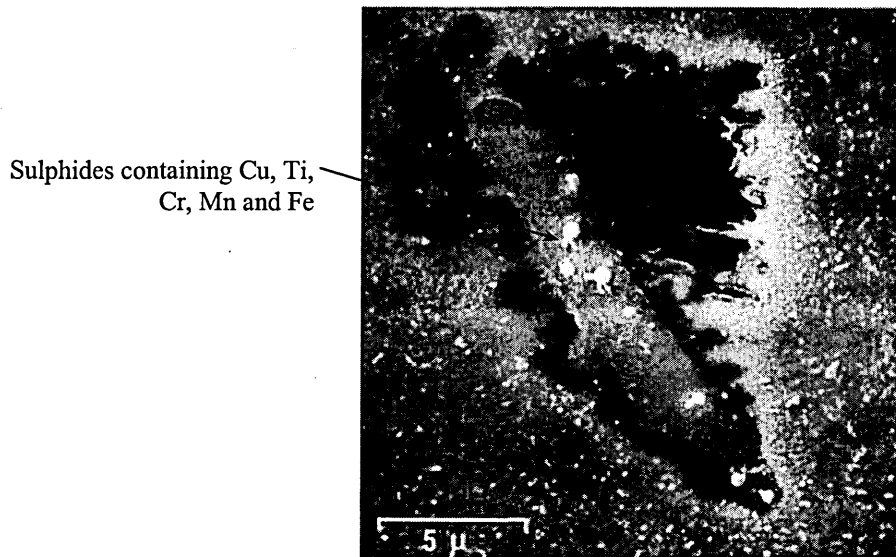


Figure 25 - Pitting at a Manganese Sulphide Inclusion in FV520B During Constant Potential Testing in the range $+50 - +200(\text{mV})_{\text{SCE}}$ in 0.1M Sodium Chloride Solution at Room Temperature.

Srivastava and Ives [88] suggested four principle ways in which a nonmetallic inclusion may effect corrosion.

- Inclusion is unstable in environment, but the matrix is stable.
- Certain phases of the inclusion are unstable, but the matrix is stable.
- The inclusion is cathodic to the alloy matrix, causing preferential dissolution of the matrix in the vicinity of the inclusion. See Figure 25.
- Inclusion is debonded from the matrix, thereby forming an incipient crevice to initiate localised corrosion.

Figure 26 [88] shows schematically the four principle ways in which a nonmetallic inclusion may effect corrosion

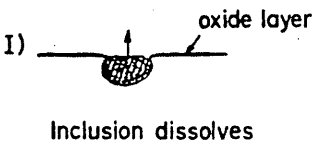
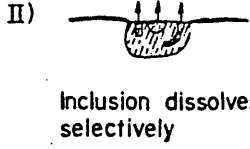
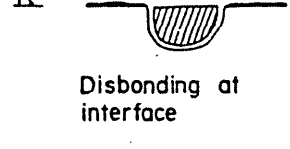
<u>PHENOMENON</u>	<u>MECHANISM</u>	
	<u>Inclusion</u>	<u>Adjacent matrix</u>
I)  Inclusion dissolves	Unstable	Unreactive or protected
II)  Inclusion dissolves selectively	Component phases unstable	Unreactive or protected
III)  Matrix (adjacent) dissolves	Cathodic site	Unstable
IV)  Disbonding at interface	Unreactive in bulk solution but dissolves within the crevice	

Figure 26 - Schematic of Pit Nucleation Processes at Inclusion Sites.

Several authors have shown that corrosion pit initiation occurs at or in close proximity to inclusion sites in stainless steel [89,90,91]. It has been noted that often pitting does not initiate at the inclusion itself but at the boundary between inclusion and matrix. Janik-Czachor et al [89] state “corrosion attack clearly starts at the boundary region between the inclusion and the matrix” they went on to note that the boundary regions are evidently the source of weak spots in the passive film where its protective properties are weakened.

Several models have been put forward to account for the prevalence of corrosion pitting at the inclusion/matrix boundary. The boundary between the inclusion and the matrix is made up from material that differs from both phases involved. There may be micro voids between the inclusion and matrix due to the difference in contraction during cooling [65] thus leaving the area open to attack. Many inclusions are more active than the matrix and may be easily dissolved in relatively mild environments thus leaving a hole that may stimulate the initiation of pitting, due to differential aeration or acidification of the electrolyte in anodic areas [89].

It is worth noting that while some inclusions are extremely active and result in corrosion pitting that may lead to fatigue crack initiation others appear inactive and no pitting results from their presence the reasons for this are not fully understood.

Parker [91] states “many authors agree that the efficiency of an inclusion as an initiator depends upon its precise composition and this explains why many inclusions are not active.”

2.9 Corrosion Monitoring and Control

2.9.1 Introduction

The monitoring or control of electrochemical potential has for many years been an essential feature of corrosion fatigue and stress corrosion cracking of metals.

Although techniques to achieve these aims are well established for testing at relatively low temperatures (below 100°C), reliable methods for testing in high temperature and pressure environments have until recently remained very much research based. The principles of electrochemical control broadly speaking remain the same despite temperature and pressure, however there are some problems associated with practicalities such as providing a stable reference potential at high temperatures and pressures.

2.9.2 Theory of Potential control

If an iron electrode is dipped into dilute sulphuric acid it will instantly start to dissolve. If another electrode that will not corrode (e.g. platinum, carbon) is inserted, and the iron electrode is connected to the negative pole of a current source, and the platinum to the positive pole the iron dissolution will slow down or even stop depending on the applied voltage. This phenomenon was detected by Sir Humphrey Davy. If one was to reverse the polarity of these connections and increase the voltage from a low value then an exponential increase in dissolution would be seen with respect to applied voltage.

This effect could be seen as the basis of the electrochemical control and measurement of corrosion.

The heart of potential control is the potentiostat. The potentiostat is an amplifier that is used to control the voltage between two electrodes, the working electrode and the reference electrode. In the above example the iron electrode is the working electrode and the platinum the reference electrode.

Reference electrodes maintain a constant voltage and in doing so provide a datum from which to measure the working electrode. However as soon as a current passes the reference electrode, it is polarised, this means that the potential of the reference electrode varies with current. Hence to maintain a stable potential no current is allowed to pass the reference electrode. Therefore one is forced to introduce a third electrode in order to maintain a constant potential difference between the reference and working electrodes. The third electrode is known as a counter or auxiliary electrode, a current is forced between the working and counter electrodes, high enough and of the correct polarity to keep the working electrode potential at a constant value with respect to the reference electrode.

The potentiostat has two tasks: to measure the potential difference between working electrode and reference electrode without polarising the reference electrode, and to compare the potential difference to a preset voltage and force current through the counter electrode towards the working electrode in order to counteract the difference between the preset voltage and existing working electrode potential.

2.9.3 The Three Electrode Cell

The three electrode cell is the standard equipment used to assess the corrosion properties of a material. A typical example of the three electrode cell is shown in Figure 27 [92].

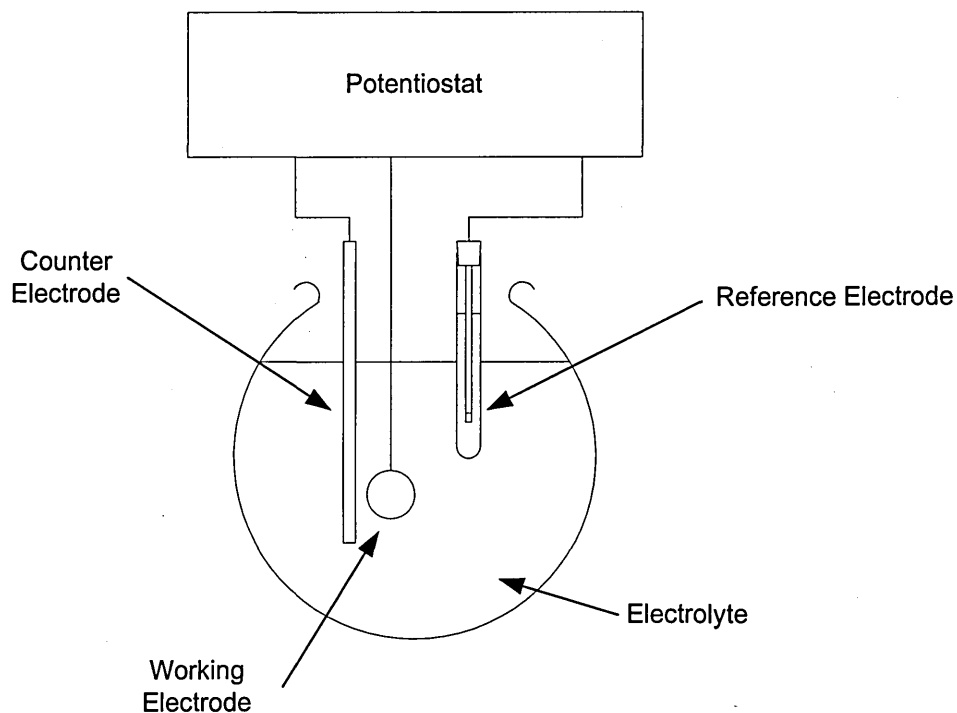


Figure 27 - Typical Three-Electrode Cell.

The three electrode cell is constructed from five main parts; reference, working and counter electrodes with an electrolyte and potentiostat.

2.9.3.1 Electrolyte

The choice of electrolyte is important as it is a fundamental part of the reaction. The temperature and whether or not the cell is aerated must be considered.

2.9.3.2 Working Electrode

The working electrode is made from the material being investigated, it should have a surface area of more than $1(\text{cm}^2)$. The surface finish of the material will have an effect on the experimental results so whenever possible the surface finish of the working electrode should be the same as the finished component under investigation. The working electrode can easily be constructed by mounting a sample of material in

a non-conductive medium, an electrical connection must be made to the sample this can be done by spot welding or a small screw thread, however care must be taken to avoid crevice corrosion between the specimen and the mounting material. Crevice corrosion can be minimised by avoiding sharp edges on the specimen.

2.9.3.3 Counter Electrode

The counter electrode is used to carry the current created in the circuit as a result of the investigation. Materials used for the counter electrode include carbon, platinum or gold any material that will not introduce contaminating ions into the electrolyte can be used.

2.9.3.4 Reference Electrode

The reference electrode provides a very stable datum to measure the potential of the working electrode. The reference electrode carries only a negligible current, this means it will not participate in the reaction and its potential will remain constant. The Saturated Calomel Electrode (S.C.E) is widely used when polarising in laboratory conditions.

2.10 Corrosion fatigue

2.10.1 Introduction

Corrosion fatigue is a phenomenon that results from the synergistic coupling of a corrosive environment and cyclic loading. The damage from corrosion fatigue is more severe than the summation of the damage wrought by each form of attack occurring separately. When considered in the broadest sense of environment-cyclic stress interaction, it can be seen that corrosion fatigue is a frequent cause of in service failure, and in fact may well be the leading cause [93]. The fatigue part of the failure is usually easily recognised by the flat fracture surface with striations and beach marks. The corrosion part of a failure is not easily seen, however a crack starting at the base of a pit is considered conclusive evidence of corrosion fatigue. Corrosion fatigue can have huge effects on the fatigue strength of materials. In many cases it has been observed that the fatigue limit seen with ferrous materials in air is lost. The loss of fatigue limit can clearly be seen in Figure 28 [94] with both air and corrosion fatigue endurance data for a BS 251A58 low alloy steel, the corrosive environment was 0.6M NaCl (pH6) aqueous environment.

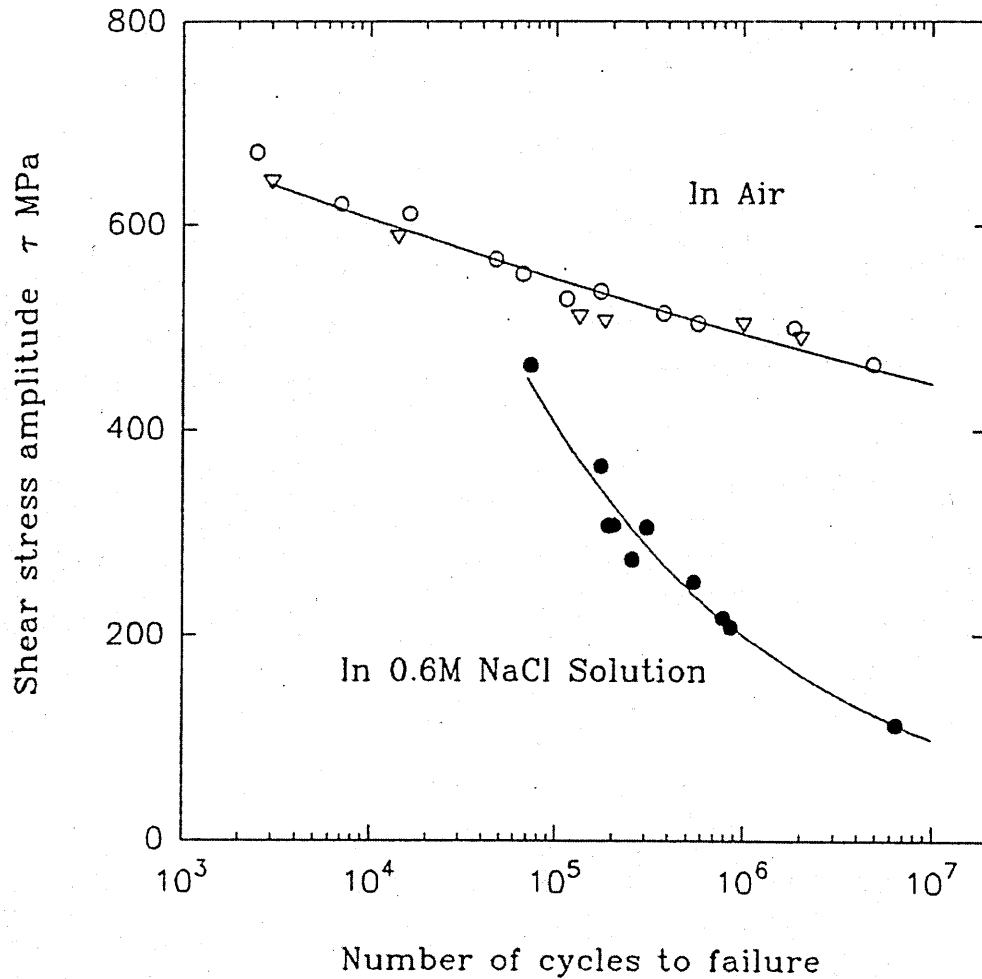


Figure 28 - Endurance Data for Air and Chloride Environments.

The work carried out by McAdam [95] is one of the founding papers of corrosion fatigue along with the work of Gough [96]. McAdam [95] conducted detailed investigations into corrosion fatigue in flowing water loaded using a rotating cantilever machine. It was observed that there were abnormalities on S-N curves for steel specimens tested in flowing water when compared with those tested in air.

McAdam [95] felt these irregularities were due to the chemical effect of water on steel, and he stated that "this chemical effect has an unexpected influence on the fatigue resisting properties of the steel."

McAdam [95] noted the presence of small spots of dull appearance of the fracture surface of failed specimens. Following closer examination these spots were identified

as oxide patches, each surrounding a non-metallic inclusion or a pit from which an inclusion had been removed. On the specimens tested in water several short transverse cracks were formed, one of these grew sufficiently to cause failure of the specimen.

McAdam [95] continued his experiments this time varying the degree of corrosion by running tests in water for the first X number of cycles and then cycling in air until failure, and secondly by pre-corroding some specimens without an applied stress. From these tests McAdam [95] noted that the effect of severe corrosion prior to fatigue loading is much less than the effect of very slight corrosion occurring simultaneously with fatigue. McAdam [95] also found that even slight intermittent corrosion, hardly sufficient to be noticeable in service would probably be sufficient to reduce the fatigue limit.

2.10.2 Corrosion Fatigue Crack Initiation

It is generally assumed that corrosion pitting is a precursor to corrosion fatigue, however this may not always be the case. Talbot et al [97] suggest the following causes for fatigue crack initiation in aqueous environments;

- Stress intensification at local corrosion damage.
- Reduced surface energy requirements for crack development.
- Local embrittlement by hydrogen from cathodic reactions.
- Stimulation of local yield by dissolution.
- Enhanced dissolution of locally yielded material.
- Dissolution of metal exposed at ruptures in passive film.

It has been suggested by some authors [98] that slip band movement could cause localised temperature increases thus heightening any chemical reaction and leading to enhanced corrosion damage due to fatigue. It has also been considered that the process of corrosion may initiate plastic deformation independent of any temperature or pitting effect. If corrosion were able to facilitate plastic deformation it would mean slip could occur at lower stresses and both the increased nucleation and growth of cracks seen in corrosion fatigue could be accounted for as well as the removal of the fatigue limit. Indeed it has been shown that adsorbed compounds can significantly reduce yield strength [97].

The ability of an environment to accelerate the slip process has been accounted for by the removal of an oxide layer that if complete would exert a strengthening effect. Alternative explanations include a reduction of surface energy and a removal of dislocation pile-ups in work hardened material.

Work carried out by Duquette and Uhlig [99] backs up the idea of chemical or electrochemical enhanced slip. Duquette and Uhlig [99] saw no linearity in fatigue damage with rate of corrosion, corrosion being controlled by level of dissolved oxygen. During investigations into the corrosion fatigue behaviour of 1015 steel in 3% sodium chloride solution as a function of dissolved oxygen concentration it was found that only a small amount of dissolved oxygen and correspondingly corrosion was required to induce slip, leading to failure at stress levels below the fatigue limit. With larger concentrations of dissolved oxygen damage was not increased as would be expected if corrosion were a key factor.

There is much evidence [100,101] to support the fact that the composition of solution within a crack or pit may vary considerably from the bulk solution, Ernst and Newman [15] write "the solution inside growing pits on stainless steels differs

immensely from the bulk solution” they go on to comment “The pH in the pit solution can be as low as zero and the chloride concentration can be as high as 12M.”.Despite the bulk solution being outside the range for the production of hydrogen from cathodic reactions the combination of potential and pH within the pit may allow such a cathodic reaction. More recent work by Panasyuk et al [102] has also shown a drop in pH at the tip of an advancing crack, by inserting a capillary tube along the plane of the crack, the tube being moved automatically such that it is in touch with the environment at the tip of the advancing crack. Using this set-up Panasyuk et al [102] were able to monitor both the pH and the electrolyte potential at the crack tip. Figure 29 [102] shows how the pH and the electrolyte potential drop during cyclic loading.

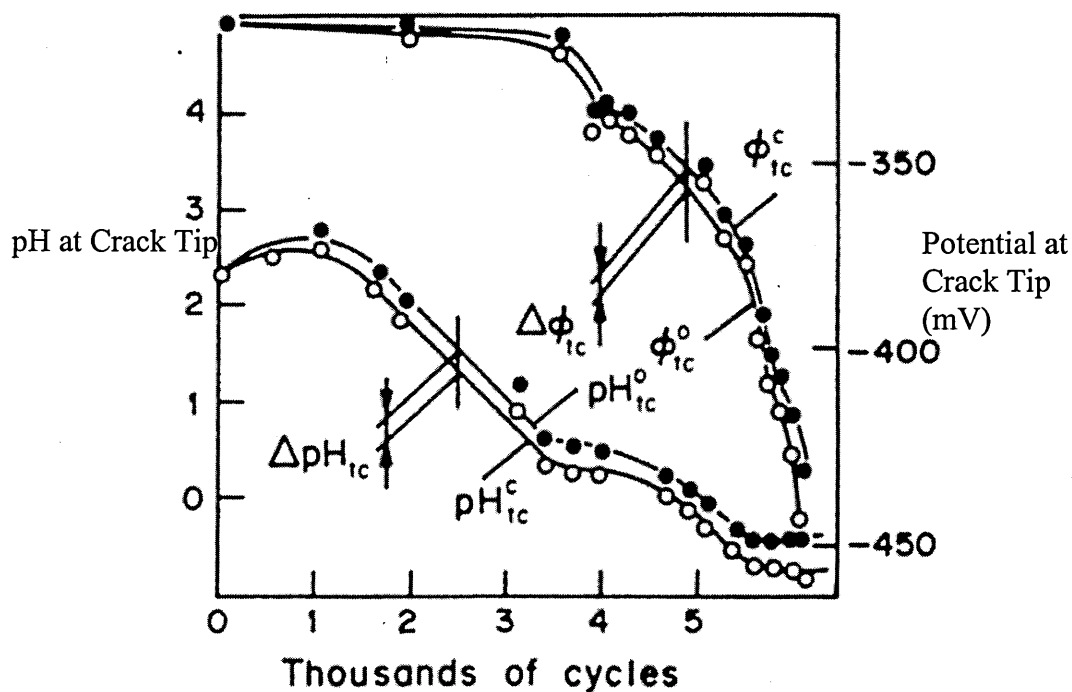


Figure 29 - Variation Of pH and Potential AT The Tip Of a Propagating Crack Under Cyclic Loading of 40Kh13 Steel Beam Specimen Exposed To An Aqueous Solution With A pH of 8.

Adsorption related mechanisms propound the idea that active species in the electrolyte degrade the mechanical integrity of the crack initiation region, thus allowing initiation at lower stress. There are several mechanisms that may allow this lower energy initiation and fracture. One method is by the species forming a metal-species bond, the energy used by the metal atoms to bond to the species reduces the metal to metal bond strength and hence allows mechanical separation at lower stress. Another adsorption related mechanism is caused by the formation of hydrogen atoms due to the reduction of hydrogen ions. These hydrogen atoms are then absorbed by the metal and cause weakening or embrittlement. This weakening is caused by the metal to metal bond being damaged, this can happen in a number of ways;

- Pockets of hydrogen gas forming within the metal, causing pressurised cavities
- Formation of metal hydrides causing embrittlement
- Weakening of metal to metal bonds

It has been shown time and time again that corrosion pitting can cause stress concentrations and hence facilitate the initiation of corrosion fatigue cracks. It has also been seen by some authors that the application of cyclic stress can stimulate corrosion pitting leading to a combined effect of corrosion and fatigue. Murtaza and Akid [103] noted a dependency of pit density on applied cyclic stress, see Figure 30 [103].

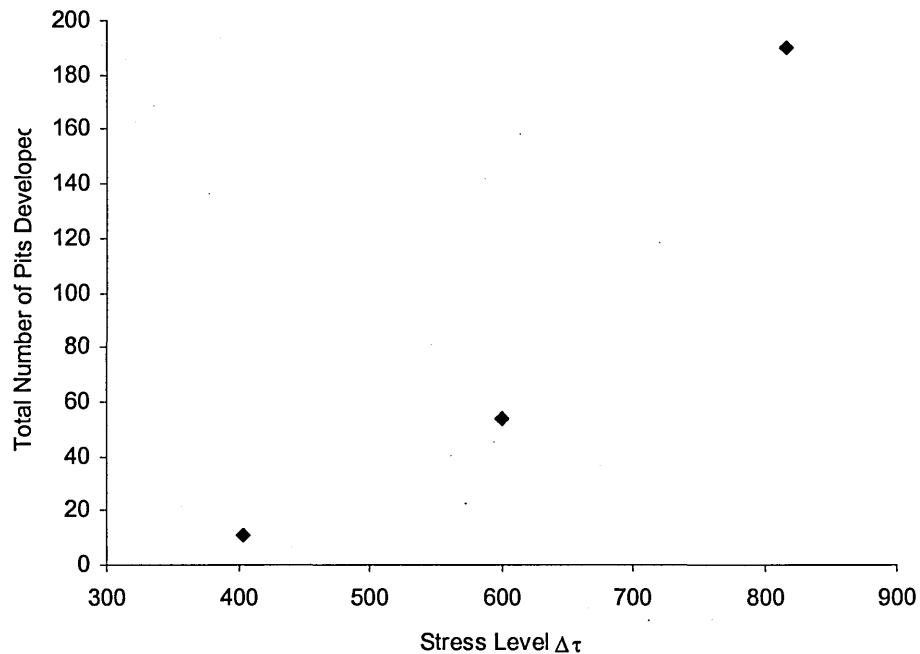


Figure 30 - Dependency of Pit Density on Applied Cyclic Stress Level Under Fully-Reversed Loading in 0.6M, Aerated Sodium Chloride Solution.

The role of non-metallic inclusions in the nucleation of corrosion pitting has also received some consideration. Murtaza and Akid [103] stated "in a corrosive environment pitting occurred at non-metallic inclusions, these sites dissolving in preference to the metal matrix". However, the role of pitting is not simply to concentrate stress, this has been observed by comparing the effect of pre-pitted corrosion fatigue tests and actively pitting corrosion fatigue tests. Many authors have reported significant reductions in fatigue strength when considering pre-pitted specimens. Lindley et al [104] showed fatigue strength could be reduced by as much as 70% by pre-existing pits of 250(μm) in depth when looking at low alloy steel. More recently Zhou and Turnbull [105] developed an electrochemical technique to allow the generation of pits at controlled depths and low density, applying this technique to a 12Cr turbine blade steel, reductions of up to 50% in fatigue strength

were observed upon subsequent air fatigue testing. Mulvihill et al [106] built on the work of Lindley et al [104]. The geometric effects of corrosion pits were investigated as in Lindley et al [104] by pre-pitting fatigue specimens in steam. However, Mulvihill et al [106] extended the study by corroding specimens during fatigue tests thus investigating the conjoint geometrical and environmental effects of actively growing pits. Mulvihill et al [106] found that actively growing pits had a more severe effect on fatigue crack initiation than the geometrical stress intensification seen with non-active corrosion pits as can be seen in the S-N plots shown in Figure 31 [106] and Figure 32 [106].

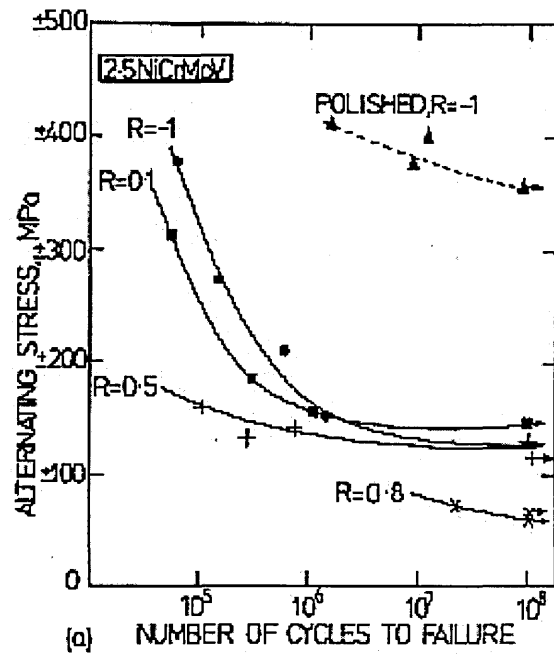


Figure 31 - Effects of Non-Active Pits on the Fatigue Strength of LP Turbine Shaft Steel.

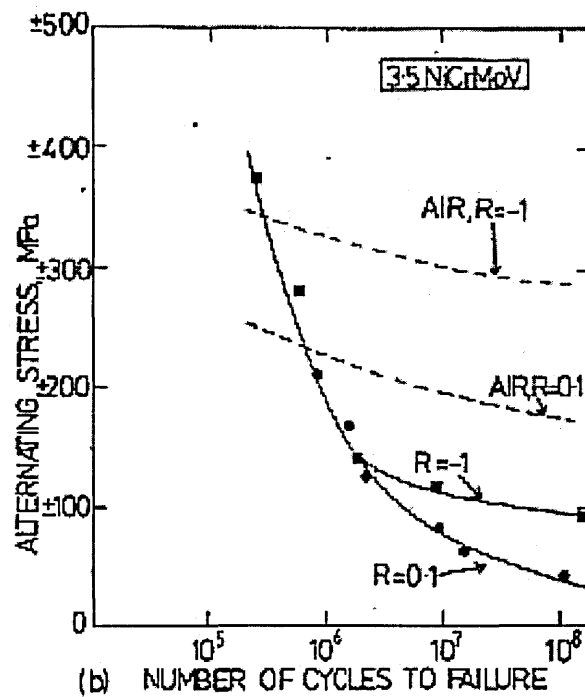


Figure 32 - Effect of Active Pits, Tests conducted in non-deaerated, deionised water at 80°C. Loading frequency = 100(Hz). Pre-Pitted in Condensing Steam.

Mulvihill et al [106] went on to conclude that actively growing pits have a more severe effect on fatigue crack initiation than pre-existing pits and attributed this

enhancement in ability to facilitate crack initiation to the influence of the environmental conditions within the pit. In considering the effect of active pitting on the initiation of fatigue cracks Mulvihill et al [106] also investigated the effect of stress ratio. From Figure 33 [106] it is clear that fully reversed loading ($R=-1$) represents the worse case scenario in terms of stress ratio for the initiation of fatigue cracks from corrosion pits whether they be active or pre-pitted. It was also demonstrated that under fully reversed fatigue crack initiation could occur more readily at both active and pre-pitted corrosion pits than sharp cracks. Figure 34 shows a fatigue crack that has initiated from an active corrosion pit.

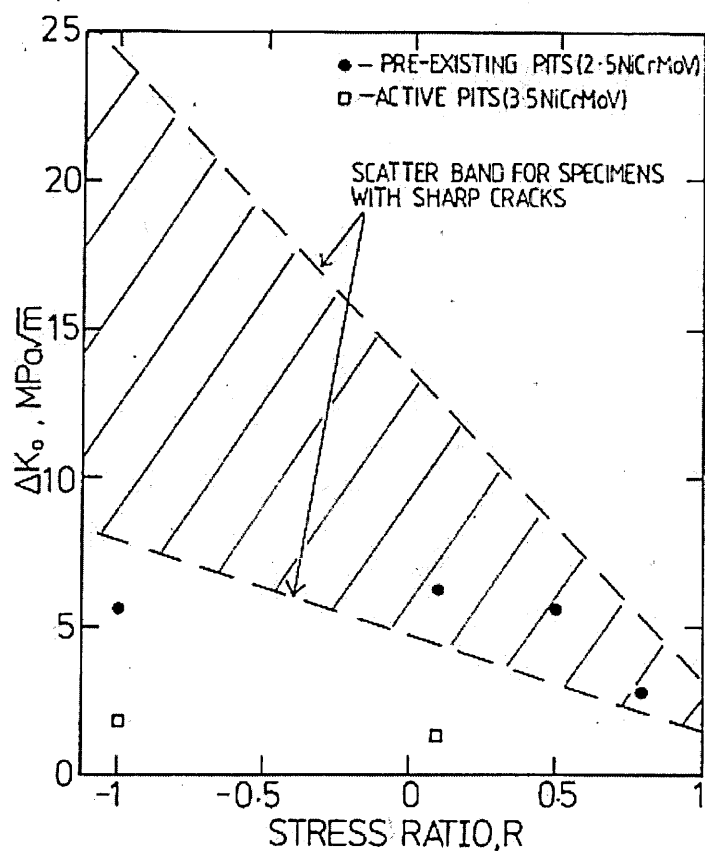


Figure 33 - Effect of Non-Active and Active Pits on the Threshold Stress Intensity Range for Fatigue Crack Initiation in LP Shaft Steel.

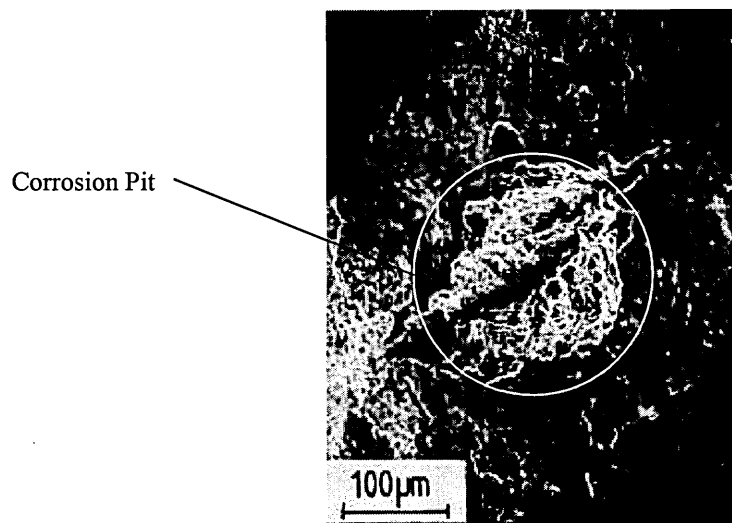


Figure 34 - SEM Micrograph of Fatigue Crack Initiation At a Corrosion Pit In 3.5%NiCrMoV Steel tested In Water At 80°C.

2.10.3 Corrosion Fatigue Crack Propagation

Early work carried out by Evans and Simnad [107] showed that removal of a corrosive environment after a certain percentage of expected life does not show any significant effect on the final life to failure of a specimen this observation led to the conclusion that once cracks had been formed in a corrosive atmosphere the subsequent rate of propagation was much the same in air as in the said environment. Recent work by Murtaza and Akid [103] looking at corrosion fatigue crack initiation and propagation in a high strength spring steel under fully reversed tensional loading in 0.6M sodium chloride solution showed agreement with the earlier observations. Murtaza Akid [103] comment "Once a crack was initiated from the original pit like defect, its growth behaviour was similar to that observed in air". It has been widely reported that crack propagation rates in corrosive environments can be lower than those seen in air. Frost [108] suggested this is due to the absence of oxygen. By conducting fatigue tests in different environments Frost [108] found that maintaining a barrier between the specimen and air crack propagation life could be increased. Frost [108] showed that moisture without oxygen appeared to have no detrimental effect, with tests carried out in tap water yielding similar results to those conducted in oil. To show that tap water created an effective barrier to oxygen was shown in testing where a sample immersed in tap water with oxygen being continuously bubbled through it, the resulting life being no less than that of a specimen immersed in tap water or oil. Further testing in hydrogen peroxide solutions with different levels of free oxygen showed a detrimental effect on fatigue crack growth in an oxygen rich environment.

Rollins et al [109] carried out corrosion fatigue testing on high carbon steel, those investigations also showed a lower crack growth rate in air than in corrosive media thus being consistent with the work of Frost [108].

In a review paper Congleton and Parkins [110] suggested that crack growth retardation is possible where conditions favour the formation of a stable film or where dissolution is so comprehensive that crack blunting occurs. They also observe that in the case of long cracks retardation may result from a build up of insoluble corrosion products within the crack to such a level that crack closure upon unloading maybe reduced thereby reducing the effective stress intensity factor.

2.10.4 Electrochemical Effects in Corrosion fatigue

It is clear that, in addition to the important fracture-mechanics considerations, there are crucial environmental aspects associated with the understanding and prediction of fatigue crack growth in a corrosive environment. And, in this respect, it is obvious that the conditions causing additional crack growth in corrosive environments must be related to the electrochemical conditions within the crack.

Patel et al [111] carried out corrosion fatigue tests on mild steel in a 3.5% sodium chloride aqueous solution. Initial tests conducted at free corrosion potential showed that both anodic and cathodic reactions were significantly stimulated by cyclic plastic deformation during both the tensile and compressive strain reversals. This increased activity was observed in the form of a current or dissolution transient at the peak tensile or compressive load. In the majority of tests carried out by Patel et al [111] at free corrosion potential the base current was seen to increase with the number of loading cycles. The increase in base current suggests that the anodic and cathodic reactions were no longer balanced and that metal dissolution was taking place at the free corrosion potential even outside of the peak loading condition under both tensile and compressive loads. The magnitude of the increase in base current and the amplitude of the current transient was seen to be greatly effected by changes in the pH of the aqueous sodium chloride solution.

The amplitude of the current transient was seen to increase with the number of load cycles applied, so too was the half life of the current transient, once again this was seen to be affected by solution pH. At almost any value of pH the current transient half life was approximately two times greater on the tensile transient than the compressive one.

Patel et al [111] also investigated the affect that the initial current density had on the current transient seen at maximum tensile and compressive loads. With an initial current density of $+1(\text{mA}/\text{cm}^2)$ the dissolution transients produced at all values of pH were greater than at free corrosion potential, similar trends were seen as when at free corrosion potential with the increase of base and peak dissolution levels with an increase in applied cycles. With an initial applied current of $-1(\text{mA}/\text{cm}^2)$ Patel et al [111] observed that the hydrogen reduction reaction was significantly stimulated by cyclic plastic strain.

From the tests carried out by Patel et al [111] it was clear that enhancement of the reactions was dependant upon several factors;

- Solution pH
- Potential
- Sign of strain reversal
- Load history

The affects of solution pH are probably due to the state of any surface film and its ability to reform after disturbance by the underlying material.

Patel et al [111] observed during their testing that very different behaviour was found when a solution of pH12 was used. At this potential and free corrosion potential it was seen that the magnitude of the dissolution peaks decreased with applied strain cycles, becoming very small by the fifteenth cycle, see Figure 35 [111].

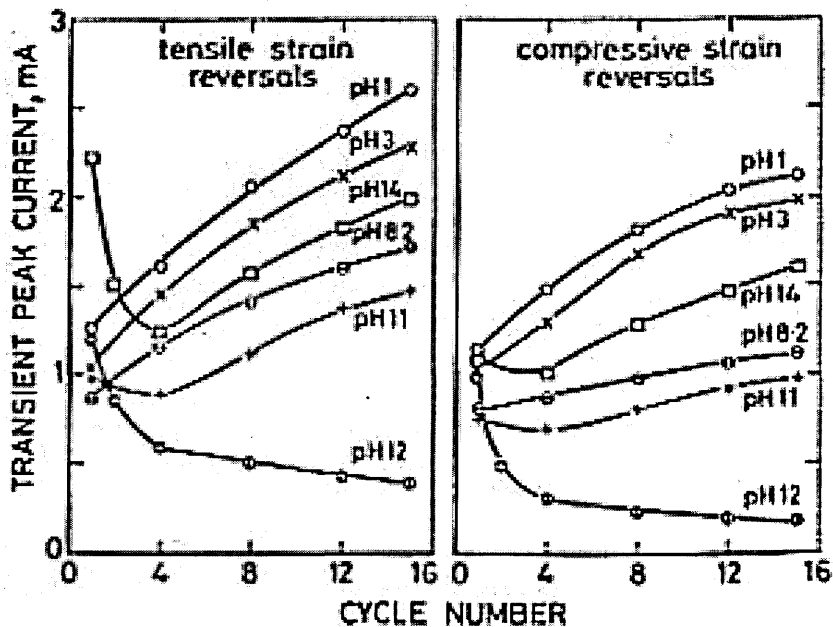


Figure 35 - Variation of Transient Peak Current at Open Circuit Potential With Respect to Number of Strain Cycles.

At a pH of 12 a protective film forms on mild steel in sodium chloride and from these tests it would appear the protection offered by this film increases with cyclic straining. The following hypothesis was produced to explain the reduction in magnitude of transient peaks at solution pH 12." the volume of metal removed from the surface of a step by dissolution is replaced by the film and that reversed slip occurs which draws the protected slip step into the metal surface with the film intact. If reversed slip on the same plane continued then decrease in the number of new steps formed per cycle. This decrease in new step production is known to occur with fatigue cycling as the strain becomes localized" [111].

Comparing the results at free corrosion potential with results from corrosion fatigue tests, it was clear that for plain metal specimens there was an emerging correlation between electrochemical effects caused by dynamic cyclic strain and the

corresponding corrosion fatigue properties, this correlation being consistent with a dissolution mechanism of crack development.

Talbot et al [97] conducted similar investigations using amongst other materials 316 stainless steel. Tests were conducted in 0.5M sodium chloride, 0.2M sodium sulphate and 0.1M potassium dichromate, these solutions were used specifically to provide depassivating and passivating media for comparison. In initial test Talbot et al [97] conducted anodic potentiodynamic tests in all three media with test pieces both in a static condition and under cyclic loading. From these tests the following observations were made under cyclic loading conditions;

- Anodic currents in the passive ranges were significantly increased.
- Breakdown and pitting potential ranges were extended to more negative values.
- The rest potentials were displaced to more negative values for the sodium chloride media and conversely more positive in the sodium sulphate and potassium dichromate solutions.

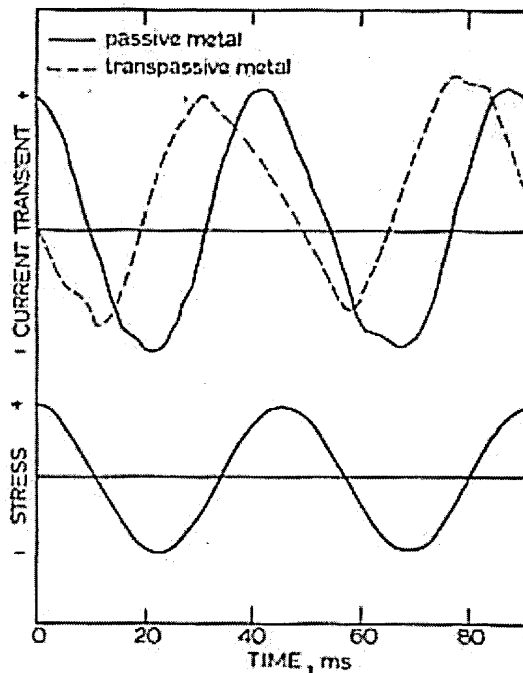


Figure 36 - Waveforms of Current Transients and Phase Relationship with Cyclic Stress for Passive and Transpassive Ranges.

Fatigue tests carried out by Talbot et al [97] showed current at peak load values much like Patel et al [111]. Talbot et al [97] shows corrosion current transients in relation to the applied stress, these transients were evident immediately upon application of the cyclic stress and persisted until fracture. Figure 36 [97] it can be seen that in the transpassive region the phase of the current transients was in advance of the applied load by approximately one quarter cycle. Talbot et al [97] carried out further tests on the stainless steel where a constant potential was applied until fracture or until 5×10^7 cycles. For surviving test pieces the amplitude of the current transients remained constant or decreased throughout the test, but for failures there was a marked increase in current transient just prior to failure. This increase in amplitude prior to failure occurred with a quarter cycle shift when in the sodium chloride media.

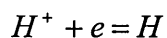
In conclusion Talbot et al [97] state "Current transients on stainless steel must inevitably be referred to the normal passive, transpassive and pitting ranges" and go

on to say "The current transient is attributed to repeated rupture of the passive film by movement within the underlying persistent slip bands". It was also noted that the transient amplitude decreases in the solutions corresponding to the increase in stability in the film.

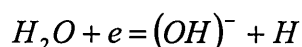
2.10.4.1 Hydrogen Embrittlement

The rates of the hydrogen producing reactions in Equation 24 and Equation 25 are extremely pH and potential dependant [112]

Equation 24



Equation 25



The production of hydrogen by these reactions is particularly favoured at low pH and low electrode potential. All the tests carried out in the present work were at relatively high electrode potentials $-200(\text{mV})_{\text{Ag}/\text{AgCl}}$, $0(\text{mV})_{\text{Ag}/\text{AgCl}}$ and $+200(\text{mV})_{\text{Ag}/\text{AgCl}}$.

However, the potentials quoted were for the bulk environment and may not accurately portray the conditions at the tip of a pit or advancing crack. Several authors have monitored the environment at the tip of advancing cracks in corrosive environments and at the bottom of pits [15,113,114,115,116,117]. There are several substances that poison the hydrogen evolution reaction. This means that more of the adsorbed hydrogen will enter the metal instead of recombining to form hydrogen gas [118], Thiourea is one such substance. If hydrogen embrittlement played a role in the corrosion fatigue process then the addition of Thiourea to the test liquor would show a decrease in time or cycles to failure. Cowling and Appleton [118] reported an increase in crack growth rate for C-Mn steel tested in sea water with an addition of Thiourea when compared to the normal sea water solution.

2.11 Models of Corrosion Fatigue

2.11.1 Introduction

Modelling of the corrosion fatigue process has very often been restricted to explaining empirical results for a particular alloy environment system (initiation and propagation). This is due to the complexity of the phenomenon and the number of variables that are known to influence the process, load frequency, temperature, water chemistry, load ratio (R), ΔK ($\Delta\sigma$), stress mode etc. There are few if any models that could be applied generally to any alloy, environment and stress situations.

2.11.2 Superposition Model of Corrosion Fatigue Crack Growth

The Superposition Model of corrosion fatigue crack growth has been well documented by Wei et al [119,120,121] and is an algebraic addition of the two processes that contribute to corrosion fatigue crack growth, namely corrosion and fatigue. The principle of this approach can be seen Equation 26

Equation 26

$$\left(\frac{da}{dN}\right)_e = \left(\frac{da}{dN}\right)_r + \left(\frac{da}{dN}\right)_{cf}$$

where $(da/dN)_e$ is the overall crack growth rate in the deleterious environment; $(da/dN)_r$ is the mechanical fatigue crack growth rate, and is obtained in an inert reference environment: $(da/dN)_{cf}$ is the environmentally assisted crack growth rate.

Wei [121] further developed this concept by breaking down the environmentally assisted crack growth rate. From Equation 28

Equation 27

$$\left(\frac{da}{dN}\right)_{cf} = \left[\left(\frac{da}{dN}\right)_e - \left(\frac{da}{dN}\right)_r\right]$$

Equation 28

$$\left(\frac{da}{dN}\right)_{cf} = \left[\left(\frac{da}{dN}\right)_c - \left(\frac{da}{dN}\right)_r\right]\Phi$$

where Φ is the fractional area of the crack that is undergoing pure corrosion fatigue; $(da/dN)_c$ is the cycle dependant or pure corrosion fatigue growth rate. This form of the equation recognises the concept that mechanical fatigue and corrosion fatigue proceed by different micromechanisms and take place concurrently or in parallel, the rates themselves being dependent upon contributions from several concurrent micromechanisms.

The Superposition Model was further enhanced by Murtaza and Akid [103] by development of the environmentally assisted crack growth term to include both long and short crack growth within the environment. The effect of strain enhanced dissolution was also included in the environmentally assisted crack growth term.

2.11.3 Process Competition Model

The process competition model was first proposed by Austen and Walker [122] it is based in a similar area as the superposition model of Wei et al [119]. Austen and Walker [122] noted that the threshold for stress corrosion (K_{ISCC}) is an important transition point between two distinctly different forms of corrosion fatigue crack growth behaviour. These types of behaviour are termed True Corrosion Fatigue (TCF) and Stress Corrosion Fatigue (SCF) and can be seen in Figure 37 [122].

TCF behaviour is where the fatigue crack growth process is enhanced by a synergistic coupling between corrosion and cyclic loading. This type of growth is observed below K_{ISCC} and applies to materials that do not stress corrode.

SCF is static load stress corrosion under fatigue loading and will occur when ever the stress intensity in the cycle is above K_{ISCC} . The most common type of behaviour pertains to material environment systems which exhibit SCF above K_{ISCC} and TCF below K_{ISCC} this type of behaviour can be seen in Figure 37.

The transformation from TCF to SCF can be made by changes in the controlling mechanical parameters, these include stress ratio (R) and load frequency (F). By reducing the stress ratio and/or increasing the frequency the SCF 'bump' such that only TCF remains.

Austen and Walker [122] suggest this phenomena occurs because the fatigue crack growth process is a cycle dependant process such that the Paris region is invariant despite changes in R and F. The stress corrosion on the other hand is time dependant such that increasing F will proportionately reduce the plateau rate in terms of crack growth per cycle. It is their suggestion that crack propagation in corrosion fatigue will occur at the fastest available rate whether that be TCF or SCF and that these processes are in competition, the fastest processes being controlled by the environmental and stress intensity at any one moment in time.

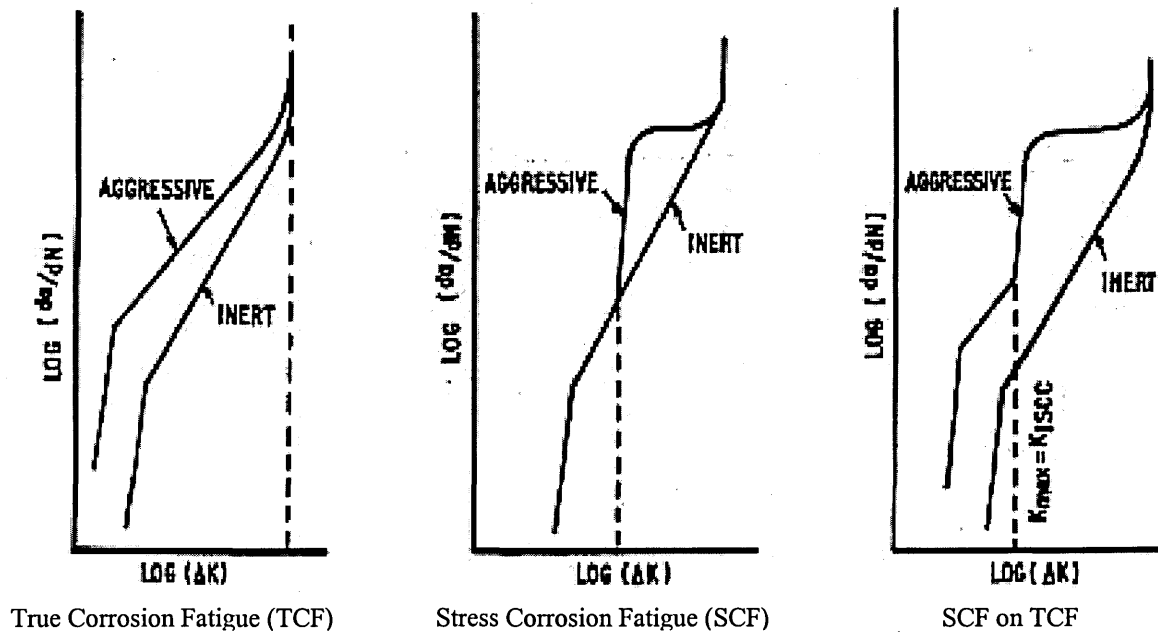


Figure 37 - Schematic Illustration of Basic Types of Corrosion Fatigue Crack Growth Behaviour.

Using the process competition model Austen and Walker [122] believed it would be possible to quantitatively predict material behaviour under any combination of environmental and mechanical behaviour.

Kondo [123] proposed a residual life prediction method for a fatigue crack growing from a corrosion pit. The method is based on the assumption that a corrosion pit is a sharp crack. Kondo [123] suggests that the corrosion fatigue crack growth is a three stage process;

- Pit growth.
- Crack formation from the pit.
- Corrosion fatigue crack propagation.

There is a critical pit size that will cause a fatigue crack to initiate, see Figure 38 [123]. Observations made by Kondo [123] suggested that once a crack initiates from a corrosion pit the pit growth becomes negligible. If this is true then the pits at the root of cracks in failed components are at the critical size at which transition from pit to crack occurred.

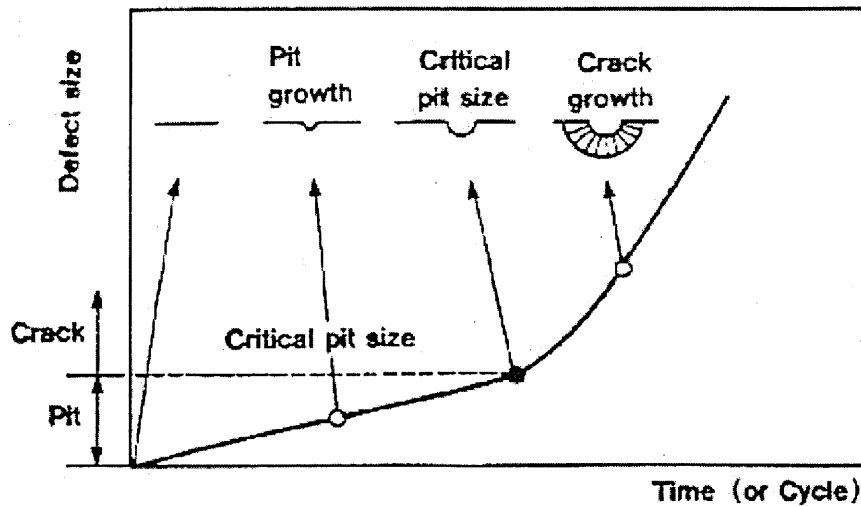


Figure 38 - Fatigue Crack Initiation Process.

Kondo [123] conducted corrosion fatigue test on 2.5 and 3.5 NiCrMoV steel in deionised water containing dissolved oxygen at 90°C a stress ratio of 0.8 and a load frequency of 50(Hz) were used. Tests were conducted at maximum stress levels up to 80MPa. Kondo [123] produced a corrosion pit growth law for both materials, it was observed that pit growth was not effected by applied stress. However tests carried out by Kondo [123] where at relatively low stress levels and subsequently strain levels may be below those required for strain enhanced dissolution.

The stress intensity range at which the pit crack transition (ΔK_p) occurred was evaluated using fracture mechanics, by treating the corrosion pit as a sharp crack. It

was found that ΔK_p was slightly dependant upon applied cyclic stress. The reason given for this by Kondo [123] is that the critical pit size is determined by the relationship between the pit growth rate and the fatigue crack propagation rate with the critical pit size being seen when the fatigue crack growth rate exceeds the pit growth rate. Since the fatigue crack growth rate is ΔK dependant then ΔK_p should be affected by the applied stress range. Figure 39 [123] is a schematic representation of Kondo's model of corrosion fatigue crack initiation.

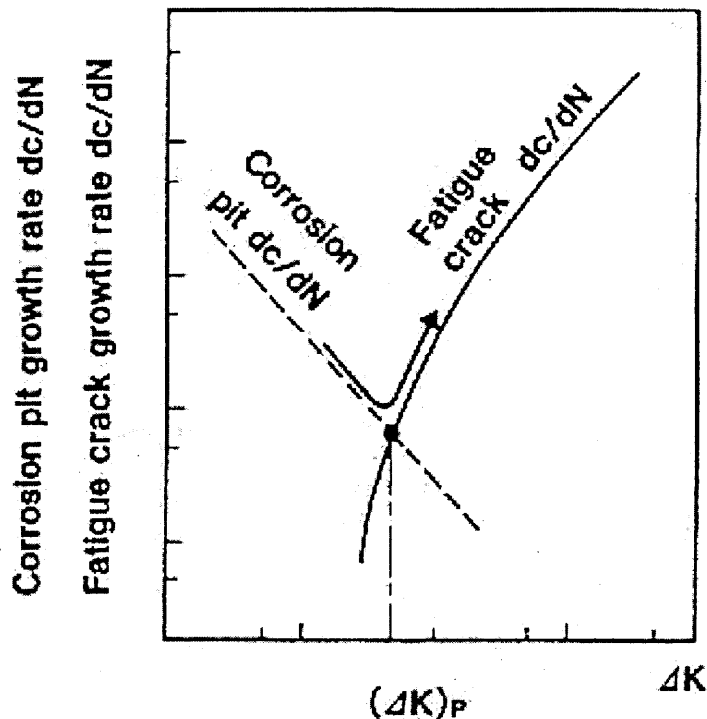


Figure 39 - Model of transition From Corrosion Pit to Fatigue Crack.

Kondo [123] goes on to consider the short crack phenomenon and the possible influence it may have in this situation. By conducting a corrosion fatigue test using a notched compact type specimen Kondo [123] found that the fatigue crack propagation for a short crack emanating from a pit occurred at ΔK below the

threshold stress intensity factor range for a long crack. Kondo [123] suggests that the acceleration in fatigue crack growth rate seen was because of the difference in electrochemical conditions at the crack tip as short crack effects due to plasticity were felt inappropriate due to the low stresses used.

Akid and Miller [124] developed a model of corrosion fatigue based on microstructural barriers. The model is based on the fact that the fatigue limit seen with ferrous materials in air is not as had previously been thought due to stress level being too low to initiate any fatigue cracks but that initiated cracks fail to propagate as a result of microstructural barriers. Therefore the fatigue limit stress in air is related to the microstructural characteristics of the material, grain size, texture and phase distribution. In an aggressive environment the corrosion processes affects the ability of microstructural features decelerate or arrest cracks.

Akid and Millers [124] model is based upon earlier models based on the growth of a crack when subjected to microstructural barriers. The Hobson et al [125] model considers the growth of a fatigue crack in two regimes, before, and after the main microstructural barrier, Figure 40 [124] shows this schematically;

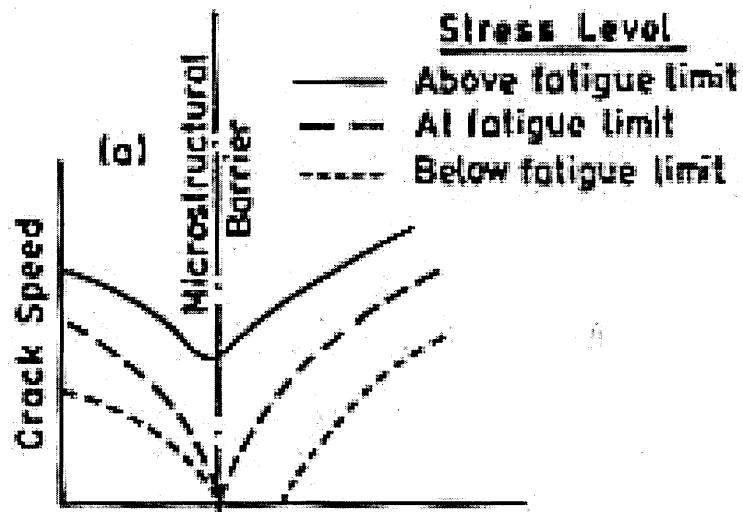


Figure 40 - Schematic of Brown-Hobson Crack Growth Model.

The second model developed by Akid and Miller [124] is that of Navarro and de los Rios [126], this model is similar to the Hobson et al model. The Navarro and de los Rios model is based on the following concept of crack growth, consider a recently initiated crack growing along an active slip band within a grain. The crack growth rate will initially be high as the rate of crack growth is controlled by the degree of plasticity ahead of the crack tip. As the crack approaches the first microstructural barrier (grain boundary) its growth rate will reduce as the degree of plasticity ahead of the crack tip will be reduced by the presence of the boundary. When the crack reaches the grain boundary one of two things can occur. If the applied stress is above the fatigue limit the stress ahead of the constrained plastic zone will eventually be high enough to initiate slip in the next grain, thus allowing crack growth to continue. As the crack grows in the new grain its rate will initially be high as the plastic zone ahead of the crack tip increases to fill the new grain. If the applied stress is below the fatigue limit the crack will arrest upon reaching the grain boundary. This process is shown schematically in Figure 41 [124].

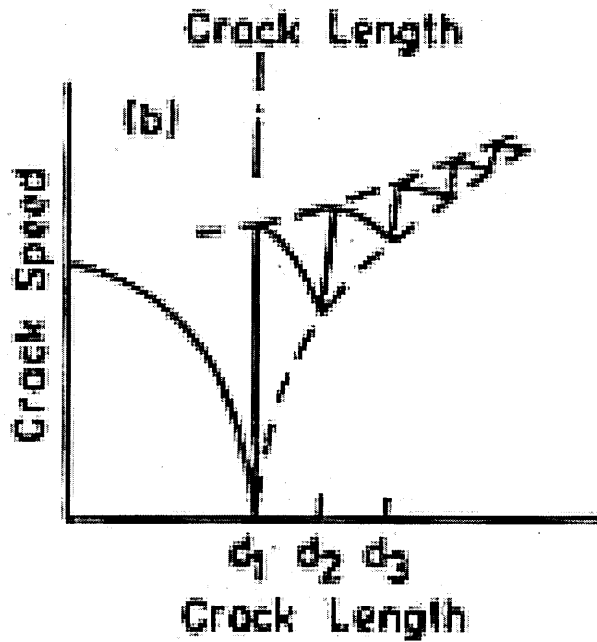


Figure 41 - Schematic of Navarro - de los Rios Crack Growth Model in Air.

Akid and Miller [124] developed these models by using the superposition model to combine them with a corrosion term. Corrosion was included in these models by expressing the crack growth rate caused by corrosion in terms of metal dissolution using Faraday's law;

Equation 29

$$\frac{da}{dN_{(diss)}} = \frac{i_{corr}}{zF\rho} M \frac{1}{\omega}$$

where,

i_{corr} = Anodic current density

ω = Cyclic Frequency

z, F, M, ρ = Constants

The affect that this metal dissolution term has on the crack growth models is to remove crack arrest at microstructural defects, this is due to the crack growth that

occurs as a result of metal dissolution. Figure 42 [124] and Figure 43 [124] show schematically the effect of including the metal dissolution term in the short crack growth models.

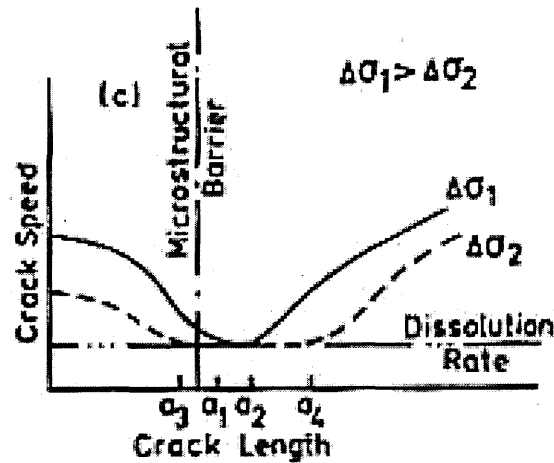


Figure 42 - Schematic of Brown-Hobson Crack Growth Model with Akid and Miller Metal Dissolution Term Included.

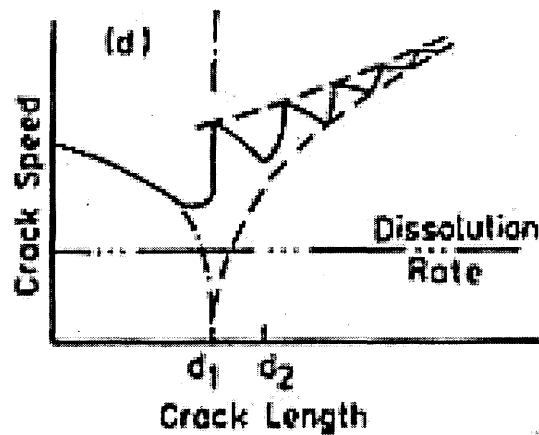


Figure 43 - Schematic of Navarro and de los Rios Crack Growth Model with Akid and Miller Metal Dissolution Term Included.

Comparison of experimental results with crack growth rate values calculated using the modified short crack growth equations showed a reasonable correlation.

Since the development of linear elastic fracture mechanics (LEFM) approaches in the 1960s and the realisation that crack growth rate in air can be predicted as a function of stress intensity range many authors have tried to explain corrosion fatigue crack initiation and growth using LEFM techniques. Lindley et al [104] aimed to quantify the geometrical stress concentrating effect of corrosion pits in terms of both a fatigue strength reduction and fatigue threshold point in order to assess the hypothesis that corrosion pits can be represented by sharp cracks from a stress intensity view point. LEFM only apply within the Paris region and may not be applicable when dealing with small cracks or large applied stresses. Lindley et al [104] reasoned that LEFM approaches are valid for sharp cracks down to about 100(μm) in depth and stress levels up to 75% of yield. By assuming corrosion pits may be treated as semi-elliptical surface flaws Lindley et al [104] developed the following equation;

Equation 30

$$\Delta K_{th} = \frac{\Delta\sigma_{th} \sqrt{\pi a} \left[1.13 - 0.07 \left(\frac{a}{c} \right)^{1/2} \right]}{\left[1 + 1.47 \left(\frac{a}{c} \right)^{1.64} \right]^{1/2}}$$

where $\Delta\sigma_{lim}$ is the overall surface stress range at the fatigue limit.

Lindley et al [104] further simplified this equation as the majority of pits had a/c ratios of approximately 0.75 giving the following equation,

Equation 31

$$\Delta K_o \approx 0.77 \Delta\sigma_{lim} \sqrt{\pi a}$$

Lindley et al [104] found the approach detailed above gave good correlation with experimental and service failures under tension-tension loading but found that under fully reversed loading corrosion pits would initiate cracks where sharp cracks of a similar depth would not grow. The discrepancy seen under fully reversed loading was attributed to the more open nature of corrosion pits causing differences in the closure behaviour under compressive loads.

Zhou and Turnbull [105] more recently used LEFM techniques to describe corrosion fatigue crack growth. Zhou and Turnbull produced fatigue specimens with maximum pit depths of 35, 110 and 250 (μm), air fatigue tests were conducted on these specimens and fatigue limits were found for each pit size. It was found that the equation developed earlier by Lindley et al [104] was not applicable in this case, Zhou and Turnbull [105] commented "The limitation of LEFM is not surprising as the overall 'crack' length is small; a crack formed at the pit may have an overall length which includes the pit but does not have the plastic wake history of a crack of the same length," in this situation the crack would be unable to grow beyond the plastic zone cause by the stress concentrating effect of the notch. El Haddad et al [127] developed an empirical relationship to account for the breakdown of LEFM concepts when considering short cracks, the concept is based on an effective crack length a_o , see Equation 32. It is still unclear exactly what a_o is, it seems to not correlate with any microstructural features, what is clear though is that as the crack length increase the effect of a_o reduces until it is negligible and long crack growth is seen.

Equation 32

$$\Delta K = \alpha \Delta \sigma \sqrt{\pi(a + a_o)}$$

Equation 33

$$\Delta K_{th} = \alpha \Delta \sigma_{th} \sqrt{\pi(a + a_o)}$$

Rearranging Equation 33 gives the equation below;

Equation 34

$$a = \frac{\Delta K_{th}^2}{\alpha^2 \pi} \Delta \sigma_{th}^{-2} - a_o$$

ΔK_{th} and a_o can easily be found using linear regression, with these values and using Equation 32 it is possible to produce a plot of pit depth against fatigue limit. Figure 44 [105] shows predicted data using a_o along with long crack approach and experimental data.

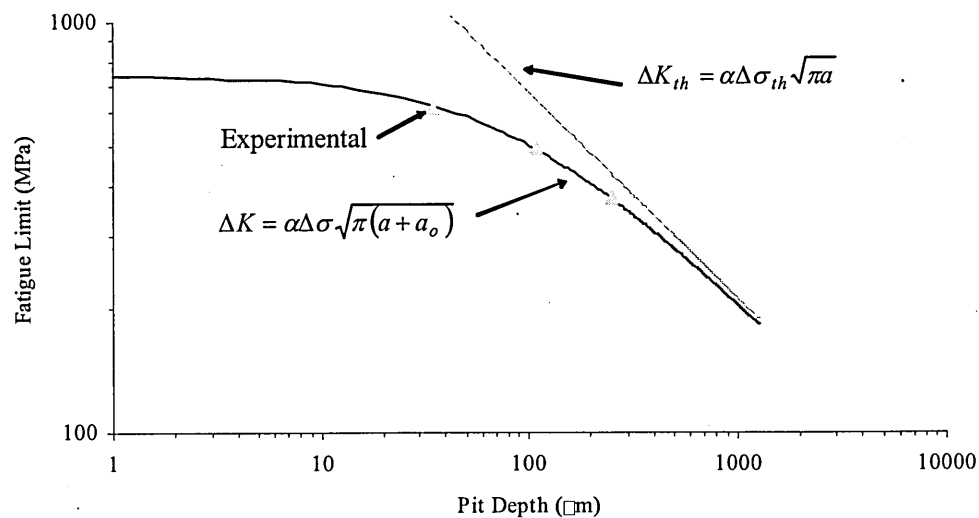


Figure 44 - Effect of Pit Depth On Endurance Limit 12 Cr stainless steel R=0.8

2.11.4 Stress Corrosion Cracking (SCC)

Stress corrosion cracking is the intergranular or transgranular cracking of a metal by the conjoint action of a static tensile stress and a corrosive environment. The stress may be applied as a residual stress left within the material as a legacy of a manufacturing process or applied externally either as a constant tensile stress or a slow ramp stress. Any combination of a number of factors may assist in a given SCC failure.

SCC is a combination of stress and an environment the removal of either will prevent cracking. In the absence of a stress the metal is usually unaffected by the SCC causing environment. The cracking of a particular metal is generally only observed for a relatively small number of specific environments. The corrosion potential of the metal can have an effect on SCC as cracking may only appear within certain potential ranges.

There are similarities between corrosion fatigue and SCC and indeed it could be said that SCC is only a special case of corrosion fatigue. Due to the different mechanisms associated with corrosion fatigue and stress corrosion cracking the characteristic crack growth behaviour seen under each condition is very different. In many air fatigue systems crack growth will only occur above a threshold stress intensity factor range, the growth per cycle first increases rapidly with stress intensity factor range above the threshold stress intensity factor then enters a region where $\log(da/dN)$ is linearly dependant upon the log of stress intensity factor range and finally becomes very rapid as the maximum stress intensity approaches the fracture toughness. When crack growth under a stress corrosion system is considered very different growth is observed. Many SCC crack growth cycles start with a definable threshold stress

intensity factor range below which no growth will occur the $\log (da/dt)$ versus $\log K$ curve rises steeply and often reaches a plateau that is independent of stress intensity, then rises steeply again as stress intensity approaches the fracture toughness. These trends can clearly be seen in the schematic illustration in Figure 45.

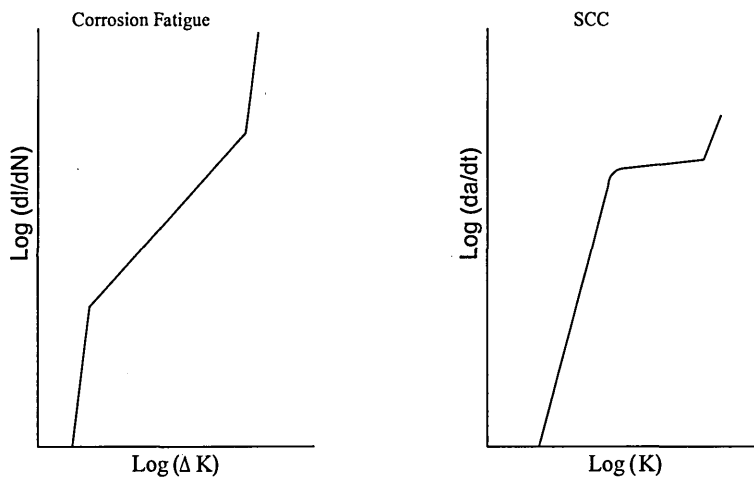


Figure 45 - Schematic Representation of Growth Characteristics For CF and SCC.

2.12 Potential Control and Monitoring of Corrosion Fatigue Tests

2.12.1 Introduction

The use of potential control in corrosion fatigue and stress corrosion cracking experiments is well established in corrosion fatigue research. The use of both internal and external reference electrodes has been published [128,129]. Due to the commercial nature of the work little of it may be found in the literature. Some work has been reported on the more general corrosion fatigue that is less commercially sensitive.

2.12.2 Effect of Potential on Corrosion Fatigue

In their work on the corrosion fatigue of stainless steels Amzallag et al [130] incorporated potential control. The effect of imposing potentials during corrosion fatigue tests can be seen in Figure 46. It can clearly be seen that an increase in corrosion fatigue strength at room temperature in 3% NaCl solution is evident when a potential of 0(mV) (SCE) is imposed, with the specimen being cathodically protected. An applied potential of 50 (mV) (SCE) is similar to that found at open circuit potential. With an applied potential of 200 (mV) (SCE) a very obvious deleterious effect is evident.

Figure 46 [130] clearly shows both the positive and negative effect potential control may have on corrosion fatigue life.

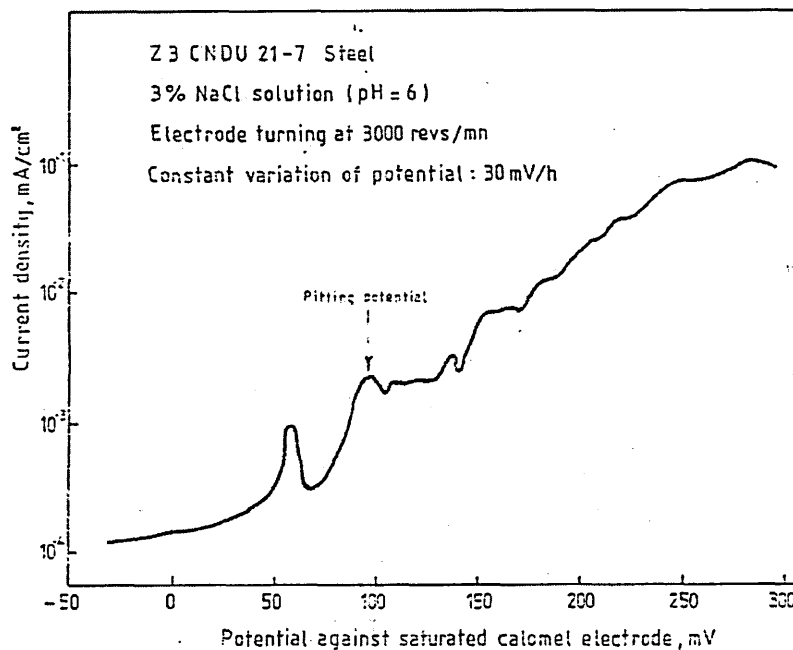


Figure 47 - Results of Potentiodynamic Testing on a 21%Cr 7Ni Stainless Steel in 3% NaCl on a Rotating Bending Fatigue Machine with Zero Load Applied.

From these tests Amzallag et al [130] identified the pitting potential of the system without any applied stress, from Figure 47 [130] it can be seen the pitting potential is approximately 100 (mV) (SCE). The effect that an applied stress has on the potential or more accurately the resistance of the steel to a given potential is evident when one considers Figure 47 [130] and Figure 48 [131]. At an applied potential of 50 (mV) (SCE) the resulting S-N curve is very close to results gained under open circuit potential, although 50 (mV) (SCE) is below the pitting potential it is still within the range for localized corrosion especially if one considers the harmful effect that an applied stress will have on the passive layer. Amzallag et al [130] suggest that an applied stress may have the effect of shifting the potentiodynamic curve by damaging the passive layer.

2.12.4 Effect of Dissolved Oxygen on The Fatigue Strength of Steels

The effect of dissolved oxygen on the fatigue strength of steels can clearly be seen in Figure 48 [131].

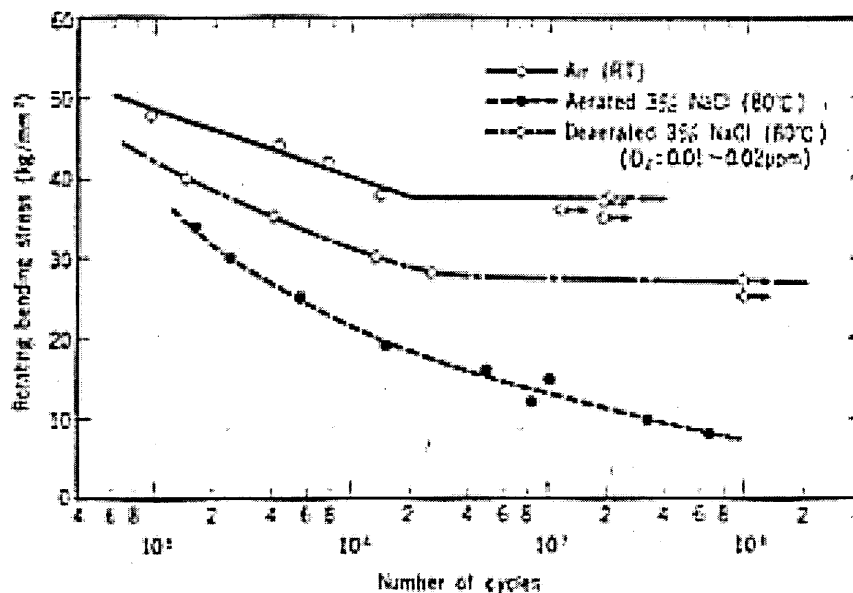


Figure 48 - S-N Curve for a 13%Cr Martensitic Stainless Steel in 3% NaCl Aqueous Solution at 80°C.

It can be seen that the greater the level of dissolved oxygen the lower the fatigue strength also under aerated (2.4 ppm at 80°C) conditions the fatigue limit visible in air and deaerated sodium chloride solution is lost. Ebara et al [131] suggested that this drop in fatigue life is not solely due to the level of dissolved oxygen, when similar tests were carried out in aerated distilled water and steam only a slight drop was seen in the fatigue life when compared to that in air. The drop in fatigue life was due to the combined effect of impurities (NaCl) and the level of dissolved oxygen. There are several works within the literature that show the recovery of fatigue life in NaCl and water to that in air by a reduction of dissolved oxygen concentration. A complete restoration of the air fatigue strength is shown by Lee and Uhlig [132] as a result of deaerating the 3% NaCl aqueous solution at 20°C in AISI 1015 steel. This resurrection was also observed by Mehdizadeh et al [133] using AISI 1035 steel in

5% NaCl, however, Ebara et al [131] also details the earlier work of Pettit [134] on SNCM 8 and drill-pipe steel where no recovery was seen due to deaeration. Further work by Lee and Uhlig [132] showed that the recovery of fatigue strength by deaeration was dependant on the tensile strength of the steel, with higher tensile strength materials failing to recover their fatigue strength in air through deaeration.

2.12.5 Effect of Dissolved Oxygen Concentration on Potential

It has been observed by many authors that as the level of dissolved oxygen in an aqueous system increases so the potential becomes more anodic. This effect is dependent upon temperature as can be seen in Figure 49 [129].

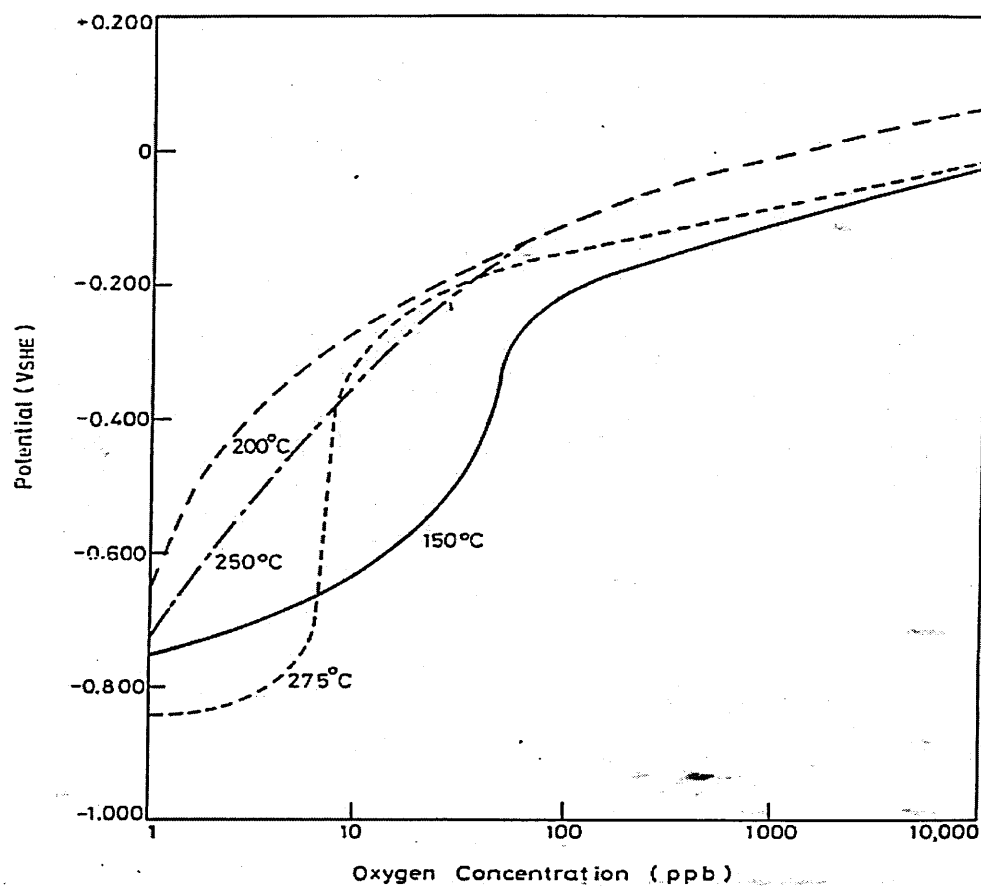


Figure 49 - Electrochemical Potential Data for SA 333-6 Carbon Steel in Water as a Function of Oxygen Concentration and Temperature.

3 Experimental

Procedure

3.1 Introduction

The literature review detailed in previous sections highlighted several areas that required further investigation and testing. The following section describes the testing that was carried out and the objectives of conducting such work.

3.2 Experimental Program

Experimental investigations were conducted in the following areas.

- Material characterisation of both steels.
- Obtain static material data and evaluation of microstructural features. Find out if retained austenite will undergo a strain induced transformation in softened overaged FV520B under tensile loading over a range of temperatures. Assess the electrochemical/corrosion responses of both steels.
- Quantify the fatigue strengths of both 18Ni maraging and FV520B in air at ambient temperature.
- Find the notch sensitivity of both steels in air.

- Find corrosion fatigue strengths for both steels in mildly corrosive environments at free corrosion potential.
- Conduct imposed potential corrosion fatigue tests on the more resilient steel.
- Conduct pulsed damage corrosion fatigue testing on notched FV520B specimens to assess the affects of transient start-up shut-down steam turbine environments.
- Carry out detailed examination of all failed specimen to better understand fatigue failures.

3.3 Material Characterisation

3.3.1 FV520B

FV520B is a low carbon martensitic stainless steel that has good strength and corrosion resistance, these properties mean that the material is well suited to the low pressure (LP) section of a steam turbine.

The material was received as rolled bar-stock of diameter 120 (mm). The bars were reduced by hot forging to plate with dimensions of approximately 5(m) long lengths of 100(mm)x40(mm) section. Two melts of the steel, FV520B-A and FV520B-B were investigated. The composition of the two melts of FV520B are given in Table 5.

3.3.2 18 % Ni Marageing Steel

18% Ni marageing steel is a low carbon martensitic steel with high strength and good ductility. This steel was found to have similar mechanical properties as FV520B when heat treated under the same conditions. However, 18% Ni marageing steel

contains no chromium and therefore has far less corrosion resistance compared to FV520B. The weight composition of the 18% Ni maraging steel is also given in Table 5.

Type of Steel	Element % (Balance Fe)											
	C	Si	Mn	Cr	Ni	Mo	Cu	Nb	P	S	Ti	Co
FV520B - A	0.06	0.29	0.57	13.9	5.29	1.41	1.51	0.25	0.01	0.01	-	-
FV520B - A	0.06	0.39	0.75	13.6	5.45	1.44	1.67	0.26	0.02	0.01	-	-
18% Ni Maraging	0.01	0.01	0.02	0.02	17.5	3.18	-	-	-	-	0.3	8.3

Table 5 - Composition of Materials Tested

3.3.3 Heat Treatment

The material blanks were treated in exactly the same way as those of Clark [5] thus facilitating a direct comparison of results. Material blanks (20(mm)x 20(mm)x130(mm)) were sectioned in the longitudinal direction to make plate form for heat treating in a Carbolite™ CFS 1200 furnace. The material was heat treated in three stages according to the schedule given in Table 6.

Heat Treated Condition	Homogenisation	Solution	Precipitation Hardening
Peak Hardened	1 hour @ 1050°C – air cooled	2 hours @ 850°C – air cooled	4 Hours @ 450°C – air cooled
Softened Overaged	1 hour @ 1050°C – air cooled	2 hours @ 750°C – air cooled	2 Hours @ 620°C – air cooled

Table 6 - Three Stage Heat Treatment Schedule

The above schedule along with the resulting mechanical properties are available in the manufacturers technical data book for FV520B [135].

The three stage heat treatment cycle was used to produce a microstructure with the required mechanical properties. Each stage was conducted for a specific reason.

3.3.3.1 Homogenisation

Hot forging the as-rolled material to form plate usually leads to a heavily deformed microstructure that is likely to be anisotropic. The initial heat treatment was designed to remove the effects of prior plastic deformation and thus provide a homogenous microstructure. The first stage of heat treatment was also required to cause the alloying elements to be absorbed into the austenitic solid solution before any further heat treatment can take place.

The homogenisation phase of the heat treatment involved heating of the material to 1050°C. Commercially the material would only be held at 1050°C for approximately 30 minutes, however in the earlier work of Clark [5] it was found that the materials microstructure was still heavily banded after only 30 minutes of heat treatment.

Increasing the time that the material was held at 1050°C would have removed the banded microstructure but may have introduced deleterious effects on the material's fatigue strength. During trials conducted by Clark [5] it was found that heat treatment at 1050°C for up to one hour did not effect the fatigue strength of the material and only light banding remained.

3.3.3.2 Hardening or Solution Treatment

Heating to 850°C partially re-austenitised the steel, tempered any martensite within the microstructure and precipitated any alloy carbides. When cooled to room

temperature the resulting microstructure would contain martensite, tempered martensite alloy carbides and retained or reverted austenite.

3.3.3.3 Artificial Precipitation Hardening Treatment

The third stage of heat treatment was precipitation hardening or ageing. Ageing at 450°C gives the material maximum strength. This is due to the formation of large coherent precipitates in the microstructure.

3.4 Determination of Static Material Properties

3.4.1 Tensile Testing

An Instron testing machine was used. The geometry of the specimens used for tensile testing is shown in Figure 50. Load and extension data were monitored thus enabling calculation of ultimate tensile strength and 0.2% proof stress.

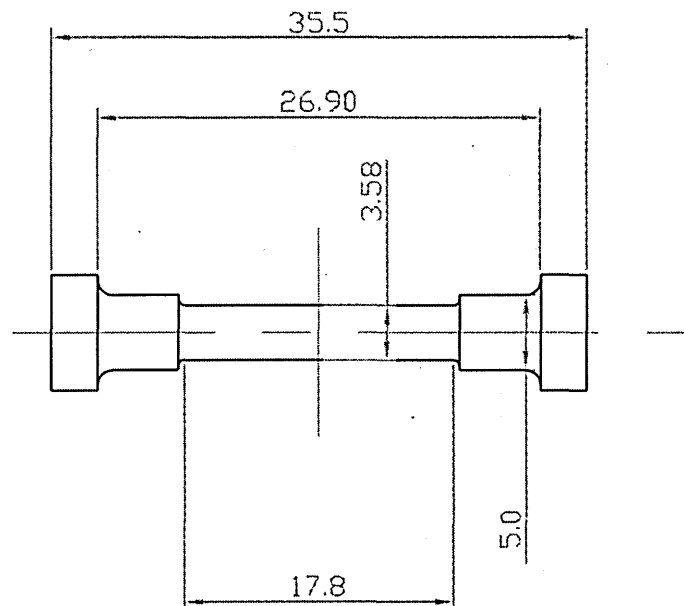


Figure 50 - Tensile Specimen Design All Dimensions in mm.

3.4.2 Material Hardness Testing

The hardness of all three steels used in the fatigue testing was measured using Vickers hardness testing machine with a 30kg load and a square based pyramid indenter.

3.4.3 Slow Strain Rate Testing

The aim of the slow strain rate testing was to investigate the tensile mechanical properties of FV520B as a function of test temperature. Slow strain rate tests were carried out on peak hardened and softened overaged FV520B.

3.4.3.1 Specimen design

All slow strain rate specimens were made to the same design shown in Figure 51.

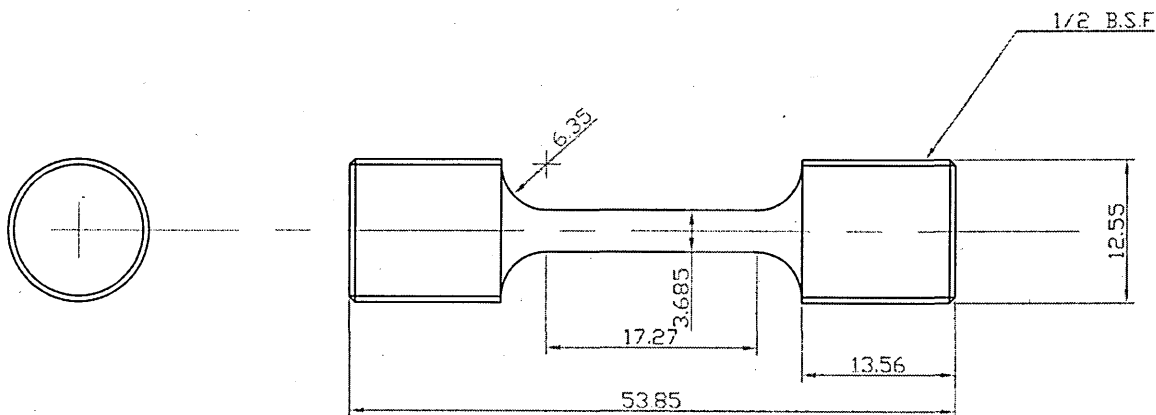


Figure 51 - Slow Strain Rate Testing Specimen Design All Dimensions in mm

All tests were carried out using a Mayes ESM100 Tension/Compression testing machine set at a 20kN load range, extension was monitored using an LVDT with a range of ± 5 (mm). All data was recorded using a pen chart recorder. The required temperature was achieved using a furnace that surrounded the specimen. The temperature was recorded throughout the test. All test were conducted at a strain rate of $2 \times 10^{-6} \text{ s}^{-1}$.

3.4.4 Electrochemical Testing

Electrochemical testing techniques were used to assess the relative corrosion properties of the materials used. Standard polarisation testing was carried out. The samples were mounted in non-conductive Bakelite polished to a 1200# grit finish with silicon carbide grit paper and then finished with 6(μm) and finally 1(μm) diamond polish. To avoid crevice corrosion in the small gap between the metal sample and the Bakelite mount the edges of the metal were covered with Lacomite varnish prior to testing. Electrical connection to the specimen was obtained via a small hole drilled and tapped through the Bakelite into which a 5(mm) brass rod was screwed. Each polarisation curve was conducted using a 0.3% aqueous sodium chloride electrolyte in a container open to laboratory air. The temperature of the solution was held at $25^{\circ}\text{C} \pm 2.5^{\circ}\text{C}$. A standard Saturated Calomel Electrode (S.C.E) reference electrode was used and a Platinum counter electrode with a surface area of 6(cm^2) was used. Each test was composed of the following routine;

- -900(mV)_{SCE} for 10(min), to allow the passive layer to form.
- 10 (min) pause at free corrosion potential, to allow a steady state to form at the surface electrolyte interface.
- Potentiodynamic control from -900(mV)_{SCE} to +600(mV)_{SCE} at 60(mV/min).

The potentiostat used was an ACM model GillAC connected to a PC for control and data acquisition.

3.4.5 Non-Metallic Inclusion Counting

Non-metallic inclusion counts were carried out on all the steels. The counts were conducted using an optical microscope connected to an image analysis system. All counts were completed at a magnification of x300 giving a field area of 12220 (μm^2). Ten random fields were chosen from each specimen. Each specimen was a section of the threaded stub of a fatigue sample approximately 2(cm) by 1(cm). The specimens were mounted in Bakelite and polished to a 1200# grit finish and then with 6 (μm) and finally 1(μm) diamond paste. The counts were carried out with the specimens in a non-etched condition.

3.4.6 Scanning Electron Microscopy

Scanning Electron Microscopy (SEM) was used to examine the microstructure of the steels investigated. SEM was also used to inspect the fracture surfaces of failed specimen and to identify and quantify corrosion damage. The Scanning Electron Microscope used was a Philip's XL40.

3.4.6.1 SEM Sample Preparation

Material for microstructural analysis was mounted in conductive Bakelite and then attached to aluminium stubs using carbon sticky pads. The failed specimens that were examined had the threaded portions removed to give a greater depth of field in the SEM. The specimens were ultrasonically cleaned to remove any corrosion debris and then mounted on to aluminium stubs using carbon sticky pads. A small bracket was designed to allow circumferential surveying of the specimen thus aiding corrosion damage assessment. Some specimens that did not fail were examined in the

SEM in such a case aluminium tape was used to fasten the specimen directly to the stage in the SEM.

3.4.7 Finite Element Analysis

Finite Element Analysis (F.E.A) was used to calculate the theoretical stress concentration factor (K_t). An axisymmetric model of the notched fatigue specimen was developed. The model uses linear element, the mesh used is illustrated in Figure 52. The model is made up from 50 nodes that define 34 elements.

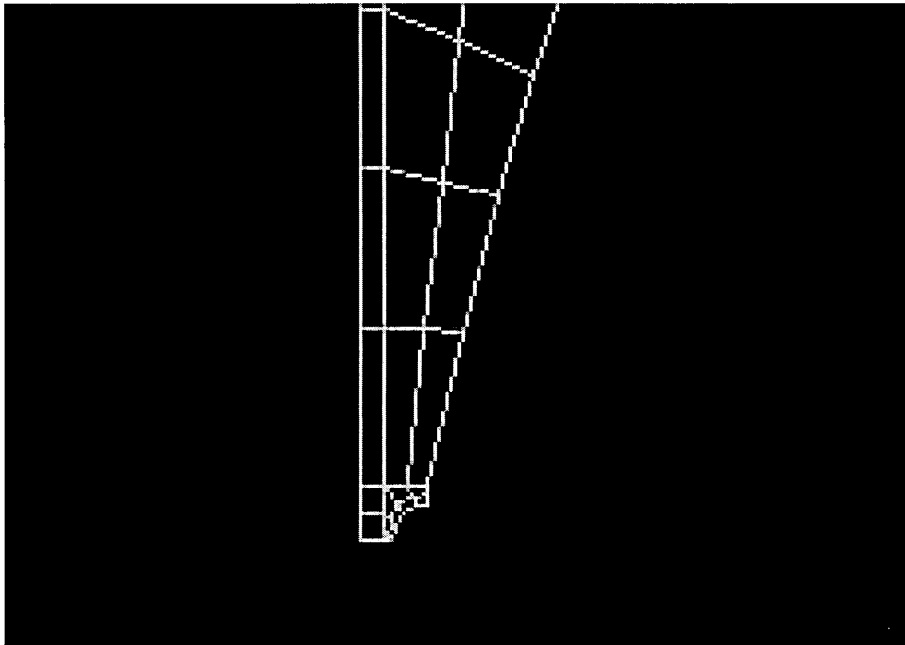


Figure 52 - F.E.A Mesh Of Notched Fatigue Specimen

3.5 Fatigue Testing Program

All fatigue testing was carried out using a Mayes 20kN servo-hydraulic testing machine. Two types of fatigue tests were conducted during the programme; air fatigue and corrosion fatigue.

3.5.1 Fatigue Specimen Design

The same specimen geometry was used for both air and corrosion fatigue tests. The hour glass fatigue specimen was selected for fatigue testing, thus enabling a direct comparison with the work of Clark [5]. The geometrical details of the plain and notched specimens used are illustrated in Figure 53 and Figure 54.

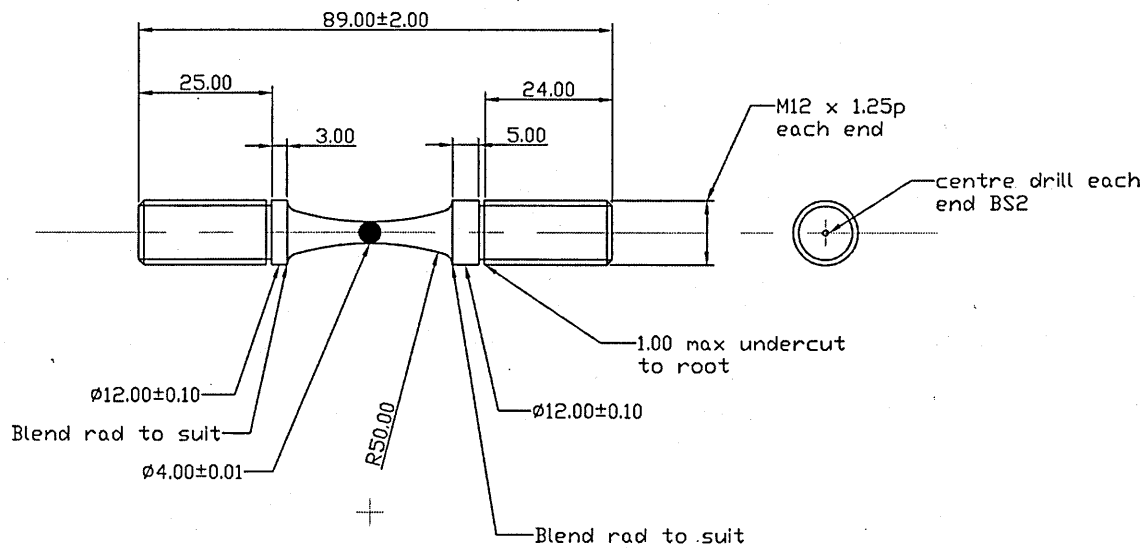


Figure 53 - Plain Fatigue Specimen Design For Air and Corrosion Fatigue. Dimensions in mm

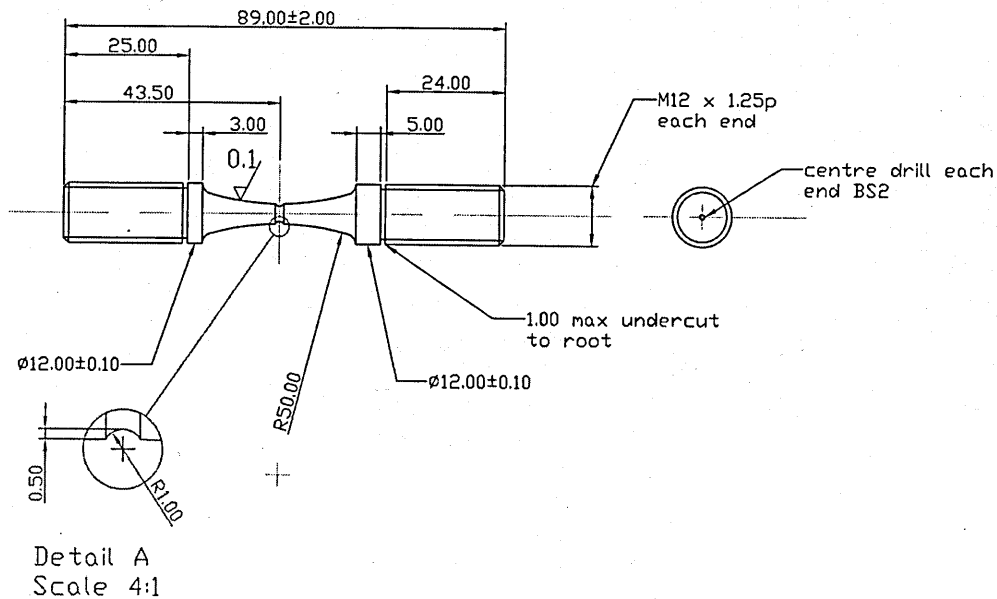


Figure 54 - Notched Fatigue Specimen Used For Air and Corrosion Fatigue All Dimensions in mm.

3.5.2 Air Fatigue Tests

Air fatigue tests were carried out in ambient laboratory air (25°C). Tests were conducted at load frequencies of between 4-7 (Hz) with a fully reversed ($R=-1$) cyclic loading. Table 7 gives details of the air fatigue tests conducted;

Test Series	Specimen	Material
A	Notched	FV520B
B	Notched	18% Ni Maraging
C	Plain	18% Ni Maraging

Table 7 – Air Fatigue Tests Conducted

3.5.3 Corrosion Fatigue

The corrosion fatigue tests were performed using a Mayes 20kN servo hydraulic fatigue test machine. In order to carry out corrosion fatigue tests in simulated steam turbine conditions ($< 150^{\circ}\text{C}$) an autoclave and water loop system were designed and constructed. A schematic arrangement of the autoclave and water loop system are shown in Figure 55. Figure 56 shows a sectioned view of the autoclave and Figure 57 shows the corrosion fatigue test rig in operation. Note that the autoclave is lagged with glass wool to minimise heat loss during testing.

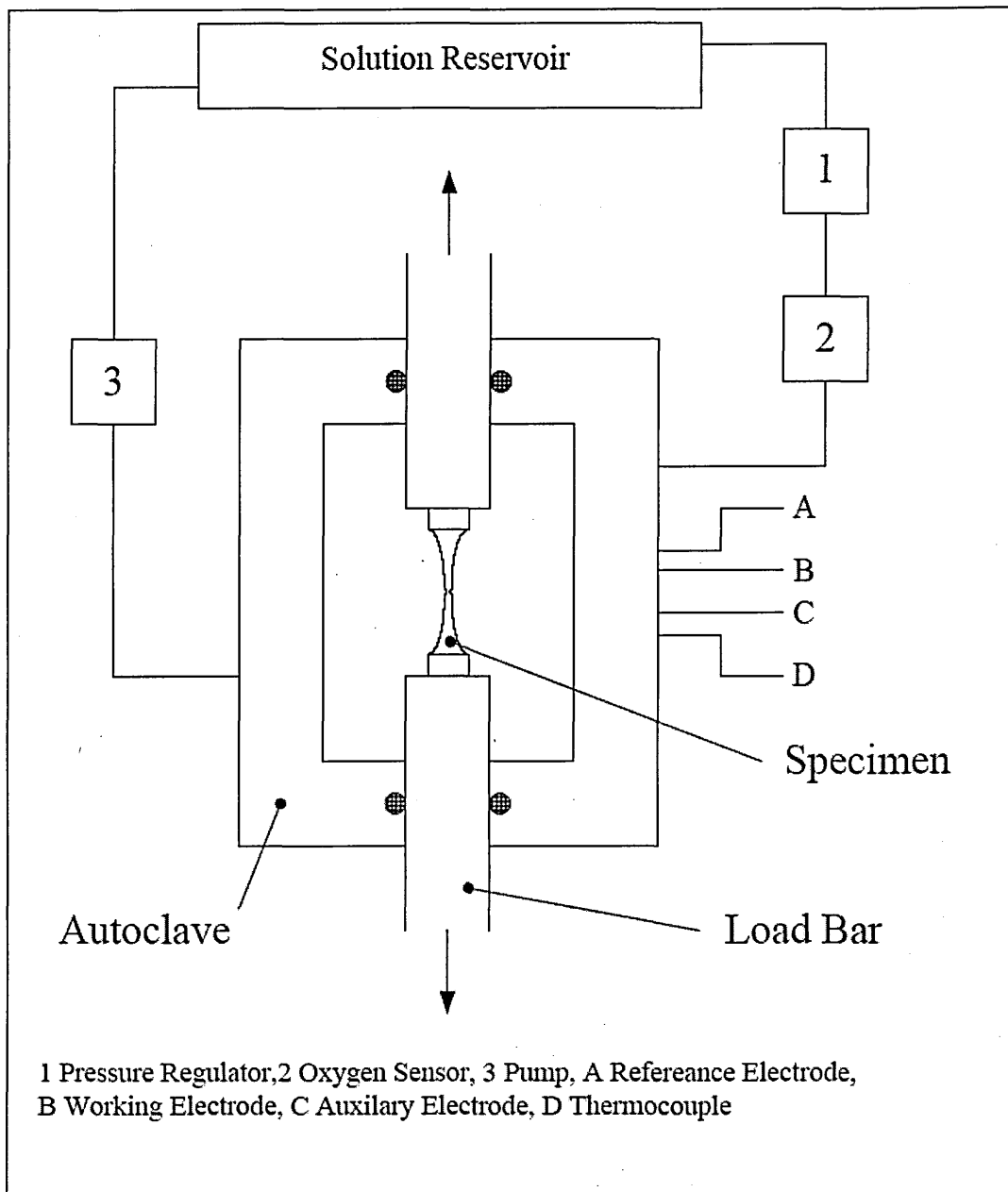


Figure 55 - Schematic Arrangement of Autoclave and Water Loop System

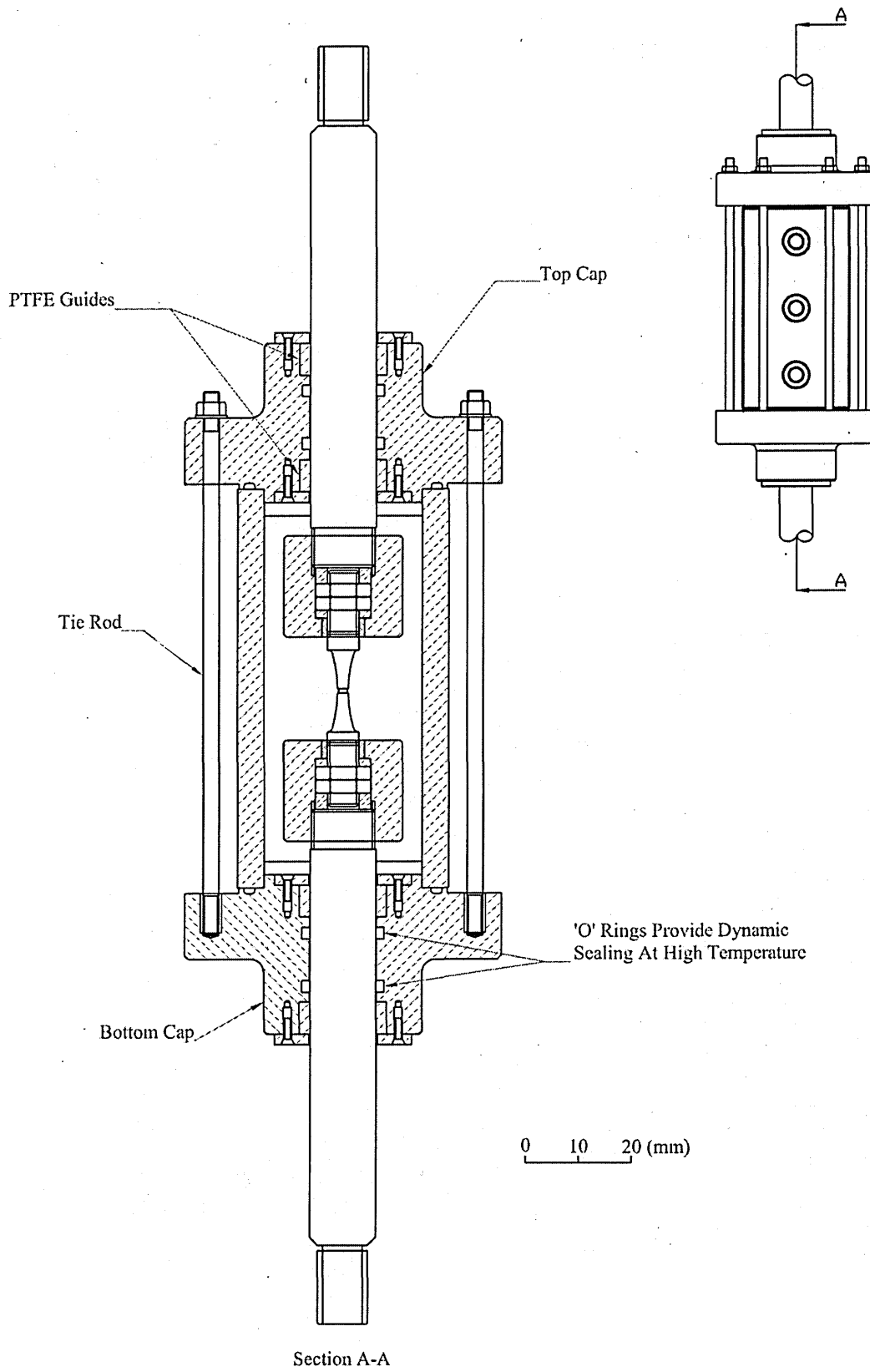


Figure 56 - Sectioned View of Autoclave

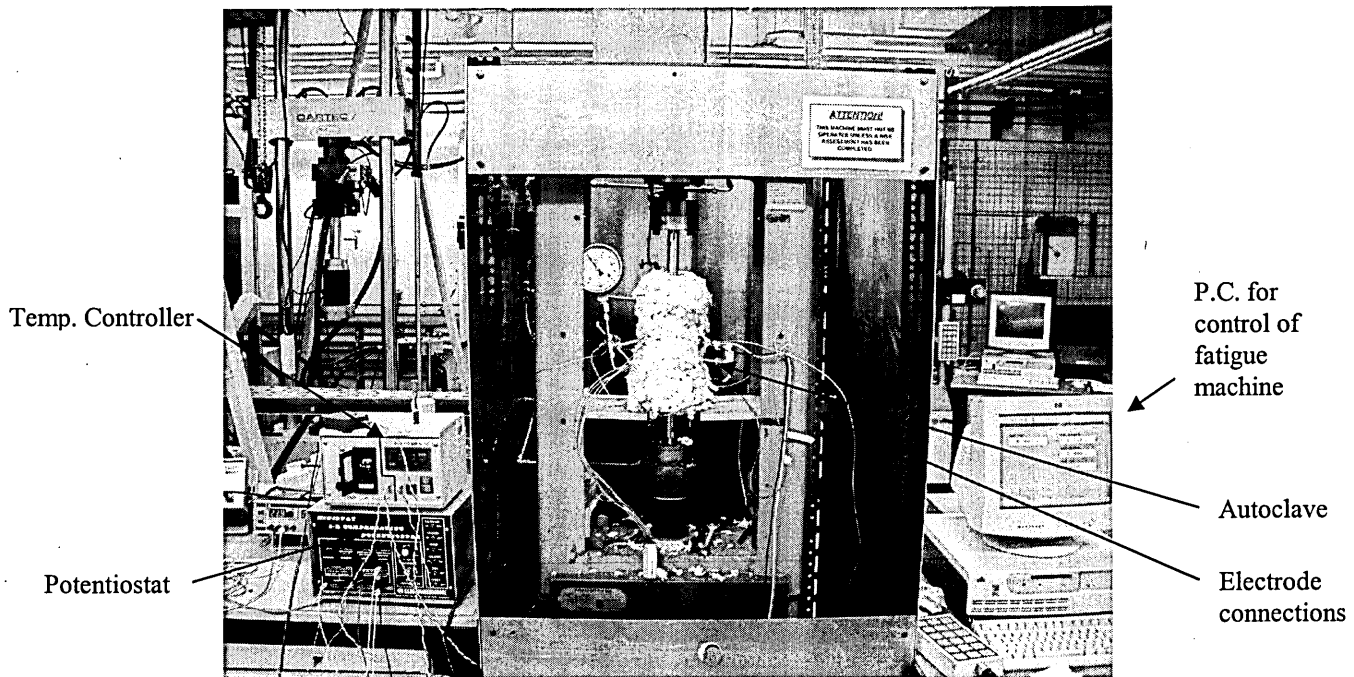


Figure 57 - Corrosion Fatigue Test Rig in Operation.

The autoclave chamber was approximately 150 (mm) long with a 60 (mm) internal diameter and was constructed from a material that would be able to withstand a hot pressurised chloride environment. It is well known that Stainless steels suffer from Stress Corrosion Cracking in chloride environments, according to Leffler [11] “The environments that most frequently cause SCC in stainless steels are aqueous solutions containing chlorides. Apart from the presence of chlorides and tensile stresses, an elevated temperature ($>60^{\circ}\text{C}$) is normally required for SCC in stainless steel”. The susceptibility of stainless steels to SCC is greatly increased if they are sensitised.

Stainless steels are noncorrosive due to levels of Chromium above 11% giving a passive layer that prevents corrosion. When sensitisation occurs the precipitation of chromium carbides causes a chromium level of below 11% in the metal adjacent to

the precipitates; this metal is no longer resistant to corrosion. Compared to the rest of the grain, the chromium-depleted region is very anodic and severe attack occurs adjacent to the grain boundary if the metal comes into contact with electrolytes. In extreme conditions whole grains become detached from the material. Although the alloy may be in an unsensitised condition after manufacture fabrication processes that involve heating above 600°C such as welding may facilitate the movement of carbides.

To prevent possible problems with stress corrosion cracking when using stressed stainless steels in a chloride environment the autoclave was designed without any welding and constructed from AISI321 stainless steel. AISI321 stainless steel contains titanium, the carbon within the steel forms titanium carbides in preference to chromium carbides thus removing the problem of sensitisation.

To accurately impose corrosion potentials upon the specimen it was essential that it be electrically isolated from the load bars and hence the fatigue testing machine. To isolate the specimen a material with good compressive strength high electrical resistance and also be chemical inert was required. After much experimentation it was found that Bakelite was able to provide all of the above qualities. Electrical insulation from the load bars was accomplished using the grip system shown in Figure 58.

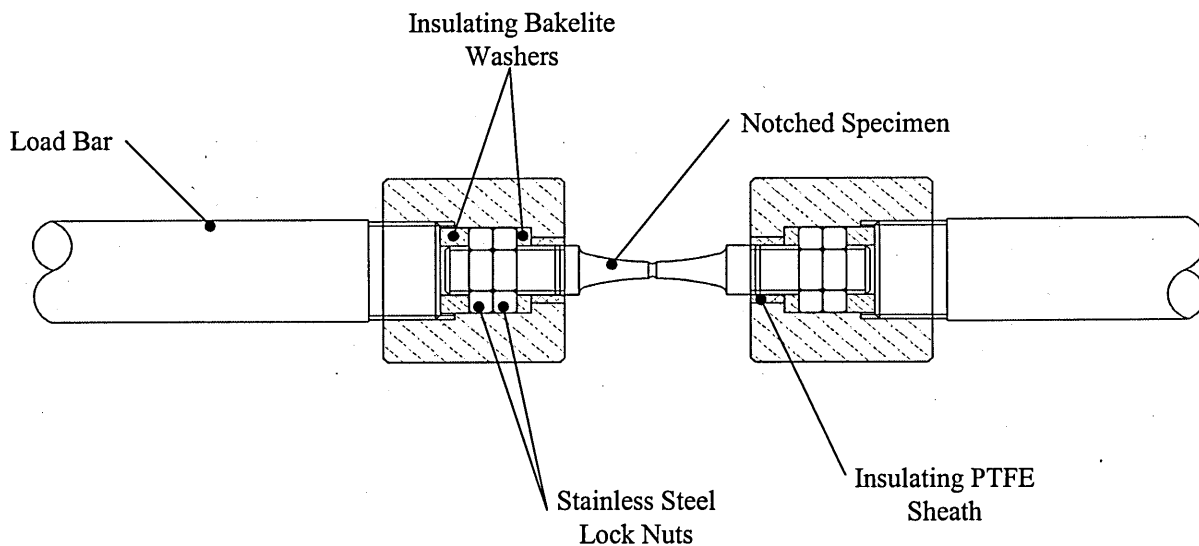


Figure 58 - Insulating Grip System Used for Corrosion Fatigue Testing

The autoclave was pressurised using a Bran + Luebbe™ metering pump to prevent the formation of steam. The pump was fed from a header tank full of liquor. Pressure within the autoclave was controlled by a pressure regulating valve. The regulating valve was placed after a condenser in the circuit to reduce problems caused by hot solution. An electronic pressure sensing device was used to monitor the solution pressure within the system. There was very little flow within the system, the only movement of solution was due to the opening and closing of the pressure regulating valve. Heat was provided by two 400 (W) band heaters, these were used to control the water temperature that was monitored via a K type thermocouple sealed in a Conax™ fitting. The autoclave was insulated using glass wool to reduce heat loss during testing and hence prevent temperature fluctuations during testing.

In order that the potential within the autoclave be controlled working, reference and auxiliary electrodes were required and a high temperature high pressure cold external silver-silver chloride electrode was used for this purpose. A Platinum auxiliary electrode of 80 (mm²) was fixed inside the autoclave and a connection was provided through the Conax fitting. The working electrode connection was provided by a

stainless steel wire spot welded to the specimen, the spot weld was sealed with Lacomit Varnish™ that was baked at 130°C for 30 (min). Where applicable the potential within the autoclave was controlled using a Thompson Ministat (25V, 1Amp). Levels of dissolved oxygen within the liquor were monitored using a Orbisphere 2713 Oxygen Analyser. A Hewlett Packard™ Data logger was used which scanned all sensors every 10 seconds throughout the test. The system was designed in such a way that the instant the specimen fractured both the potentiostat and the heaters were turned-off thus minimising any damage to the specimen after fracture had occurred. To allow potential monitoring and control of the solution within the autoclave it was essential that the reference electrode should remain stable within the autoclave environment. When considering reference electrodes for use within high temperature high pressure environments there are principally two types: internal hot electrodes or external cold electrodes only the latter will be considered here as it was used throughout the corrosion fatigue tests conducted, due to space constraints within the autoclave.

3.5.3.1.1 External Reference Electrodes

Many designs of external reference electrode have been published and reviewed [136,137]. Most of these electrodes are of a similar generic type, having a chloridised silver rod immersed in a solution of known chloride concentration in a container that is cold but pressurised with a luggin probe providing a connection to the autoclave. An example of this design is given in Figure 59.

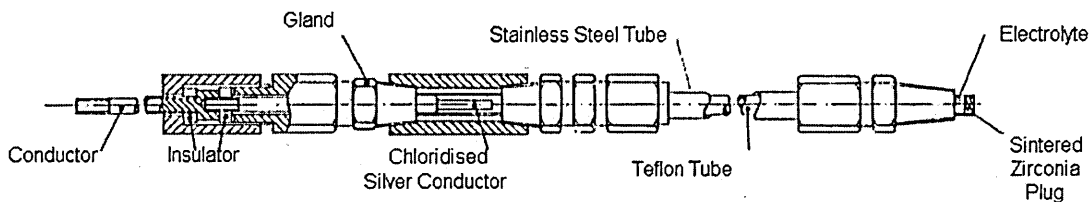


Figure 59 - An External Ag/AgCl Electrode for High Temperature, High Pressure Use. 138.

The main areas for concern in the design of such an electrode are; retention of the soft silver sensing element in an electrically isolated pressure fitting, maintenance of a constant chloride activity around the sensing element, loss of electrical conductivity due to gas bubble formation, internal electrode body materials of high enough strength to withstand the temperature and pressure while insulating the electrode from the pressurised test system.

The basic electrode shown in Figure 59 has been developed over the years to overcome most problems Scott and Bamford [138] state "The best overall experience in high temperature (288°C) high pressure (17MPa) has been gained with external, cold but pressurised silver/silver chloride electrodes" and go on to suggest that potential readings made using Ag/AgCl electrodes are accurate to within 20(mV).

3.5.3.1.2 Construction of an External Electrode for Use at High Temperatures and Pressures.

In the construction of a silver-silver chloride electrode there are several key points that must be considered; electrical insulation of the silver-silver chloride rod, high impedance frit, working temperature, working pressure, retention of silver-silver chloride rod at high pressure. To overcome these problems the design shown in Figure 60 was used.

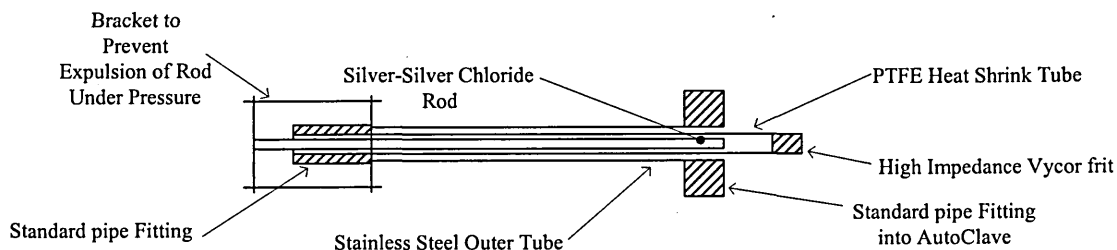


Figure 60 - Schematic of an External Reference Electrode

3.5.3.1.3 Production of Silver Chloride Coating on Silver Rod

There are several key steps in the construction of an external silver-silver chloride reference electrode;

Prior to chloridising the Silver rod was cleaned in concentrated Ammonia and the surface roughened using fine Silicon Carbide paper. The silver rod was anodically chloridised in a solution of 1 N HCL by passing a current of approximately 2 (mA/cm²) overnight, using a carbon counter electrode.

3.5.3.1.4 Assembly of Electrode

The High impedance VycorTM glass frit was fitted using Teflon heat shrink, thus providing a bond that was able to withstand high pressure and temperature (>300°C). Before fitting the silver-silver chloride rod the filling solution was added. A filling solution of 0.025 M KCl was used, to minimise the likelihood of bubbles forming and disrupting conduction the filling solution was degassed. Using a syringe with a long needle attachment the tube was filled. The silver rod was fitted to the PTFE heat shrink tube using a Teflon bush. With the anti expulsion bracket and the protective outer stainless steel pipe fitted the electrode is ready. The electrode was allowed to settle overnight before use.

3.5.3.2 Corrosion Fatigue Tests Conducted

The rig detailed above allowed a great number of test scenarios to be considered. A list of the corrosion fatigue tests performed is given in Table 11 and Table 12 (see page 148). Unless otherwise stated test load frequency was 2Hz and stress ratio (R) was -1.

4 Results of Experimental Program

4.1 Introduction

The results from experimental work are presented in the following chapter. All stresses are based on minimum cross sectional area as per Frost et al [38].

4.2 Static Material Testing

4.2.1.1 Tensile Test Results

The results from the tensile testing of peak Hardened FV520B are given in Table 8.

Material	UTS (MPa)	0.2% Proof Stress (MPa)	% Elongation	% Reduction in Area
FV520B-A	1313-1325	1127-1156	3.8	52-63
18 % Ni	1311-1325	1248-1270	3.7	42-47
FV520B-B	1442	1333	3.5	53

Table 8 - Tensile Test Results For Peak Hardened FV520B

4.2.1.2 Vickers Hardness Results

The results from the Vickers Hardness tests are given in Table 9. All hardness tests were completed using a square based pyramid indenter with a load of 30kg.

Material	Hardness (Hv ₃₀)
FV520B-B	418
FV520B-A	409
18%Ni Maraging	411

Table 9 - Vickers Hardness Results, 30(N) Load

4.2.1.3 Slow Strain Rate Test Results

The results from the slow strain rate tensile tests are plotted on stress-strain graphs in Figure 61 and Figure 62. The tensile strength, percentage elongation and percentage reduction in area are plotted with respect to test temperature in Figure 63 and Figure 64.

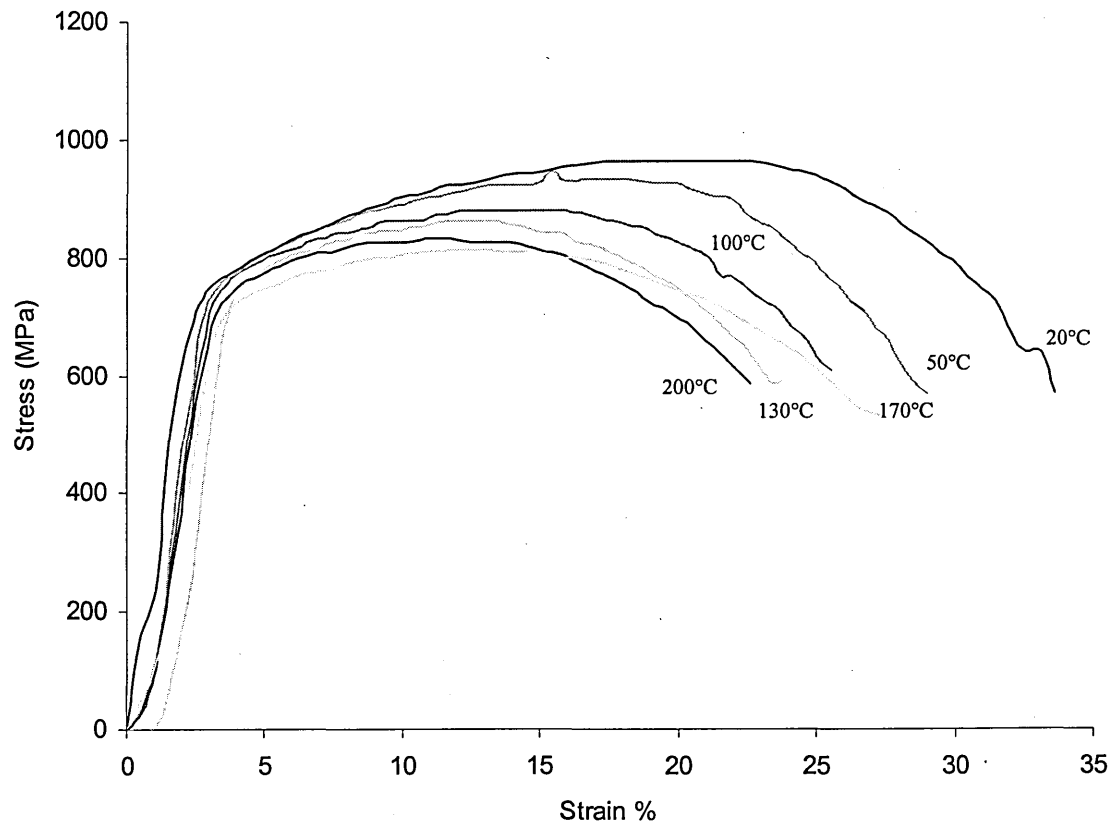


Figure 61 - Effect of Temperature on the Slow Strain Rate Response of Softened Overaged FV520B-B

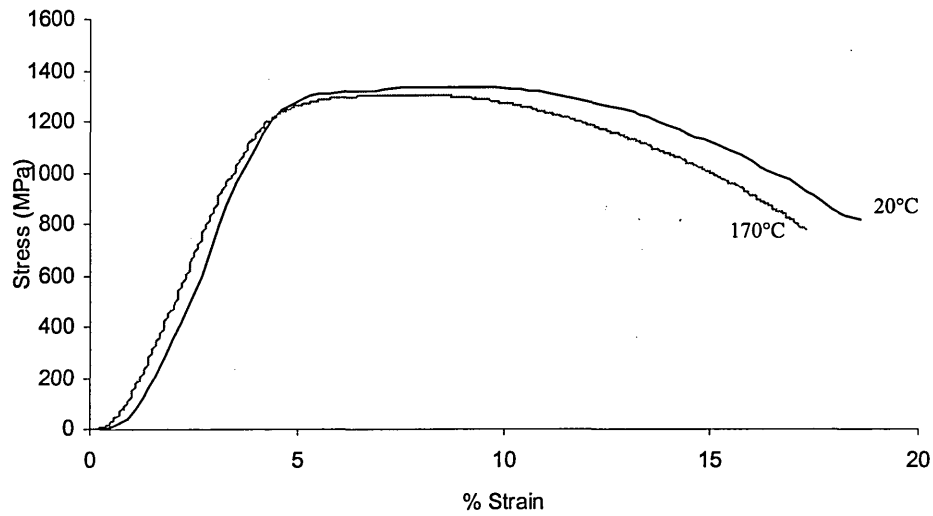


Figure 62 - Graph To Show Effect of Temperature on the Slow Strain Rate Response of Peak Hardened FV520B-A.

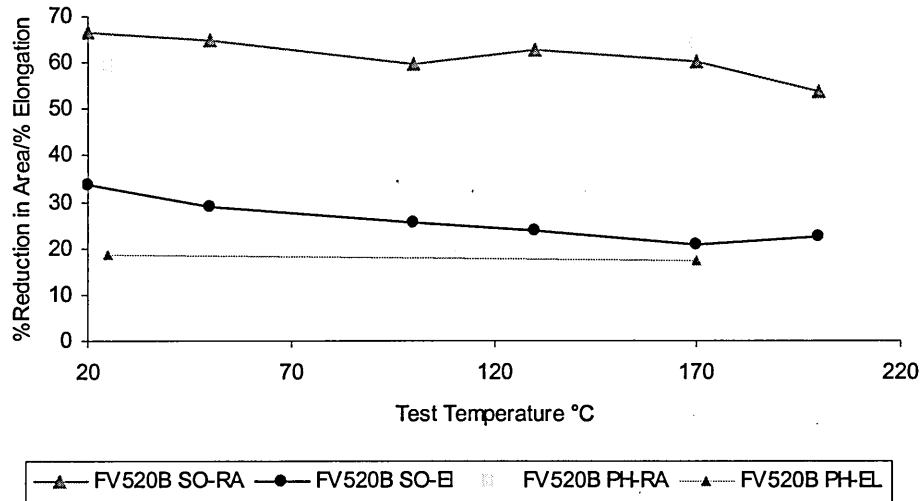


Figure 63 - The Effect of Temperature on Reduction in Area and Elongation for Slow Strain Rate Tests on Various Blading Materials.

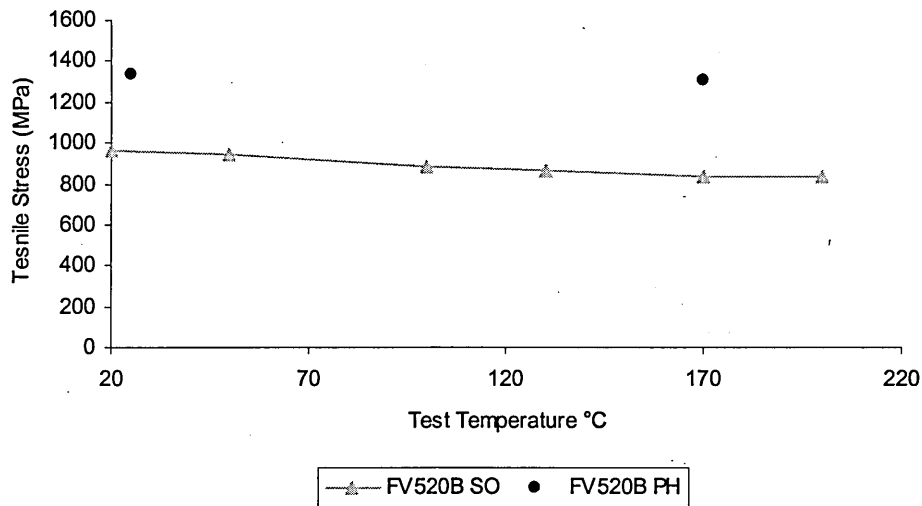


Figure 64 - The Effect of Temperature on Tensile Strength for Slow Strain Rate Tests on Various Blading Materials.

4.2.2 Potentiodynamic Test Results

The results of the potentiodynamic testing are plotted on a current density versus potential graph shown in Figure 65.

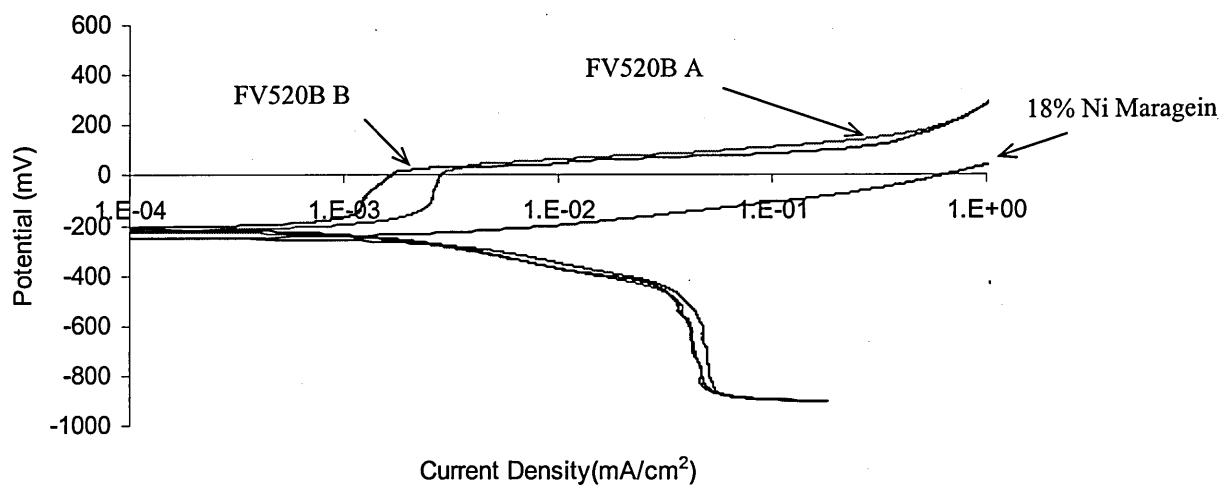


Figure 65 - Polarisation Curves For 18%Ni Maragein Steel and Peak Hardened FV520B. Tests Conducted Open To Air in 0.3% NaCl At Room Temperature, S.C.E Reference Electrode, Scan Rate = 10(mV/s)

4.2.3 Non-Metallic Inclusion Count Results

The results from the non-metallic inclusion count are plotted in Figure 66.

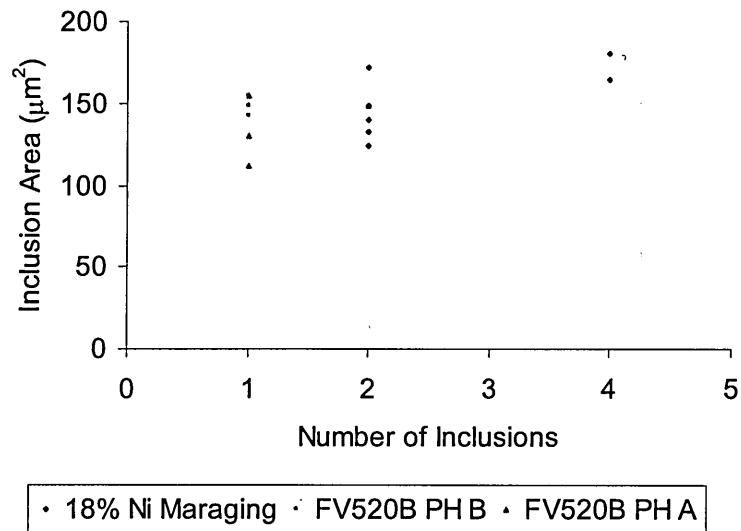


Figure 66 - A Graph of Show The Number and Size of Inclusions In FV520B and 18%Ni Maraging Steel.

The chart in Figure 67 shows the ratio between the total area of inclusions and the total area checked for each steel.

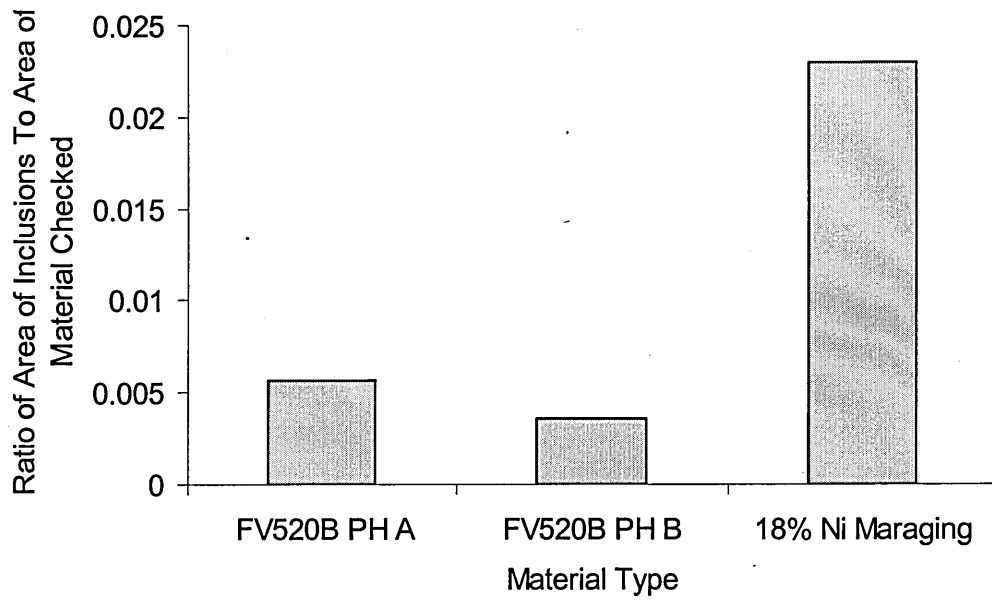


Figure 67 - The Ratio of Area of Inclusions For FV520B and 18% Ni Maraging Steels to the Total Area Checked.

4.2.4 F.E.A Test Results

A plot of the loaded mesh is given in Figure 68. Von Mises equivalent stresses are plotted on the mesh.



**Figure 68 - Deformed F.E.A. Mesh Showing Von Mises Equivalent Stresses at the Notch Root.
Stress in Pa.**

4.3 Air Fatigue Test Results

The raw data from both notched and plain specimen fatigue tests conducted in laboratory air at 25°C are presented in Table 10. The data is shown on S-N curves in Figure 69 and Figure 70.

Test No.	Specimen ID	Specimen	Material	Stress Amplitude (MPa)	Frequency (Hz)	Cycles To Failure
AFT 1	sam1	Notched	FV520B - A	354	4	325770
AFT 2	sam2	Notched	FV520B - A	283	4	5*10 ⁶ NF
AFT 3	sam3	Notched	FV520B - A	318	4	7*10 ⁶ NF
AFT 4	sam4	Notched	FV520B - A	390	4	158090
AFT 5	sam5	Notched	FV520B - A	600	4	17760
AFT 6	sam6	Notched	FV520B - A	500	4	26670
AFT7	C6	Plain	18 Ni Marageing	600	4	82131
AFT8	C7	Plain	18 Ni Marageing	300	4	10 ⁶ NF
AFT9	C8	Plain	18 Ni Marageing	450	4	10 ⁶ NF
AFT10	C9	Plain	18 Ni Marageing	700	4	93716
AFT11	C10	Plain	18 Ni Marageing	800	4	14968
AFT12	C2	Notched	18 Ni Marageing	300	4	127080
AFT13	C13	Notched	18 Ni Marageing	150	4	10 ⁶ NF
AFT14	C12	Notched	18 Ni Marageing	600	4	8384

Table 10 Air Fatigue Test Results, For All Tests R=-1, Stresses Based on Minimum C.S.A., NF = No Failure

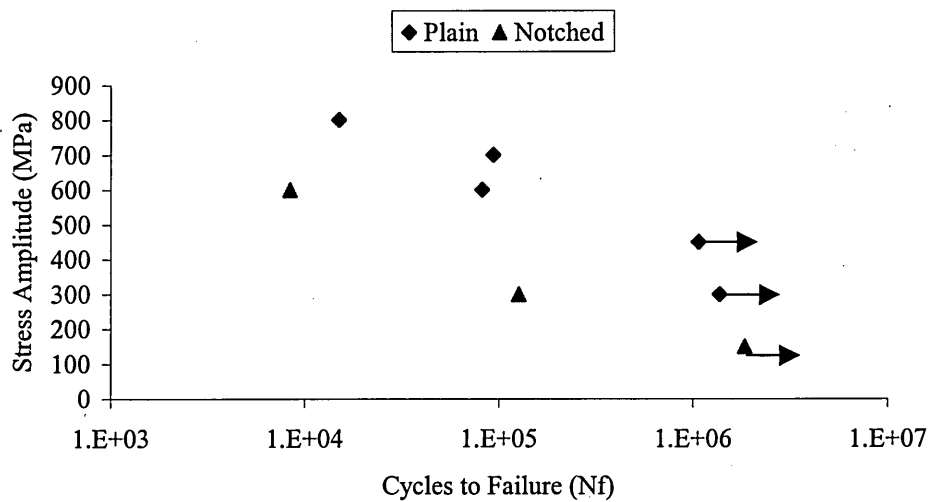


Figure 69 - Cycles To Failure Against Applied Stress Amplitude For Both Notched and Plain Specimen 18% Ni Maraging Steel, R=-1, K_t of Notch = 2.29 All Tests Conducted in Laboratory Air.

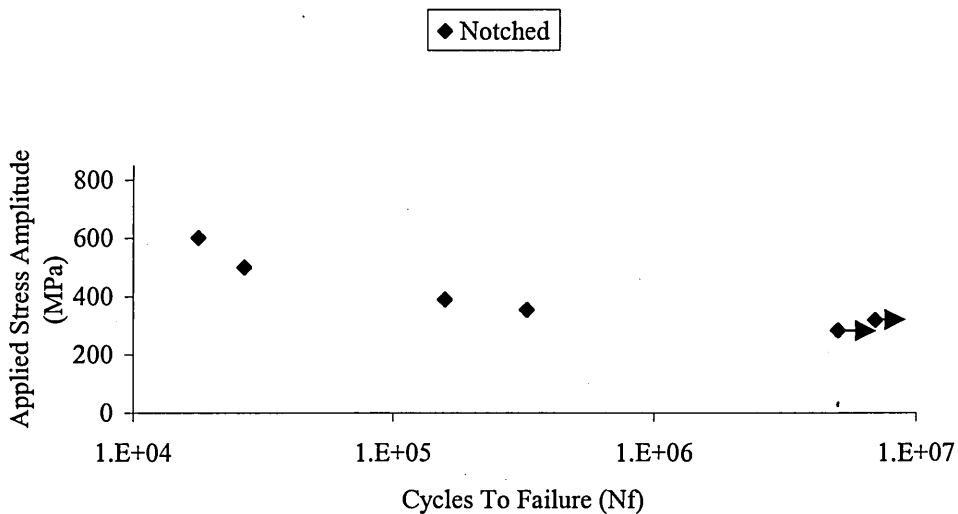


Figure 70 - Cycles To Failure Against Applied Stress Amplitude For Notched Specimen FV520B Peak Hardened FV520B, R=-1, K_t of Notch = 2.29 All Tests Conducted in Laboratory Air.

4.3.1 Corrosion Fatigue Test Results

The raw data from fatigue tests on notched and plain specimen conducted in various heated environments are given in, Table 11 and Table 12. The results for notched and plain specimen corrosion fatigue tests are presented on cycles to failure (N) against applied stress amplitude (S) graphs in Figure 69 to Figure 76.

Test No.	Specimen ID	Material	Stress Amplitude (MPa)	Environment	Potential (mV) _{Ag/AgCl} FCP = -120mV	Temp. °C	Frequency (Hz)	Cycles To Failure
CFtest 1	A1	FV520B	300	Deionised Water	FCP	50	2	10 ⁶ NF
CFtest 2	A2	FV520B	600	Deionised Water	FCP	50	2	9380
CFtest 3	A6	FV520B	300	Deionised Water	FCP	100	2	10 ⁶ NF
CFtest 4	A4	FV520B	600	Deionised Water	FCP	100	2	6010
CFtest 5	A5	FV520B	450	Deionised Water	FCP	100	2	9230
CFtest 6	A9	FV520B	300	0.3 % NaCl	FCP	100	2	332450
CFtest 7	A7	FV520B	300	0.3 % NaCl	FCP	100	2	10 ⁶ NF
CFtest 8	A10	FV520B	300	0.3 % NaCl	+200	100	2	32610
CFtest 9	A8	FV520B	150	0.3 % NaCl	+200	100	2	52580
CFtest 10	A11	FV520B	75	0.3 % NaCl	+200	100	2	211280
CFtest 11	A12	FV520B	300	0.3 % NaCl	-200	100	2	10 ⁶ NF
CFtest 14	A14	FV520B	600	0.3 % NaCl	-200	100	2	6460
CFtest 15	A15	FV520B	75	0.3 % NaCl	+200	100	0.5	29660
CFtest 16	A16	FV520B	300	0.3 % NaCl	+200	100	0.5	7810

CFtest 17	B1	FV520B	150	0.3 % NaCl	+200	100	2	77040
CFtest 18	B3	FV520B	300	0.3 % NaCl	FCP	100	2	10 ⁶ NF
CFtest 19	B4	FV520B	300	0.3 % NaCl	0	100	2	39390
CFtest 20	B5	FV520B	150	0.3 % NaCl	0	100	2	148120
CFtest 21	B6	FV520B	75	0.3 % NaCl	0	100	2	323310
CFtest 26	B11	FV520B	300	0.3 % NaCl +2.5 % CS(NH ₂) ²	-200	100	2	28180
CFtest45	C19	18 Ni Marageing	600	0.3%NaCl	FCP	100	2	3570
CFtest31	C1	18 Ni Marageing	300	0.3%NaCl	FCP	100	2	44280
CFtest44	C18	18 Ni Marageing	150	0.3%NaCl	FCP	100	2	10 ⁶ NF
CFtest 43	C17P	18 Ni Marageing	300	0.3%NaCl	FCP	100	2	203179
CFtest 32	C5P	18 Ni Marageing	400	0.3%NaCl	FCP	100	2	33608
CFtest40	C16P	18 Ni Marageing	150	0.3%NaCl	FCP	100	2	10 ⁶ NF

Table 11 - Corrosion Fatigue Test Results, For All Tests R = -1, Stresses Based on Minimum C.S.A. NF = No Failure

Test No.	Specimen ID	Stress Amp. (MPa)	Environment	Frequency (Hz)	N ₁	E ₁ (mV) _{Ag/AgCl}	N ₂	N ₃
CFtest 22	B7	400	0.3 % NaCl	2	0	200	90	14050
CFtest 23	B8	300	0.3 % NaCl	2	0	200	90	10 ⁶ NF
CFtest 24	B9	300	0.3 % NaCl	2	0	200	600	10 ⁶ NF
CFtest 25	B10	300	0.3 % NaCl	2	0	200	2400	5280
CFtest 37	B23	530	0.3 % NaCl	2	0	200	1800	65828
CFtest 38	B24	300	0.3 % NaCl	2	0	200	1800	10 ⁶ NF

Table 12 - Corrosion Fatigue Potential Pulse Test Results, All Tests R=-1, at 100°C, Stresses Based on Minimum C.S.A. NF = No Failure, All Specimens Notched
FV520B

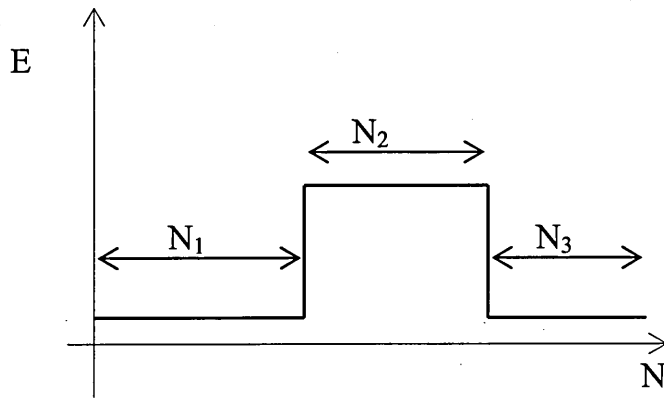


Figure 71 - Schematic showing Notation for Pulsed Potential Testing

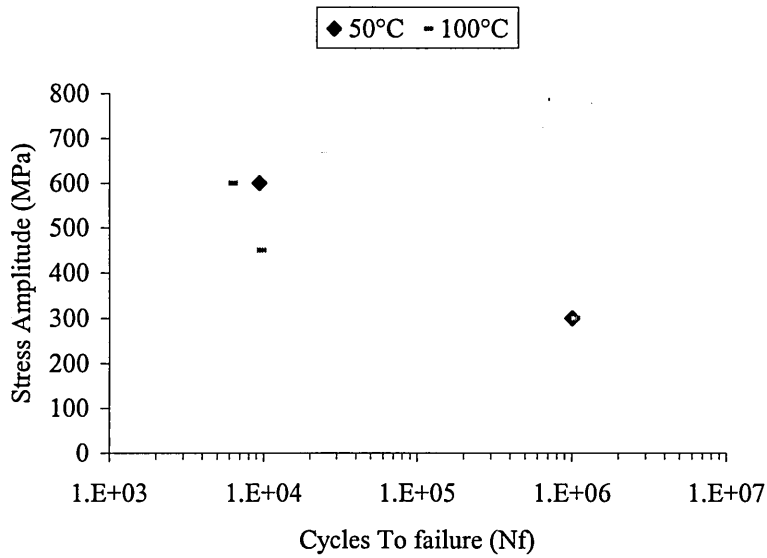


Figure 72 - Cycles To Failure Against Applied Stress Amplitude For Notched Specimen Peak Hardened FV520B-A, $R=-1$, K_t of Notch = 2.29 All Tests Conducted Within The Autoclave in Distilled Water at 2Hz.

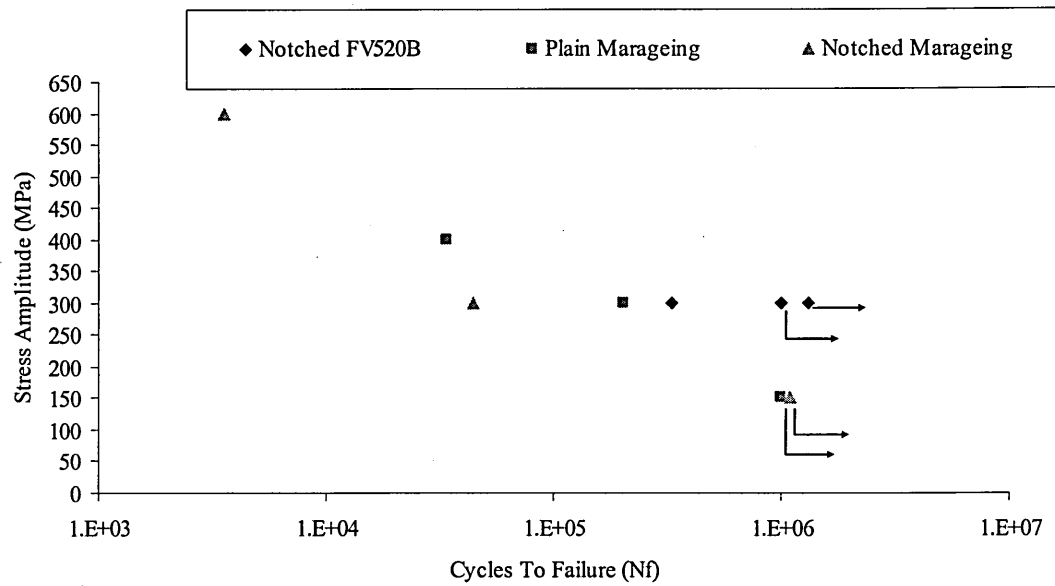


Figure 73 - Cycles To Failure Against Applied Stress Amplitude For Notched and Plain Specimen Peak Hardened FV520B-A and 18% Ni Marageing Steel, $R=-1$, K_t of Notch = 2.29. All Tests Conducted Within The Autoclave in 0.3% Sodium Chloride at 100°C at 2Hz.

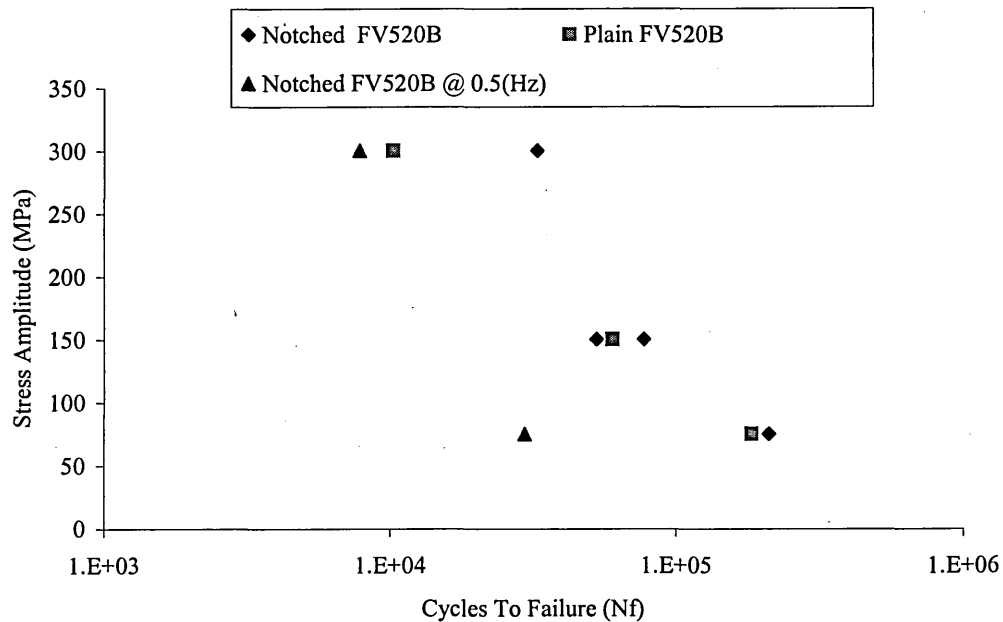


Figure 74 - Cycles To Failure Against Applied Stress Amplitude For Notched and Plain Specimen Peak Hardened FV520B-B and 18% Ni Maraging, R=-1, K_t of Notch = 2.29. All Tests Conducted Within The Autoclave in 0.3% Sodium Chloride at 100°C at +200(mV)_{Ag/AgCl}. All Tests at 2 (Hz) Unless Otherwise Stated.

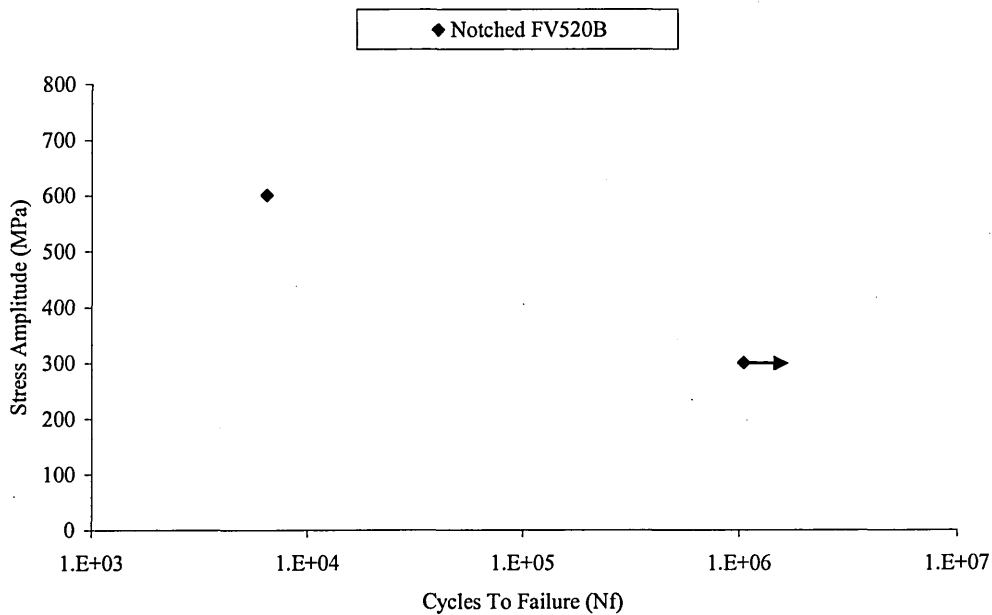


Figure 75 - Cycles To Failure Against Applied Stress Amplitude For Notched Specimen Peak Hardened FV520B-B, R=-1, K_t of Notch = 2.29. All Tests Conducted Within The Autoclave in 0.3% Sodium Chloride at 100°C at -200(mV)_{Ag/AgCl} at 2(Hz).

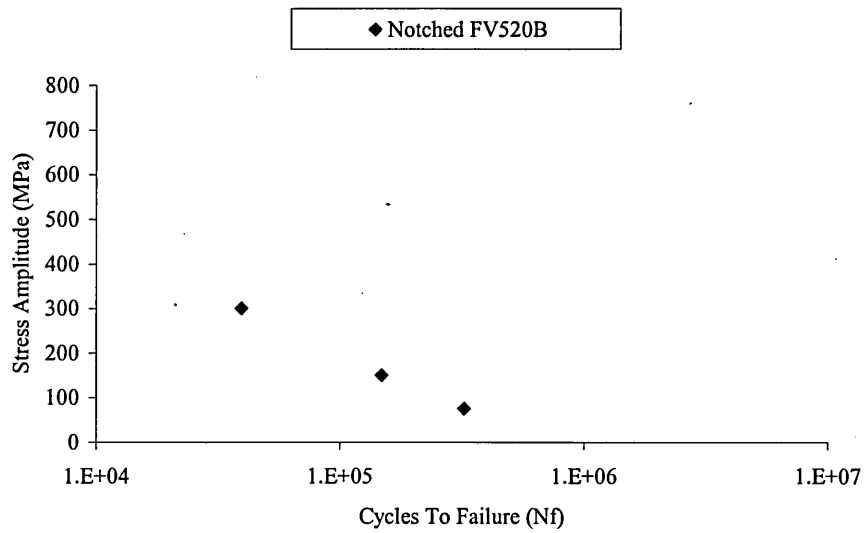


Figure 76 - Cycles To Failure Against Applied Stress Amplitude For Notched Specimen Peak Hardened FV520B-B, R=-1, K_t of Notch = 2.29. All Tests Conducted Within The Autoclave in 0.3% Sodium Chloride at 100°C at $-0(mV)_{Ag/AgCl}$ at 2(Hz)

4.3.2 Pulse Damage Corrosion Fatigue Test Results

The results from fatigue tests conducted in high temperature environments with pulsed electrochemical damage are presented on cycles to failure (N) against applied stress amplitude (S) graph in Figure 77. During these tests the specimens were lacquered such that only the notch was exposed thus concentrating any corrosion effects on the notch area. The raw data is given in Table 12, Figure 71 shows the notation used in Table 12.

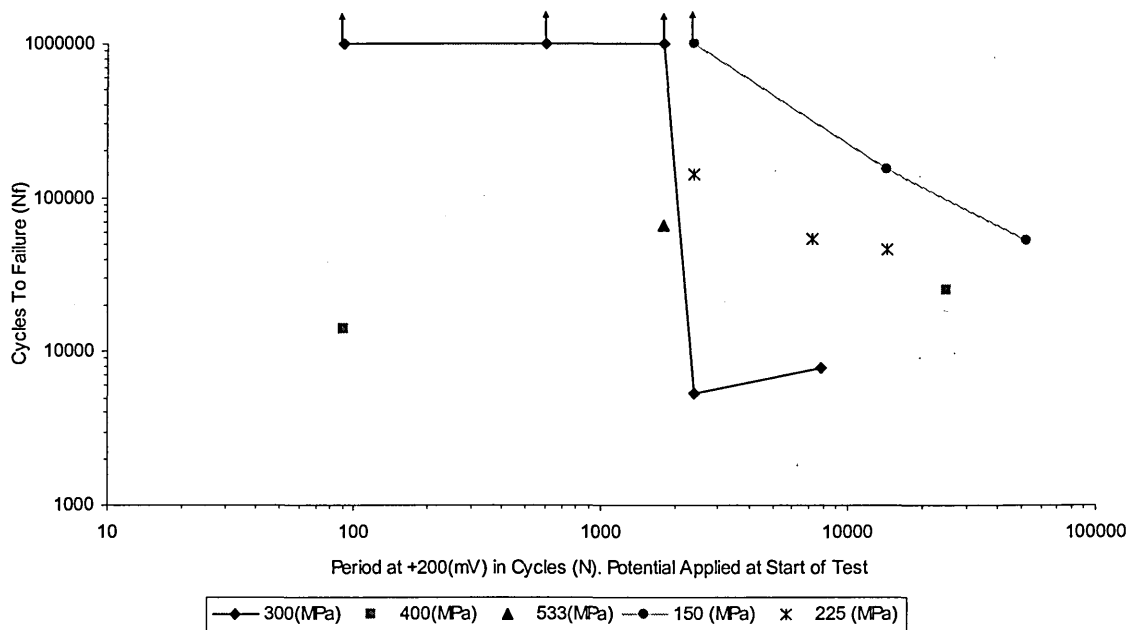


Figure 77 - Cycles To Failure Against Period at +200(mV)_{Ag/AgCl} in cycles. For Notched Specimen Peak Hardened FV520B-B, R=-1, K_t of Notch = 2.29. All Tests Conducted Within The Autoclave in 0.3% Sodium Chloride at 100°C at 2(Hz).

5 Discussion

5.1 Introduction

The aim of the following chapter is to discuss the influence of the microstructural features and the environment on the corrosion fatigue behaviour of the two steels tested. The effect of grain size on the air fatigue strength of the steels is modelled along with the influence of inclusion size. The size of pits was predicted using a model based on Faraday's law. The number of cycles to initiate a fatigue crack from the root of a corrosion pit is predicted considering the pit root radius. A linear elastic fracture mechanics type model is developed to predict the resultant life once a crack has initiated from a pit, for both notched and plain specimens, subjected to both constant corrosion and pulsed corrosion potentials. Electrochemical data from pulsed corrosion fatigue tests were used to develop an empirical model that predicts the effect of the number of start-ups and shut-downs on the fatigue life of a steam turbine blade.

5.2 Interpretation of Slow Strain Test Results

The slow strain rate tensile response of FV520B showed a significant dependence of temperature, see Figure 61. It has previously been noted that some maraging steels, known as TRIP steels, undergo a strain induced transformation whereby retained austenite is converted to martensite [139] (p18.) The current work is the first clear observation confirming that FV520B does show the TRIP effect.

Clark [5] used X-ray diffraction to show that FV520B in the softened overaged condition contains around 43% reverted austenite. This is due to the heat treatment required to produce large precipitates (2 hours at 620°C). The reverted austenite is metastable at room temperature in the sense that it transforms back to martensite during deformation [28]. The M_{d30} temperature [23] is the temperature at which 50% martensite is created for a plastic strain of 30%. There are empirical relationships to find M_{d30} , for example equation below [23].

Equation 35

$$M_{d30} \text{ } ^\circ\text{C} = 497 - 462(C + N) - 8.1(Mn) - 20(Ni) - 13.7(Cr) - 18.5(Mo) - 9.2(Si)$$

The M_{d30} is used as an approximation of the M_d temperature. M_d is the temperature above which strain induced transformation will no longer occur. Using Equation 35 a M_{d30} temperature of 140°C was calculated for FV520B. This compares well with the value of 150°C for M_d found empirically for an 18% Ni maraging steel by Markfield and Rosen [29].

It is the opinion of the author that the increase in elongation seen in the slow strain rate tests around room temperature is due to the strain induced transformation of the retained austenite in the softened overaged FV520B to martensite. From Figure 61 it can be seen that the level of elongation stabilised above 140°C, the M_{d30} temperature for FV520B. To add further credence to this hypothesis no temperature effect was seen in the slow strain rate testing of the peak hardened FV520B, see Figure 62. The peak hardened FV520B is heat treated for 4 hours at 450°C, a temperature insufficient to cause the martensite to revert to austenite. Clark [5] reported a 3% volume of reverted austenite in peak hardened FV520B, some 40% lower than in the softened overaged condition.

As further evidence of the phase transformation hardness tests were conducted on the failed specimen stubs. The hardness results are shown in Figure 78.

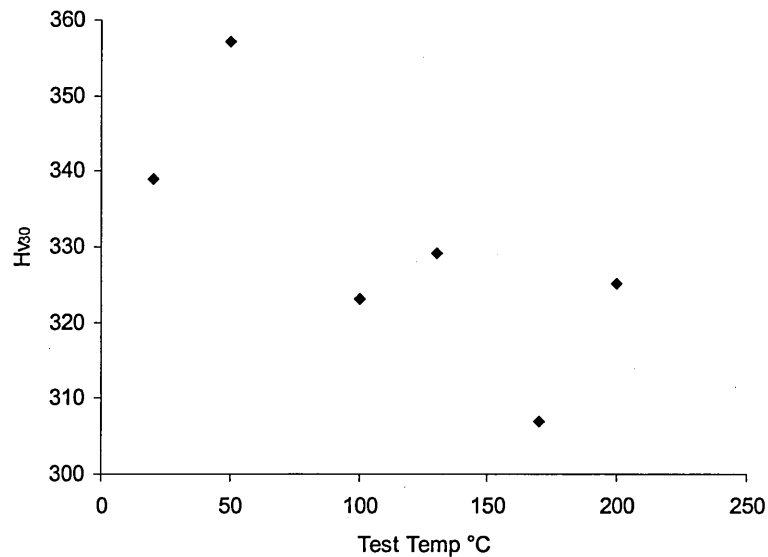


Figure 78 - Vickers Hardness Results For Slow Strain Rate Specimen Stubs

Figure 78 shows that the hardness of the plastically deformed specimens tested below 150°C was higher than that of those tested above 150°C. This would suggest that the harder material has indeed undergone a phase transformation to martensite due to the applied strain. This could be substantiated using X-ray diffraction techniques to assess the levels of austenite and martensite post plastic deformation.

5.3 Interpretation of Potentiodynamic

Electrochemical Test Results

There are fundamental differences in the way the two materials responded to potentiodynamic testing. These differences were considered to be a direct result of the composition of the steels. The two FV520B steels tested contained around 14% chromium thus making them stainless. A level of chromium above 11% is considered to give the steel a strong passive layer of chromium oxide and for corrosion to take place this layer must be compromised in some way. As shown in Figure 65, there is a clear point where the current density increases rapidly, the level of current density is an indication of the amount of corrosion taking place. The point where the current density increases rapidly corresponds to the breakdown of the passive layer and the corresponding potential is known as the critical pitting potential. However, 18% Ni maraging steel contains very little chromium and therefore has no passive layer. Hence there is no critical pitting potential for this material and the current density increases at a more constant rate.

5.4 Effect of Microstructure on Air Fatigue

Behaviour

It is generally accepted that the resistance of a metal to plastic deformation increases as the grain size decreases [45], thus it would not be unreasonable to expect that the cyclic stress to cause continued slip would also increase with decreasing grain size. Conventional indicators of a materials resistance to plastic deformation are hardness and yield stress. Several empirical relationships between hardness or yield stress and fatigue strength have been proposed [40,49]. There is no significant difference in the hardness or the yield stress values of the 18% Ni maraging and the FV520B steel. Yet there is a significant difference in the grain sizes and the plain air fatigue strength of the two steels, Figure 79 and Figure 80 show the typical microstructures of 18% Ni maraging and FV520B steels respectively. When compared one can easily see that the FV520B has a much finer microstructure than the maraging steel.

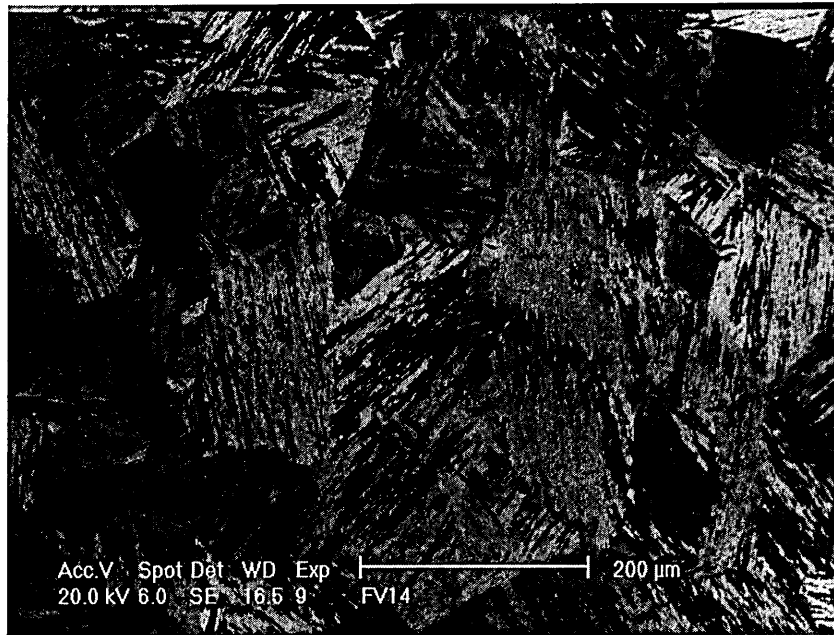


Figure 79 - Microstructure of Maraging Steel (Etched With 2% Picral)

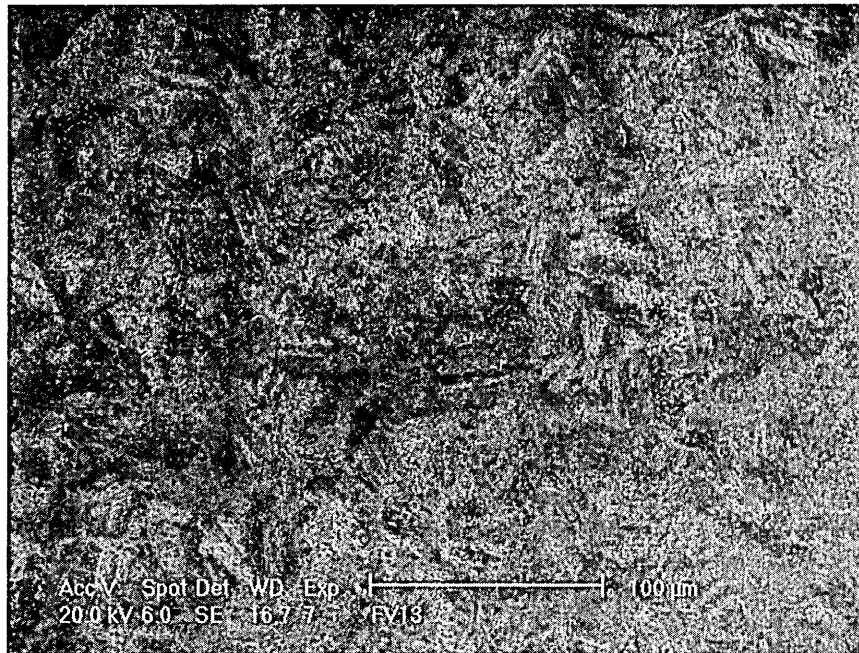


Figure 80 - Microstructure of FV520B Peak Hardened (Etched With 2% Picral)

Apart from the effect of grain size on the resistance to plastic deformation, the grain size could influence the transition from a microcrack to a macrocrack as previously

discussed in the literature review (p29). Once a fatigue crack is initiated fatigue life can be divided into two distinct phases, namely;

Stage I - the number of cycles to develop a microcrack to the point where transition occurs to a macrocrack growth mechanism

Stage II - the subsequent number of cycles to grow the macrocrack to failure.

As the grain size increases the number of boundaries crossed by a microcrack will decrease. If a microcrack reaches a grain boundary it may be retarded or accelerated as the slip characteristics of the next grain could be different. This means that the grain size of a material will effect microcrack growth and hence fatigue life. The graph in Figure 81 shows the relationship between grain size and fatigue limit for the 18% Ni maraging steel and FV520B-B steels, along with, the data for a low carbon steel taken from Taira et al [47]. All specimens were plain and tested in air. Clark [5] reported the grain size of FV520B in the peak hardened condition as 14 (μm).

Estimation of the grain size of the 18% Ni maraging steel from Figure 79 resulted in a value of 120 (μm).

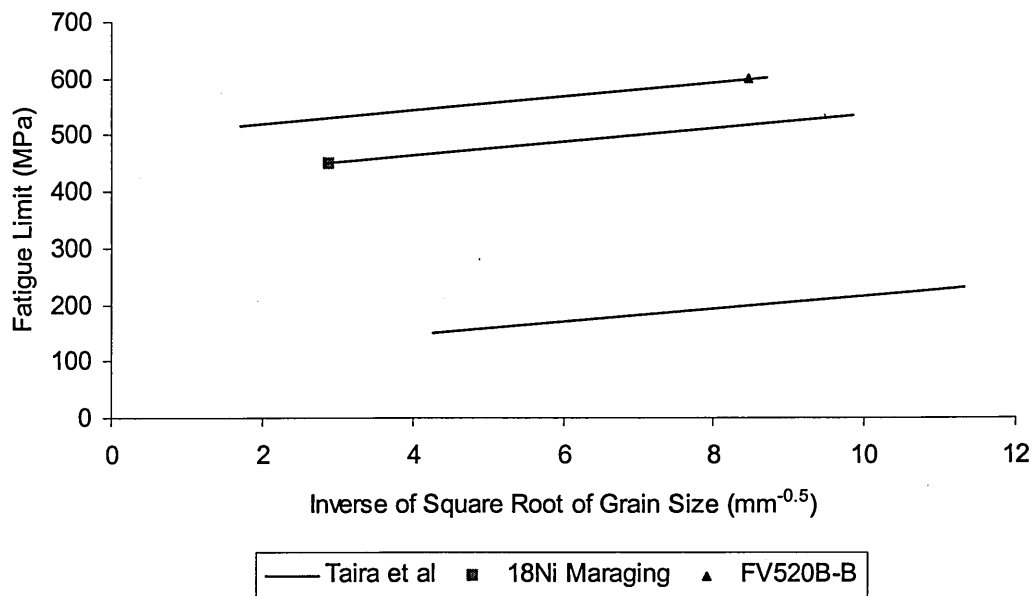


Figure 81 - Fatigue Limit Verses Inverse Root of Grain Size. Taira et al Data for a low Carbon Steel.

The lines in Figure 81 were calculated with the assumption that the 18Ni maraging steel and FV520B have the same gradient as the low carbon steel used by Taira et al [47]. The work conducted by Taira et al [47] shows there is a grain size dependence in the fatigue response of materials. This dependence is seen in the current work. It is suggested that the difference in the 18Ni maraging and FV520B lines is due to the difference in the number and size of non-metallic inclusions in the two materials.

5.4.1 The Effects of Non-Metallic Inclusion on Air Fatigue Strength

There is a difference in the number and size of non-metallic inclusions in the 18% Ni maraging and FV520B steels, as shown in Figure 67. Several equations have been proposed to account for the effect of inclusion size on the fatigue strength of a metal. Murakami et al [71] suggested the following relationship,

$$\sigma_w \cong \frac{1.43Hv + 120}{(\sqrt{area})^{\frac{1}{2}}} \quad \text{For a surface inclusion}$$

Where Hv is the Vickers hardness value, the area is the projected area of the inclusion and σ_w is the fatigue limit. Using the above equation the fatigue strengths shown in Table 13 were calculated.

Steel	Inclusion Area μm^2	Hv	Calculated Fatigue Strength (MPa)	Experimental Fatigue Limit In Air(MPa)
FV520B	110-130	410	$\pm 210-225$	± 600
Marageing	160-180	410	$\pm 190-200$	± 450

Table 13 - Calculated and Experimental Fatigue Limits Based on Inclusion Area

The difference in the two calculated fatigue limits compares well with the difference due to inclusions of 33 (MPa) suggested by Figure 81. The relationship proposed by Murakami et al [71] is relatively insensitive to the microstructure of the steel, unless the microstructure has an effect on the hardness of the metal.

Other authors have used inclusion length to assess the deleterious effect of non-metallic inclusions on the fatigue limit. Frost [68] proposed Equation 36 that was later used with success by Congleton and Wilks [69] when investigating the fatigue strength of a 13% Cr turbine blade material.

Equation 36

$$515 = F^3 l$$

where, F is the fatigue limit (MPa) and l is the inclusion length in meters.

Results predicted using the above equation are plotted in Figure 82. Using Equation 36 values of 1222.6 and 2462.8 were found for the constant (F) when fitting the 18% Ni maraging and the FV520B-B steels respectively.

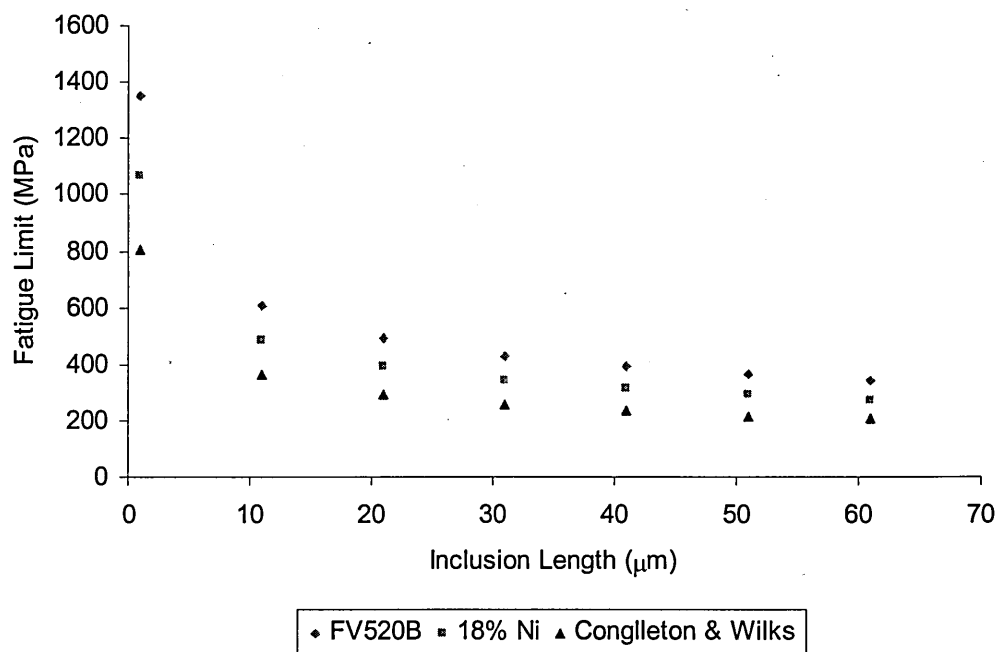


Figure 82 - Calculated and Experimental Values of Fatigue Limit Versus Inclusion Size.

There is a difference in the fatigue lives for the 13% Cr turbine blade steel tested by Congleton and Wilks [69] and the similar FV520B steel. The reason for this difference is that the tests conducted by Congleton and Wilks were carried out in a condensing steam environment at a frequency of 0.016(Hz). The combined effect of an aggressive environment and non-metallic inclusions can have a deleterious effect on the fatigue life of a steel (p68). It can be seen from Figure 66 (p.141) that the inclusion sizes seen in the steels used in this work are relatively similar, however, there is a difference in the fatigue limits in air. The difference in the air fatigue limits may be a result of microstructural features other than the inclusion size. It is true that

the 18% Ni marageing steel is more notch sensitive, meaning that for inclusions of, the same size a greater reduction in fatigue strength would be seen in the 18% Ni marageing steel. When coupled with the fact that larger inclusions where found in the marageing steel it can be understood that the marageing steel suffers more in terms of fatigue strength reduction due to the presence of inclusions than FV520B.

5.4.2 Air Fatigue Notch Response

5.4.2.1 Calculation of Notch Fatigue Response Based on Plain Fatigue Data

There are several empirically based models that are used to assess notched fatigue strength based on plain data, these models are used to reduce the need for expensive testing. The simplest approach is the theoretical stress concentration factor (K_t), K_t is an elastic parameter solely dependant on geometry and mode of loading.

Shown below are simple stress calculations based on a load of 2000(N) over the nominal area of the specimen

$$\text{Force} = 2000 \text{ (N)}$$

$$\text{Area} = 1.256 \times 10^5 \text{ (m}^2\text{)}$$

$$\text{Stress} = \frac{\text{Force}}{\text{Area}} = \frac{2000}{1.256 \times 10^5}$$

$$\text{Stress} = 160 \text{ (MN/m}^2\text{)}$$

From the FEA model it was found that when a force of 2000(N) was applied to the mesh a stress of 367(MN/m²) occurred at the notch root, see Figure 68.

Equation 37

$$K_t = \frac{\sigma_{\max}}{\sigma_{\text{nom}}} = \frac{367}{160}$$

$$K_t = 2.29$$

The fatigue notch factor is the ratio between the fatigue strength of a plain component and a notched component at a given life and therefore does take into account the material effects, see Equation 38.

Equation 38

$$K_f = \frac{\sigma_{(unnotched)}}{\sigma_{(notched)}}$$

Peterson proposed a relationship to calculate the fatigue notch factor (K_f) based on (K_t), [140] see Equation 39

Equation 39

$$K_f = 1 + \frac{K_t - 1}{\left(1 + \frac{a}{(r \times 39.37)}\right)}$$

where, a is a material constant and r is the notch root radius in meters. The constant 'a' depends on material strength and ductility. Petersons constant 'a' can be estimated for steels in a number of conditions using Figure 83.

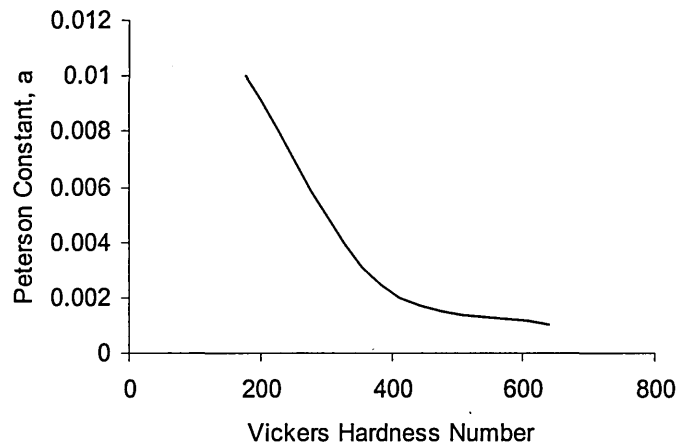


Figure 83 - Peterson Constant (a) Versus Vickers Hardness Number 40.

Using Equation 39 and getting a value for a of 0.0021 from Figure 83 based on a Vickers hardness number of 410 (Hv) a fatigue notch factor of 2.21 was calculated for the notch used. Figure 84 and Figure 85 shows S-N curves for experimental plain

specimens, calculated notch specimens, and experimental notch results for FV520B and 18Ni maraging steels respectively.

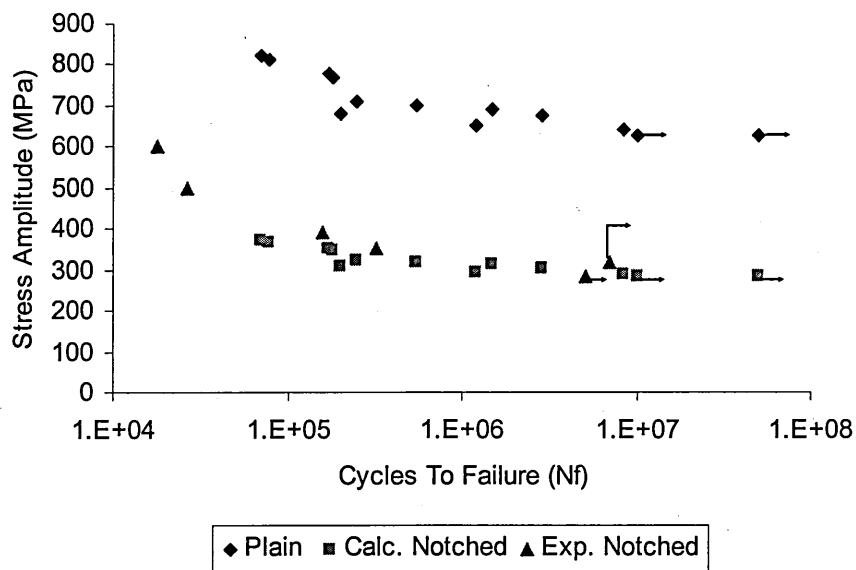


Figure 84 - Graph To Show Plain Fatigue Data for FV520B Plotted With Calculated Notched Data.

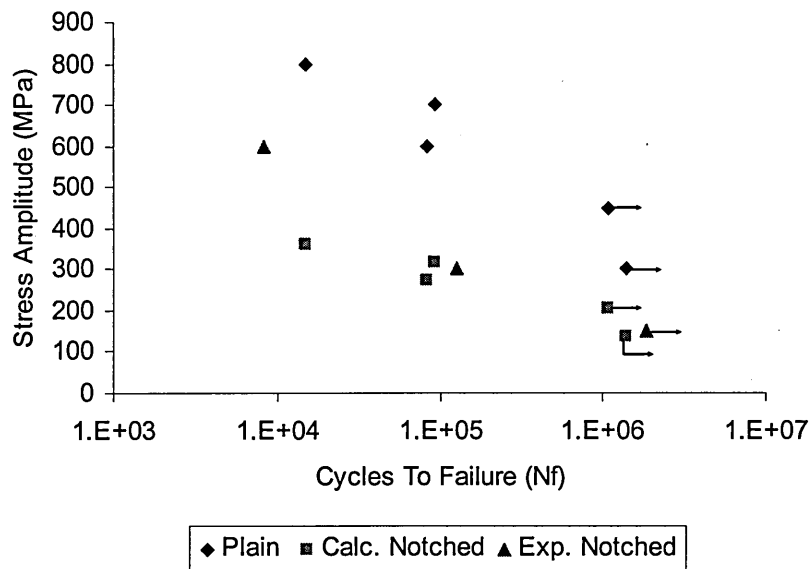


Figure 85 - Graph To Show Plain Fatigue Data for 18Ni Maraging Steel Plotted With Calculated Notched Data

Figure 84 and Figure 85 show a good correlation between the values calculated using the Peterson equation and the actual experimental results of both steels.

5.4.2.2 Calculation of Notch Sensitivity

Clark [5] conducted work looking into the fatigue mechanisms of plain specimen FV520B. Figure 86 shows experimental air fatigue data for plain and notched peak hardened FV520B with fitted curves.

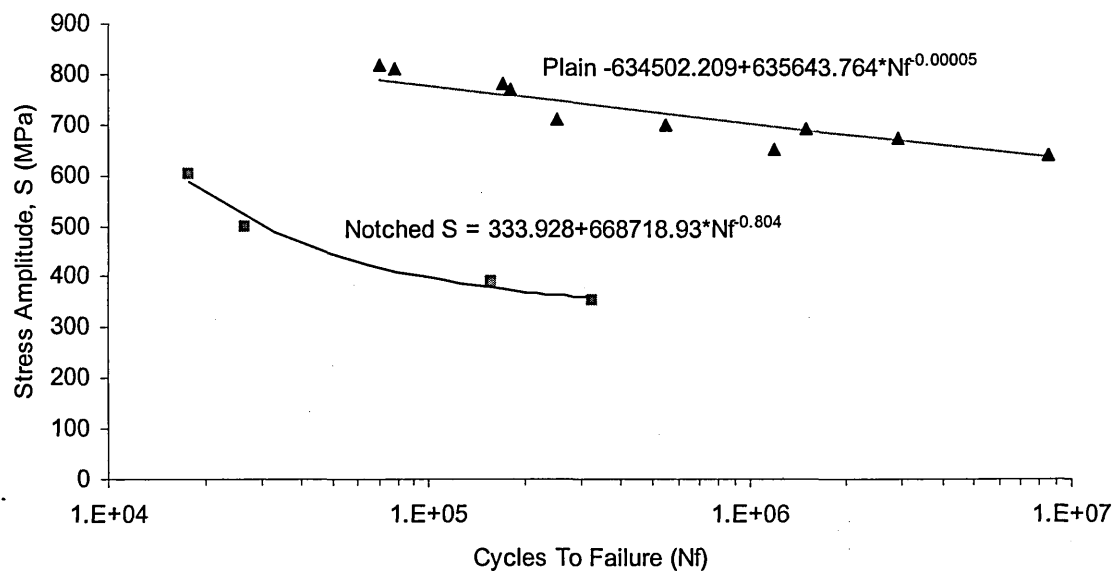


Figure 86 - Cycles To Failure Versus Stress Amplitude For Peak Hardened FV520B.

Figure 87 contains notched and plain air fatigue data for the 18% Ni maraging steel.

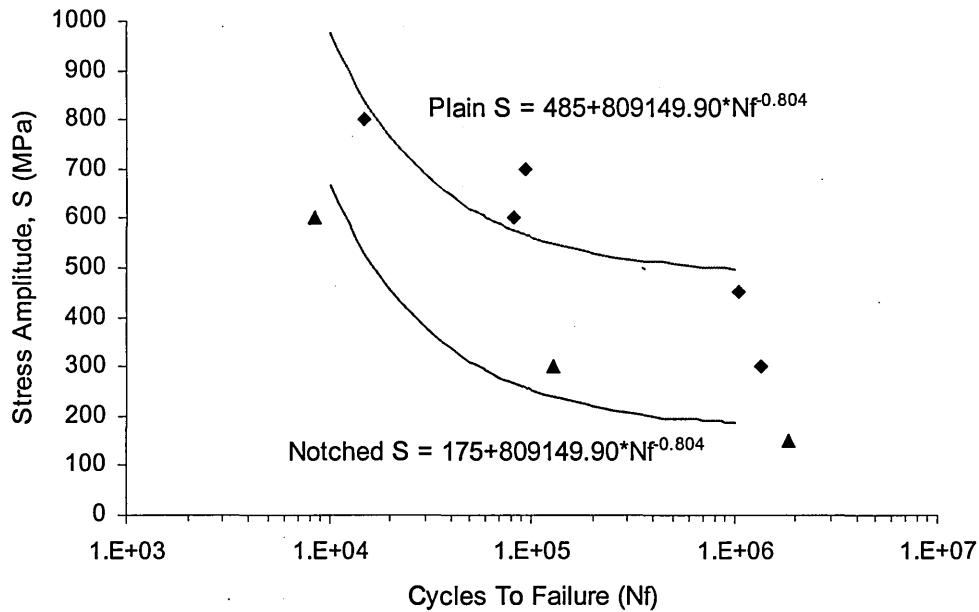


Figure 87 - Cycles To Failure Versus Stress Amplitude For 18% Ni Maraging Steel

Using the equations given in Figure 86 and Figure 87 values of (K_f) were calculated for both the FV520B and the 18% Ni maraging steel, see Figure 88.

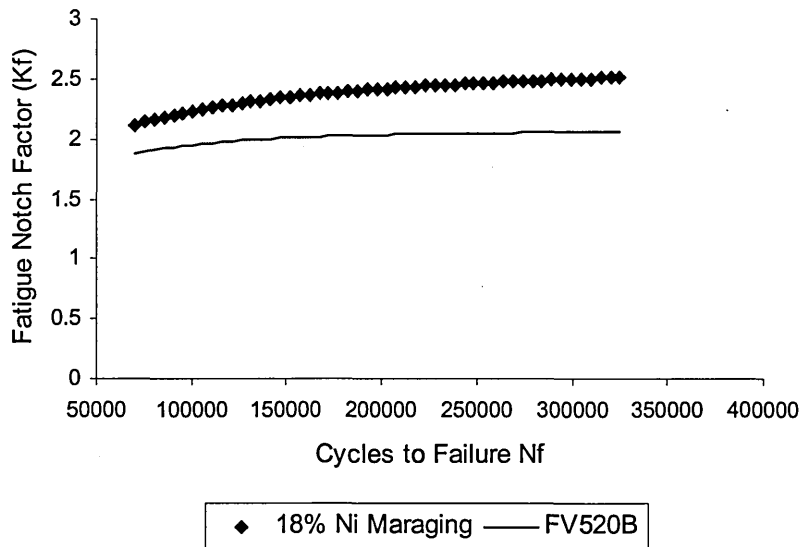


Figure 88 - Fatigue Notch Factor Versus Cycles To Failure For FV520B and 18% Ni Maraging Steel

The Notch Sensitivity Factor (q) is used to define how sensitive a material is to notches.

Equation 40

$$q = \frac{K_f - 1}{K_t - 1}$$

the values of q calculated from the experimental results are plotted as a function of cycles to failure in Figure 89.

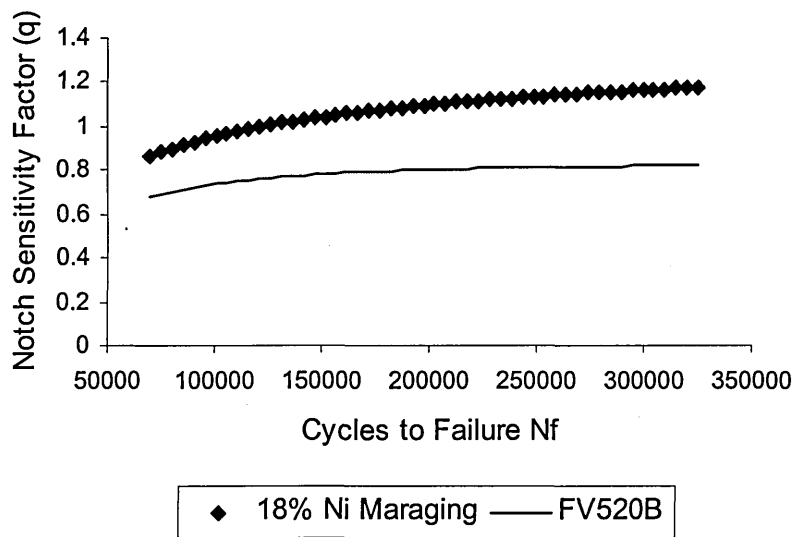


Figure 89 - Notch Sensitivity Factor Versus Cycles To Failure For FV520B and 18% Ni Maraging Steel.

It can be seen from Figure 89 that values of q greater than one were calculated, however q can only range from zero, where there is no notch effect ($(K_f) = 1$) to 1 where there is full notch effect ($(K_f) = (K_t)$). Values of q greater than one are due to rounding/extrapolation during calculation.

From notched and plain specimen air fatigue testing of both the maraging and the FV520B steel it appears the maraging is more sensitive to the presence of a geometrical notch. This increased sensitivity to notches is evident from the higher notch fatigue and sensitivity factors.

The increased notched sensitivity seen in the maraging steel is felt to be due to the presence of a greater number of larger non-metallic inclusions when compared to the precipitation hardened steel. The greater the number of inclusions the more likely that one of the inclusions will be in or around the notch root and hence have a detrimental effect on the fatigue strength of the steel. Having larger grains will also make a steel more likely to fail due to the presence of a notch. The fatigue strength of a material should not be thought of as the stress level below which cracks will not initiate but rather the stress level below which a crack will initiate and grow as a microcrack but fail to grow and reach the crossover length from microcrack to macrocrack. The presence of a notch will increase the chance of a microcrack initiating and growing to the crossover length required for growth as a macrocrack. As previously discussed in the literature review (see p39) a notch aids crack initiation and growth by providing an area of plasticity at the notch root. Cracks will initiate and grow readily in the plastic zone associated with the notch root however once they grow beyond the plastic zone if they have not reached a size whereby they are able to produce a large enough plastic zone of their own to facilitate further crack growth they will arrest and therefore fail to propagate. If a crack reaches the edge of the plastic zone caused by the presence of the notch, the path of the crack and hence its own plastic zone may be blocked by a grain boundary thus preventing growth and transition into a macrocrack. The larger the grains in a material the greater the chance that a crack will be able to reach and pass the macrocrack length after growth within

the notch plastic zone. These effects account for the greater notch sensitivity seen in the maraging steel. It is also true that the larger the grain size the larger the plastic zone associated with the notch. Grain boundaries act as a barrier to plasticity as the slip system in one grain may well differ considerably from that of the adjacent grain.

5.4.2.3 Calculation of Air Fatigue Crack Growth Rate for 18Ni Maraging Steel

Under air fatigue conditions the 18% Ni maraging steel exhibited concentric fatigue striations close to the point of final brittle fracture. Figure 90, Figure 91 and Figure 92 show the striations at increasing magnifications. By measuring the distance between striations it is possible to determine the fatigue crack growth rate just prior to brittle fracture.

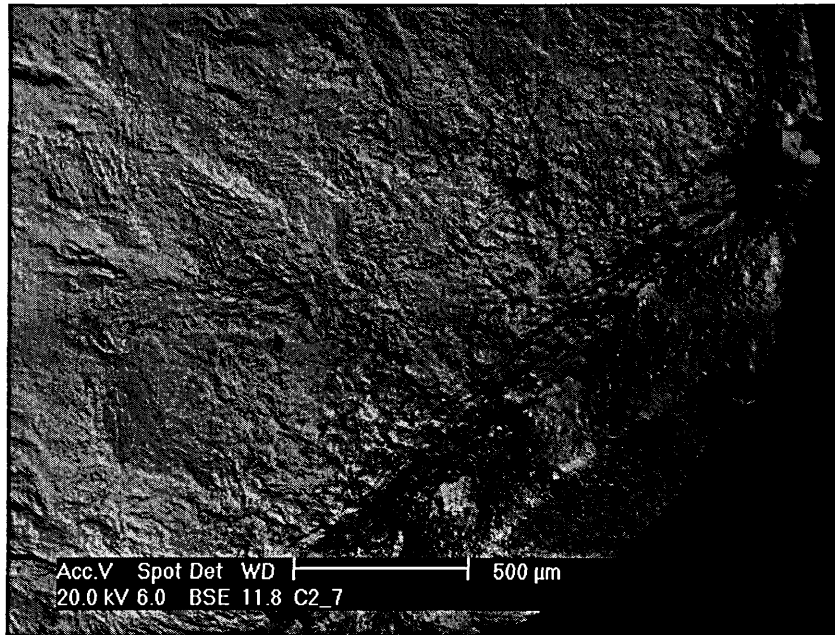


Figure 90 - Fracture Surface of 18% Ni Maraging Steel Tested in Air at ± 300 (MPa), 7(Hz), $N_f = 127080$

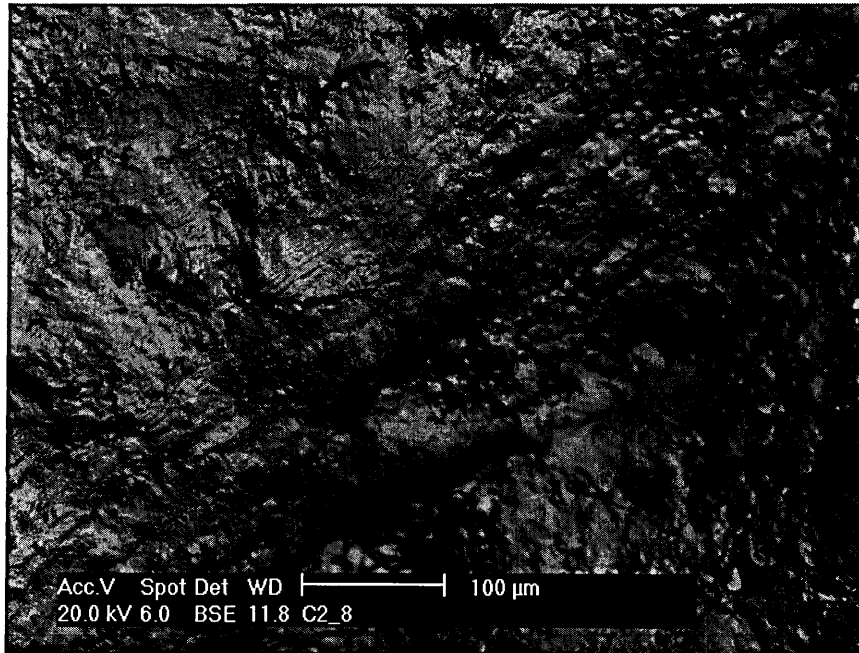
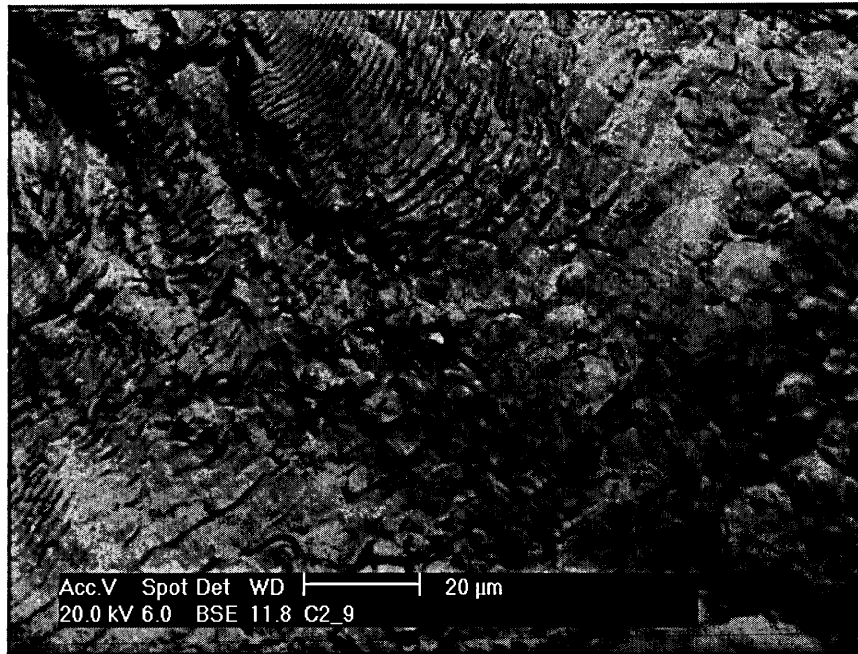


Figure 91 - Fracture Surface of 18% Ni Maraging Steel Tested in Air at ± 300 (MPa), 7(Hz), $N_f = 127080$. Showing Striations



Fast

Fracture

Figure 92 - Fracture Surface of 18% Ni Maraging Steel Tested in Air at ± 300 (MPa), 7(Hz), $N_f = 127080$. Showing Striations.

From the higher magnification image shown above the fatigue crack growth rate just prior to brittle fracture is around 6 ($\mu\text{m}/\text{cycle}$).

No such features were evident on the fracture surfaces of the peak hardened FV520B specimen. Figure 93 shows a typical fracture surface from a failed peak hardened FV520B specimen tested in laboratory air.

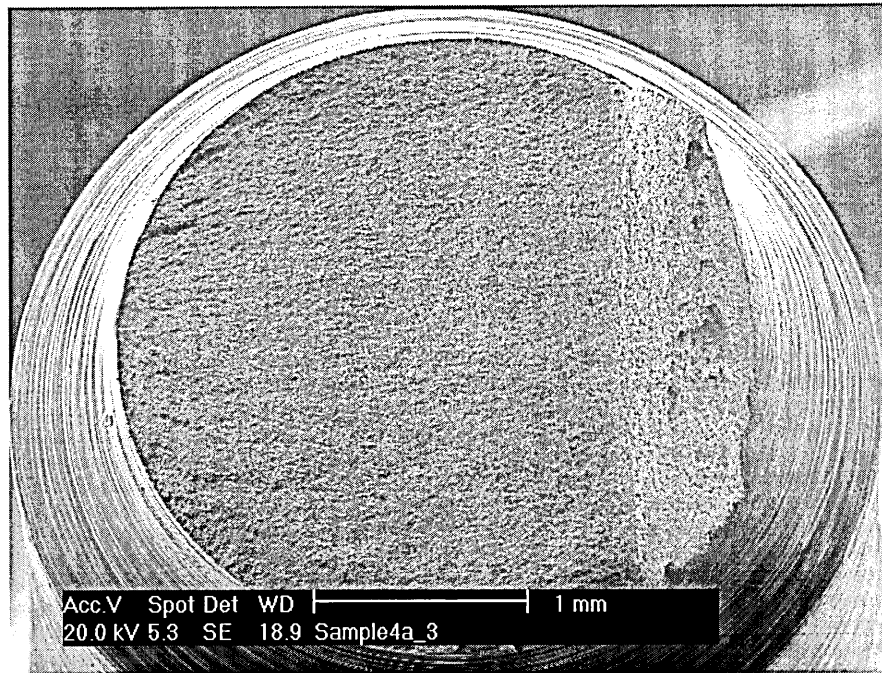


**Figure 93 - Typical Fracture Surface from Failed Peak Hardened FV520B Fatigue Specimen
Tested in Laboratory Air (20°C) ± 390 (MPa) $N_f = 158090$.**

5.5 Corrosion Fatigue

5.5.1 Role of Environment

When tested in deionised water and in a 0.3% sodium chloride solution at 100°C and 50°C at free corrosion potential the FV520B showed no environmental effect, see Figure 97. However, the maraging steel showed a definite environmental effect.

There appears to be very little difference in the life in cycles to failure for the notched maraging steel in laboratory air and in the 0.3% sodium chloride solution, this may at first suggest that the environment has little or no effect on the life of a notched maraging steel specimen. However, when one considers the life in cycles to failure of the plain maraging steel in both air and in the 0.3% sodium chloride solution there is a clear reduction in life associated with the more aggressive environment.

Figure 94 shows the life in cycles to failure for maraging notched and plain specimens in both laboratory air and 0.3% sodium chloride solution.

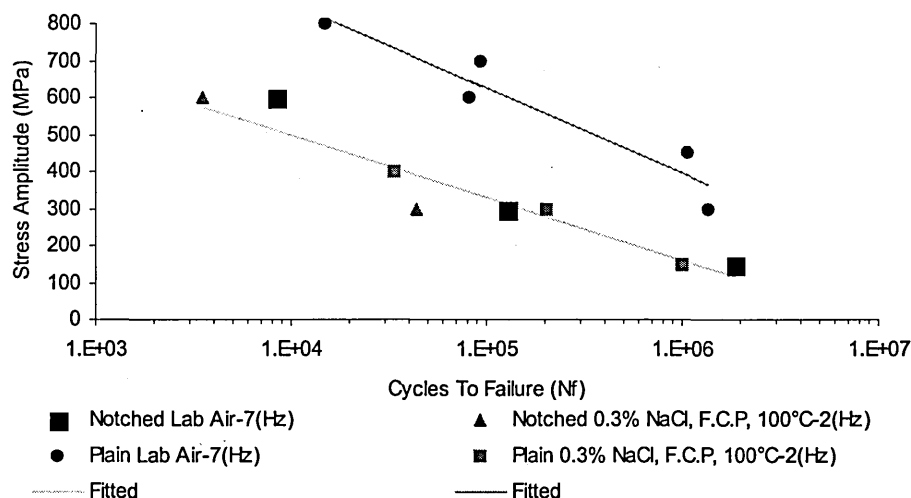


Figure 94 - Stress Amplitude Versus Cycles To Failure For Plain and Notched Maraging Steel

Figure 94 suggests that the notch has no effect, that is, the effect of the environment combined with the applied cyclic load (corrosion fatigue) is greater than any notch

effect. If a specimen with a different K_t were to be tested in air it would fall on a different curve. Figure 94 implies that if the different notch was tested in the aggressive environment it would fall on the same curve as the other specimens tested. Therefore it is simply coincidence that the effect of the notch should be similar to that of the aggressive environment.

Equally if one were to change the environment the curve for the plain and notched specimen tests in the sodium chloride solution would move relative to the air notched specimen curves.

The plain specimen managing fatigue tests in both air and sodium chloride solution compare well with those found in the literature [33], shown in Figure 95. In the work of Cottis and Husain [33] an environmental effect was only seen at longer lives ($N_f > 100000$), with only a negligible effect of environment being observed in high stress low life scenarios. This was not the case for the testing detailed in this thesis.

5.5.2 Effect of Temperature

Cottis and Husain [33] conducted tests at laboratory temperature (approx. 25°C) while the author's testing was conducted at 100°C. The raised temperature would have the effect of reducing the activation energy required for corrosion to take place and would increase corrosion rates. The two sets of environmental tests were also conducted at different sodium chloride concentrations, with Cottis and Husain [33] using a 3.5% sodium chloride solution and the author using a 0.3% chloride solution. The results shown in Figure 95 would suggest that the life of the specimen is relatively unaffected by chloride concentration within limits, as at longer lives there is little difference between the 3.5% and 0.3% sodium chloride solution lives.

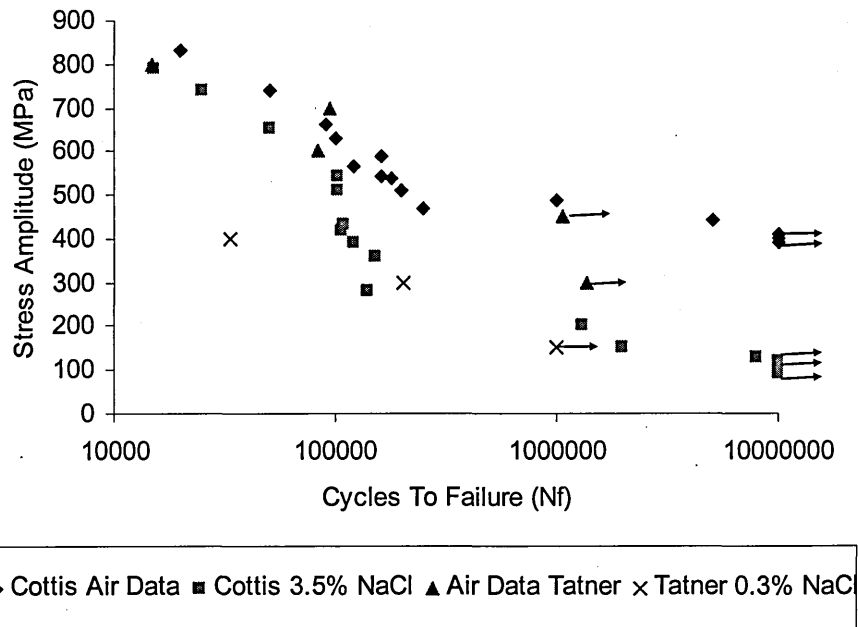


Figure 95 - Stress Amplitude Versus Cycles To Failure Data for Plain 18 Ni Maraging Steel, Cottis Data @ 14(Hz) Laboratory Temperature, Tatner Data @ 2(Hz) 100°C

When considering the effect of 0.3% sodium chloride and deionised water on the FV520B steel it is clear from visual examination that no corrosion had taken place. All the maraging steel specimens tested in 0.3% sodium chloride solution showed very clear evidence of general corrosion, see Figure 96. From Figure 97 it can be seen that the environments used had no significant effect on the FV520B steel, with the notched air specimen failing at similar lives as the notched environment specimen when fatigued at the same stress level. If the environment caused a reduction similar to the notch as was the case with the maraging steel one would expect to see

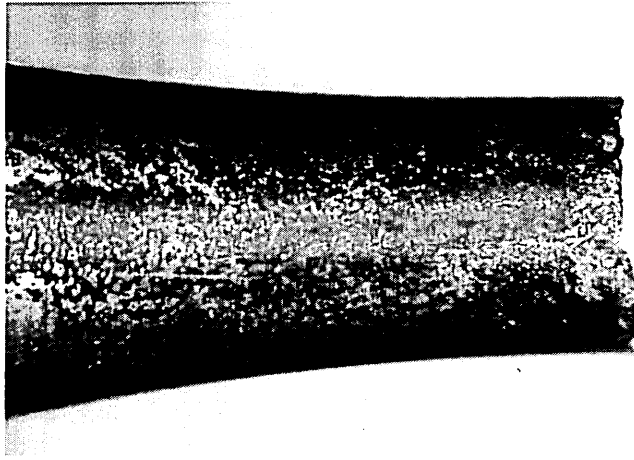


Figure 96 - View of A Fractured Plain Maraging Steel Specimen Showing General Corrosion. Tested At ± 300 (MPa), $R=-1, 2$ (Hz), in 0.3% NaCl at FCP at 100°C, $N_f = 33608$.

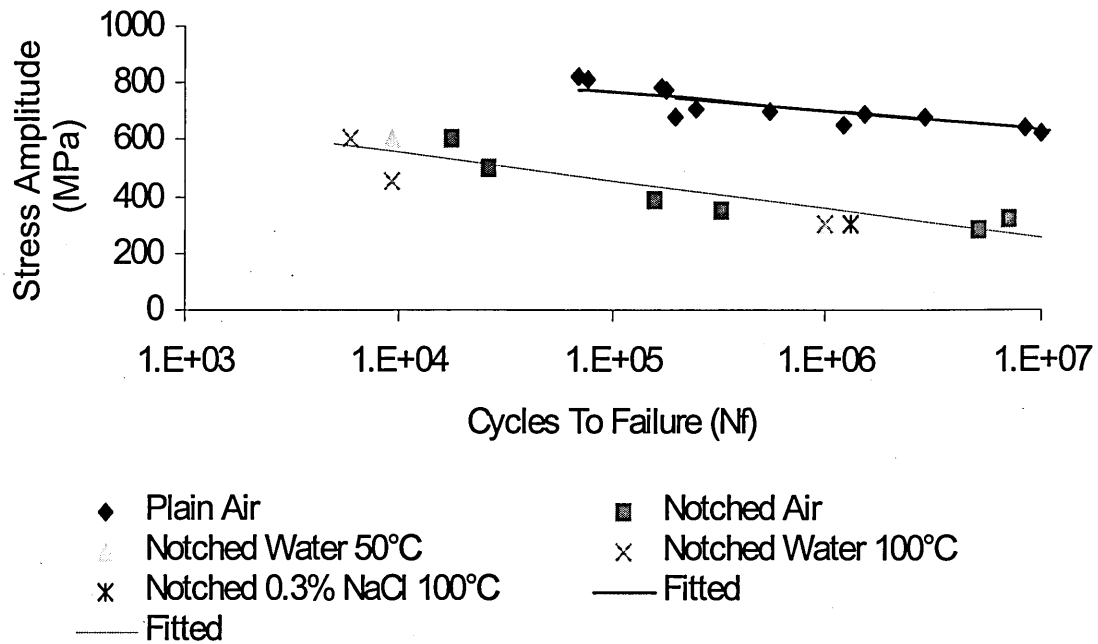


Figure 97 - Cycles To Failure Versus Stress Amplitude For Notched and Plain FV520B In Air , Water And 0.3%NaCl.

evidence of corrosion on the surface of the failed specimen, however, this is not the case as can be seen from Figure 98.

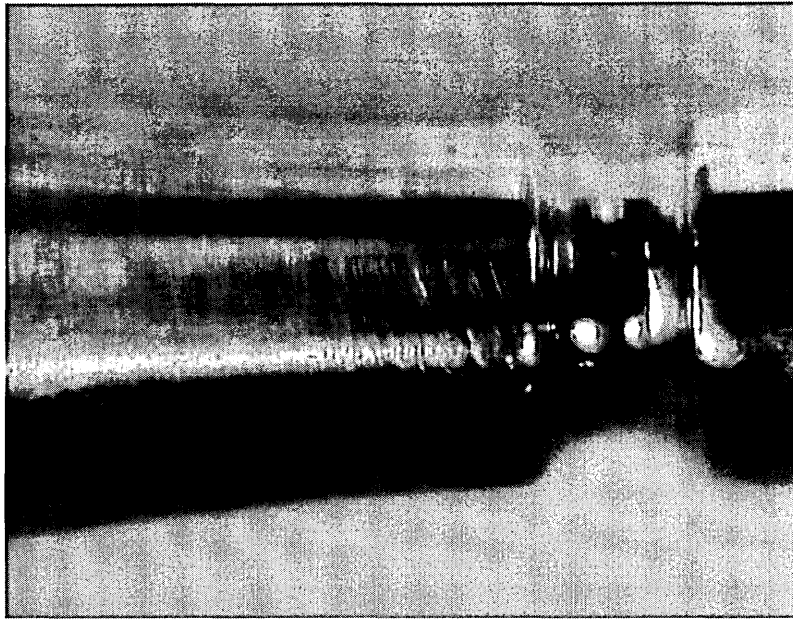


Figure 98 - View of A Fractured Notched FV520B Steel Specimen Showing No General Corrosion. Tested At ± 300 (MPa), $R=-1, 2$ (Hz), in 0.3% NaCl at FCP at 100°C , Tested for 10^6 Cycles No Failure.

Notched testing of FV520B was conducted in three environments. If there had been an environmental effect in the failures one would expect a variation in the number of cycles to failure across the spectrum of environments tested, this was not the case, see Figure 97.

The differences in the compositions of the two steels tested further justify the above hypothesis. FV520B contains 13-14% chromium thus making it a stainless steel that will remain protected by a passive layer even in relatively aggressive environments.

The 18% Ni maraging steels contain 0.02%Cr and are known for their lack of corrosion resistance and the requirement for some form of corrosion protection to be used in most applications [18,20].

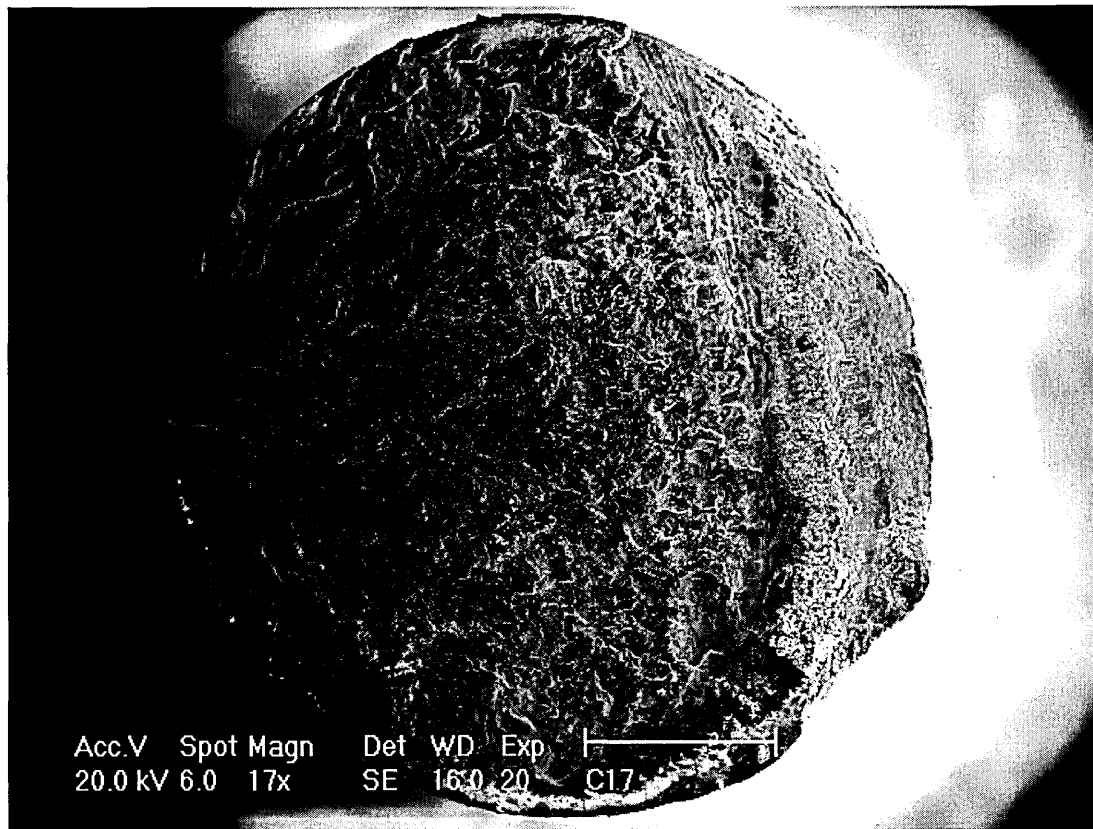


Figure 99 - Fracture Surface of a Plain Maraging Specimen Subjected to ± 300 (MPa) in 100°C 0.3% NaCl at FCP.

5.5.3 Imposed Potential Corrosion Fatigue Behaviour

Corrosion fatigue tests were conducted with peak hardened FV520B notched specimens at $+200(\text{mV})_{\text{Ag}/\text{AgCl}}$, $0(\text{mV})_{\text{Ag}/\text{AgCl}}$ and $-200(\text{mV})_{\text{Ag}/\text{AgCl}}$ imposed potentials, Figure 100 shows the results of the corrosion fatigue tests.

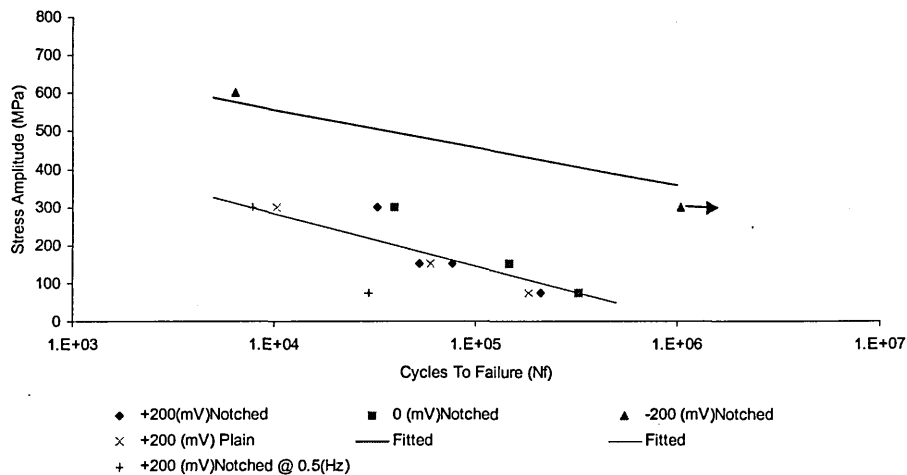


Figure 100 - Cycles To Failure Versus Stress Amplitude For Notched And Plain Specimen Precipitation Hardening Peak Hardened FV520B Tested In 0.3% NaCl Solution At Various Values of Applied Potential ($_{\text{Ag}/\text{AgCl}}$), All Tests conducted At 2 (Hz) unless stated, 100°C.

It is clear from Figure 100 that the applied potential of $-200(\text{mV})_{\text{Ag}/\text{AgCl}}$ had no effect on the period to failure for the steel tested with the same life in cycles being observed for $-200(\text{mV})_{\text{Ag}/\text{AgCl}}$ as for in air, see Figure 97. However the application of an anodic polarisation potential of either $+200$ or $0(\text{mV})_{\text{Ag}/\text{AgCl}}$ has a significant effect on the corrosion fatigue performance of the steel with a complete loss of the fatigue limit occurring. Changing the test frequency appears to change the response, e.g. altering the effect of the applied potential by reducing the load frequency is evident when one considers the data from tests conducted at a load frequency of 0.5 (Hz). At 0.5(Hz) the specimen is subjected to corrosion for a longer time period for the same number of cycles when compared to the tests conducted at 2(Hz). This effect can clearly be

seen when the lower stress amplitude level results are observed. The longer the life the greater the effect of lowering the load frequency. At the higher stress level the lower frequency result falls on the same curve as the 2(Hz) test.

It was observed that whilst the majority of the failures occurred at the root or in the vicinity of the notch there were a few exceptions. The specimen shown in Figure 101 is the most extreme example of this with the fracture occurring some distance from the notch.

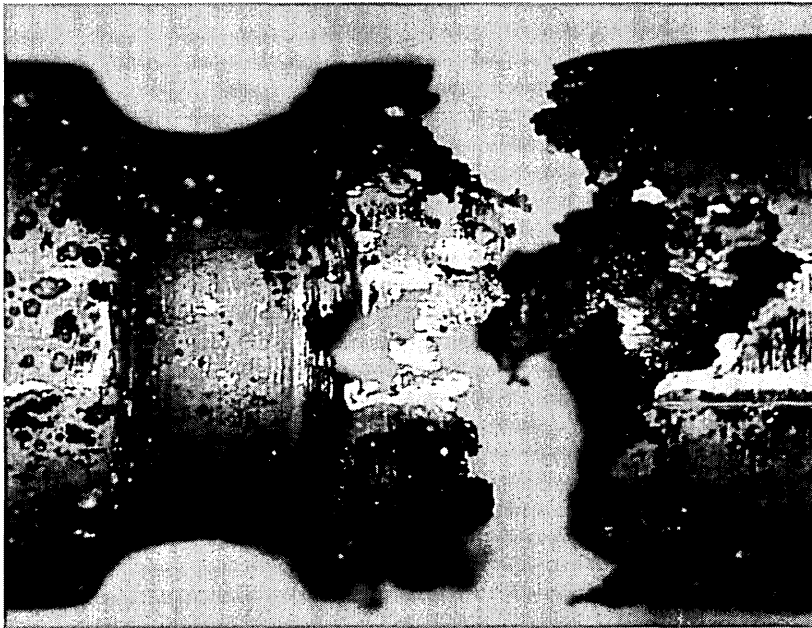


Figure 101 - Fracture Away From Notch. Notched FV520B Specimen Subjected to $\pm 75\text{MPa}$ at 2Hz, 100°C 0.3% NaCl, $0(\text{mV})_{\text{Ag}/\text{AgCl}}$ $N_f = 323310$.

Failure away from the notch is probably a result of the low applied stress ($\pm 75\text{MPa}$) producing little fatigue action thus allowing corrosion to be dominant, especially if the corrosion rate is enhanced by the presence of a non-metallic inclusion in the fracture area. Under imposed anodic potentials large quantities of iron oxide formed within the autoclave during testing. Figure 102 shows the build up of iron oxide around one end of a failed specimen.

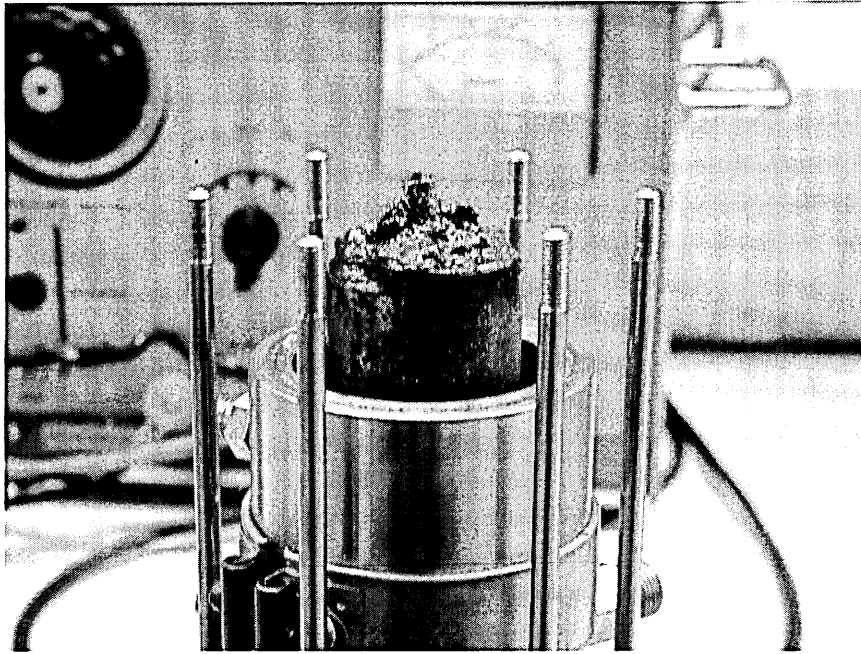


Figure 102 - Failed Specimen Showing Iron Oxide (Magnetite) Deposited During Testing of Plain Specimen FV520B at 100°C in 0.3% NaCl +200 (mV)_{Ag/AgCl} ±75(MPa) 2(Hz), N_f = 127080

The fracture surfaces seen with plain specimen appear more straight forward with corrosion that produces fatigue crack growth on a single plane. Typical fracture surfaces from notched tests conducted at a constant applied corrosion potential of +200 (mV)_{Ag/AgCl} are shown in Figure 103, Figure 104 and Figure 105.

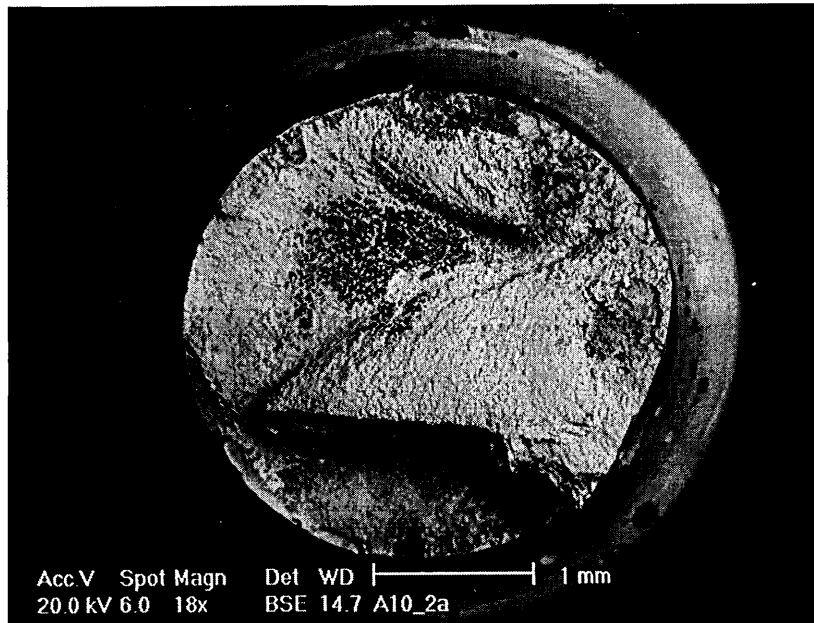


Figure 103 - Fracture Surface of Peak Hardened FV520B, ± 300 (MPa) 2(Hz), R = -1, 0.3% NaCl, 100°C, +200 (mV)_{Ag/AgCl}, $N_f = 32610$

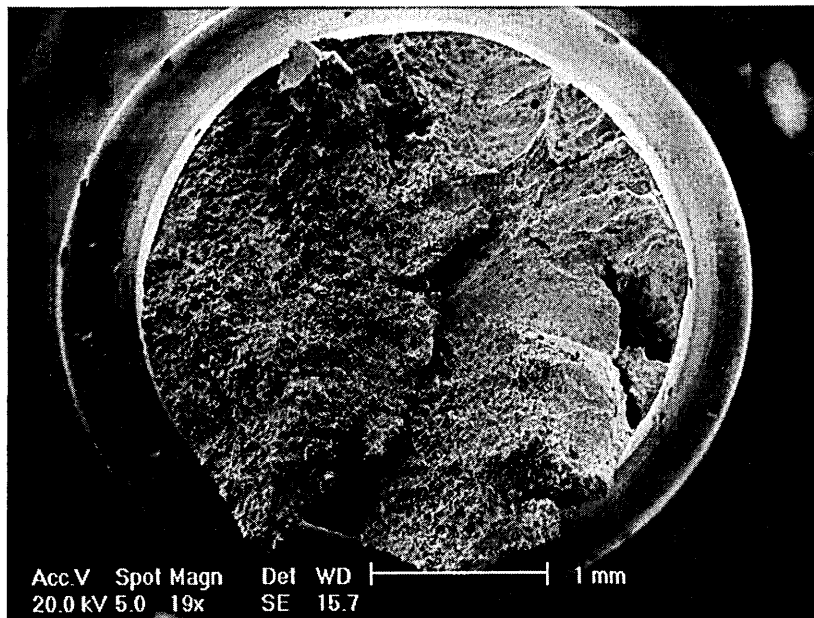


Figure 104 - Fracture Surface of Peak Hardened FV520B, ± 150 (MPa) 2(Hz), R = -1, 0.3% NaCl, 100°C, +200 (mV)_{Ag/AgCl}, $N_f = 52580$

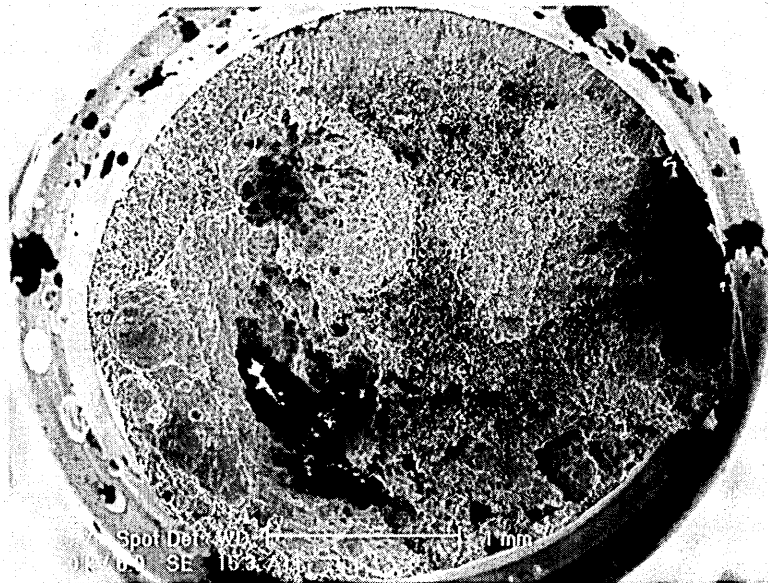


Figure 105 - Fracture Surface of Peak Hardened FV520B, ± 75 (MPa) 2(Hz), R = -1, 0.3% NaCl, 100°C, $+200(\text{mV})_{\text{Ag}/\text{AgCl}}$, $N_f = 211280$

It can clearly be seen from the life to failure for the notched specimen tested at $+200(\text{mV})_{\text{Ag}/\text{AgCl}}$ with a loading frequency of 2(Hz) that there is a strong stress effect. The area of flat slightly grainy fatigue type fracture decreases as the level of applied stress is reduced. Tests conducted at a lower loading frequency show similar trends as can be seen in Figure 106 and Figure 107. The fracture surfaces of specimen tested at lower corrosion potential also showed similar trends, see Figure 108, Figure 109 and Figure 110.

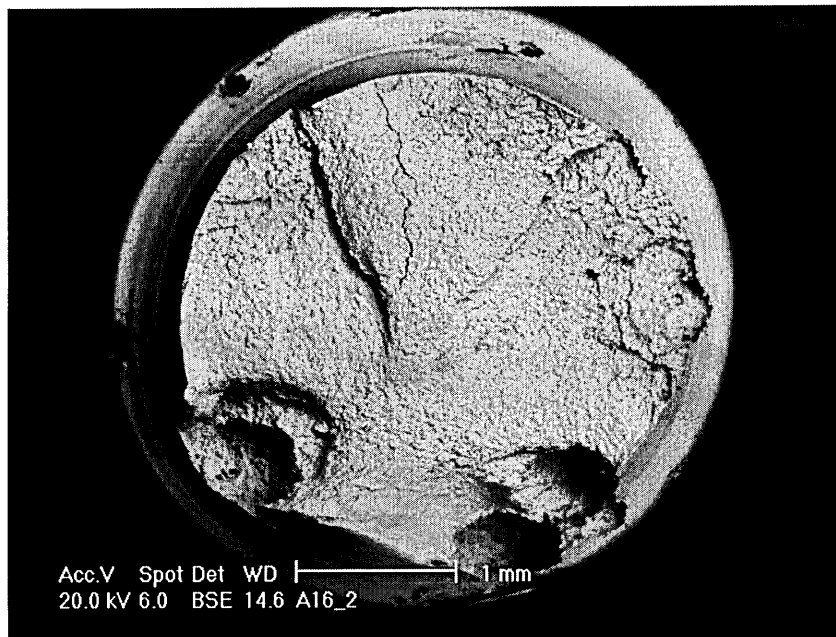


Figure 106 - Fracture Surface of Peak Hardened FV520B, ± 300 (MPa) 0.5(Hz), R = -1, 0.3% NaCl, 100°C, +200(mV)_{Ag/AgCl}, $N_f = 7810$

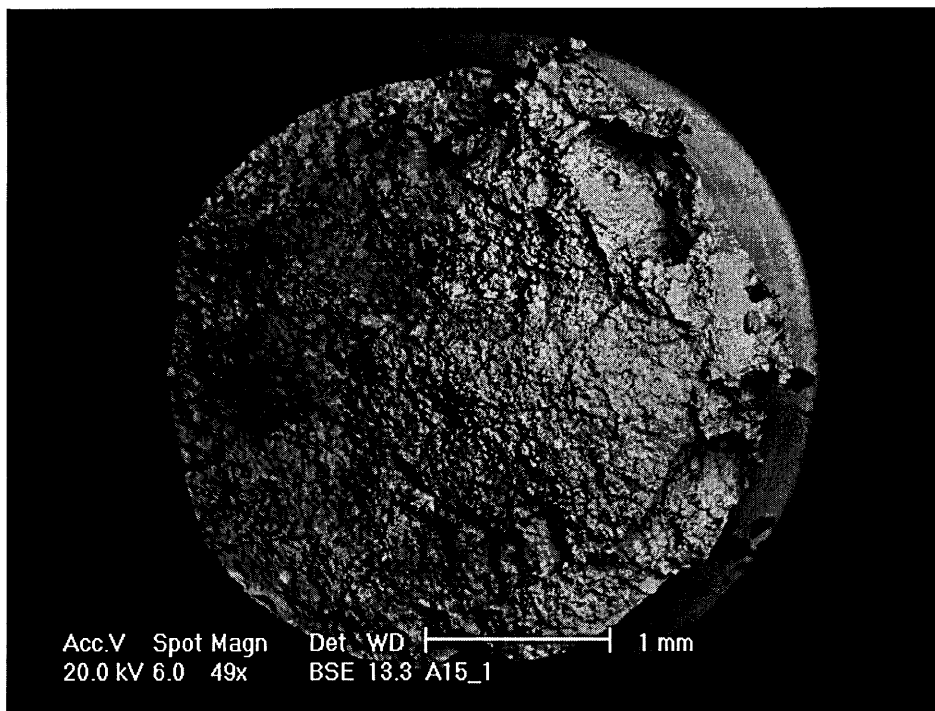


Figure 107 - Fracture Surface of Peak Hardened FV520B, ± 75 (MPa) 0.5(Hz), R = -1, 0.3% NaCl, 100°C, +200 (mV)_{Ag/AgCl}, $N_f = 29660$

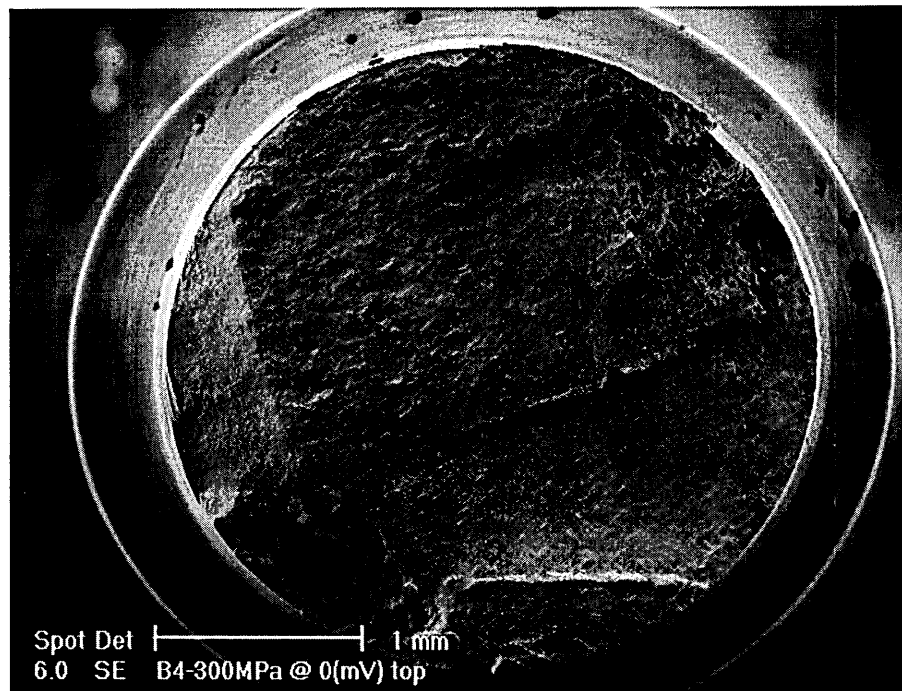


Figure 108 - Fracture Surface of Peak Hardened FV520B, ± 300 (MPa) 2(Hz), R = -1, 0.3% NaCl, 100°C, 0(mV)_{Ag/AgCl}, $N_f = 39390$

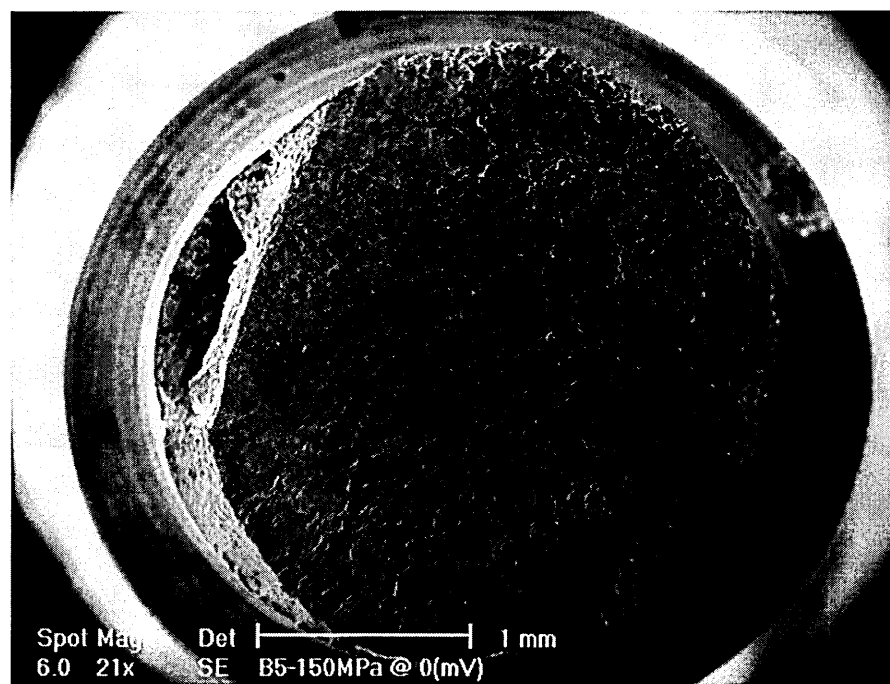


Figure 109 - Fracture Surface of Peak Hardened FV520B, ± 150 (MPa) 2(Hz), R = -1, 0.3% NaCl, 100°C, 0(mV)_{Ag/AgCl}, $N_f = 148120$

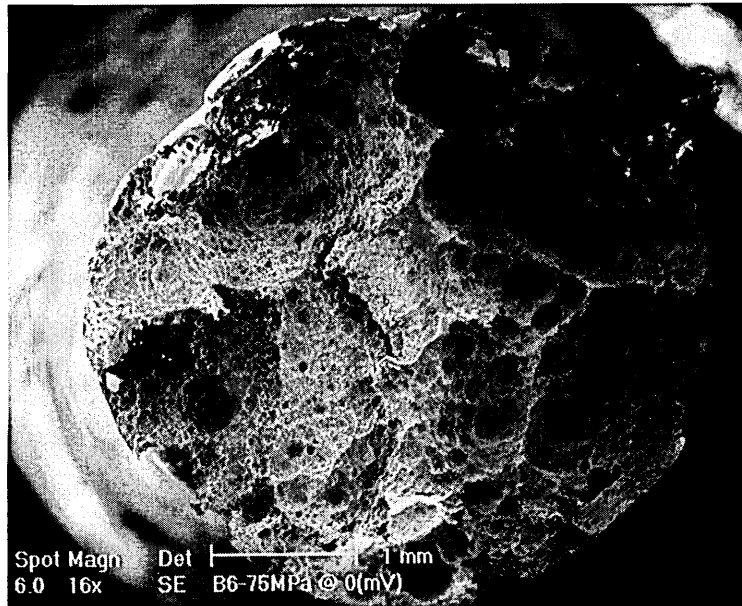


Figure 110 - Fracture Surface of Peak Hardened FV520B, ± 75 (MPa) 2(Hz), R = -1, 0.3% NaCl, 100°C, 0(mV)_{Ag/AgCl}, $N_f = 323310$

From the above figures it is clear there is a link between the level of applied stress and the amount of corrosion damage. Figure 113 shows a plot of transition from corrosion to fatigue damage versus applied stress. Figure 111 defines how the transition depth was measured.

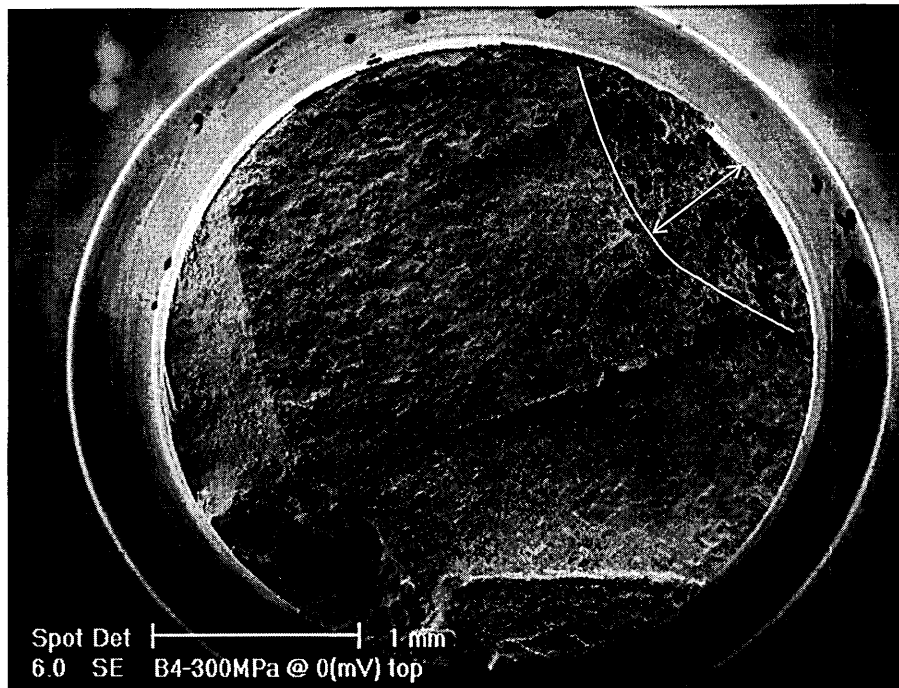


Figure 111 - Definition of Corrosion-Fatigue Transition Point

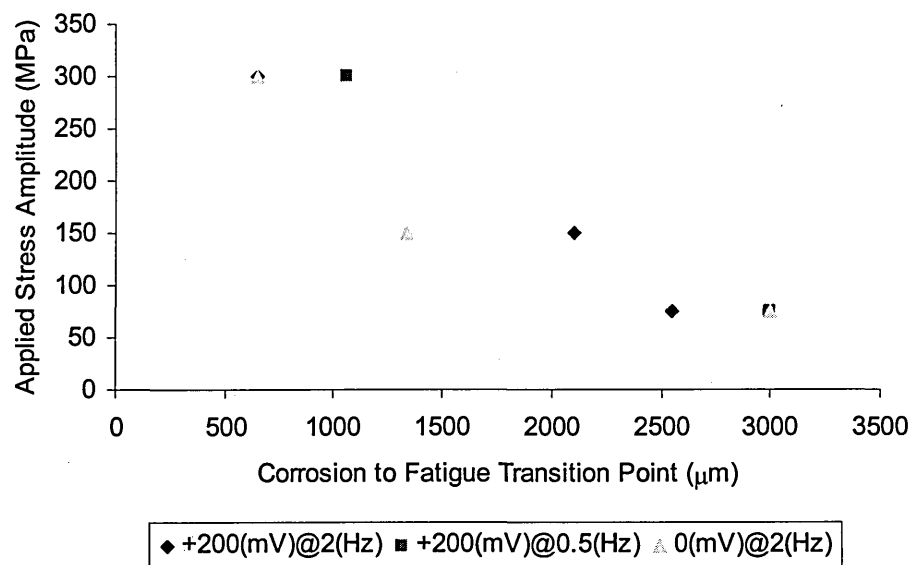


Figure 112 - Corrosion-Fatigue Transition Point Versus Applied Stress Amplitude For FV520B Notched Specimen.

From the above graph one can see a clear stress effect on the fracture surface. Those specimens tested at a higher applied stress amplitude showing a greater area of fatigue damage. There is some interpretation in determining the transition point from

corrosion damage to fatigue damage however it is felt the broad trend shown in Figure 112 is correct. The possibility of corrosion damage occurring to the fracture surface after crack initiation could affect these values with smaller areas of corrosion leading to fatigue crack growth. Kondo [123] found that the pit size remained almost constant after the transition into a crack from a pit. The reason given by Kondo [123] for the arrest in pit growth once a crack had initiated was that the anodic site would move from the pit. Kondo [123] goes on to state that "the pit size observed on the fracture surface is considered to give the critical pit size at which the transition occurred."

5.5.3.1 Superposition of Intergranular Corrosion and Corrosion Fatigue

There is evidence of intergranular cracking in many of the notched specimen fracture surfaces, see Figure 113.

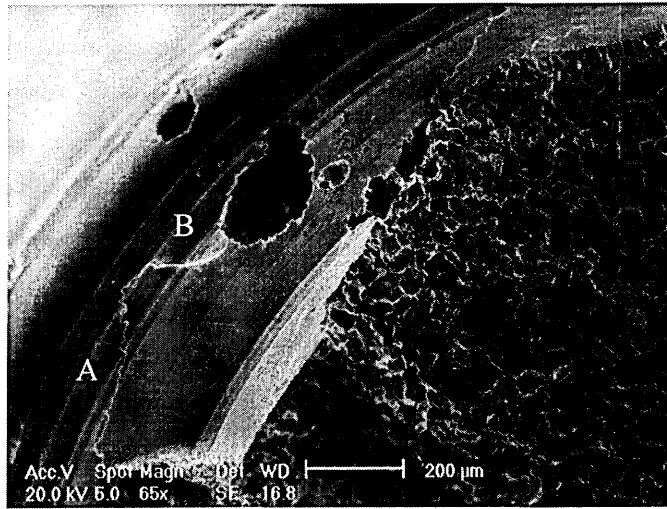


Figure 113 - Fracture Surface of Peak Hardened FV520B, ± 150 (MPa) 2(Hz), R = -1, 0.3% NaCl, 100°C, +200(mV)_{Ag/AgCl}, $N_f = 52580$

Superposition of intergranular corrosion and corrosion fatigue has previously been observed [141]. The grain boundaries are preferentially attacked by intergranular corrosion and form the origin of cracks. Initially the crack propagation is intergranular. Wiegand et al [141] state "having crossed the outer crystallite layers the crack then propagates in the transgranular mode". They go on to note that if there is heavy intergranular attack many cracks are formed, in this case the fracture appearance can be easily distinguished from a fatigue failure in air.

From Figure 113 it is possible to see the pitting that occurred around the circumference of the notch away from the fracture surface, it is also possible to clearly make out the cracks (A,B) joining the corrosion pits. This is the reason for the cracking on different planes seen on the notched specimen fracture surfaces as in Figure 104.

5.5.4 Corrosion Fatigue in Plain Specimens

Tests were conducted with plain specimen peak hardened FV520B in order that the role of the notch under imposed potential condition may be assessed, the results from these tests are also plotted in Figure 100. The resultant life to failure for imposed

potentials of $+200(\text{mV})_{\text{Ag}/\text{AgCl}}$ with plain specimen are no different than those for notched specimen. This result clearly shows that in highly corrosive conditions the effect of the notch in terms of both a stress and electrochemical concentrator is negligible. There is however still a clear stress effect in the failures with the lower stressed specimens showing longer life to failure.

Figure 114, Figure 115 and Figure 116 show SEM images of the plain specimen subjected to constant potential. It can be seen from these images that the lower the applied stress the greater the damage caused by the applied potential. In each image there was a strong transition between corrosion damage and fatigue damage. Figure 117 shows a higher magnification image of the transition between corrosion and fatigue damage.

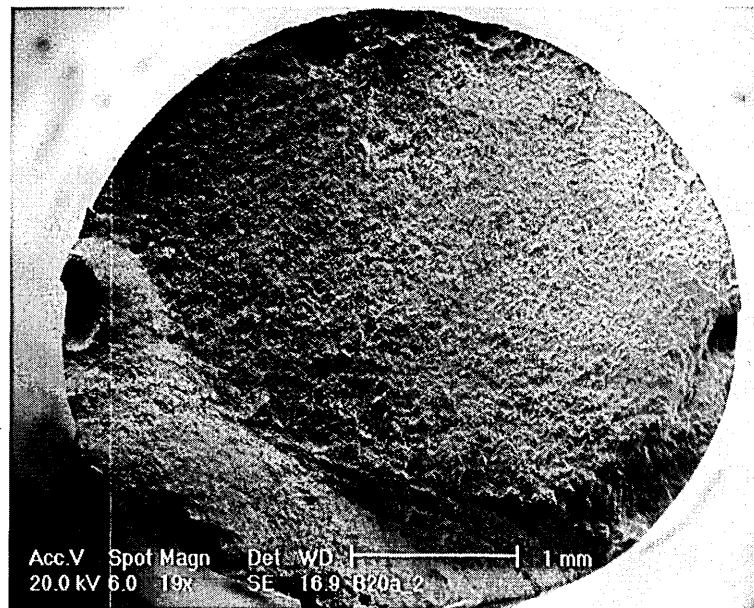


Figure 114 - Fractured Stub of FV520B-B Plain Specimen Tested at $+200(\text{mV})_{\text{Ag}/\text{AgCl}}$ in 100°C NaCl, ± 300 (MPa), 2(Hz), $R=-1$, $N_f=10221$

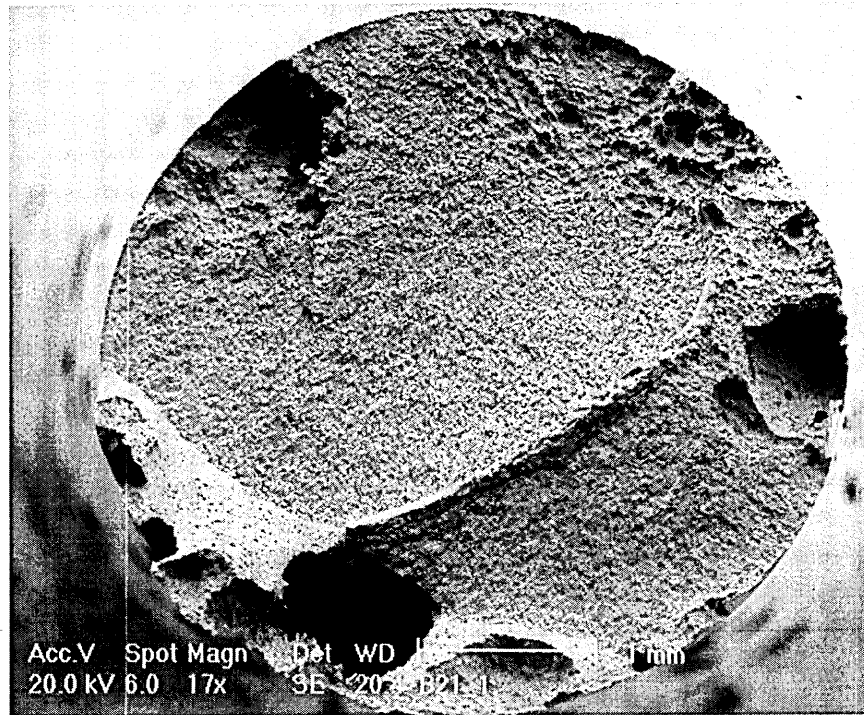


Figure 115 - Fractured Stub of FV520B-B Plain Specimen Tested at $+200(\text{mV})_{\text{Ag/AgCl}}$ in 100°C NaCl, ± 150 (MPa), 2(Hz), $R=-1$, $N_f = 59836$

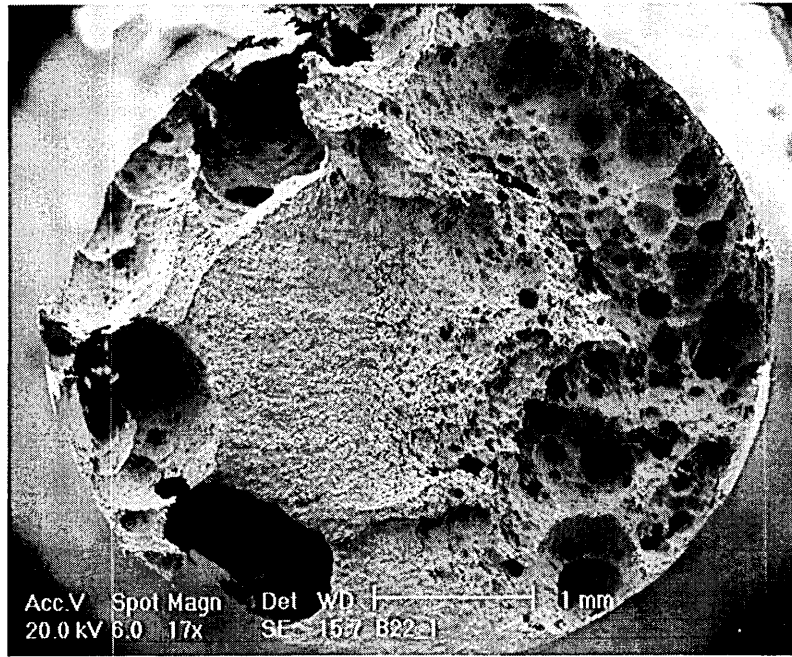


Figure 116 - Fractured Stub of FV520B-B Plain Specimen Tested at $+200(\text{mV})_{\text{Ag/AgCl}}$ in 100°C NaCl, ± 75 (MPa), 2(Hz), $R=-1$, $N_f = 184024$

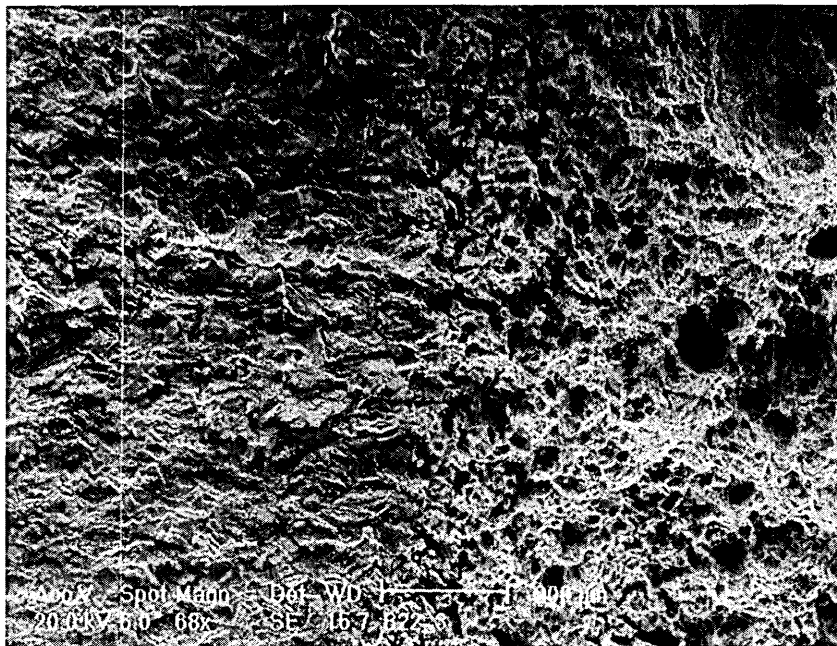


Figure 117 - Transition Point from Fractured Stub of FV520B-B Plain Specimen Tested at $+200(\text{mV})_{\text{Ag/AgCl}}$ in 100°C NaCl, ± 75 (MPa), 2(Hz), $R=-1$, $N_f = 184024$

There is a clear stress effect on the depth of transition from corrosion to fatigue damage. Figure 118 shows the correlation between corrosion-fatigue transition depth and the applied stress level

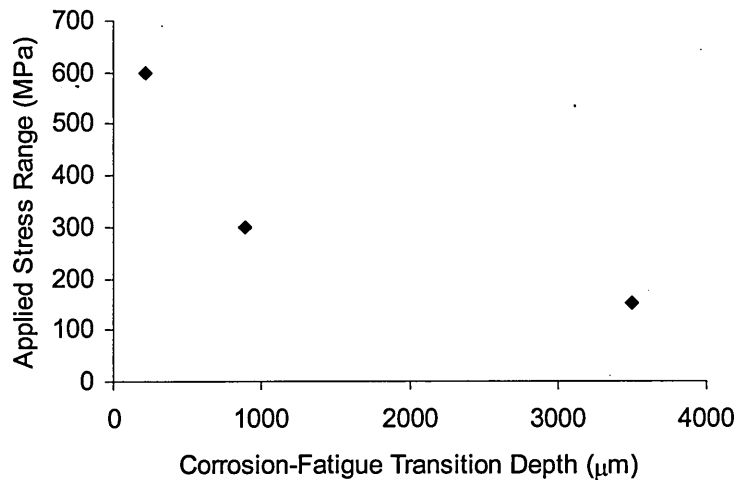


Figure 118 - Effect of Applied Stress Range on Crack Transition Depth for Plain FV520B-B Corrosion Fatigue Specimen Tested at +200(mV)_{Ag/AgCl}, R=-1, 2(Hz), 100°C in 0.3% NaCl.

Using fracture mechanics the areas of corrosion damage can be normalised with the applied stress to find a transition stress intensity factor range. Table 14 gives pit data for the specimen shown. Figure 111 shows how the transition from corrosion to fatigue was defined.

Spec.	a (μm)	$\Delta\sigma$	ΔK	Nf
B20	385	600	13.98078	10221
	165	600	9.152568	
	44	600	4.726366	
	220	600	10.56848	
	220	600	10.56848	
	360	600	13.51924	
average	232.3333	600	10.41932	
B21	885	300	10.59846	59836
	1062	300	11.61003	
B22	3500	150	10.53841	184024

Table 14 - Crack Data for a Constant Imposed Potential of +200(mV)_{Ag/AgCl}, Plain Specimen FV520B-B Corrosion Fatigue Tests Conducted at 100°C in 0.3% NaCl, R=-1, 2(Hz). a = depth of corrosion damage.

Using Equation 2 (page 31) stress intensity factors were calculated for the transition point from corrosion to fatigue damage, these are given in Table 14. It can be seen

from Table 14 that the value of transition ΔK is around $10 \text{ MPa}\sqrt{m}$ irrespective of applied stress range.

For the tests with applied higher stress there is a greater number of pits, and hence wider scatter in pit size. This is due to the fact that at a higher applied stress the specimen fails at a lower number of cycles, meaning there is less time for corrosion to take place. Some smaller pits seen at higher applied stress levels would coalesce to form the less densely populated larger pits similar to that seen in the lower applied stress tests. The lower the applied stress range the longer the fatigue life, and hence the greater the time spent under imposed potential conditions allowing the pits to grow larger. The transition point from pit to crack is defined as the point where the rate of fatigue crack growth exceeds corrosion growth. Using the Paris equation it is possible to calculate the fatigue crack growth rate for a crack with a given stress intensity factor. The Paris relation is given in Equation 3 (page 32).

C and m are constants in Equation 3 and are dependent on material and environment. There were no values of C and m in the literature for FV520B in an aggressive environment. The values of C and m used ($C = 10^{-11}$ and $m = 3$) are for ferrous materials in air [49,142]. The above values give a fatigue crack growth rate of 4.23×10^{-8} (m/cycle) for a transition stress intensity factor of $10 \text{ MPa}\sqrt{m}$. At the stage of transition the corrosion rate is considered to be equal to the fatigue crack growth rate. So it is therefore possible to predict the corrosion rate.

Tests were conducted at 2(Hz) giving a corrosion rate of $0.846 \text{ } (\mu\text{m}/\text{sec})$ at the point of transition. The Paris equation is only applicable during stage II cracking. The above calculation is only valid if the ΔK at the point of transition occurs during stage II crack growth.

5.5.4.1 Corrosion Fatigue of Notched Specimens

For a given stress amplitude crack growth rates obtained for a notched specimen in air are in excess of plain specimen. It was also found that notched specimen can suffer from nonpropagating cracks. The enhancement of crack growth rate for notched specimens was due to the stress zone caused by the notch. Cracks usually initiate and grow in the notch plastic field, however as the crack grows to the limit of the notch plastic field, crack growth rate will reduce. If the crack is unable to generate it's own plastic zone large enough to allow continued growth then crack growth will arrest. A crack growing from a notch is illustrated in Figure 119.

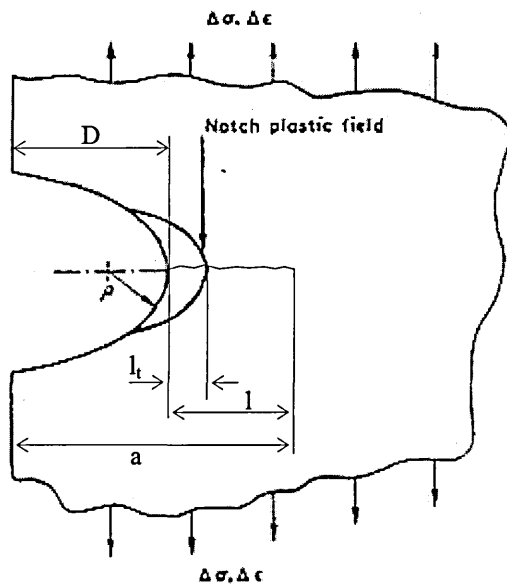


Figure 119 - Crack Growth at Notch

Smith and Miller [51] proposed the transition length l_t that characterises the transition from the accelerated crack growth within the notch plastic field to the standard linear elastic fracture mechanics (LEFM) type crack growth beyond the influence of the notch. Smith [143] comments that the size of the zone of yielded

material is a function of the notch shape. Smith and Miller [51] use the equation below to calculate the transition length (l_t).

Equation 41

$$l_t = 0.13\sqrt{D\rho}$$

Using the notch geometry tested in this study a transition length of 91(μm) was calculated.

Once the crack has grown beyond the influence of the notch LEFM principles can be used with an effective crack length (a) ($a = l + D$) [144] to calculate the stress intensity factor.

Since all the pit depths on the constant potential notched specimens were greater than 91(μm) stress intensity factors were calculated using an effective crack length (a) rather than l .

The transition depth of 91(μm) is greater than the grain size for the FV520B. Having a transition depth greater than the grain size means that the fatigue crack will have passed a grain boundary whilst still being enhanced by the plastic zone field.

The stress intensity factor ranges were calculated using pit depths taken from failed specimens. These results are shown in Table 15. The geometrical factor α was taken as 0.67 as proposed by Lindley et al [104]. The stresses used in the calculation of the stress intensity factors in Table 15 were based upon an unnotched specimen cross-section. This was felt to be justified as the notch is accounted for in the increased crack length. The definition of pit depth is given in Figure 111.

Stress Amp. (MPa)	Cycles to Failure	Potential (mV) _{Ag/ACI}	Pit Depth (μm)	ΔK
168.75	148120	0	1238.10	8.35
168.75	52580	+200	1588.24	9.16
337.50	39390	0	550.00	12.99
337.50		0	650.00	13.59
337.50	32610	+200	1238.10	16.71
337.50	7810	+200	722.23	14.01
337.50		+200	416.67	12.13
337.50		+200	222.22	10.77
337.50		+200	666.66	13.69

Table 15 - Stress Intensity Ranges for Constant Potential Tests Conducted on Notched Specimen

The stress intensity factor for typical pits found in notched test samples subjected to constant applied potential was approximately $10 \text{ MPa } \sqrt{m}$, with a nominal spread from $8 \text{ MPa } \sqrt{m}$ to $16 \text{ MPa } \sqrt{m}$. There is some deviation but an average value of around $10 \text{ MPa } \sqrt{m}$ is evident. It is possible that there may be some error in the measurement of the pit depth but it is the opinion of the author that this would be minimal as all pit depths were measured at high magnifications thus reducing the margin of error. It has been suggested that when a fatigue crack initiates from the base of a corrosion pit the pit growth is stopped due to the movement of the anodic site from the bottom of the pit [123]. Due to this the ΔK values given in Table 15 are considered to correspond to the transition point where fatigue crack growth exceeds corrosion pit growth.

5.5.4.2 Assessment of Hydrogen Embrittlement in Corrosion

Fatigue

As was previously discussed in the Literature Review it has been shown by several authors that at the tip of an advancing cyclically loaded crack the pH and electrolyte potential can drop, thus providing the correct conditions for hydrogen production

even during anodic polarisation (see p.95). Hydrogen embrittlement in some environment systems was shown to greatly influence the corrosion fatigue process, [118]. To this end a test was conducted with the addition of thiourea. Thiourea will poison the hydrogen evolution reaction this means more of the adsorbed hydrogen will enter the metal instead of recombining to form hydrogen gas. Thus if hydrogen embrittlement is a factor in the corrosion fatigue process the addition of thiourea will show an increase in the fatigue crack growth rate or a decrease in number of cycles to failure.

The addition of thiourea showed no significant effect on the failure time in the testing reported in this study as shown in Table 16.

Environment	Potential (mV)	Nf
0.3 % NaCl	+200	28180
0.3 % NaCl + 2.5 % CS(NH ₂) ₂	+200	32610

Table 16 - Results of Thiourea Test. Both Tests Conducted at 100°C, R=-1 2(Hz)

It is not possible to make a statement based on simply one observation, however, it is felt some remarks should be made about this test. The specimens used in this work are hour glass type specimens and the failure of these tests is dominated by short crack propagation. The work reported in the literature (see p95) are predominantly for propagating cracks in thick CT or beam type specimen where there is sufficient time to allow a separate environment to develop at the crack tip before fracture. It may be the case that the notch would aid the creation of this local environment with the hour glass type specimen and that for a longer term test (lower stress amplitude) some effect may be seen. The tests detailed in the literature were mostly carried out at

room temperature, whereas this test was conducted at 100°C thus increasing the diffusion rate of the hydrogen.

In conclusion there was no effect of the thiourea in this test, this may be because hydrogen embrittlement plays no role in the corrosion fatigue process in the system being investigated. Alternatively that there is an effect but this initial testing failed to show any effect. In either case further work is required.

To assess the effect of hydrogen embrittlement on the mechanical properties of FV520B a slow strain rate test specimen was charged with hydrogen. Hydrogen charging was achieved by holding the specimen at -1.2(V) (S.C.E) for five hours in a solution of 1% thiourea + 3.5% NaCl + 0.1M sulphuric acid. Once the charging process was complete the specimen was tested in air at room temperature at a strain rate of $1 \times 10^{-6} \text{ (s}^{-1}\text{)}$, as soon as possible to reduce the amount of hydrogen discharge. There was a clear band of material around the fracture surface that was affected by the hydrogen charging process, see Figure 120. In the damaged band fracture occurred through transgranular cracking.

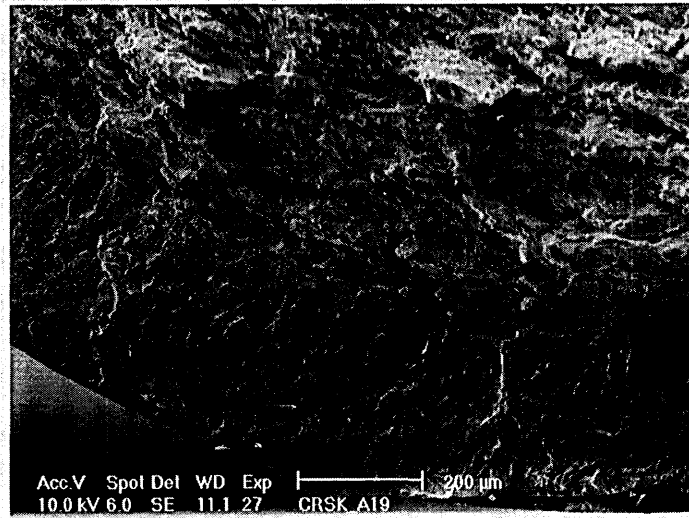


Figure 120 - Band of Material Damaged Due to Hydrogen Charging Process

5.5.4.3 Calculation of Critical Pit Depth Based on Corrosion Current

Several authors have used a modified version of Faraday's law to predict pit depth based on corrosion current, see p.65. Equation 22 was used to calculate the depth of pit that would be produced after a given number of cycles at $+200(\text{mV})_{\text{Ag}/\text{AgCl}}$. Figure 121 show the results of these calculations plotted along with pit depths measured from failed specimens.

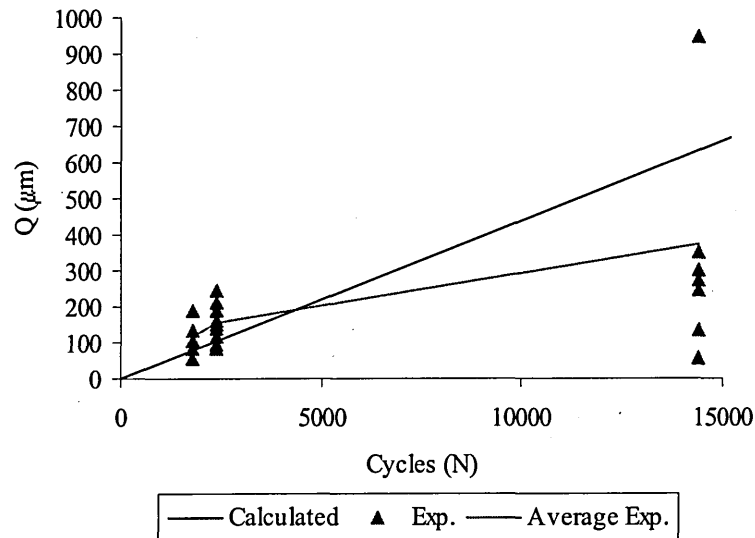


Figure 121 - Q Versus N, With an Exposed Area of $2.29 \times 10^{-5} \text{ (m}^2\text{)}$ 75(MPa) 2(Hz), $+200 \text{ (mV)}_{\text{Ag/AgCl}}$ in 0.3% NaCl at 100°C

The calculated values of the depth of material removed, Q , show a good correlation with the pit depths seen experimentally. However it can be seen that at long lives the experimental value of Q may become conservative. Equation 22 gives a pit depth based on a pit shape approximated to a semi-ellipse. If the shape of the pits is different the depth of Q would need to be corrected. Turnbull and Zhou [145] found no correlation between Equation 22 and their pit depths, they attributed this to the difference in pit geometry.

5.5.5 Pulsed Imposed Potential Corrosion Fatigue Test Remarks

The aim of the pulsed imposed potential corrosion fatigue tests was to simulate the transitory electrochemical environment seen during start-up and shut down of a steam turbine. The results are thought to assess the effect of a similarly transitory aggressive environment on the corrosion fatigue of a notched steam turbine blade material specimen.

From the results shown in Figure 77 (page 154). There appears to be an incubation period before which the effect of the imposed potential is ineffective up to the one million cycle cut off. It is clear from SEM work that the imposed potential did have a corrosive effect on the notched area of the specimen however it appears this effect was insufficient to cause a failure in the specimen. Figure 122 shows corrosion pitting in the notched region of a corrosion fatigue specimen that was subjected to $+200(\text{mV})_{\text{Ag}/\text{AgCl}}$ for 90 cycles and did not fail before the 1 million cycles cut off. Figure 123 and Figure 124 show the corrosion damage caused to a notched specimen due to 600 cycles at $+200(\text{mV})_{\text{Ag}/\text{AgCl}}$, the specimen did not fail. Figure 125, Figure 126, Figure 127 and Figure 128 show the corrosion damage caused to a notched specimen subjected to 1800 cycles at $+200(\text{mV})_{\text{Ag}/\text{AgCl}}$, the specimen did not fail, however, there is evidence of cracks growing across the corrosion pits. These figures clearly show it is possible for peak hardened FV520B to withstand severe pitting whilst being subjected to cyclic loading without failure within the 1 million cycle cut off.

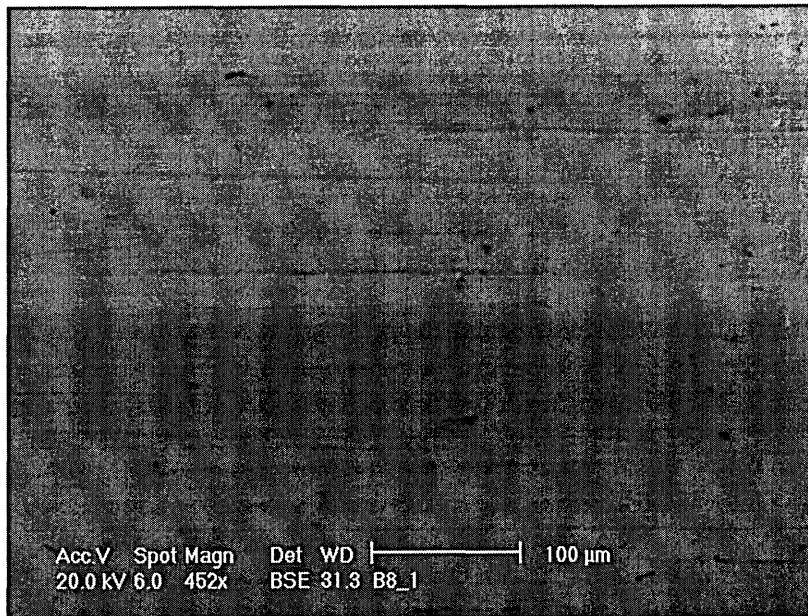


Figure 122 - Notch Area of FV520B-B Corrosion fatigue Specimen Subjected to 90 cycles at +200(mV)Ag/AgCl at The Start of Testing in 0.3% NaCl at 100°C, ±300(MPa) 2(Hz).

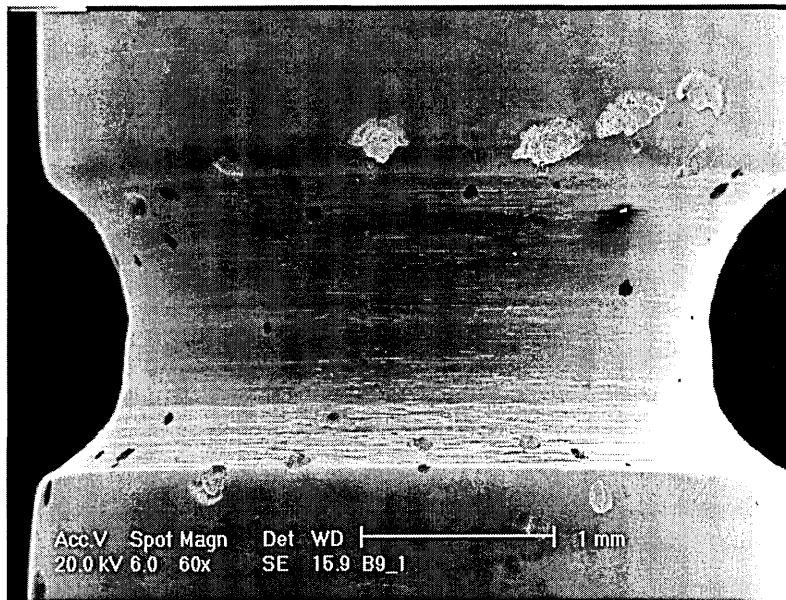


Figure 123 - Notch Area of FV520B-B Corrosion fatigue Specimen Subjected to 600 cycles at $+200(\text{mV})_{\text{Ag}/\text{AgCl}}$ at The Start of Testing in 0.3% NaCl at 100°C , $\pm 300(\text{MPa})$ 2(Hz).

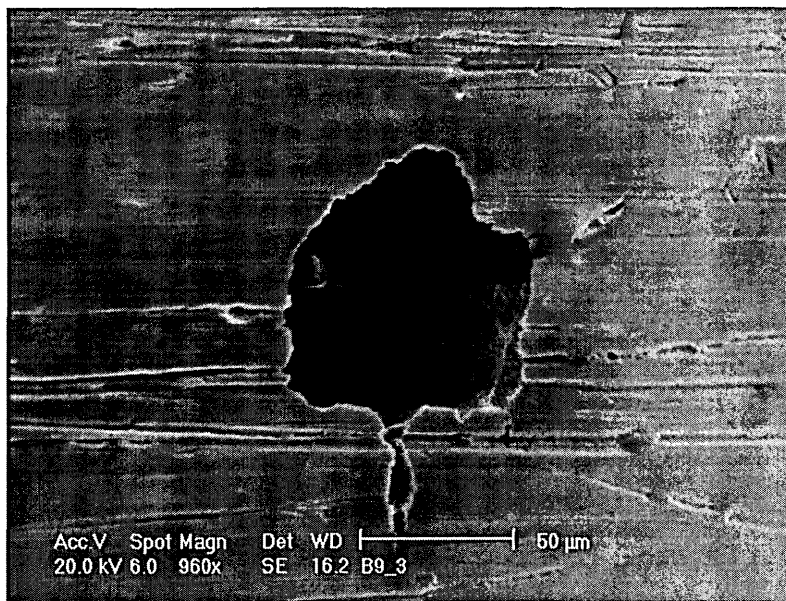


Figure 124 - Notch Area of FV520B-B Corrosion fatigue Specimen Subjected to 600 cycles at $+200(\text{mV})_{\text{Ag}/\text{AgCl}}$ at The Start of Testing in 0.3% NaCl at 100°C , $\pm 300(\text{MPa})$ 2(Hz).

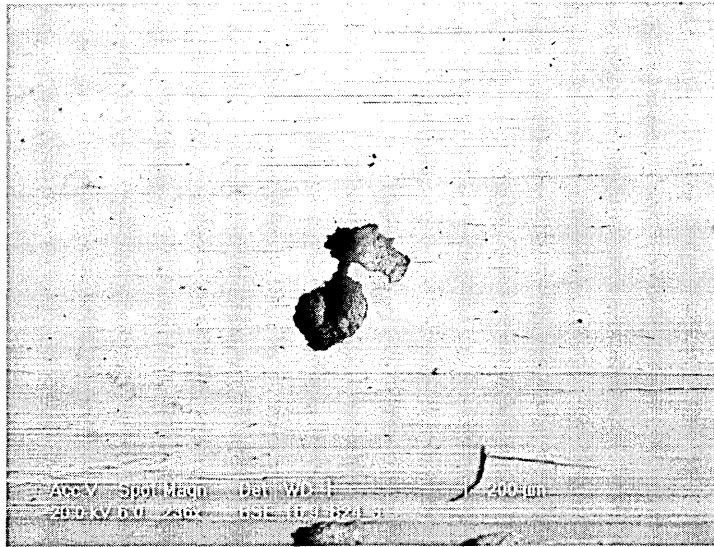


Figure 125 - Notch Area of FV520B-B Corrosion fatigue Specimen Subjected to 1800 cycles at $+200(\text{mV})_{\text{Ag}/\text{AgCl}}$ at The Start of Testing in 0.3% NaCl at 100°C , $\pm 300(\text{MPa})$ 2(Hz).

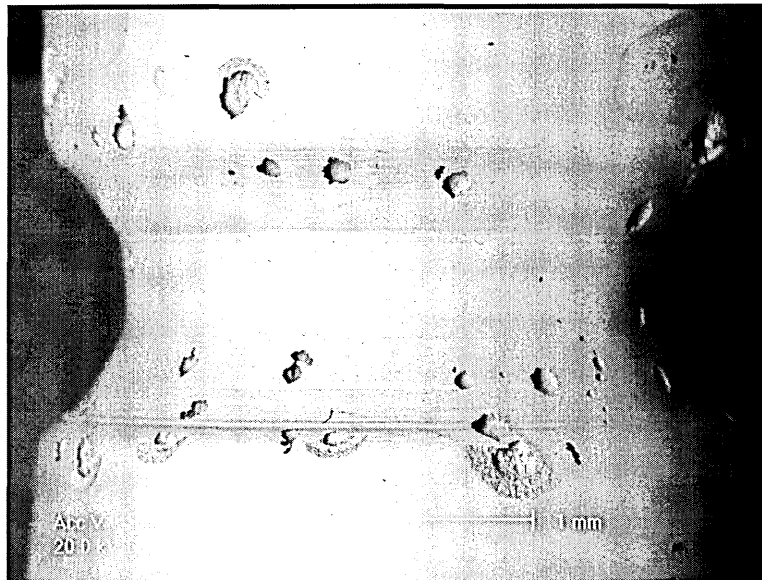


Figure 126 - Notch Area of FV520B-B Corrosion fatigue Specimen Subjected to 1800 cycles at $+200(\text{mV})_{\text{Ag}/\text{AgCl}}$ at The Start of Testing in 0.3% NaCl at 100°C , $\pm 300(\text{MPa})$ 2(Hz).

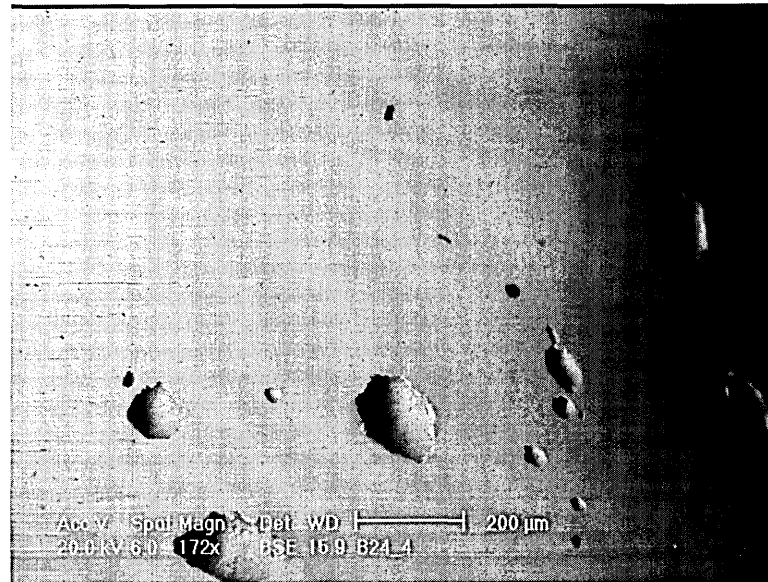


Figure 127 - Notch Area of FV520B-B Corrosion fatigue Specimen Subjected to 1800 cycles at $+200(\text{mV})_{\text{Ag}/\text{AgCl}}$ at The Start of Testing in 0.3% NaCl at 100°C , $\pm 300(\text{MPa})$ 2(Hz).

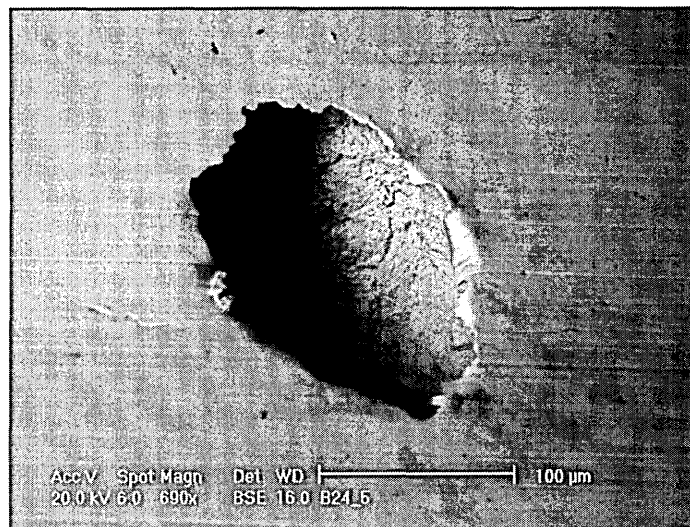


Figure 128 - Notch Area of FV520B-B Corrosion fatigue Specimen Subjected to 1800 cycles at $+200(\text{mV})_{\text{Ag}/\text{AgCl}}$ at The Start of Testing in 0.3% NaCl at 100°C , $\pm 300(\text{MPa})$ 2(Hz). Showing a Crack Growing From a Corrosion Pit.

The incubation period required to cause sufficient damage that a fracture would occur is a function of stress as can be seen from the data in Table 17 and Table 18.

±300 MPa	
Duration at +200(mV) in cycles	Cycles To Failure
1800	10 ⁶ NF
2400	5280

Table 17 - Results of Pulsed Imposed Potential Corrosion Fatigue Tests Conducted at ±300MPa, R=-1, 2(Hz), NF = no failure.

±150 MPa	
Duration at +200(mV) in cycles	Cycles To Failure
2400	10 ⁶ NF
14400	153347

Table 18 - Results of Pulsed Imposed Potential Corrosion Fatigue Tests Conducted at ±150MPa, R=-1, 2(Hz), NF = no failure.

The drop in life seen at an applied stress level of ±300 (MPa) is far greater than that seen at the other two stress levels (±225 (MPa)) and ±150 (MPa)). An applied stress level of ±300 (MPa) corresponds to the fatigue limit of the notched specimen in air. The fatigue limit is the stress level where fatigue cracks initiate but fail to propagate. So in the specimens tested at ±300 (MPa) cracks would be initiating. It could be that the cracks that initiate in the plastic zone of the notch are either fully or partially removed by the faster corrosion process thus preventing the crack from initiating fully. Eventually the stress concentrating effect of the notch and the corrosion pit would mean that even a small crack would be sufficient to cause fracture.

5.5.6 Fracture Surfaces of Pulsed Potential Corrosion Fatigue Tests

The fracture surfaces of specimens tested under pulsed potential conditions are shown in Figure 130 through Figure 137.

There is clear evidence of corrosion pitting at the cracking origin on many of the fracture surfaces of the pulsed potential test specimens. All of the fractured pulsed

potential specimens showed a substantial drop in the number of cycles to failure compared to those tested in air. The only exception being the specimen tested at ± 533 (MPa).

Cycles To Failure in Air	Cycles To Failure in 0.3% NaCl at 100°C at F.C.P after 1800 cycles at +200(mV)
25000	65828

Table 19 - Comparison of Number of Cycles To Failure for Specimens Tested in Air and Under Pulsed Potential Conditions. Both Test Conducted at ± 533 (MPa)

It may at first seem paradoxical that the specimen tested within an aggressive environment and subjected to an applied corrosion potential for a short period has a longer life than one tested in air. However, cases where corrosion extends life have previously been reported. Prolonged fatigue life due to corrosion may occur as a result of several factors; corrosion products blocking the crack and preventing further corrosion, blunting or complete removal of the fatigue crack are known to increase fatigue life. As can be seen from Figure 137 there are a number of corrosion pits around the edge of the fracture that have grown in from the notch during the period of applied potential. These pits act as stress concentrations. The way stress concentrators interact in close proximity to each other is very important in this instance. It was noted by Simnad and Evans [146] that " the concentration of stress at a discontinuity is appreciably modified by the presence of adjacent discontinuities". They then went on to comment " the mutual interference of the stress concentrations around a group of adjacent fissures will dilute the intensity of a stress". This dilution of the stress intensity factor may account for the increased fatigue life seen at the higher stress level.

It is also evident from Figure 137 that there was more than one active crack that propagated and caused failure of the specimen. The raised ridge on the fracture surface is the point where two or more cracks collided. The final failure of this specimen occurred perpendicular to the fracture surface with fracture taking place on the edges of the ridge. This crack interaction would also cause the time to failure to increase as is seen with this specimen.

The pit ringed in Figure 137 is shown below in Figure 129 at a higher magnification using back scattered electrons. There is a very clear change in texture of the fracture surface, there is a halo of flat fracture around the pit that changes to the more faceted structure associated with intergranular corrosion, see line A-A. The flat structure in a band around the base of the pit is an area of stage two fatigue crack growth, fatigue cracks can clearly be seen fanning from the bottom of the corrosion pit.

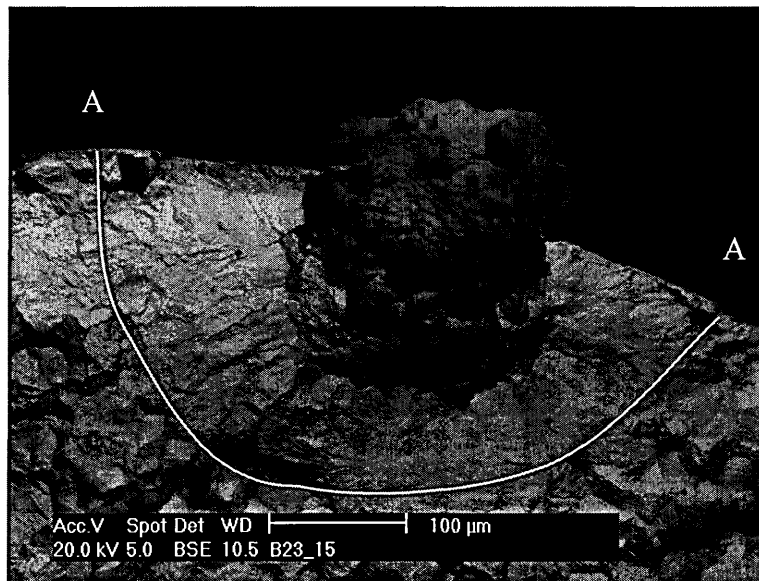


Figure 129 - Fatigue Crack Initiating From Corrosion Pitting on Fracture Surface of Notched Specimen Subjected to 1800 cycles at $+200(\text{mV})_{\text{Ag}/\text{AgCl}}$ at The Start of Testing in 0.3% NaCl at 100°C , $\pm 533(\text{MPa})$ 2(Hz) $R=-1$. $N_f = 65828$

The transition from transgranular growth to intergranular growth may be related to a change in cracking mechanism from fatigue or corrosion fatigue to stress corrosion

cracking (SCC). In a given environment the SCC will only occur above the SCC threshold stress intensity factor, K_{ISCC} . In the present study the transition to intergranular corrosion occurs at a crack depth of approximately 238(μm). Using only the tensile portion of the fatigue cycle a SCC threshold stress intensity factor of $9.7(\text{MPa}\sqrt{m})$ was calculated. The stress intensity factor was calculated using an effective crack length (a) of $l+D$ in Equation 2, see Figure 119.

It is well understood [122] that throughout a corrosion fatigue failure there are several stages controlled by either corrosion, fatigue or a combination. The change from fatigue to intergranular corrosion could be a result of yield assisted dissolution taking over as the stress at the crack tip growing from the pit exceeds yield [147]. Stress intensity factors for the corrosion pits formed during the applied potential phase were calculated using Equation 2, and are given in Table 21.

For notched specimen

crack length $a = l$, where $l < l_t$

$a = l + D$ where $l > l_t$, see Figure 119.

The values of stress intensity factor range given in Table 21 around the threshold value of 10 ($\text{MPa}\sqrt{m}$) is similar to the constant potential plain specimen in Table 14 and constant potential notched specimen in Table 15.

Material and Environment	ΔK ($\text{MPa}\sqrt{m}$)	Reference
316L Cl ⁻ Solution, pH = 3	3.69	González-Sánchez [83]
12Cr Martensitic, 0.1M NaCl	6.16	Zhou and Turnbull [105]
2.5Ni-Cr-Mo-V, Steam 90°C	7.9	Lindley et al [104]
3.5Ni-Cr-Mo-V, 90°C water	7.0	Kondo [123]

Table 20 - Pit-Crack Transition Stress Intensity Factor Ranges From Previous Works

As shown in Table 20 the transition ΔK value of 10 (MPa \sqrt{m}) found in the current work compares well with previous work reported in the literature.

Stress Amp. (MPa)	Cycles to Failure	Potential (mV) _{Ag/AgCl}	Pit Depth (μm)	ΔK
84.4	153347	+200(mV)_14400cycles at start	350	6
84.4			135	5
84.4			54	5
84.4			135	5
84.4			243.2	5
84.4			270.3	6
126.6	45810	+200(mV)_14400cycles at start	300	9
126.6			350	9
126.6			300	9
126.6			350	9
126.6			350	9
126.6	139712	+200(mV)_2400cycles at start	85	7
168.8	5280	+200(mV)_2400cycles at start	93	10
168.8			151.2	10
168.8			162.8	10
168.8			116.3	10
168.8			140	10
168.8			162.8	10
168.8			209.3	11
168.8	25993	500kcycles_2400cyclesat+200(mV)	243.24	11
168.8			162.2	10
168.8			189.14	11
299.8	65828	+200(mV)_1800 at start	135	18
299.8			135	18
299.8			135	18
299.8			108.12	18
299.8			189.2	19
299.8			81	17
299.8			108	18
299.8			108	18
299.8			135	18
299.8			54	17

Table 21 - Stress Intensity For Corrosion Pits Formed Due To Applied Corrosion Potential

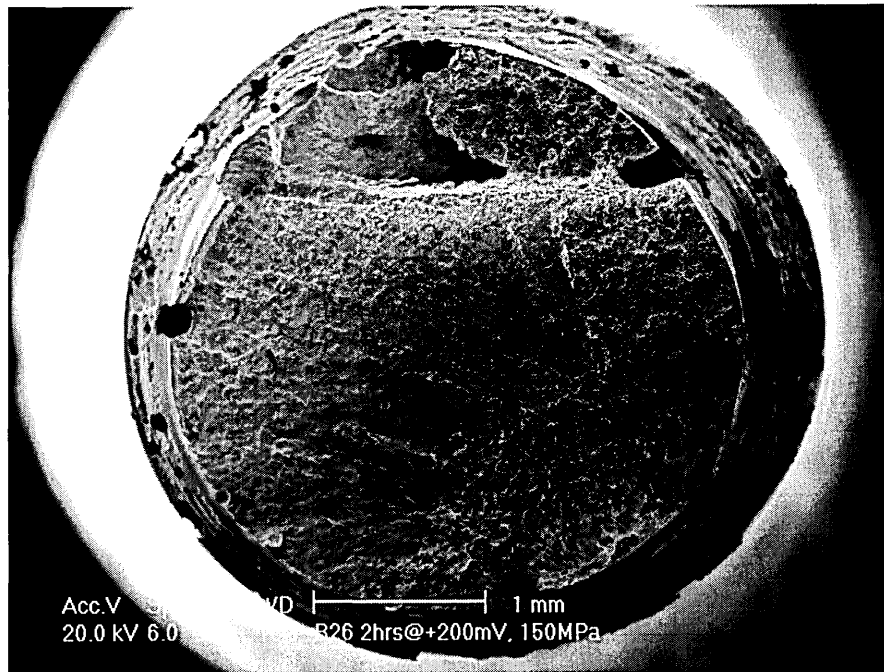


Figure 130 - Fracture Surface of Notched Specimen Subjected to 14400 cycles at +200(mV)_{Ag/AgCl} at The Start of Testing in 0.3% NaCl at 100°C, ±150(MPa) 2(Hz) R=-1. $N_f = 153347$

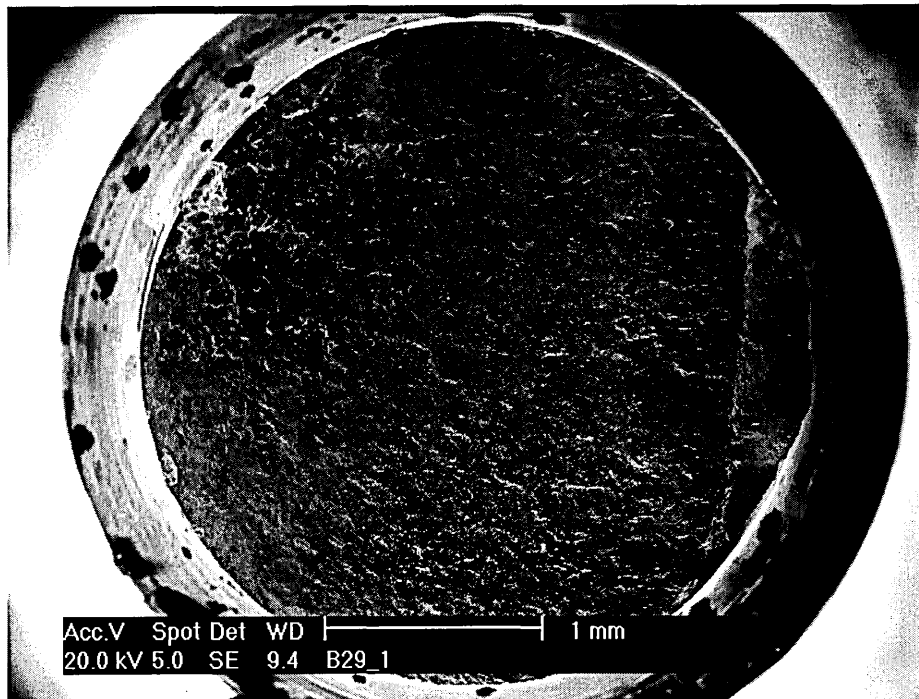


Figure 131 - Fracture Surface of Notched Specimen Subjected to 2400 cycles at +200(mV)_{Ag/AgCl} at The Start of Testing in 0.3% NaCl at 100°C, ±225(MPa) 2(Hz) R=-1. $N_f = 139712$

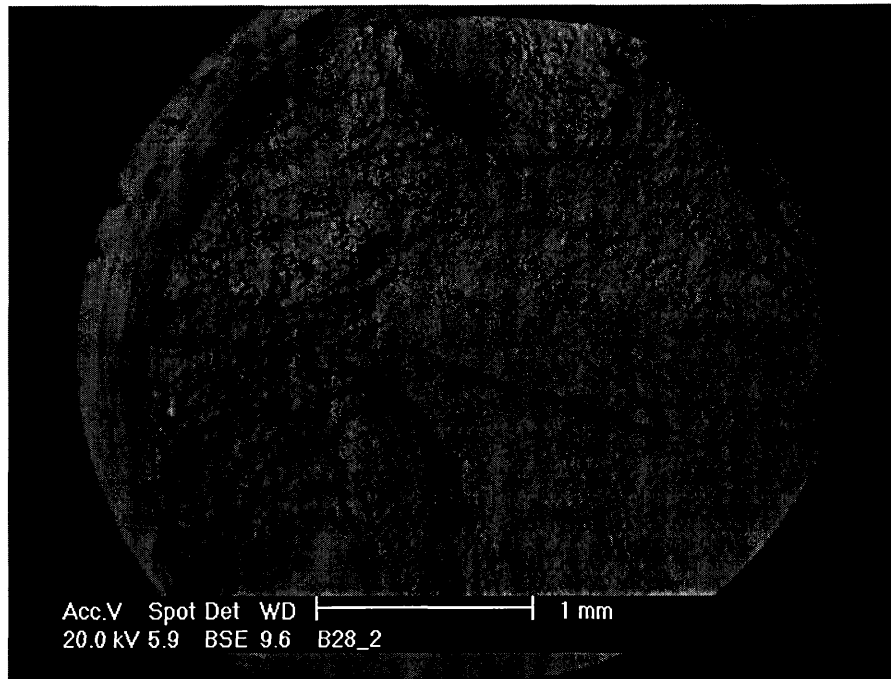


Figure 132 - Fracture Surface of Notched Specimen Subjected to 7200 cycles at $+200(\text{mV})_{\text{Ag}/\text{AgCl}}$ at The Start of Testing in 0.3% NaCl at 100°C , $\pm 225(\text{MPa})$ 2(Hz) $R=-1$. $N_f = 53264$

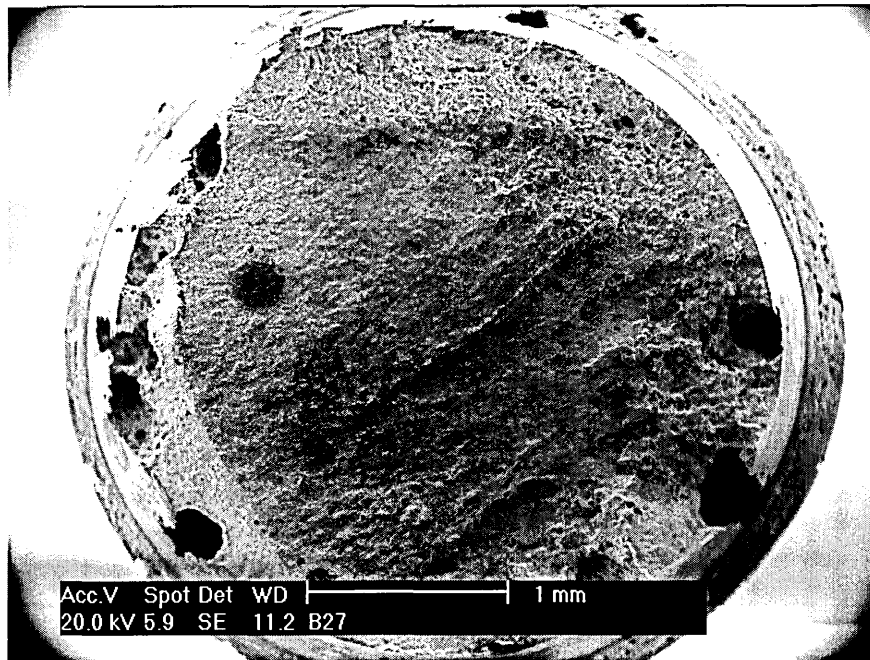


Figure 133 - Fracture Surface of Notched Specimen Subjected to 14400 cycles at $+200(\text{mV})_{\text{Ag}/\text{AgCl}}$ at The Start of Testing in 0.3% NaCl at 100°C , $\pm 225(\text{MPa})$ 2(Hz) $R=-1$. $N_f = 45810$



Figure 134 - Fracture Surface of Notched Specimen Subjected to 2400 cycles at $+200(\text{mV})_{\text{Ag/AgCl}}$ at The Start of Testing in 0.3% NaCl at 100°C , $\pm 300(\text{MPa})$ 2(Hz) R=-1. $N_f = 5280$

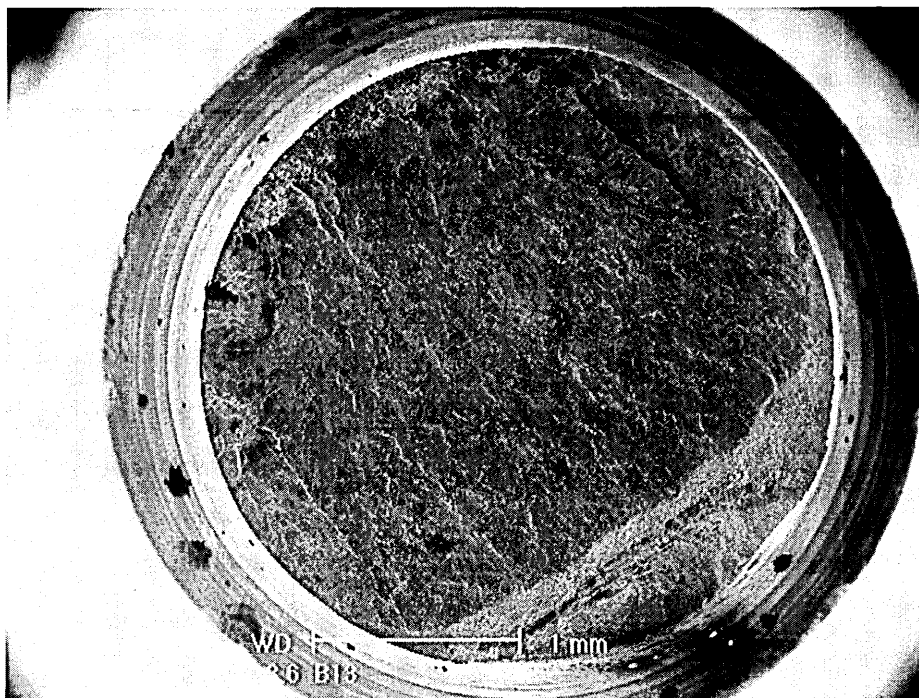


Figure 135 - Fracture Surface of Notched Specimen Subjected to 2400 cycles at $+200(\text{mV})_{\text{Ag/AgCl}}$ After 500,000 cycles at $\pm 75(\text{MPa})$ in 0.3% NaCl at 100°C , $\pm 300(\text{MPa})$ 2(Hz) R=-1. $N_f = 25993$



Figure 136 - Fracture Surface of Notched Specimen Subjected to 90 cycles at $+200(\text{mV})_{\text{Ag/AgCl}}$ at The Start of Testing in 0.3% NaCl at 100°C , $\pm 400(\text{MPa})$ 2(Hz) $R=-1$. $N_f = 14050$

Enlarged view shown in Figure 129

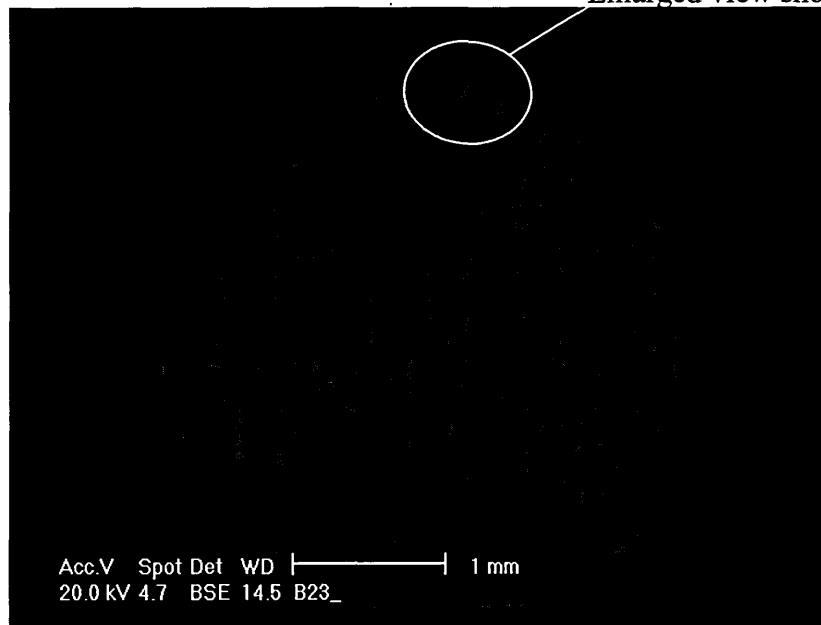


Figure 137 - Fracture Surface of Notched Specimen Subjected to 1800 cycles at $+200(\text{mV})_{\text{Ag/AgCl}}$ at The Start of Testing in 0.3% NaCl at 100°C , $\pm 533(\text{MPa})$ 2(Hz) $R=-1$. $N_f = 65828$

The comparison of the results is not possible as the author was unable to find details of any similar pulsed potential fatigue testing in the literature. However, interrupted corrosion fatigue tests have been reported since the pioneering work of McAdam

[95]. McAdam conducted fatigue tests where specimens were subjected to varying numbers of cycles in a corrosive environment, the environment was then removed and the specimen was fatigued in air until failure. Later work by Simnad and Evans [148] and Rollins et al [147] was of a similar theme. Simnad and Evans [146] subjected specimens of cold-drawn mild steel to varying periods of fatigue loading in potassium chloride solution before fatigue loading in air until fracture. Later work by Rollins et al [147] subjected high carbon steel to different periods of fatigue loading in sodium chloride solutions before once again fatigue loading in air until fracture. It is the opinion of the author that the results of pulsed potential experiments conducted in this work would show similar trends as those of both Simnad and Evans [148] and Rollins et al [147].

Figure 138 shows the results of the present work along with earlier results from Simnad and Evans [148] and Rollins et al [147]. It is clear from this graph that although different materials were used in different conditions the same broad trend of a sudden drop in fatigue life is evident, when anodic polarisation produces pitting.

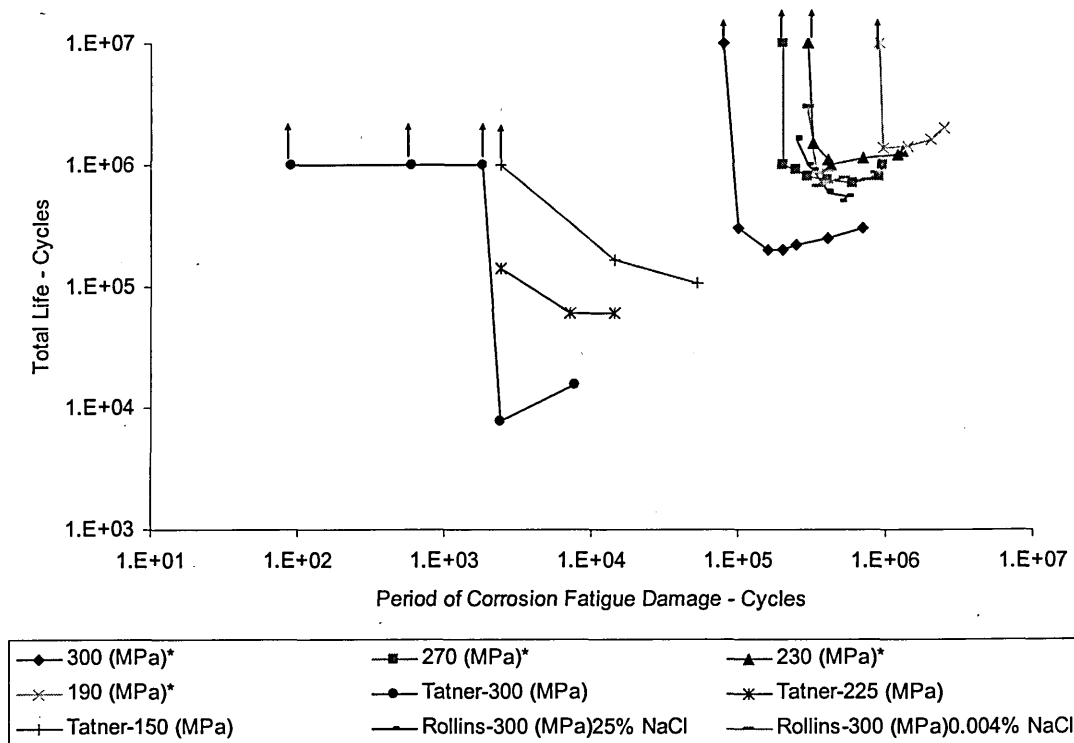


Figure 138 - The Effect of Pulsed Corrosion Damage Fatigue Testing. *=Simnad and Evans Mild Steel Corrosion Fatigue in 0.1M Potassium Chloride Solution at 100 (Hz). Rollins et al High Carbon Steel Tested at 25 (Hz). Tatner FV520B Corrosion Fatigue in 0.3% NaCl at +200(mV)_{Ag/AgCl} ±75 (MPa), 2(Hz), then Fatigue in Solution, FCP at Stress Level Indicated Until Failure. Arrow Indicates No Failure.

5.5.7 Modelling of Pulsed Corrosion Testing Threshold

Figure 138 shows the results of pulsed corrosion potential corrosion fatigue testing.

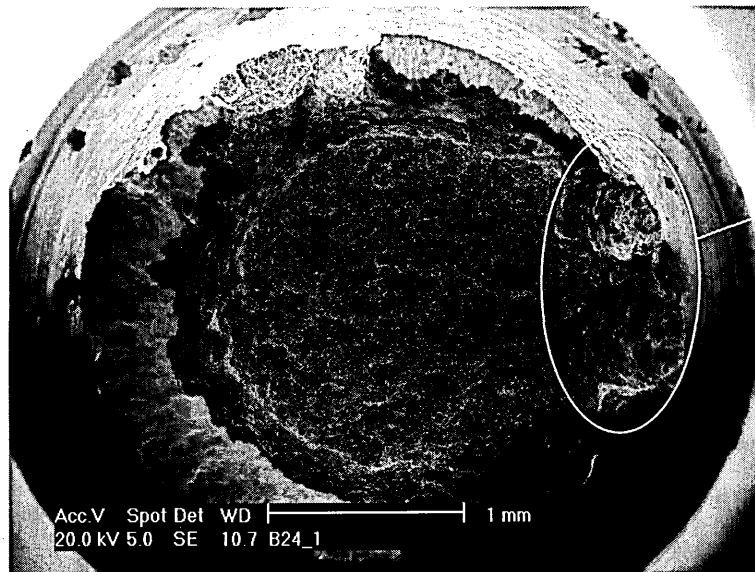
As was previously discussed there is a clear threshold below which the specimens do not fail within the 10^6 cycle cut off used in the current testing. This threshold was also seen in similar tests conducted by earlier authors [95,146-148]

Duration at +200(mV) _{Ag/AgCl}		
$\Delta\sigma$ (MPa)	Cycles	Time (s)
600	1800	900
450	2100	1050
150	2400	1200

Table 22 - Threshold Conditions From Pulsed Corrosion Potential Corrosion Fatigue Testing

It can be seen from Table 22 that the threshold condition is a function of applied stress range, with duration at +200 (mV) for the threshold condition increasing as the stress range lowers. Linear elastic fracture mechanics were used to model the threshold condition to assess whether there was a constant threshold that existed regardless of stress range or duration at +200(mV).

All the specimens were fatigue at a stress of ± 75 (MPa) while the corrosion potential was applied, it is therefore possible to ignore any changes in pit growth that may have resulted from the combination of different stress levels and corrosion potential. The specimens at the threshold condition did not fail. Therefore it was not possible to measure corrosion pit depth. To expose the pit depths the specimens were soaked in liquid nitrogen for a short time and then fractured to reveal the fracture surfaces shown in Figure 139 and Figure 140.



Shown at higher magnification
in Figure 141.

**Figure 139 - Fracture Surface of a Specimen Subjected to 1800 Cycles at $+200(\text{mV})_{\text{Ag/AgCl}}$
 $\pm 75(\text{MPa})$ Prior to Testing at FCP at $\pm 300(\text{MPa})$ at 100°C in 0.3% NaCl. Specimen did not Fail
During Test and was Subsequently Pulled to Cause Failure.**



Shown at higher magnification
in Figure 142

**Figure 140 - Fracture Surface of a Specimen Subjected to 2400 Cycles at $+200(\text{mV})_{\text{Ag/AgCl}}$
 $\pm 75(\text{MPa})$ Prior to Testing at FCP at $\pm 150(\text{MPa})$ at 100°C in 0.3% NaCl. Specimen did not Fail
During Test and was Subsequently Pulled to Cause Failure.**

Figure 141 shows a higher magnification view of the area indicated in Figure 139.

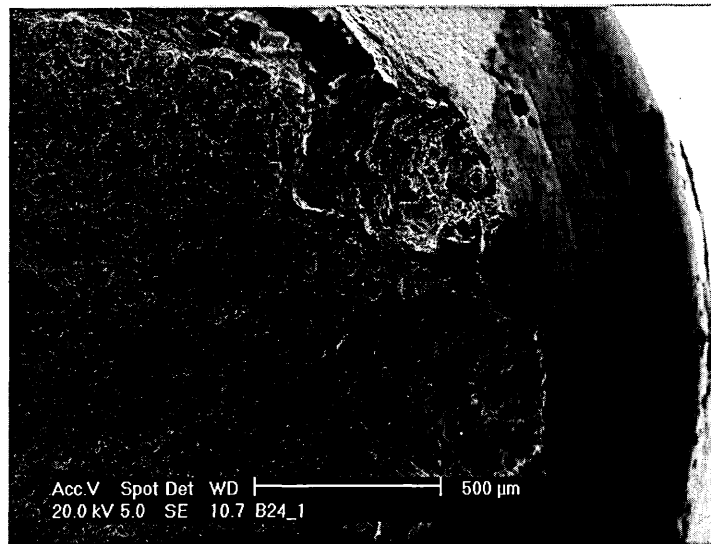


Figure 141 - High magnification of Fracture Surface of a Specimen Subjected to 1800 Cycles at +200(mV)_{Ag/AgCl} ±75(MPa) Prior to Testing at FCP at ±300(MPa) at 100°C in 0.3% NaCl. Specimen did not Fail During Test and was Subsequently Pulled to Cause Failure.

From Figure 141 it can be seen there are two relatively large pits at the origin of the fatigue crack.

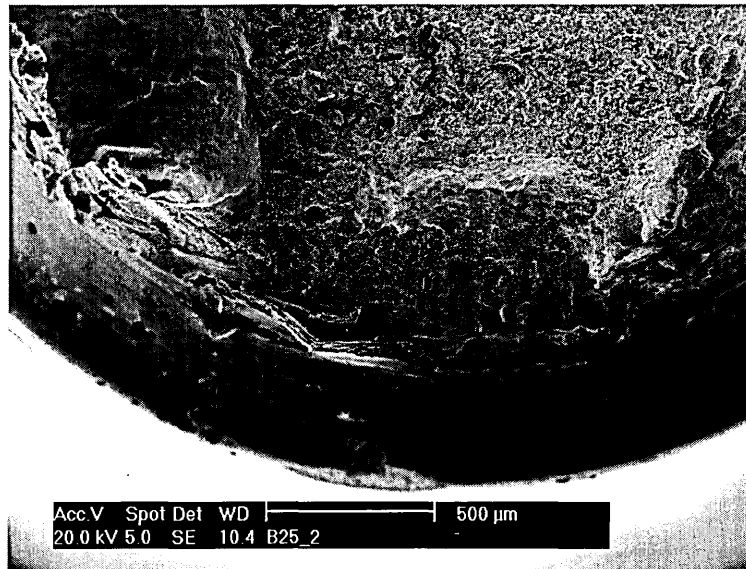


Figure 142 - High magnification of Fracture Surface of a Specimen Subjected to 2400 Cycles at +200(mV)_{Ag/AgCl} ±75(MPa) Prior to Testing at FCP at ±150(MPa) at 100°C in 0.3% NaCl. Specimen did not Fail During Test and was Subsequently Pulled to Cause Failure.

Figure 142 shows a high magnification view of the area outlined in Figure 140, showing a pit, however there is no clear evidence that cracking had initiated.

The corrosion pit depths for both pulsed potential specimens were measured. The stress intensity factor ranges given in Table 23 were calculated using the pit depths. The stress intensity factor ranges were calculated using Equation 2, a value of 0.67 was used for α . Because all pit depths were greater than the notch transition length (l_t) a crack length of the pit depth plus the notch depth was used, see Figure 119, stresses are based on the nominal diameter.

Specimen ID	Stress Amp. (MPa)	Pit Depth (μm)	ΔK ($\text{MPa m}^{1/2}$)
B24	300	384	11.92
B24	300	432	12.24
B25	150	471	6.24

Table 23 - Calculated Pit Depths and Stress Intensity Factor Ranges for Threshold Conditions

It can be seen from Table 23 that the stress intensity range values at the bottom of the pits on specimen B24 are above the threshold value seen previous tests.

At $6.24 \text{ MPa}\sqrt{\text{m}}$ the stress intensity range at the bottom of the pit on specimen B25 is below the threshold and hence there is no evidence of cracking.

5.6 Modelling of Experimental Fatigue Life

5.6.1 Introduction

The following chapter aims predict the lives seen experimentally. The total life will be broken down into two distinct phases; Fatigue crack initiation from a corrosion pit and the propagation of the initiated fatigue crack to complete failure.

5.6.2 Fatigue Crack Initiation from a Corrosion Pit

As discussed in the Literature Review (p. 42) a number of works have found good correlation between the number of cycles to initiate a fatigue crack from a blunt

notch and $\frac{\Delta K}{\rho^{1/2}}$, [53-60].

Jack and Price [53] proposed the following relationship (Equation 42) that relates the number of cycles to initiate a crack from a blunt notch to the stress intensity factor range;

Equation 42

$$N_i = D\Delta K^{-4}$$

where D is a constant.

Jack and Price [53] noted that when the number of cycles to initiate a crack was equal to $\frac{1}{2}$, the value of stress intensity factor range (ΔK) showed good correlation with the fracture toughness (ΔK_c) of the material being tested. The fracture toughness of FV520B has previously been found to be $80 (MPa\sqrt{m})$ [5]. Using the fracture toughness values proposed by Clark [5] a value of 2.048×10^7 for the constant D in Equation 42 was calculated. Thus enabling calculation of the number of cycles to

initiate a fatigue crack from a blunt notch. Values of stress intensity factor range were calculated using Equation 2, a crack length transition depth (l_t) was used for calculating the stress intensity factor range for notched specimens (Equation 41). A survey of the pits on fracture surfaces showed that the root radius of the pit is equal to 0.6 of the pit depth, this approach was also used by Kondo [123]. Figure 143 shows the calculated number of cycles to initiate a crack using Equation 42.

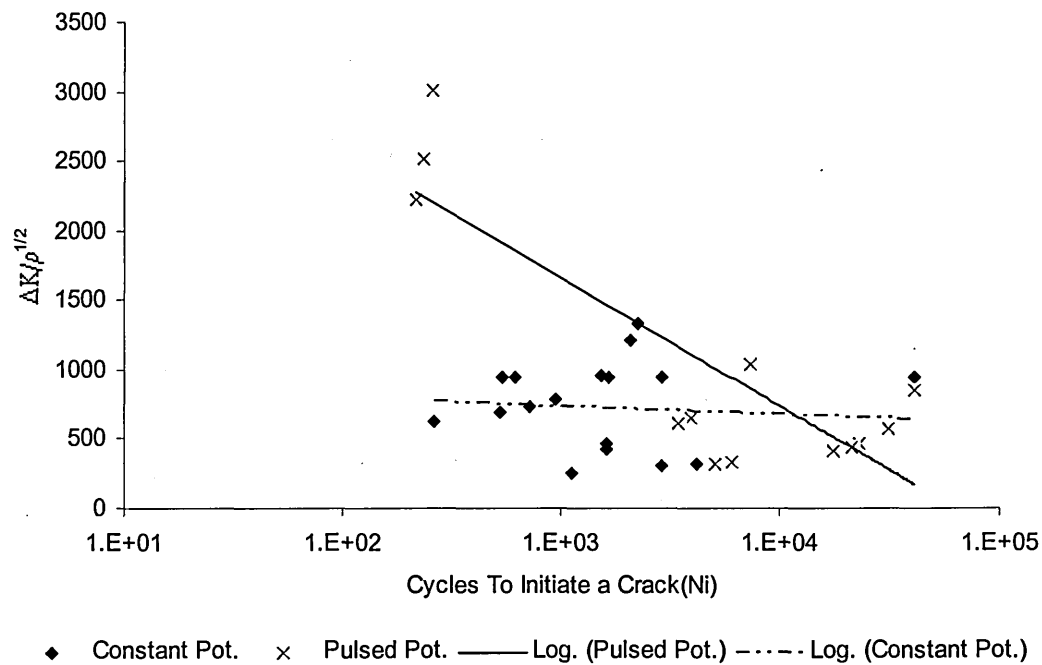


Figure 143 - Number of Cycles To Initiate a Fatigue Crack Versus $\frac{\Delta K}{\rho^{1/2}}$.

The number of cycles to initiate a fatigue crack whilst under a constant applied

anodic potential is independent of $\frac{\Delta K}{\rho^{1/2}}$. The reason for this lack of dependence is

due to the accelerated levels of corrosion seen during the constant applied potential

tests. The high levels of corrosion attack will prevent fatigue cracks forming as the corrosion acts at a faster rate than the fatigue.

Under a pulsed applied potential the number of cycles to initiate a fatigue crack is

seen to be dependent upon $\frac{\Delta K}{\rho^{1/2}}$, this relationship has previously been observed by

several authors, [54,57,58]. Equation 43 was developed to show the relationship

between N_i and $\frac{\Delta K}{\rho^{1/2}}$ observed in this study.

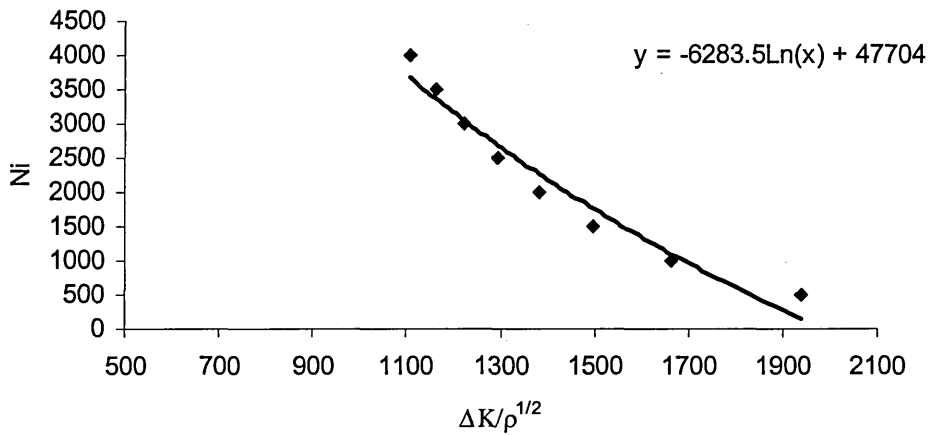


Figure 144 - $\frac{\Delta K}{\rho^{1/2}}$ Versus The Number of Cycles To Initiate a Fatigue Crack During Pulsed

Applied Potential.

Equation 43

$$N_i = -6283.5 \ln \left(\frac{\Delta K}{\rho^{1/2}} \right) + 47704$$

Figure 145 shows the calculated values of N_i from this study with experimental ones from earlier experimental observations.

It can be seen from Figure 145 that there is some scatter at low initiation life, however Figure 145 shows good agreement with the calculated initiation lives and experimental ones taken from the literature.

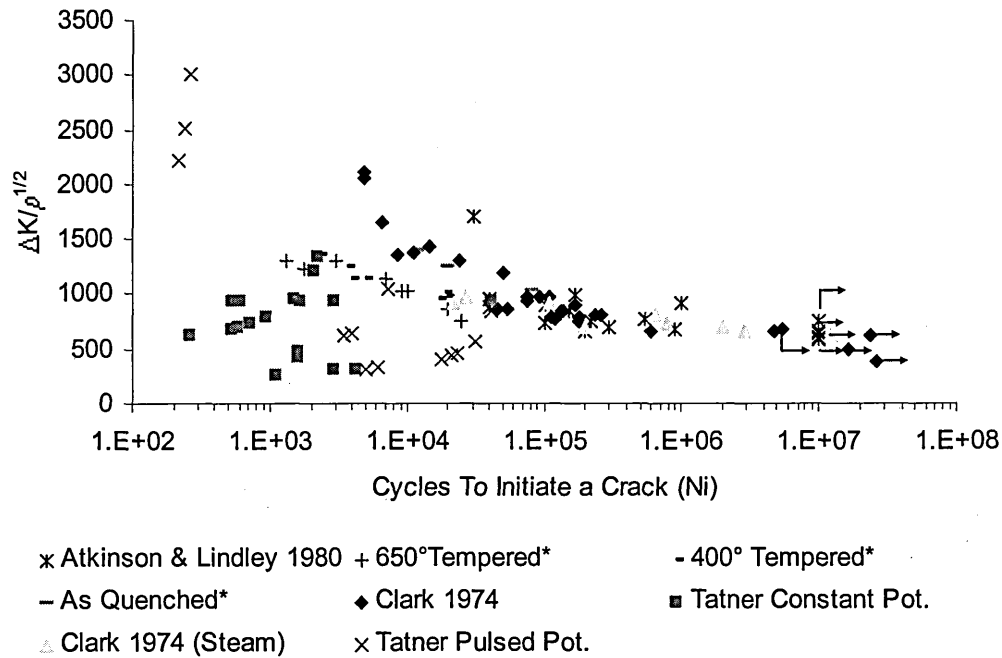


Figure 145 - $\frac{\Delta K}{\rho^{1/2}}$ Versus The Number of Cycles To Initiate a Fatigue Crack For Various Notch

Root Radii. From Atkinson and Lindley 2.5%NiCrMoV 54, *Kim et al 4140 Steel 58 and Clark 403 Type SS 57. With Clark Type 403 SS in Steam at 100°C and Tatner in 0.3% NaCl at 100°C.

5.6.3 Fatigue Crack Propagation

As previously stated the crack growth rate can be related to the stress intensity factor range using Equation 2 and Equation 3 shown respectively below.

$$\Delta K = \alpha \Delta \sigma \sqrt{\pi a}$$

$$\frac{da}{dN} = C(\Delta K)^m$$

Substituting Equation 2 into Equation 3 gives Equation 44.

Equation 44

$$\frac{da}{dN} = C(\alpha\Delta\sigma\sqrt{\pi a})^m$$

Separating variables and integrating (for $m \neq 2$) gives

Equation 45

$$N_f = \int_{a_i}^{a_f} \frac{da}{C(\alpha\Delta\sigma\sqrt{\pi a})^m}$$

This gives,

Equation 46

$$N_f = \frac{2}{(m-2)C(\alpha\Delta\sigma\sqrt{\pi})^m} \left(\frac{1}{a_i^{(m-2)/2}} - \frac{1}{a_f^{(m-2)/2}} \right)$$

Before Equation 46 could be solved to calculate residual life from an initial defect size (a_i) one must know the final or critical crack size (a_f). Rearranging Equation 2 gives Equation 47

Equation 47

$$a = \frac{1}{\pi} \left(\frac{\Delta K}{\alpha\Delta\sigma} \right)^2$$

For the critical crack condition when $a = (a_f)$ Equation 47 can be rewritten as;

Equation 48

$$a_f = \frac{1}{\pi} \left(\frac{K_c}{\alpha \sigma_{\max}} \right)^2$$

where

K_c = Fracture Toughness (MPa \sqrt{m})

The fracture toughness of FV520B was reported as 80 (MNm^{-3/2}) by Clark [5]. Using the values used previously in this work ($\alpha = 0.67$, $A = 10^{-11}$ and $m = 3$) the following graphs were produced the corrosion pit depth was taken as the initial defect size. For notched specimen, see figure Figure 119.

$$a = l, \text{ when } l < l_t$$

$$a = l + D \text{ when } l > l_t$$

Stresses were calculated based on the nominal cross section.

The calculated propagation lives in cycles are plotted with the calculated propagation lives in Figure 146. Experimental propagation life was calculated by subtracting the calculated initiation life from the total life observed experimentally.

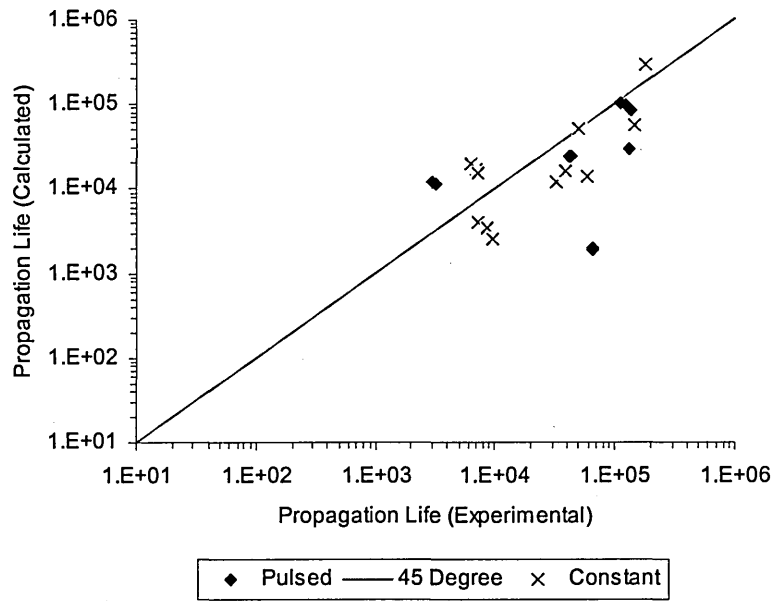


Figure 146 - Calculated Crack Propagation Life Versus Experimental Crack Propagation Life

5.6.4 Calculation of Total Life

By summing the number of cycles to initiate a fatigue crack (N_i) and the number of cycles to propagate an initiated crack to failure (N_p) the total life of a specimen may be found.

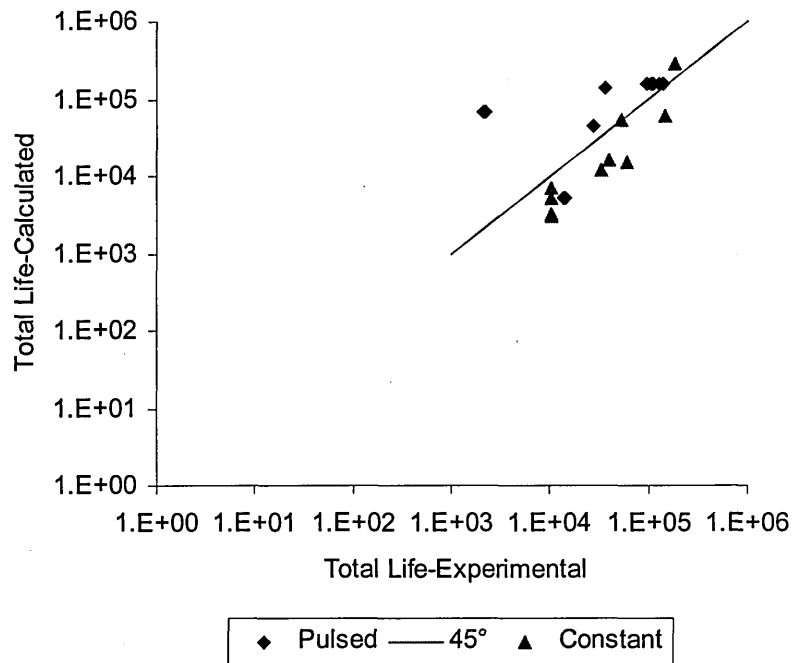


Figure 147 - Experimental Values of Total Life Versus Calculated Values.

Figure 147 shows total life gained through experiment plotted against calculated total life, this plot shows more clearly the broad correlation between calculated and experimental values.

This approach does not account for time period required to initiate and grow a corrosion pit to a point where fatigue cracking will initiate. Assuming corrosion pit growth will cease once a fatigue crack has initiated, [123], it can be postulated that the total life of the specimens will be gained with the addition of the time period to

cause the corrosion pit depth/notch root radius that lead to a fatigue crack initiating as is evident on the fracture surface.

5.7 The Effect of The Number of Start-Up Cycles on The Life of a Steam Turbine Blade

5.7.1 Introduction

In the introduction to this thesis it was stated that since privatisation the number of steam turbine generator sets being operated on a two-shifting basis had increased. Testing has been completed on FV520B a steam turbine blade material to show the effect of transient damage similar to that seen during the start-up and shut-down of a steam turbine. The following model is based upon the testing and aims to show that the number of start-up and shut-down cycles a steam turbine blade is subjected to will have a drastic effect on its servicable life.

5.7.2 Assumptions

The model is based on a corrosion pit growing to a critical size leading to fatigue crack initiation. This critical pit size is a function of applied stress and is generally expressed a threshold stress intensity factor. Several authors have produced models based on this approach [83,104,106,122,123]. The fundamental philosophy of the approach is evident in Figure 148. Kitagawa and Takahashi [149] first found the effect when studying the growth of short cracks initiated from very small surface notches. As the corrosion pit propagates it moves from the safe area in Figure 148 across the fatigue threshold represented by the sloping line. Beyond the fatigue threshold cracks will initiate and then propagate to failure.

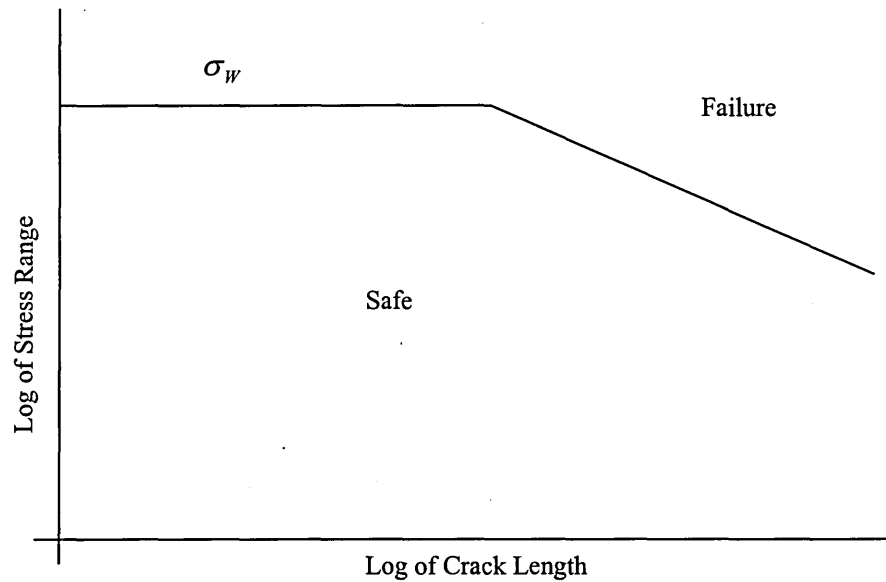


Figure 148 - Effect of Crack Length on Fatigue Thresholds

In the present work it was found that a stress level/crack length combination giving a stress intensity factor of $10 \text{ MPa}\sqrt{\text{m}}$ was sufficient to cause a fatigue crack to initiate and propagate to failure.

Sparkes et al [106] produced a pit growth law to calculate maximum pit depth (d) with respect to immersed time for unstressed NiCrMoV steels in 65°C condensing steam, see Equation 49 [106].

Equation 49

$$d = 9.97 t^{0.47}$$

Pit growth laws of this form have been used with success by several authors to model the growth of corrosion pits with respect to time, see p.63.

Using Equation 49 and assuming one start-up/shut-down cycles is equal to 36 hours immersed in 65°C condensing steam the affect of the number of start-up/shut-down cycles on corrosion pit depth was calculated, see Figure 149.

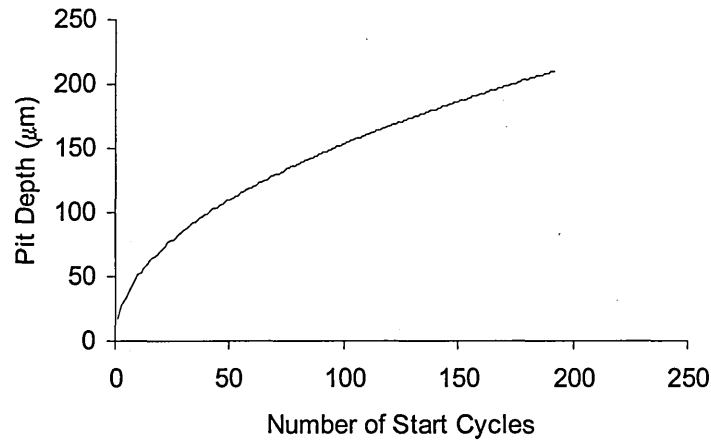


Figure 149 - Pit Size Versus The Number Of Start Cycles For A Steam Turbine Blade.

The pit sizes in Figure 149 were used to calculate the stress intensity factor ranges in Figure 150.

The stress intensity factor ranges were calculated using Equation 2.

$$\Delta K = \alpha \Delta \sigma \sqrt{\pi a}$$

where,

$$\alpha = 0.67$$

$$\Delta \sigma = 600 \text{ (MPa) whilst the turbine is running at full speed.}$$

$$a = \text{Pit depth (m).}$$

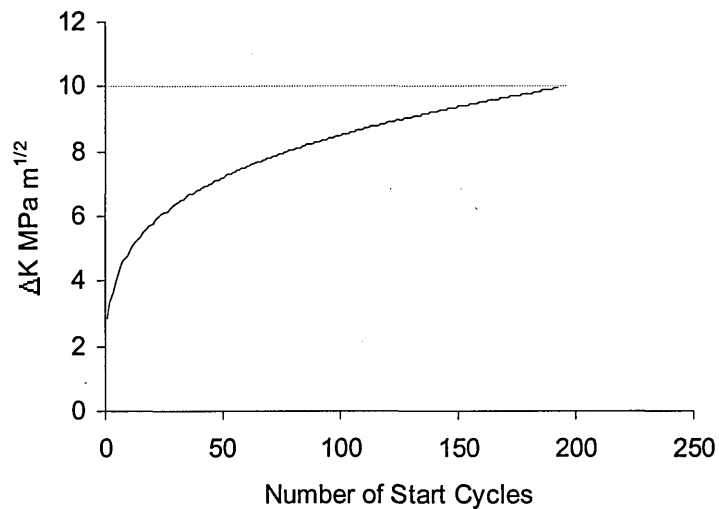


Figure 150 - A Graph To Stress Intensity Factor Range (MPa m^{1/2}) Versus The Number Of Start Cycles For A Steam Turbine Blade.

In the current work it was found there is a characteristic value of stress intensity factor range (10 MPa \sqrt{m}) below which cracks will not propagate. This limiting value has been plotted on Figure 150. Once a stress intensity factor of 10 MPa \sqrt{m} is reached it is assumed that a fatigue crack will propagate in the blade.

Figure 151 shows how the number of start cycles affects the life of the turbine blade based on the time period before the threshold stress intensity factor range is reached.

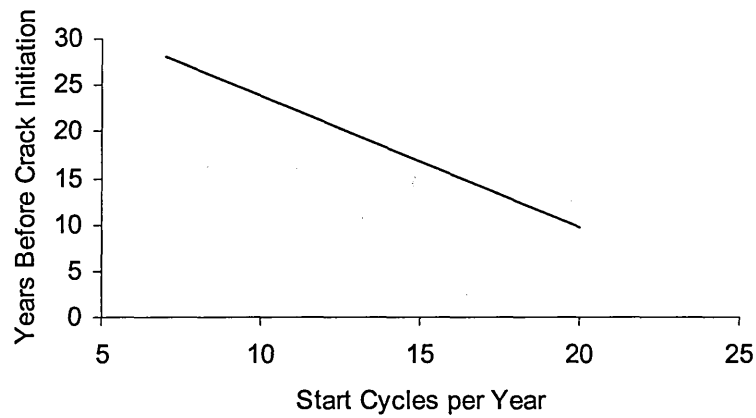


Figure 151 - The Number of Start Cycles Versus Life Prior To Crack Initiation In A Turbine Blade.

Although the pit growth law parameters used may be in correct for an FV520B blade it is believed this model is a good demonstration of the effect that two shifting can have on the serviceable life of a steam turbine blade. The model is sensitive to the variables that have been seen in the current work to affect the serviceable life of a peak hardened FV520B specimen when subjected to intermittent aggressive low load and non aggressive high load conditions. Improvements to the model could be made by producing a pit growth law based on the growth of pits on blades as a function of the number of start cycles. Possible applications of the model include use to schedule preventative maintenance. Pits found to be approaching the transition size could be polished out to prevent fatigue crack initiation.

6 Conclusions

The investigation lead to the following conclusions;

- A method allowing the fatigue testing of notched and plain specimens in high temperature solutions at varying corrosion potentials was developed.
- There is a clear transition between corrosion damage and fatigue damage. The point of transition is dependent upon applied stress range.
- A fracture mechanics type approach was used to normalise transition depth for applied stress. It was found a threshold or transition stress intensity factor range or approximately $10 \text{ MPa } \sqrt{m}$ for FV520B exists below which crack will not propagate.
- FV520B in the softened overaged condition shows a TRIP effect during slow strain rate testing.
- The presence of a notch on a FV520B specimen has no effect on the number of cycles to failure when tests are conducted in aggressive environments.
- The notch response of both FV520B and 18 Ni maraging steels can be predicted using plain fatigue data.
- A good correlation was found to exist between the number of cycles to initiate a fatigue crack from a notch and $\frac{\Delta K}{\rho^{1/2}}$.
- By combining the calculated number of cycles to initiate a fatigue crack from a pit with residual life calculated using fracture mechanics a total

fatigue life was calculated. The total calculated fatigue lives compare well with those found experimentally.

- A model has been produced to show how the number of start-up cycles a steam turbine is subjected to will effect the period of service before a propagating crack will form.

7 Future Work

- The rig designed to carry out the tests in the current work is versatile and will allow for tests to be conducted under a range of environmental (chloride, O₂, temperature) and stress (stress ratio, notch geometry) conditions.
- Empirical determination of the Paris constants for FV520B in air and an aggressive environment will allow a more accurate calculation of the corrosion growth rate at the point of transition from corrosion to fatigue.
- Further testing and X-ray analysis will aid understanding of the TRIP effect seen during SSRT of FV520B in the softened overaged condition
- Detailed electrochemical work should be conducted to allow the number of cycles to grow a pit large enough to cause a threshold stress intensity factor of 10 MPa \sqrt{m} . This work would allow a calculation of the total corrosion fatigue life.

8 References

1 *Starr F. Following the Load - An Unsuitable Job for a Power Plant? Materials World. pp 13-15 April 2001.*

2 *Ward J. The Trials of Life. Engineering. Vol. 244 No. 3. pp. 31-33.*

3 *Lindley T. C. Fatigue Cracking in Power Plant. In Fatigue 93, The 5th International Conference on Fatigue and Fracture Thresholds Vol. 3. Canada 3-7 May 1993.*

4 *Atkinson J. D. 2002 Private Communication.*

5 *Clark A. Fatigue Mechanisms in FV520B, A Turbine Blade Steel. PhD. Sheffield Hallam University. 1999.*

6 *Rust T. M. and Steltz W. Titanium for Steam Turbine Blades. Journal of Metals. Sep 1982. pp. 42-46.*

7 *Mayer & Nürnberg. From Failure Statistics to Research Program - Study of Corrosion Fatigue Behaviour Under Conditions of Incipient Steam Wetness. In: Jaffee R. I. (ed.) Corrosion Fatigue of Steam Turbine Blade Materials Workshop Proceedings, Palo Alto, California 21-24 September 1981. EPRI 1983.*

8 *Viswanathan R. Jaffee R. & Syrett B. Corrosion Problems in Steam Turbines and Nuclear Power Stations. 10th ICMC. 1988. pp2601-2616.*

9 *Atkinson J.D. 2001 Private Communication.*

10 *Schofield M. J. and Kane R. D. Defining Safe Use Limits for Duplex Stainless Steel. From Duplex Stainless Steels 91. Ed. Charles J. Vol. . 1991. pp 241-249.*

11 *Leffler B. Stainless - Stainless Steels and Their Properties. 2nd Revised Edition. Avesta Sheffield AB Research Foundation. 1998.*

12 *Birch P. The Effect of Heat Treatment on the Structure and Mechanical Properties of FV520B. A Precipitation Hardening Martensitic Stainless Steel. BSc. Project Thesis. Sheffield City Polytechnic. 1984.*

13 *Jaffee R. I. Foreword. In: Jaffee R. I. (ed.) Corrosion Fatigue of Steam Turbine Blade Materials Workshop Proceedings, Palo Alto, California 21-24 September 1981. EPRI 1983.*

14 *Starr F. Private Communication 2002.*

15 *Ernst and Newman. Pit Growth Studies in Stainless Steel Foils. I. Introduction and Pit Growth Kinetics. Corrosion Science Vol. 44. 2002. pp927-941.*

16 *Panasyuk and Ratych. Inhibitor Protection of Metals at the Corrosion Fatigue Crack Growth Stage. Corrosion Science Vol. 51.1995.*

17 *Denk and Scarlin Private Communication 1996.*

18 *Jarman R.A. Burstein G.T. and Shreir L.L. Corrosion, Eds. Corrosion Vol.1 Metal/environment reactions. Edition 3rd ed. Published Butterworth-Heinemann, 1994.*

19 *Floreen S. The Physical Metallurgy of Maraging Steels. Metallurgical Reviews. Vol. 13 No. 126. September 1968. pp. 115-128.*

20 *Contractor G.P. The Marvel of Maraging - Some Aspects of 18 Ni-Co-Mo Steel. Journal of Metals. August 1966.*

21 *Wilson E A. Private Correspondence. 2002..*

22 *Honeycombe R.W.K. Steels : Microstructure and Properties. E. Arnold 1981.*

23 **Pickering F.B.** *Physical Metallurgy and the Design of Steels* . Applied Science Publishers. 1978.

24 **Hammond C.M.** *The Development of Marageing Stainless Steels Containing Cobalt*. *Cobalt Vol. 25*. 1964. pp.195-202.

25 **Pickering F.** *Physical Metallurgical Development of Stainless Steels*. In: *Stainless Steels 84*. Gothenburg Sweden 1984. In: Lindgren L. Domkin K. *Modelling of Austenitic Stainless Steel Properties*. 2002 (work in progress). [online] Last accessed on 23/04/2003 at URL: http://www.users.du.se/~kdo/kk-project/publications/Austenitic_stainless_steels.pdf.

26 **Fahr D.** *Stress- and Strain-Induced Formation of Martensite and Its Effects on Strength and Ductility of Metastable Austenitic Stainless Steels*. *Metallurgical Transactions*. Vol. 2. 1971. pp. 1883-1892.

27 **Zackay V. Parker E Fahr D. and Busch R.** *The Enhancement of Ductility in High-Strength Steels*. *Transactions of the American Society of Metals*. Vol. 60. 1967. pp. 252-259.

28 **Atsmon N. and Rosen A.** *Reverted Austenite in Marageing Steel*. *Metallography*. Vol. 14. 1981. pp. 163-167.

29 **Markfeld A. and Rosen A.** *The Effect of Reverted Austenite on the Plastic Deformation of Maraging Steel. Materials Science and Engineering. Vol. 46. 1980. pp. 151-157.*

30 **Bressanelli J.P. and Moskowitz A.** *Effects of Strain Rate, Temperature, and Composition on Tensile Properties of Metastable Austenitic Stainless Steels. Transactions of the American Society of Metals. Vol. 59. 1966. pp. 223-239.*

31 **Gorkunov E.S. Rigmant M.B. Gladkovsky S.V. Matafonov P.P. and Smirnov S.V.** *Non-destructive Magnetic Inspection of Elastoplastic Strains in Metastable Austenitic Steels. In: 15th World Conference on Nondestructive Testing. Roma, Italy. Oct 15-21 2000. [online] Last accessed on 23/04/2003 at URL:<http://www.ndt.net/article/wcndt00/papers/idn028/idn028.htm>.*

32 **Kenyon N.Kirk W.W. Van Rooyen D.** *Corrosion of 18Ni 180 and 18Ni 200 Maraging Steels in Chloride Environments. Corrosion. Vol.29 No. 9. 1971. pp.390-400.*

33 **Cottis R. A. and Husain Z.** *Corrosion-Fatigue Initiation Processes in a Maraging Steel. Metals Technology. Vol. 9. 1982. pp. 104-108.*

34 **Alp T. Husain Z. and Cottis R.A.** *Corrosion Fatigue Crack Initiation and Growth in 18 Ni Maraging Steel. Journal of Material Science. Vol. 21. 1986. pp. 3263-3268.*

-
- 35 **Wöhler A.** *Wöhlers Experiments on The Fatigue of Metals. Engineering Vol. 11.* 1871. pp199-200.
- 36 **Hood C.** 1842. *Phil. Mag. Series 3, 21, 130.* In Mann J. Y. 1958. *The Historical Development of Research on The Fatigue of Materials and Structures. The Journal of The Australian Institute of Metals. Vol. 3 No. 3. 1958. pp 222-241.*
- 37 **Mann J. Y.** *The Historical Development of Research on The Fatigue of Materials and Structures. The Journal of The Australian Institute of Metals. Vol. 3 No. 3. 1958. pp 222-241.*
- 38 **Frost N.E. Marsh K.J. and Pook L.P.** 1974. *Metal Fatigue. Oxford University Press.*
- 39 **Metal Improvement Company.** [online]. last accessed on 18 November 2002 at URL: <http://www.metalimprovement.com>.
- 40 **Bannantine J.A. Comer J.J. Handrock J. L.** 1990 *Fundamentals of Metal Fatigue Analysis. Prentice Hall. 1990.*
- 41 **Laird and Duquette.** *Mechanisms of Fatigue Crack Nucleation. In Devereux O. McEvily A.J. and Staehle R.W. (eds.) Corrosion Fatigue: Chemistry, Mechanics, and Microstructure. Conference held at University of Connecticut, June 14-18, 1971. Volume published in 1973 by NACE.*

42 *Forsyth P.J.E. Some Metallographic Observations on The Fatigue of Metals.*

Journal of The Institute of Metals. Vol. 80. 1951. pp. 181-186.

43 *Suresh 1999. Fatigue of Materials. Cambridge University Press.*

44 *Paris P.C. and Erdogan F. A Critical Analysis of Crack Propagation laws.*

Journal of Basic Engineering Vol. 85. 1963. pp. 528-534.

45 *Higgins R. A. The Properties of engineering materials. 2nd ed. Industrial Press, 1994.*

46 *Masounave J. and Baflon J.P. Effect of Grain Size on the Threshold Stress*

Intensity Factor in Fatigue of a Ferritic Steel. Scripta Metallurgica. Vol. 10. 1976. pp. 165-170.

47 *Taira S. Tanaka K. and Hoshina M. Grain Size Effect on Crack Nucleation and*

Growth in Long-Life Fatigue of Low-Carbon Steel. In; Fong J.T. (Ed.) Fatigue

mechanisms. Proceedings of an ASTM-NBS-NSF Symposium. Kansas City Mo.22-24 May 1978. ASTM STP 675 1979. pp134-173.

48 *Yoder G.R. Cooley L. A. and Crooker T.W. Quantitative Analysis of*

Microstructural Effects on Fatigue Crack Growth in Widmanstätten Ti-6Al-4V and

Ti-8Al-1Mo-1V. Engineering Fracture Mechanics. Vol. 11. 1979. pp. 805-816.

49 **Dowling N. E.** *Mechanical Behaviour of Materials: Engineering Methods for Deformation, Fracture and Fatigue.* Prentice-Hall 1993.

50 **Hammouda M. M. Smith R. A. & Miller K. J.** *Elastic-Plastic Fracture Mechanics For Initiation and Propagation of Notch Fatigue Cracks. Fatigue and Fracture of Engineering Materials and Structures. Vol. 2 1979. pp.139-154.*

51 **Smith & Miller.** *Fatigue Cracks at Notches. International Journal of Mechanical Sciences. Vol. 19.1977. pp. 11-22.*

52 **Smith R. A. & Miller K. J.** *Prediction of fatigue Crack Regimes in Notched Components. International Journal of Mechanical Sciences. Vol. 20. 1978. pp. 201-206.*

53 **Jack A.R. and Price A.T.** *The Initiation of Fatigue Cracks from Notches in Mild Steel Plates. International Journal of Fracture Mechanics. Vol. 6 No. 4. Dec 1970. pp. 401-409.*

54 **Atkinson J. D. Lindley T.C.** *Fatigue Crack Initiation at Notches In a 2.5% NiCrMoV Rotor Steel. Central Electricity Research Laboratories Report RD/L/N 38/80. February 1980.*

55 **Jack A.R. and Price A.T.** *Effects of Thickness on Fatigue Crack Initiation and Growth in Notched Mild Steel Specimens. Acta Metallurgica. Vol. 20. July 1972. pp. 857-866.*

56 **Barsom J.M. and McNicol R.C.** *Effect of Stress Concentration on Fatigue - Crack Initiation in HY-130 Steel. In; Fracture Toughness and Slow - Stable Cracking: Proceedings of the 1973 National Symposium on Fracture Mechanics, Part 1. University of Maryland. 27-29 August 1973. ASTM STP 559 1974. pp. 183-204.*

57 **Clark W.G.** *Evaluation of the Fatigue Crack Initiation Properties of Type 403 Stainless Steel in Air and Steam Environments. In; Fracture Toughness and Slow - Stable Cracking: Proceedings of the 1973 National Symposium on Fracture Mechanics, Part 1. University of Maryland. 27-29 August 1973. ASTM STP 559 1974. pp. 205-224*

58 **Kim Y.H. Mura T. and Fine M.E.** *Fatigue Crack Initiation and Microcrack Growth in 4140 Steel. Metallurgical Transactions A. Vol. 9A. November 1978. pp. 1679-1683.*

59 **Rolfe S.T. and Barsom J.M.** *Fracture and Fatigue Control in Structures, p213, Prentice-Hall, Englewood Cliffs, N.J. 1977. In: Kim Y.H. Mura T. and Fine M.E. 1978. Fatigue Crack Initiation and Microcrack Growth in 4140 Steel. Metallurgical Transactions A. Vol. 9A. November 1978. pp. 1679-1683.*

60 **Barsom J.M.** *Concepts of Fracture Mechanics - Fracture and Fracture Control.* Unpublished Report U.S. Steel Corp. Monroeville. Pa 1977. In Kim Y.H. Mura T. and Fine M.E. 1978. *Fatigue Crack Initiation and Microcrack Growth in 4140 Steel.* Metallurgical Transactions A. Vol. 9A. November 1978. pp. 1679-1683.

61 **Yates J. R. & Brown M. W.** *Prediction of the length of Non-Propagating Fatigue Cracks.* *Fatigue and Fracture of Engineering Materials and Structures.* Vol. 10 No. 3 1987. pp.187-201.

62 **Pickering F.B.** *Some Effects of Non-Metallic Inclusions on the Properties of steels.* In: 31st Mechanical Working and Steels Processing held in Illinois USA 22-25 Oct 1989. pp.381 401.

63 **Atkinson M.** *The Influence of non-metallic inclusions on the fatigue properties of ultra-high-strength steels.* *Journal of the Iron and Steels Institute* Vol. 195 1960. pp. 64-75.

64 **Lankford J. & Kusenburger F. N.** *Initiation of Fatigue Cracks in 4340 Steel.* *Metallurgical Transactions* Vol. 4 1973. pp. 553-559.

65 **Brooksbank D. and Andrews K. W.** *Thermal Expansion of Some Inclusions Found in Steels and Relation to Tessellated Stresses.* *Journal of The Iron and Steel Institute.* Vol. 206. 1968. pp. 595-599

66 **Kiessling R.** 1989 *Inclusions in Steel. Part V. The Institute Of Metals London*

67 **Murakami Y. & Endo M.** *Quantitative Evaluation Of Fatigue Strength Of Metals Containing Various Small Defects Or Cracks. Engineering Fracture Mechanics Vol. 17 No. 1 1983. pp. 1-15.*

68 **Frost N.E.** *A Note on the Behaviour of Fatigue Cracks. Journal of Mechanics of Physical Solids, Vol. 9. 1961. pp 143-151.*

69 **Congleton J. Wilks T.P.** *The Air Fatigue and Corrosion Fatigue of a 13% Cr Turbine Blade Steel. Fatigue and Fracture of Engineering Materials and Structures. Vol. 11 No. 2. 1988. pp. 139-148*

70 **Kobayashi H. & Nakazawa H.** *In: The Proceedings of the 1st International Conference of the Mechanical Behaviour of Materials. Japan. Vol. II. 1969 pp 199-208.*

71 **Murakami Y. Kodama S. and Konuma S.** *Quantitative Evaluation of Effects of Non-Metallic Inclusions on the Fatigue Strength of High Strength Steels. In: Basic Fatigue Mechanisms and Evaluation of Correlation Between the Fatigue Fracture Stress and the Size and Location of Inclusions. International Journal of Fatigue. Vol. 11 No. 5 1989. pp. 291-298.*

72 **Sedriks A.J.** *New Stainless Steels for Seawater Service. Corrosion. Vol. 45 No.6. June 1989. pp. 510-518*

73 **Isaacs H. S.** *The Localized Breakdown and Repair of Passive Surfaces During Pitting. Corrosion Science. Vol. 29 No.2/3. 1989. pp 313-323.*

74 **Rosenfeld I. L and Danilov I.S.** *Electrochemical Aspects of Pitting Corrosion. Corrosion Science. Vol. 7. 1967. pp129-142.*

75 **Burstein G.T. Pistorius P.C. and Mattin S.P.** *The Nucleation and Growth of Corrosion Pits on Stainless Steel. Corrosion Science. Vol. 35. 1993. pp 57-62.*

76 **Scully.** *The Fundamentals of Corrosion. 3rd Ed. Published Pergamon. 1990.*

77 **Ernst P. Laycock N.J. Moayed M.H. and Newman R.C.** *The Mechanism of Lacy Cover Formation in Pitting. Corrosion Science. Vol. 39 No. 6. 1997. pp. 1133-1136.*

78 **Rowe L. C.** *The Measurement and Evaluation of Pitting Corrosion. In: Galvanic and Pitting Corrosion – Field and Laboratory Studies, ASTM STP 576, American Society for Testing and Materials, 1976, pp. 203-216.*

79 **Mulvihill P.** *The Effect of Growing Corrosion Pits on The Fatigue Properties of a Low Pressure Turbine Rotor Steel. CEGB Research Report RD/L/3378/R88. December 1988.*

80 *ASTM G46 – 94 Standard Guide for Examination and Evaluation of Pitting Corrosion. ASTM Standard.*

81 *Godard H. P. The Corrosion Behaviour of Aluminium in Natural Waters. Canadian Journal of Chemical Engineering. Vol. 38. October 1960. In ASTM G46 – 94 Standard Guide for Examination and Evaluation of Pitting Corrosion. ASTM Standard.*

82 *Akid R. and Dmytrakh I. Influence of Surface Deformation and Electrochemical Variables on Corrosion Fatigue Crack Development. Fatigue and Fracture of Engineering Materials and Structures. Vol. 21 No. 7. 1998.*

83 *González-Sánchez J. A. Corrosion fatigue Initiation in Stainless Steels: The Scanning Reference Electrode Technique. Ph. D. Sheffield Hallam University. 2002.*

84 *Harlow D. & Wei R. P. A. Probability Model For The Growth Of Corrosion Pits In Aluminium Alloys Induced By Constituent Particles. Engineering Fracture Mechanics. Vol. 59 No. 3. 1999. pp. 305-325.*

85 *Dmytrakh I. M. Akid R. Miller K.J. Electrochemistry of Deformed Smooth Surfaces and Short Corrosion Fatigue crack Growth Behaviour. British Corrosion Journal. Vol. 32 No. 2. 1997.*

86 *Panasyuk V.V. Dmytrakh, I.M. Pluvinage, G and Qylafku, G. Corrosion Fatigue Emanating from Notches: Stress Field and Electrochemistry. Materials Science. Vol. 37 No. 2. 2001. pp. 184-198.*

87 *Hetterley L. The Initiation of Pits at Inclusions in FV520B Martensitic Stainless Steel. CERL. Laboratory Note No. RD/L/N 164/78. 1978.*

88 *Srivastava S.C. and Ives M.B. Dissolution of Inclusions in Low Alloy Steel Exposed to Chloride Containing Environments. Corrosion. Vol. 43 No. 11. 1987. pp. 687-692.*

89 *Janik-Czachor N. Szummer A and Szklarska-Smialowska Z. Effects of Sulphur and Manganese on Nucleation of Corrosion Pits in Iron. British Corrosion Journal. Vol. 7. 1972. pp. 90-93.*

90 *Smialowski M. Szklarska-Smialowska Z Rychcik M. and Szummer A. Effect of Sulphide Inclusions in a Commercial Stainless Steel on the Nucleation of Corrosion Pits. Corrosion Science. Vol. 9. 1969. pp. 123-125.*

91 *Parker J.G. Initiation of Stress Corrosion Cracks in a Low Alloy Steel. British Corrosion Journal. Vol. 8 No. 3. 1973. pp.124-127.*

92 *Trethewey K & Chamberlain J. 1996. Corrosion for Science and Engineering Second Edition. Longman.*

93 **McEvily. A.J and Wei R.P.** *Mechanisms of Fatigue Crack Nucleation. In Devereux O. McEvily A.J. and Staehle R.W. (eds.) Corrosion Fatigue: Chemistry, Mechanics, and Microstructure. Conference held at University of Connecticut, June 14-18, 1971. Volume published in 1973 by NACE.*

94 **Wu X. D.** *Experimental and Theoretical Studies of Corrosion Fatigue in a high Strength Steel. Ph. D. Sheffield University. 1995.*

95 **McAdam.** *Stress-Strain Relationships and Corrosion Fatigue of Metals. ASTM 26. 1926. pp. 224-254.*

96 **Gough.** *Corrosion-Fatigue of Metals. Eleventh Autumn Lecture to the Institute of Metals, Delivered September 12, 1932.*

97 **Talbot D. Martin J. Chandler C. Sanderson M.** *Assessment of Crack Initiation in Corrosion Fatigue by Oscilloscope display of Current Transients. Metals Technology. Vol.9. 1982. pp. 130-134.*

98 **Evans U.R.** *The Corrosion and Oxidation of Metals : Scientific Principles and Practical Applications. 1960. Edward Arnold..*

99 **Duquette and Uhlig.** *Effect of Dissolved Oxygen and NaCl on Corrosion Fatigue of 0.18% Carbon Steel. Transactions of the American Society for Metals. Vol. 61. 1968. pp. 449-456.*

100 **Brown B. F., Fujii C. T. and Dahlberg E. P.** *Methods for Studying the Solution Chemistry Within Stress Corrosion Cracks. Journal for the Electrochemical Society. Vol. 116 No. 2.1969. pp.218-219.*

101 **Sandoz G. Fujii C. T. and Brown B. F.** *Solution Chemistry Within Stress-Corrosion Cracks in Alloy Steels. Corrosion Science. Vol. 10. 1970. pp. 839-845.*

102 **Panasyuk V.V. Ratych L.V. and Dmytrakh I.N.** *Fatigue Crack Growth in Corrosive Environments. Fatigue and Fracture of Engineering Materials and Structures. Vol. 7 No. 1. 1984. pp. 1-11.*

103 **Murtaza G. & Akid R.** *Empirical corrosion fatigue life prediction models of a high strength steel. Engineering Fracture Mechanics. Vol.67. 2000 pp. 461-474.*

104 **Lindley T.C. McIntyre P. Trant P.J.** *Fatigue-Crack Initiation at Corrosion Pits. Metals Technology. Vol. 9. 1982.*

105 **Zhou S. and Turnbull A.** *Influence of Pitting on The Fatigue Life of Turbine Blade Steel. Fatigue and Fracture of Engineering Materials and Structures. Vol. 22. 1999. pp. 1083-1093.*

106 **Sparkes G.M. Mulvihill P. McIntyre P.** *The Implications of Corrosion Pitting for the Refurbishment of Low-pressure turbine rotor shafts. In; Refurbishment and life extension of steam plant. London. 14-15 Oct 1987. ImechE.*

107 **Evans U.R. and Simnad M.T.** *The Mechanism of Corrosion Fatigue of Steel in Acid Solution. Journal of The Iron and Steel Institute. 1947. pp. 531-539.*

108 **Frost N. E.** *The Effect of Environment on the propagation of fatigue cracks in mild steel. Applied Materials Research. Vol. 3 No. 3. 1964.*

109 **Rollins V. Arnold B. and Lardner E.** *Corrosion Fatigue in High Carbon Steels. British Corrosion Journal. Vol. 5. 1970. pp. 33-40.*

110 **Congleton J. and Parkins R.N.** *Degradation of Mechanical Properties by Corrosion Fatigue. Journal of Mechanical Engineering Science. Vol. 203. 1989. pp. 73-84.*

111 **Patel C. Pyle T. and Rollins V.** *The Influence of Cyclic Plastic Deformation on Electrode Reactions on Mild Steel in Aqueous Chloride Solutions of Varying pH. Metal Science. 1977. pp 185-195.*

112 **Hodgkiess T. and Cannon M. J.** *An Experimental Study of Crack -Tip Electrochemistry During Corrosion Fatigue of Structural Steel in Sea Water. IMechE C146/86. 1986. pp. 69-76.*

113 **Brown B. F., Fujii C. T. and Dahlberg E. P.** *Methods for Studying the Solution Chemistry Within Stress Corrosion Cracks. Journal for the Electrochemical Society. Vol. 116 No. 2. 1969. pp. 218-219.*

114 **Smith J. A. Peterson M. H. and Brown B. F.** *Electrochemical Conditions at the Tip of an Advancing Stress Corrosion Crack in AISI 4340 Steel. Corrosion. Vol. 26 No. 12.1970. pp. 539-542.*

115 **Barsom J. M.** *Mechanisms of Corrosion Fatigue Below KISCC. International Journal of Fracture Mechanics. Vol. 7 No. 2. 1971. pp.163-182.*

116 **Turnbull A.** *The Solution Composition and Electrode Potential in Pits, Crevices and Cracks. Corrosion Science. Vol. 23 No. 8. 1983. pp. 833-870.*

117 **Panasyuk V.V. Ratych L.V. and Dmytrakh I.N.** *Fatigue Crack Growth in Corrosive Environments. Fatigue and Fracture of Engineering Materials and Structures. Vol. 7 No. 1. 1984. pp. 1-11.*

118 **Cowling M. J. and Appleton R. J.** *Corrosion Fatigue of a C-Mn Steel in Sea Water Solutions. In Fatigue and Crack Growth in Offshore Structures C145/86. London. 7-8 Apr. 1986. pp. 77-92.*

119 **McEvily A.J. and Wei R.P.** *Fracture Mechanics and Corrosion Fatigue. In Devereux O. McEvily A.J. and Staehle R.W. (eds.) Corrosion Fatigue: Chemistry, Mechanics, and Microstructure. Conference held at University of Connecticut, June 14-18, 1971. Volume published in 1973 by NACE.*

120 **Wei R. P. Simmons G. W.** *Recent Progress in Understanding Environment Assisted Fatigue Crack Growth. Journal of Fracture. Vol. 17 No. 2. 1981.*

121 **Wei R.P.** *Environmental Considerations. In Fatigue Crack Growth. Fatigue of Engineering Materials and Structures, Held at University of Sheffield. IMechE Conference Publications 1986-9. 1986.*

122 **Austen I. and Walker E.** *Quantities Understanding of The Effects of Mechanical and Environmental Variables on Corrosion Fatigue Crack Growth Behaviour. In The Influence of Environment on Fatigue, IMechE Conference Publications 1977-4. 1977.*

123 **Kondo.** *Prediction of fatigue Crack Initiation Life Based on Pit Growth. Corrosion Science. Vol. 45 No. 1. 1989.*

124 **Akid R. and Miller K.J.** *Short Fatigue Crack Growth Behaviour of Corrosion Fatigue Conditions. Fatigue and Fracture of Engineering Materials and Structures. Vol. 14 No. 6. 1991.*

125 **Hobson P. B.** *The Growth of Short Fatigue Cracks in a Medium Carbon Steel. Sheffield University. Ph.D. 1985.*

126 *Navarro A. and de los Rios E.R. A Microstructurally-short Fatigue Crack Growth Equation. Fatigue and Fracture of Engineering Materials and Structures. Vol. 11 No. 5 1988.*

127 *El Haddad M.H. Topper T.H. and Topper T.N. Fatigue Life Predictions of Smooth and Notched Specimens Based on Fracture Mechanics. Journal of Engineering Materials and Technology. Vol. 103. April 1981. pp. 91-96.*

128 *Scott and Bamford. The Development and Use of Electrochemical Potential Monitoring in Environment Assisted Cracking Tests in High Temperature, High Pressure, Aqueous Environments. AERE-R11741. April 1985.*

129 *Navas M. and Gomez Briceno M. D. Behaviour of Reference Electrodes in the Monitoring of Corrosion Potential at High Temperature. Nuclear Engineering and Design. Vol. 168. 1997. pp 183-189.*

130 *Amzallag C. Rabbe P. and Desestret A. Corrosion Fatigue Behaviour of Some Special Stainless Steels. pp. 117-132. In: Craig H.L. Crooker T.W. and Hoepfner D.W. (eds.). Corrosion-Fatigue Technology. Held in Denver, Colo. 14-19 Nov. 1976. ASTM STP 642 1978.*

131 *Ebara R. Kino H. Takano Y. Nakashima K and Hatano K. Influence of Dissolved Oxygen Content and Stress Concentration Factor on Corrosion Fatigue Strength of Turbine Moving Blades. In R. I. (ed.) Corrosion Fatigue of Steam Turbine Blade Materials Workshop Proceedings, Palo Alto, California 21-24 September 1981. EPRI 1983.*

132 *Lee and Uhlig. Corrosion Fatigue of Type 4140 High Strength Steel. Metallurgical Transactions. Vol. 3. 1972. pp2949-2957.*

133 *Mehdizadeh P. McGalasson R. L. Landers J.E. Corrosion Fatigue Performance of a Carbon Steel in Brine Containing Air, H₂S and CO₂. Corrosion. Vol. 22 No. 12. 1966. pp 325-335.*

134 *Pettit D.E. Hoepfner D.W. and Hylar W.S. Evaluation of Methods to Alleviate Corrosion Fatigue in Type 135 Drill-Pipe Steel for Offshore-Drilling Applications. pp. 541-257. In; Effects of Environment and Complex Load History on Fatigue Life. Held in Atlanta Ga., 29 Sept-4 Oct 1968. ASTM STP 462 1970.*

135 *Firth Vickers Special Steels Ltd. 1989. FV520B A Precipitation Hardening Martensitic Stainless Steel. Manufactures Material Data Handbook.*

136 *MacDonald. Reference Electrodes for High Temperature Aqueous Systems - A Review and Assessment. Corrosion. Vol. 34 No. 3. 1978. pp. 75-84.*

137 **Danielson**. *A Long-Lived External Ag/AgCl Reference Electrode for Use in High Temperature/Pressure Environments*. *Corrosion*. Vol. 39 No. 5. 1983. pp. 202-203.

138 **Scott P. M. and Bamford W. H.** *The Development and use of Electrochemical Potential Monitoring in Environment Assisted Cracking Tests in High Temperature, High Pressure, Aqueous Environments*. AERE-R11741. April 1985.

139 **Wilson E. A.** *Private Communication* 2002.

140 **Peterson R.E.** *Analytical Approaches to Stress Concentrating Effects in Aircraft Materials*. Technical Report 59-507, U.S. Air Force-WADC Symp. *Fatigue of Metals*, Dayton, Ohio, 1959. In **Bannantine J.A. Comer J.J. Handrock J. L.** 1990 *Fundamentals of Metal Fatigue Analysis*. Prentice Hall. 1990.

141 **Wiegand H.H. Speckhardt and Spann H.** *Archiv fur das Eisennüttenwesen* 40. 1969, S. pp 685-692.

142 **Knott J. and Withey P.** *Fracture Mechanics*. *The Institute of Materials*. 1998.

143 **Smith R. A.** *Propagation of Cracks from Notches*. *Materials Science and Technology*. Vol. 1. July 1985. pp. 537-543.

144 **Xu R. X. Thompson J. C. and Topper T.H.** *Mode I Stress Intensity Factor Equations For Cracks at Notches and Cavities. Fatigue and Fracture of Engineering Materials and Structures. Vol. 20 No. 9. 1997. pp.1351-1361.*

145 **Zhou S. & Turnbull.** *Development of a Pre-pitting Procedure for Turbine Disc Steel. A NPL Report CMMT(B) 282. 1999.*

146 **Simnad M.T. and Evans U.R.** *The Mechanism of Corrosion Fatigue of Steel in Acid Solution. Journal of the Iron and Steel Institute. 1947. pp. 531-539.*

147 **Rollins V. Arnold B. and Lardner E.** *Corrosion Fatigue of High Carbon Steel. British Corrosion Journal. Vol. 5. 1970. pp. 33-40.*

148 **Simnad M.T. and Evans U.R.** *Proceedings of the Royal Society. Series A. Vol. 188. 1947. pp. 372-392.*

149 **Kitagawa H. and Takahashi S.** *Applicability of Fracture Mechanics to Very Small Cracks or The Cracks in The Early Stage. In: Second International Conference on Mechanical Behaviour of Materials. Boston, Massachusetts, 16-20Aug 1976. pp 627-631.*